

PDF hosted at the Radboud Repository of the Radboud University Nijmegen

The following full text is a publisher's version.

For additional information about this publication click this link.

<http://hdl.handle.net/2066/145576>

Please be advised that this information was generated on 2018-07-07 and may be subject to change.

Electron Spin Echo Envelope Modulation
Spectroscopy of Disordered Solids

J.J. Shane

ELECTRON SPIN ECHO ENVELOPE MODULATION SPECTROSCOPY OF DISORDERED SOLIDS

An investigation of ^{14}N coordination in transition metal complexes

ELECTRON SPIN ECHO ENVELOPE MODULATION SPECTROSCOPY OF DISORDERED SOLIDS

An investigation of ^{14}N coordination in transition metal complexes

een wetenschappelijke proeve op het gebied van de Natuurwetenschappen

PROEFSCHRIFT

TER VERKRIJGING VAN DE GRAAD VAN DOCTOR
AAN DE KATHOLIEKE UNIVERSITEIT NIJMEGEN,
VOLGENS BESLUIT VAN HET COLLEGE VAN DECANEN
IN HET OPENBAAR TE VERDEDIGEN OP
MAANDAG 13 DECEMBER 1993,
DES NAMIDDAGS TE 3.30 UUR PRECIES

DOOR

JOHAN JACOB SHANE
GEBOREN OP 2 JULI 1966 TE LEIDEN.

FEBOdruk, Enschede
1993

promotor: Prof. Dr. E. de Boer
co-promotor: Dr. E.J. Reijerse

CIP-GEGEVENS KONINKLIJKE BIBLIOTHEEK, DEN HAAG

Shane, Johan Jacob

Electron spin-echo envelope modulation spectroscopy of
disordered solids : an investigation of ^{14}N coordination
in transition metal complexes / Johan Jacob Shane. -

[S.l. : s.n.] (Enschede : FEBODruk). - III.

Proefschrift Nijmegen. - Met lit. opg.

ISBN 90-9006621-7

Trefw.: spectroscopie / EPR / ESEEM

Voorwoord

Op deze plaats wil ik een aantal mensen bedanken die direct en indirect bijgedragen hebben aan de totstandkoming van dit proefschrift. Ik heb bijzonder veel te danken aan Harry Verhulst en Pieter van der Heiden die, in het kader van hun hoofdvakstage, zeer intensief hebben bijgedragen aan de metingen en de simulaties waarover in hoofdstuk 5 gerapporteerd wordt. Peter Hofer mochte ik danken für unsere Zusammenarbeit und für seine Hilfe bei den HYSORE Experimenten.

Adri Klaassen is in de afgelopen jaren mijn leermeester op technisch gebied geweest. Veel van het technische werk beschreven in dit proefschrift is in nauwe samenwerking met Adri gedaan. Wanneer Adri niet beschikbaar was kon ik altijd vertrouwen op Gerrit Janssen wanneer technische ondersteuning noodzakelijk was.

Mijn dank gaat uit naar Arno Kentgens en Fred Hagen voor het kritisch doorlezen van het manuscript. Hun commentaren zijn zeer waardevol gebleken. De vele opmerkingen van mijn collega's hebben er ook toe bijgedragen dat het proefschrift leesbaarder is geworden. Verder wil ik in het bijzonder mijn vader bedanken die ervoor zorg gedragen heeft dat het engels niet al te gruwelijk is.

De cartoons die dit proefschrift opvrolijken zijn bedacht door Gerrit Janssen, Pieter van Dam en Jean Paul Willems. Deze laatste heeft de taak op zich genomen de bedenkzels te tekenen. Het resultaat van hun moeite is in de computer overgebracht door John Shippens van de afdeling illustratie, die tevens de tekening van de resonator op pagina 17 gemaakt heeft.

Peter van Campen, Jos Alsters en Willem Jan Karman van de afdeling C&CZ stonden altijd gereed met raad, daad en diskrimtie wanneer dat nodig was. Ook daarvoor mijn dank. Het secretariale werk kon ik met een gerust hart aan Desiree van der Wey overlaten.

Velen hebben mij in de laatste jaren verteld dat het leven niet alleen uit werk alleen bestaat. Misschien hebben ze daar gelijk in. Mijn dank gaat in ieder geval uit naar alle leden van de vakgroep Molecuulspectroscopie, de leden van 'Casus Belli' en andere vrienden en kennissen die invulling hebben gegeven aan het leven buiten het werk. In het bijzonder wil ik Rita bedanken voor alle gesprekken over het werk en over het leven.

Jaap Shane
Nijmegen 7 Oktober 1993

Manuscriptcommissie:

Dr. W.R. Hagen, Landbouw Universiteit Wageningen

Dr. A.P.M. Kentgens, Katholieke Universiteit Nijmegen

Contents

1	Introduction	3
1 1	The ESEEM experiment	4
1 2	Summary	5
2	Instrumental	9
2 1	The X-band CW/pulse microwave bridge	9
2 2	The C band ESE microwave bridge	11
2 3	Accumulation of the echo intensity	14
2 4	The resonator	14
2 5	The pulse generator	18
2 6	Data acquisition using an IBM PC/AT computer	20
3	The theory of ESEEM	31
3 1	The density matrix in EPR	31
3 2	The Electron Spin-Echo Phenomenon	39
3 3	Phase cycling in three- and four-pulse experiments	46
3 4	An expression for the nuclear modulation effect	52
3 5	A shorthand notation	56
3 6	The HYSCORE experiment	58
3 7	The modulation intensity in HYSCORE	61
3 8	Simulating HYSCORE spectra	68
4	HYSCORE of Disordered Solids	73
5	ESEEM on copper-doped <i>l</i>-histidine	83
5 1	Introduction	83
5 2	Experimental	85
5 3	Theory	87
5 4	ESEEM of single crystals	88
5.5	ESEEM of Powders	95
5 6	Conclusions	107
6	ESEEM of Nitrogen-coordinated Oxo-Vanadium(IV) Complexes	111
6 1	Introduction	111
6 2	Experimental	112
6 3	ESEEM experiments	112

6.4	Interpretation of sharp features in powder ESEEM	116
6.5	Interpretation of powder ESEEM spectra	117
6.6	Spectral simulations	119
6.7	Interpretation of orientation-selective ESEEM spectra	120
6.8	Conclusions	122
7	1- and 2-D ESEEM of Oxo-Vanadium Complexes	125
7.1	Introduction	126
7.2	Experimental	128
7.3	EPR and orientation selective ESEEM	128
7.4	2D-ESEEM experiments	137
7.5	Discussion	138
7.6	Concluding remarks	138

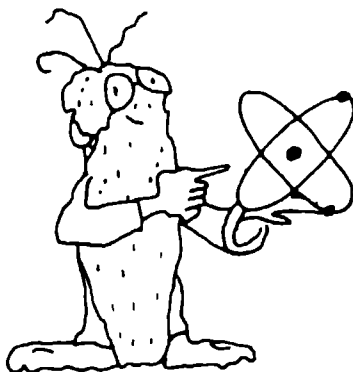
Chapter 1

Introduction

The last 15 years have seen a dramatic growth in the field of pulsed EPR. The developments in fast electronics and microwave equipment have overcome the serious problems that had stood in the way of pulsed EPR since the first experiments were performed in 1958. A great number of new pulsed EPR techniques have been proposed in recent years, and since 1988 a commercial FT-EPR spectrometer has been available.

Electron paramagnetic resonance spectroscopy was invented nearly fifty years ago by E. Zavoiskii [1, 2]. Shortly after, the technique was extended to nuclear spins by Bloch, Purcell, and Pound [3, 4]. Because the nuclear magnetic resonance experiment is technically less demanding than the EPR experiment, the developments in pulsed magnetic resonance were concentrated in NMR. In 1946, Bloch [5, 6] presented the first pulsed NMR experiments. Unfortunately, these developments could not easily be carried over to electron paramagnetic resonance because the direct detection of the free induction decay in the pulsed NMR experiment is not usually feasible in EPR.

The discovery of spin-echoes by Erwin Hahn in 1950 [7] provided a way out of this dilemma. The first electron spin-echo experiments were done in 1958 by Gordon and Bowers [8] with the aim of determining spin relaxation rates. One year earlier, Blume [9] had measured the electron spin relaxation rates in sodium-ammonia solutions using pulsed EPR at a frequency of 17.4 MHz (6.2 Gauss), but Gordon and Bowers's experiment is perhaps more significant in the development of pulsed EPR techniques because it used a frequency in the microwave region.



The next step in the development of pulsed EPR occurred in 1961, when Mims *et al* [10] reported the observation of ^{183}W modulations on the electron spin-echo decay envelope in CaWO_4 . These experiments were subsequently explained in more detail in a paper by Rowan, Hahn and Mims [11], titled 'Electron-Spin-Echo Envelope Modulation' published in 1965. Seven years later, W.B. Mims, one of the pioneers in the field of ESEEM, published a number of well-known papers on ESEEM [12, 13], in which he explained in detail the working of the ESEEM experiment and also presented the expressions that govern the modulation intensity of the spin-echo signal under idealized conditions. These expressions formed the basis of much of the research of later years.

In the wake of the development of two-dimensional NMR experiments by Jeener [14], Merks and de Beer [15] developed a two-dimensional variant of the ESEEM experiment. The 1980's saw the emergence of a multitude of new experiments. This was facilitated by the availability of the electronics and microwave components necessary for these experiments. Note especially the development of the HYSORE technique by Hofer in 1986 [16] and the emergence of multifrequency techniques by Singel and co-workers [17, 18, 19]. Together with the orientation selection technique known from ENDOR these techniques form the basis of the experiments discussed in this thesis.

1.1 The ESEEM experiment

In CW-EPR, small electron-nuclear interactions are often hidden within the inhomogeneous linewidth. These interactions can, however, often be resolved using ESEEM or ENDOR spectroscopy. With these techniques it becomes possible to determine the coupling parameters of weakly bound or remote nuclei, making these techniques very suitable for elucidating the electronic and spatial structure of paramagnetic metallo-organic compounds, among which many transition metal compounds. The mechanism of the ESEEM experiment is discussed in chapter 3 and [20]. The latter reference gives an excellent overview of the field of ESEEM.

An important application of ESEEM spectroscopy is in the field of metalloenzyme research, where it is used for the elucidation of the electronic structure of the active site. The parameters describing the electronic and nuclear spin systems, such as the hyperfine and quadrupole parameters, give accurate information on the electronic and spatial structure of the local environment of the metal ion. These parameters are most accurately determined from single crystals. A significant problem in the investigation of metalloenzymes and other biologically relevant systems is that they are generally not available as single crystals, limiting investigations to the use of powders or frozen solutions.

This thesis addresses the problems associated with ESEEM spectroscopy of ^{14}N (spin $I = 1$) nuclei in orientationally disordered systems, especially those present in ligands of the metal ion in metalloenzymes. Model compounds for two classes of enzymes with significantly different spectroscopic properties have been studied.

- Chapter 5 discusses single crystals and powders of copper-doped *l*-histidine, which is a model system for Type II copper-containing enzymes, such as laccase and β -dopamine hydroxylase.

- Chapters 6 and 7 discuss a number of model compounds for oxo-vanadium containing enzymes as bromoperoxidase.

We have investigated these systems using multidimensional, multifrequency and orientation selective ESEEM techniques in an attempt not only to determine the structure of these model compounds but also to demonstrate and investigate the applicability of these methods.

1.2 Summary

This thesis consists of seven chapters, including this introduction. Chapter 2 describes the equipment that was developed and used in the course of the project described in this thesis. The first part of this chapter contains a description of the spectrometer hardware, including the microwave bridges and resonators used. The second part describes the computer and software that was used for data acquisition. This chapter represents a significant part of the project.

Chapter 3 introduces the theory of ESEEM. In contrast to many texts, the spin echo phenomenon is introduced using the density matrix formalism which is then used throughout the chapter to discuss the nuclear modulation effect and the theory of the HYSCORE experiment. In this chapter, general expressions are derived that describe the modulation patterns observed in the HYSCORE experiment. Chapter 4 then continues with a description of the use of the HYSCORE experiment in the investigation of disordered solids. This chapter has been published in the *Journal of Magnetic Resonance* [21].

Chapters 5 through 7 describe the experiments performed on a number of model compounds. Chapter 5 compares the results of single crystal ESEEM experiments of copper-doped *l*-histidine with those obtained from the powdered material. In this way it is possible to investigate the accuracy of information derived from powder-ESEEM experiments, including multifrequency experiments, multidimensional (2-D three-pulse) experiments and orientation selective ESEEM. The coupling parameters of the remote imidazole nitrogen are used for the determination of the local structure around the metal ion. The copper-doped *l*-histidine sample is taken as a model system for many blue (type II) copper enzymes. This type of system has attracted great attention from a number of research groups [22, 23, 24, 25]. This chapter has been submitted for publication in *Applied Magnetic Resonance* [26].

Model systems representing a second class of metalloenzymes are studied in chapters 6 and 7. For oxo-vanadium systems the spectral properties are completely different from those of the type II copper enzymes. In this case the nitrogen nuclei that are studied are directly bound to the metal ion, but the electron nuclear coupling is very weak. The multifrequency experiments that were so significant in the study of the copper system of chapter 5 are now less useful, but for these systems it appears that the two-dimensional HYSCORE technique is very powerful. These two articles have been published in the proceedings of the 1989 (chapter 6) and 1991 (chapter 7) conferences on Electron Magnetic Resonance of Disordered Solids, held in Pravitz and in Gjulechitsa, Bulgaria [27, 28].

References

- [1] E. Zavoiskii Paramagnetic relaxation of liquid solution for perpendicular fields. *Fyz Zh* **9** (1945) 211
- [2] E. Zavoiskii Spin-magnetic resonance in paramagnetic substances. *Fyz Zh* **9** (1945) 245
- [3] F. Bloch Nuclear Induction. *Physical Review* **69** (1946) 127
- [4] E. M. Purcell, H. C. Torrey, and R. V. Pound. Resonance absorption by nuclear magnetic moments in a solid. *Physical Review* **69** (1946) 37
- [5] F. Bloch. Nuclear Induction. *Physical Review* **70** (1946) 460
- [6] F. Bloch, W. W. Hansen, and M. Packard. The Nuclear Induction Experiment. *Physical Review* **70** (1946) 474
- [7] E. L. Hahn. Spin Echoes. *Physical Review* **80** (1950) 580.
- [8] J. P. Gordon and K. D. Bowers. Microwave spin echoes from donor electrons in silicon. *Physical Review Letters* **1** (1958) 368
- [9] R. J. Blume. Electron Spin Relaxation Times in Sodium-Ammonia Solutions. *Physical Review* **109** (1958) 1867
- [10] W. B. Mims, K. Nassau, and J. D. McGee. Spectral Diffusion in Electron Resonance Lines. *Physical Review* **123** (1961) 2059
- [11] L. G. Rowan, E. L. Hahn, and W. B. Mims. Electron Spin Echo Envelope Modulation. *Physical Review A* **137** (1965) 61.
- [12] W. Mims. Electron Spin Echoes. In S. Geschwind, editor, *Electron Paramagnetic Resonance*, p. 263. Plenum Press, New York, 1972
- [13] W. B. Mims. Envelope Modulation in Spin-Echo Experiments. *Physical Review* **5** (1972) 2409
- [14] J. Jeener, 1971. Ampère International Summer School, Basko Polje - Yugoslavia.
- [15] R. P. J. Merks and R. de Beer. Two-dimensional Fourier transform of electron spin echo envelope modulation. An alternative for ENDOR. *Journal of Physical Chemistry* **83** (1979) 3319.
- [16] P. Hofer, A. Grupp, H. Nebenfur, and M. Mehring. Hyperfine sublevel correlation (HYSCORE) spectroscopy: A 2D ESR Investigation of the squaric acid radical. *Journal of Chemical Physics* **132** (1986) 279.

1.2. SUMMARY

- [17] H. L. Flanagan and D. J. Singel. The impact of excitation frequency on the nuclear modulation of electron spin echoes: ^{14}N hyperfine and quadrupole interactions of DPPH in disordered solids. *Chemical Physics Letters* **137** (1987) 391.
- [18] H. L. Flanagan and D. J. Singel. Analysis of ^{14}N ESEEM patterns of randomly oriented solids. *Journal of Chemical Physics* **87** (1988) 5606.
- [19] S. A. Cosgrove and D. J. Singel. Implications of Hyperfine Anisotropy on the Determination of ^{14}N Quadrupole Interactions from Double Quantum ESEEM Frequencies. *Journal of Physical Chemistry* **94** (1990) 8393.
- [20] S. A. Dikanov and Y. D. Tsvetkov. *Electron Spin Echo Envelope Modulation (ESEEM) Spectroscopy*. CRC Press, Boca Raton, 1992.
- [21] J. J. Shane, P. Höfer, E. J. Reijerse, and E. de Boer. Hyperfine Sublevel Correlation Spectroscopy (HYSCORE) of Disordered Solids. *Journal of Magnetic Resonance* **99** (1992) 596.
- [22] W. B. Mims and J. Peisach. Assignment of a ligand in Stellacyanin by a Pulsed Electron Paramagnetic Resonance method. *Biochemistry* **15** (1976) 3863.
- [23] W. B. Mims and J. Peisach. The Nuclear Modulation effect in Electron Spin Echoes for Complexes of Cu^{2+} and Imidazole with ^{14}N and ^{15}N . *Journal of Chemical Physics* **69** (1978) 4921.
- [24] F. Jiang, J. McCracken, and J. Peisach. Nuclear Quadrupole Interactions in Copper(II)-Diethylenetriamine-substituted Imidazole Complexes and in Copper(II) Proteins. *Journal of the American Chemical Society* **112** (1990) 9035.
- [25] D. Goldfarb, J. M. Fauth, O. Farver, and I. Pecht. Orientation Selective ESEEM Studies on the Blue Oxidases Laccase and Ascorbate Oxidase. *Applied Magnetic Resonance* **3** (1992) 333.
- [26] J. J. Shane, P. A. A. M. van der Heijden, E. J. Reijerse, and E. de Boer. An ESEEM investigation of single crystals and powders of copper-doped *l*-histidine hydrochloride monohydrate. Submitted for publication in *Applied Magnetic Resonance*.
- [27] E. J. Reijerse, J. J. Shane, E. de Boer, and D. Collison. ESEEM of nitrogen coordinated Oxo-Vanadium(IV) complexes. In N. D. Jordanov, editor, *Electron Magnetic Resonance of Disordered systems I*, pp. 189–204. World Scientific, Singapore, 1989.
- [28] E. J. Reijerse, J. J. Shane, E. de Boer, P. Höfer, and D. Collison. One and two dimensional ESEEM of nitrogen coordinated Oxo-Vanadium(IV) complexes. In N. Jordanov, editor, *Electron Magnetic Resonance of Disordered systems II*, p. 253. World Scientific, Singapore, 1991.

Chapter 2

Instrumental

This chapter describes the home-built ESE spectrometer used in many of the experiments presented in this thesis. The following sections describe in detail the microwave bridges and echo registration, the microwave resonator, the pulse formation and the data acquisition computer and program. The home-built spectrometer is an extensive redesign of the spectrometer described earlier [1]. The upgraded spectrometer supports multifrequency experiments and complex multi-pulse sequences, such as those used in the HYSORE experiment [2].

2.1 The X-band CW/pulse microwave bridge

The X-band pulse bridge, shown in figure 2.1, is built around a modified Varian E-101 CW-bridge with some additions specific to the pulsed experiments. These additions consist of a two-channel pulse former-unit⁶⁻¹⁰, an amplifier chain¹¹⁻¹³ and echo detection components²⁰⁻²⁴. The numbers refer to figure 2.1.

The external HP 8620C sweep oscillator², equipped with an 86250D RF plug-in unit, can be used for microwave frequencies between 8 and 11 GHz. When operating the spectrometer at microwave frequencies around 9.5 GHz it can be advantageous to use the klystron¹, especially with HYSORE experiments that benefit from the higher available power and better frequency stability of the klystron compared to the sweep oscillator. Approximately 20% of the available source power is used for the pulse and CW reference arms^{3,4}, and the remainder is channelled to a home-built waveguide switch⁵. This switch can bypass the pulse-former unit and amplifier chain to operate the spectrometer in a CW-mode.

The pulse former unit contains two independent channels capable of generating short microwave pulses of 10 ns or longer. The channels are attached to a magic T⁶, whose outputs are balanced by two isolators. Each channel contains a manually controlled waveguide attenuator, used to set the microwave power level of the channel, and a high-speed microwave switch⁷ (Aerotech ASD 1003-1N). One of the channels also contains a manual waveguide phase shifter, which is used to balance the phases of the channels. The phase of the combined output⁸ of the two channels can be changed by 180° using a high-speed digital phase shifter⁹ (Triangle Microwave Inc. DP-61). A high-speed microwave switch¹⁰ (Alpha MT8675H1) with a switch-time of less than 2 ns generates the microwave pulse train.

The amplifier chain can be bypassed for tuning using manually controlled microwave switches¹¹. If the amplifier chain is enabled, the output power of the pulse former unit is

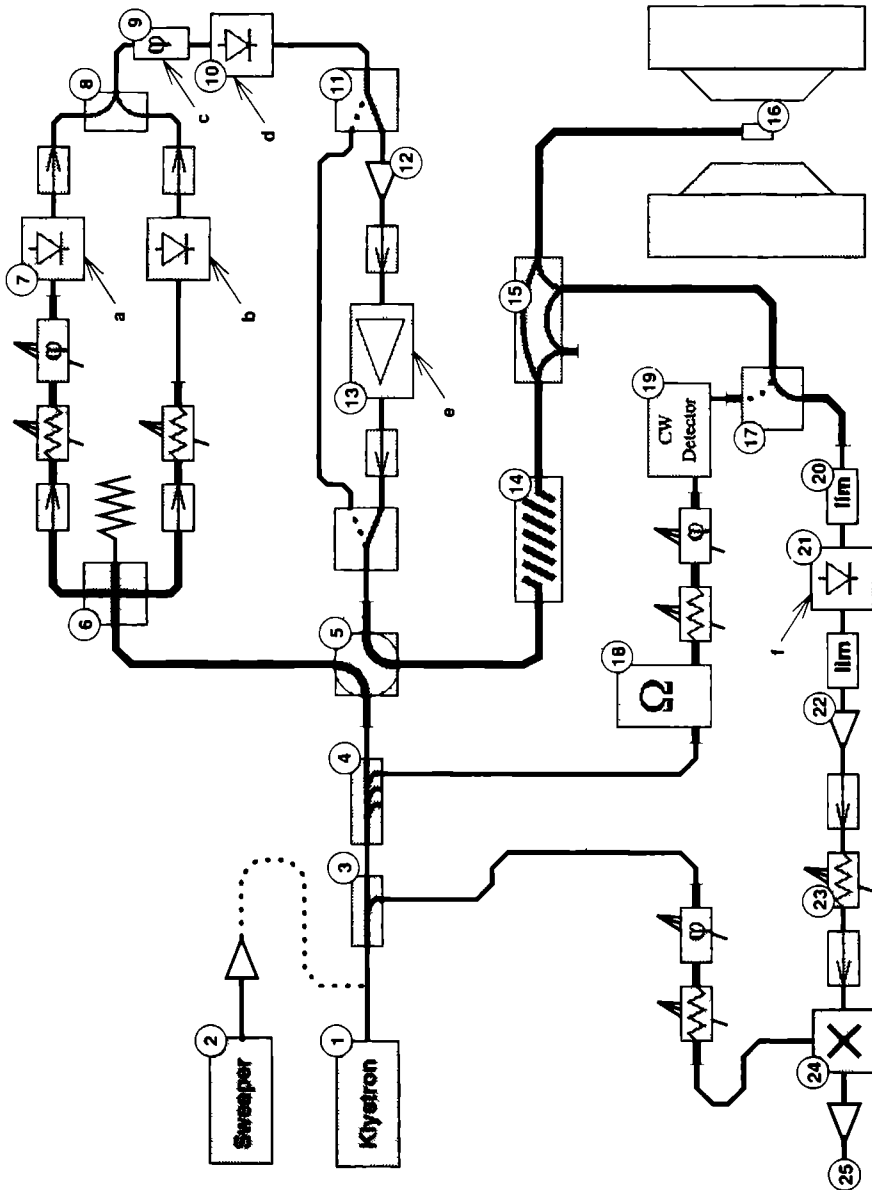


Figure 2.1: Schematic diagram of the hybrid X-band bridge. See text for a description of its operation. Arrows a through f indicate outputs of the pulse generator.

fed into a Miteq AMF-3B-8012-20P medium power solid state pre-amplifier¹², which boosts the microwave power to about 100 mW, near the saturating input for the main pulse amplifier¹³, a modified Litton 624 with a rated output power of 1000 W. The saturated output power of the main amplifier passes through the rotating vane attenuator¹⁴ of the Varian bridge, used for setting the correct microwave pulse amplitude, and is channelled into the four-port circulator¹⁵. The reflected power and echo signals from the resonator¹⁶ are diverted by the circulator into a second waveguide-switch¹⁷. This switch is used to select between pulse and CW detection. The built-in AFC circuitry of the CW detector¹⁹ is used to lock the microwave frequency to the resonant frequency of a HP X532B frequency meter¹⁸ when the klystron is used as a microwave source. In this case, the CW detector is also used for tuning. The presence of the switches (5) and (17) allows the bridge to be used as a CW bridge.

When pulse experiments are performed, the switch (17) diverts the microwave energy to the pulse detection arm²⁰⁻²⁴. A high-power limiter²⁰ is used in conjunction with a fast microwave switch²¹ to protect the detection circuit from the 1000W excitation pulses. A Miteq AMF-3S-8998-22L low-noise GaAs-FET amplifier²², protected from any remaining pulse power by a P&H Labs C1-X153112 medium-power limiter, boosts the very weak echo signal by about 27 dB. The echo signal is passed through a Merrimac AUMP-25AKX coaxial attenuator²³, into a mixer. The attenuator is used to limit extremely strong echo signals. The resultant RF signal from the Aertech MX12000A mixer²⁴ is amplified by a Trontech W250K-1 wideband video amplifier²⁵ to levels appropriate for the echo registration equipment. The detection circuit is enclosed in an aluminum box to shield it from stray microwave radiation from other parts of the bridge, which may cause additional noise or spurious signals.

The waveguide attenuators, phase shifters and isolators used in this microwave bridge are from a number of different manufacturers. Isolators have been placed at appropriate places in the bridge as indicated in the figure. At some places, notably near the mixer, DC-blocks have been placed to prevent ground-loops.

2.2 The C-band ESE microwave bridge

The C-band bridge shown in figure 2.2 is very similar in design to the X-band bridge. The most notable difference between the two bridges is the lack of CW capabilities of the C-band bridge.

The microwave power source of the C-band bridge is a Giga Modules GMY 0408-17 YIG oscillator¹, the output frequency of which is controlled by the highly stable home-built voltage source described below. A MAC P8205-2 power divider² directs one half of the source power to the reference signal, while the other half is used in the excitation arm. A digital phase modulator, consisting of an MRC H412-180 hybrid splitter/combiner³ and a high-speed Norsal E 169119-1 bi-throw switch⁴, is used to select in-phase or 180° out-of-phase microwave signals. The output of this phase modulator is amplified to levels near 1 W by a HP 493A TWTA⁵. An attenuator⁶ reduces the power level to protect the pulse former unit⁷⁻¹¹.

The pulse-former unit in the C-band bridge is somewhat simpler than that of the X-band bridge. The outputs of a Merrimac PDM-22-6G power splitter/combiner⁷ are balanced by two isolators to supply the two branches with equal in-phase microwave power. One of the channels⁸

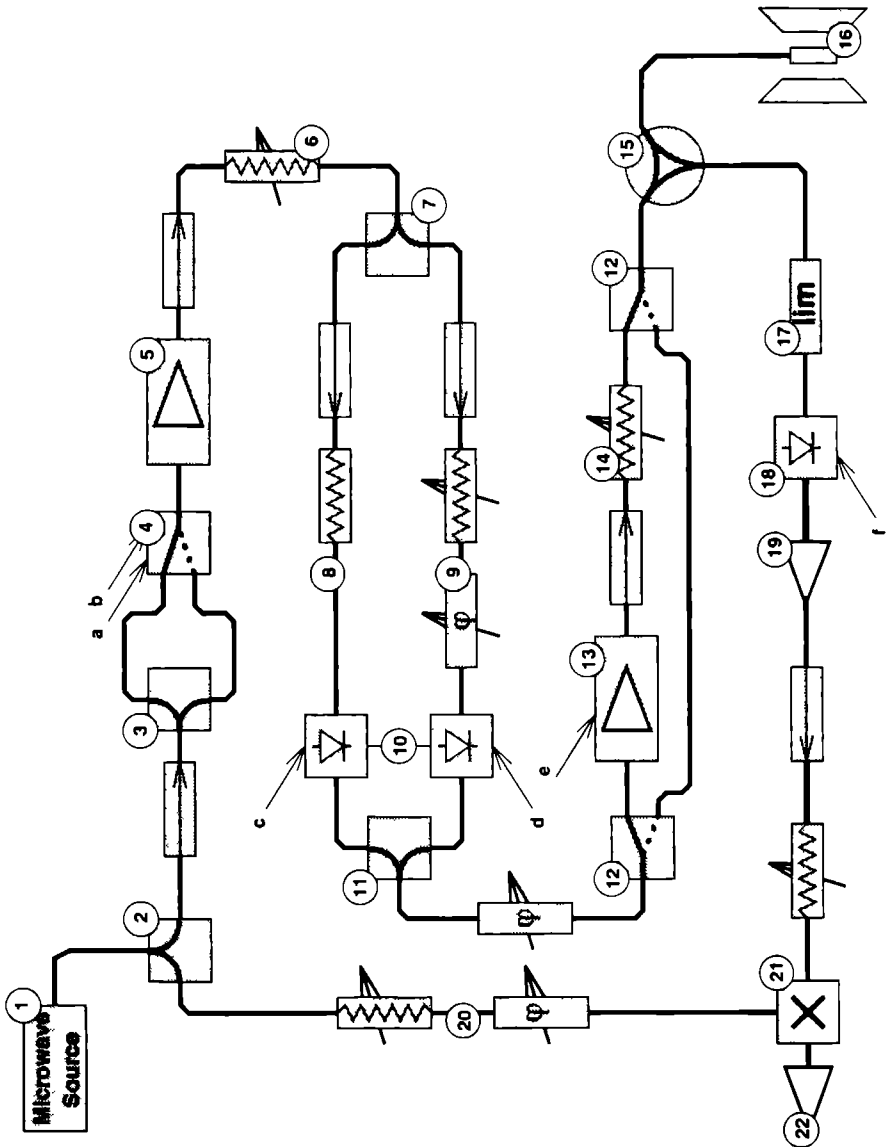


Figure 2.2: Schematic diagram of the C-band pulse bridge. Its operation is explained in the text. The devices that are switched by the pulse generator are indicated by arrows labelled a through f.

is limited to a fixed attenuation and phase. The other channel⁹ is freely variable in both amplitude and phase. Using high-speed Norsal S1970D switches¹⁰, each of the two channels can be enabled to form short (5 ns) pulses. The output of the two channels is fed into a Merrimac combiner similar to (7). A phase shifter at the output of this combiner is used to influence the overall phase of the microwaves. The overall power can be adjusted using the attenuator (6).

The amplifier chain of the C-band bridge contains only one amplifier, since pre-amplification of the microwave signal is done earlier⁵. Using the Teledyne CS33S10 relays¹², the amplifier chain can be bypassed for tuning. The amplifier is a custom-built M-square Microtek M303 amplifier¹³ with a frequency range of 4–8 GHz and a rated output power of 200 W. Alternatively, for frequencies above 6.5 GHz, the Litton 624 amplifier can be used. The pulse energy can be reduced by the attenuator¹⁴. A high-power Teledyne C-4S63U-50 circulator¹⁵ channels the excitation pulses into the resonator¹⁶ and diverts the reflected power into the detection circuit^{17–22}.

This detection circuit, protected by a MACOM 2690-1006 fast-recovery high-power limiter¹⁷, consists of a third Norsal S1970D switch¹⁸ and a Miteq AMF-AFS4-04000800-16-10P-L-5 low-noise amplifier¹⁹. The output signal of this amplifier can be attenuated if required and is mixed with a reference signal²⁰ using a Miteq M0408 mixer²¹. The same Trontech W250K-1 RF amplifier²² used in the X-band bridge is used for final amplification of the mixer signal.

Except for the high-power attenuator¹⁴, all attenuators used in the C-band bridge are manufactured by Merrimac, type AUMP 15ATX. The coaxial phase shifters are built from a circulator (Marconi F7119-05) and a sliding short (Maury 1909D2). As for the X-band bridge, isolators have been placed at the indicated places, and DC-blocks are used at strategic points to prevent ground loops.

Stability of the C-band YIG oscillator

To utilize the full capability of the C-band bridge, the YIG oscillator must be able to generate microwave radiation with a frequency between 4 GHz and 8 GHz. At the same time, it must have sufficient long-term stability to perform HYSORE experiments and the FM noise should not contribute significantly to the overall noise level. To estimate the maximum allowable frequency drift and FM noise, we must compare these to the width of the resonant band of the resonator, defined by its Q -factor and resonant frequency. For a frequency of 5 GHz and a Q -factor of 500, which are typical values for a C-band spectrometer, this width is about 10 MHz. The influence of the FM noise and frequency drift expresses itself mainly in a change in the microwave field intensity in the resonator. To ensure that this intensity is constant, the microwave frequency must not change more than approximately 10% of the resonant width, i.e., it must be constant to within about 1 MHz.

The output frequency of the YIG oscillator can be regulated by applying a voltage between 0 and 10 V to its frequency modulation input, where 0 V corresponds to a frequency of 4 GHz, and 10 V to a frequency of 8 GHz. The required frequency stability necessitates an input voltage that is stable to within 2.5 mV. This stability can be achieved using an active feedback circuit that corrects for changes in the microwave frequency or it can be obtained using a regulated voltage source that is stable to within those limits. The use of an active feedback circuit using a source-locking frequency counter, such as an EIP model 575B, has been proposed earlier

(see e.g. [3] for an application) Using this technique, it is possible to achieve a frequency stability better than 50kHz, which is sufficient even for CW applications. Our spectrometer uses a stabilized voltage source with a low frequency noise level and long term stability of better than 1 mV, which is sufficient for pulsed applications involving echo detection but precludes the use of the oscillator in a CW spectrometer or for FT EPR. The high frequency component of the noise of the regulator voltage is in all cases effectively filtered out by the response-time of the oscillator, but never exceeds 2 mV in our spectrometer.

2.3 Accumulation of the echo intensity

The output signal of the video amplifier of the microwave bridges, (25) in figure 2.1 and (22) in figure 2.2, shows not only the echo signal, but also a number of spurious signals from microwave pulses that were not stopped by the limiters and switches in the detection circuits of the microwave bridges. By selectively measuring only when the echo signal occurs, these spurious signals can be eliminated. In most ESEEM experiments there are also a number of unwanted echo signals present [1, 4] which can be removed by an appropriate phase cycling, to be discussed later.

An EG&G PAR 162 boxcar averager with two PAR 164 gated integrator input modules is used to measure and accumulate the intensity of the echo signal. One of the integrators is gated to detect only the peak echo intensity (see figure 2.5). The typical gate duration is about 50 ns, but can be as low as 20 ns. The second gated integrator is used to eliminate the noise contribution caused by the instability of the baseline of the echo signal. This integrator samples only the baseline, but not the echo signal. The gate duration and amplification factor of the two gated integrators are carefully matched so that their difference gives the true echo intensity. When the baseline is sufficiently stable the second integrator is not used, because it would only add noise to the echo signal.

To further increase the signal to noise ratio, the pulse sequence is usually repeated 10–1000 times, depending on the noise level. The boxcar averager records the total echo intensity, which is probed by the analog-to-digital converter connected to the data acquisition computer when all repetitions have been performed. The boxcar averager is then reset clearing all previously accumulated signals. In this way a linear (unweighted) averaging of the echo intensity is performed. The optimum repetition rate for pulse sequences strongly depends on the T_1 relaxation time of the magnetization in the sample. It can be shown numerically that the optimum repetition time $t_{\text{rep}} \approx 1.1 T_1$. Typical repetition rates are between 400 and 4000 sequences per second.

2.4 The resonator

Introduction

The types of resonators used in ESE experiments vary widely. The classic TE₁₀₂ rectangular cavity is not very well suited to pulsed EPR experiments, due to its high Q and low filling factor and thus many authors have proposed other geometries for resonators [5, 6]. One of the most

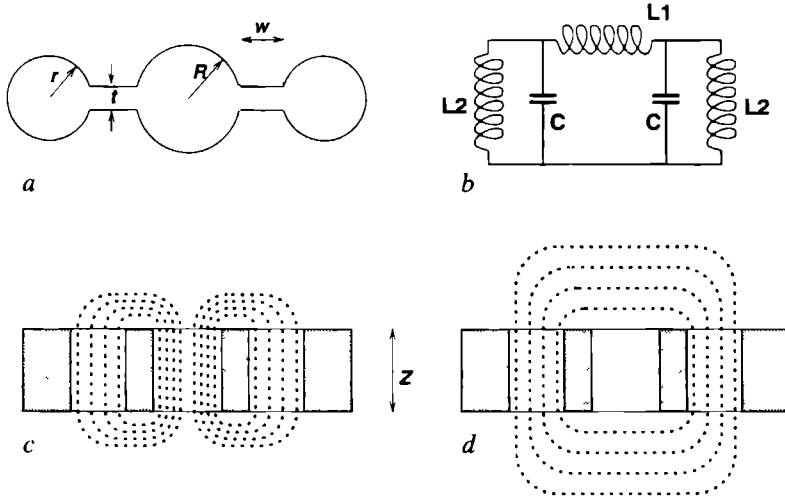


Figure 2.3: Schematic diagrams of the 3-loop-2-gap resonator. *a*: geometry of the resonator. *b*: RCL equivalent circuit of the resonator. Dissipative resistances are not shown. *c* and *d*: resonant modes of the three-loop two-gap resonator. Only the mode shown in *c* is used.

popular resonators is the loop-gap resonator [7, 8], which combines a low Q-factor with a high filling-factor, making it very suitable for pulsed EPR applications.

There are a great variety in implementations of the lumped-circuit loop-gap resonator, such as the bridged loop-gap resonator [9], the split-ring resonator [10], and a number of variations of two-slit [11, 12], two-loop one-gap [13] and three-loop two-gap resonators [14, 15]. The resonators used in the ESE spectrometer described here are loop-gap resonators of the three-loop two-gap type.

Electromagnetic properties of the three-loop two-gap resonator

The three-loop two-gap resonator is schematically shown in figure 2.3*a*. In our design, the two outer loops have the same diameter, which may be different from that of the inner loop. Both gaps have the same width t . The equivalent circuit, consisting of two capacitances and three inductances, is shown in figure 2.3*b*. The resonant frequency of this equivalent circuit can be calculated [15] as:

$$\nu = \frac{1}{2\pi} \left(\frac{L_1 + 2L_2}{L_1 L_2 C} \right)^{1/2}, \quad (2.1)$$

where the lumped-circuit inductances L_1 and L_2 and the capacitance C are

$$L_1 = \frac{\mu_0 \pi R^2}{Z}, \quad L_2 = \frac{\mu_0 \pi r^2}{Z}, \quad C = \frac{\epsilon_0 w Z}{t}, \quad (2.2)$$

where Z is the height of the resonator. R , r , w and t are defined in figure 2.3*a*. Note that the height Z of the resonator does not occur in the expression for the resonant frequency of its equivalent circuit. This frequency of the equivalent circuit is only an approximation to the

resonant frequency of the resonator itself, since we have neglected all edge effects. Expressions for the frequency in which some of these effects are included have been derived by Wood *et al* [14].

The three-loop two-gap resonator has two resonant modes, displayed in figures 2.3c and d, that differ significantly in resonant frequency. The high-frequency mode (figure 2.3c) has a higher Q than the fundamental mode (figure 2.3d), as determined by Wood *et al*. As shown in figure 2.3, the high-frequency mode is confined to a much smaller region of space than the fundamental mode. In our designs, only the high-frequency mode is used because the sample is placed in the central loop. This mode can be coupled to a coaxial transmission line by placing a single-turn loop at the end of the coaxial line directly above either of the outer loops, as used in our resonator, or directly above the central loop [16]. Alternative coupling strategies have been proposed by Hyde and co-workers [15, 17].

Mechanical design and performance

Figure 2.4 shows an exploded view of the loop-gap resonator and of the structure in which it is mounted. The resonator allows the use of both single crystal samples and powdered or liquid samples in a quartz tube. When single crystals are used, these can be rotated within the resonator. When used with a magnet which is mounted on a rotating base, the crystal can be placed in any orientation with respect to the external magnetic field. Coupling of microwave energy to the resonator is accomplished by a single-turn coil at the end of a coaxial transmission line which is mounted above one of the side loops. The distance of the coupling coil from the resonator can be varied to change the coupling characteristics, the latter can also be changed by rotating the coil. When used in a bath- or flow cryostat, the entire structure can be isolated to prevent liquid helium from entering the gaps and changing the resonant frequency.

The resonator itself always has a standard geometry, it consists of two parts that are tightly screwed together, forming a block of standard size (27 mm \times 9.7 mm \times 6 mm). The center of each outer loop is always exactly 7 mm from the center of the middle loop. Using this standard geometry, resonators with different resonant frequencies or other characteristics can be used in the same mount, and changing resonators becomes very easy. Resonators are manufactured from standard size aluminum blocks. These are screwed together and milled to the standard size, after which the loops are drilled at the appropriate places. The resonator is then taken apart and the two protrusions in each of the halves are carefully milled to the correct height, after which the two halves are thoroughly cleaned and screwed together again. The entire procedure takes only a few hours.

The resonant frequency of the resonator can be selected by choosing appropriate values for the loop diameters (R and r) and gap width (t). The length w in mm of the gaps is fixed by the loop diameters, $w = 7.0 - (R + r)$. The central loop is generally 5.2 mm in diameter, to accommodate standard EPR tubes, but resonators having a sample loop diameter of less than 2 mm have been manufactured and used. For most resonators, the outer loops are 4 mm in diameter. Resonators have been manufactured for microwave frequencies ranging from 4.1 GHz to 10.5 GHz. Gap widths are usually around 0.4 mm, but resonators with gap widths of about 0.1 mm have also been used. The required gap width t for a given r , R and resonant frequency

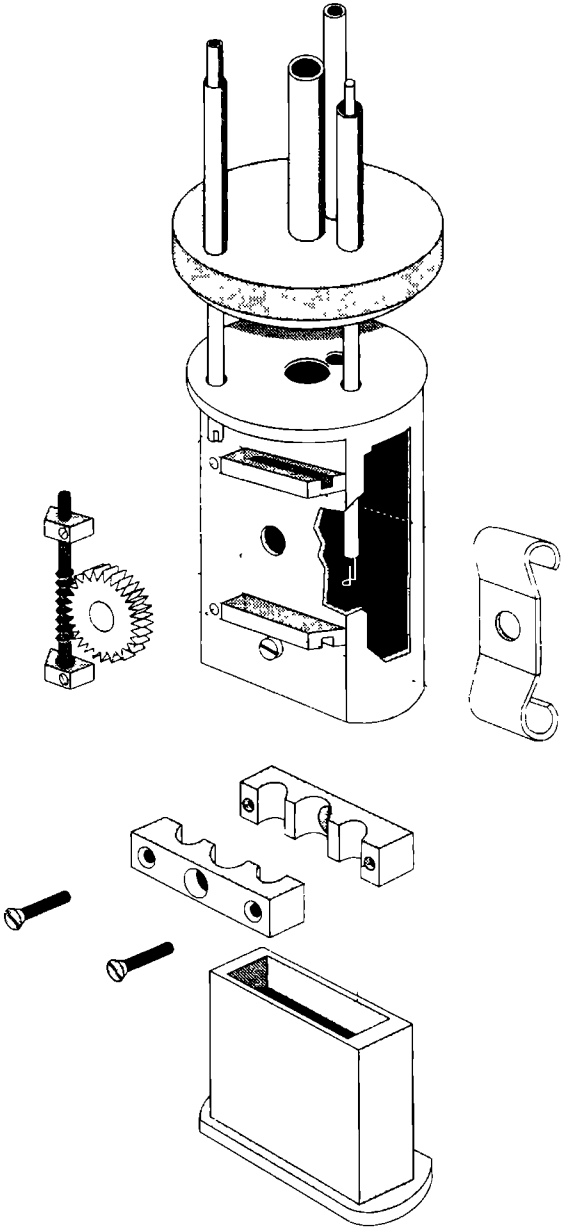


Figure 2 4 Exploded view of the loop-gap resonator and the mounting structure. See text for an explanation

can be calculated before the resonator is manufactured using an variation of equation (2.1) that accounts for fringe effects by an empirical correction

If necessary, the resonant frequency of a resonator can be changed during mounting by introducing a dielectric material, such as teflon, into the gaps. During operation, the resonant frequency can be adjusted by about 200 MHz by introducing a metal rod into the third loop (the loop that is not used for the sample or for the coupling coil). The resonant frequency is typically not very temperature dependent, but this varies strongly with the quality of the electrical contact between the two halves of the resonator. It does, however, change significantly when the resonator is loaded, due to the high filling factor. This negative frequency shift is higher for powdered or liquid samples in a quartz tube than for single crystals and may exceed 0.5 GHz. The Q -factor of the resonator is mainly determined by the relative dimensions of the resonator with respect to the microwave wavelength and cannot easily be changed. Typical Q factors of these resonators are between 200 and 1000. The Q -factor depends somewhat on the conductivity of the metal from which the resonator has been manufactured, but attempts to employ resonators from stainless steel which has a low conductivity at low temperatures, were not successful, as the resonator had a tendency to spark when large microwave powers were applied. Some loop-gap resonator designs have a tendency to radiate strongly, requiring the use of a shield to confine the microwave radiation. The three-loop two-gap structure does not radiate strongly [14], but the use of a microwave shield is still advisable, because the coupling loop does tend to radiate, and the proximity of conducting objects may influence the coupling characteristics. The mounting structure of the resonator described here effectively acts as a shield.

The use of this resonator in ESE spectroscopy is very easy. With critical coupling the ringing of the resonator is limited to about 300 ns, but this can be reduced by overcoupling. This can very easily be achieved for higher frequencies (above 7 GHz), but at lower microwave frequencies it becomes progressively more difficult to achieve overcoupling because the resonator to coupling-coil distance for critical coupling gets progressively smaller. Also, the wavelength of the microwaves becomes progressively larger than the dimensions of the resonator, thus increasing the Q -factor. Dead-times of 120 ns can routinely be achieved for higher frequencies, but this increases to above 200 ns for lower frequencies. The dead-time can be as low as 60 ns under ideal circumstances. The performance of this resonator is typically better than that of the resonator used previously [5], and is comparable to the dielectric resonator used in the commercial Bruker ESP380 FT-EPR spectrometer, although it is more difficult to handle. The Bruker resonator is, however, available only at 9.8 GHz, and cannot be used for dual rotation single crystal investigations when it is necessary that the crystal be placed in an arbitrary orientation with respect to the external magnetic field.

2.5 The pulse generator

The pulse-generator used in the ESE spectrometer is an enhanced version of that described in [1]. It features 8 independent output channels capable of generating sequences of many pulses and delays with lengths between 10 ns and several seconds in increments of 5 ns. The design of the pulse generator is closely linked to the ESEEM experiment. A common timebase defines the duration of the various pulses and delay intervals. The eight output gates can be independently

2.5. THE PULSE GENERATOR

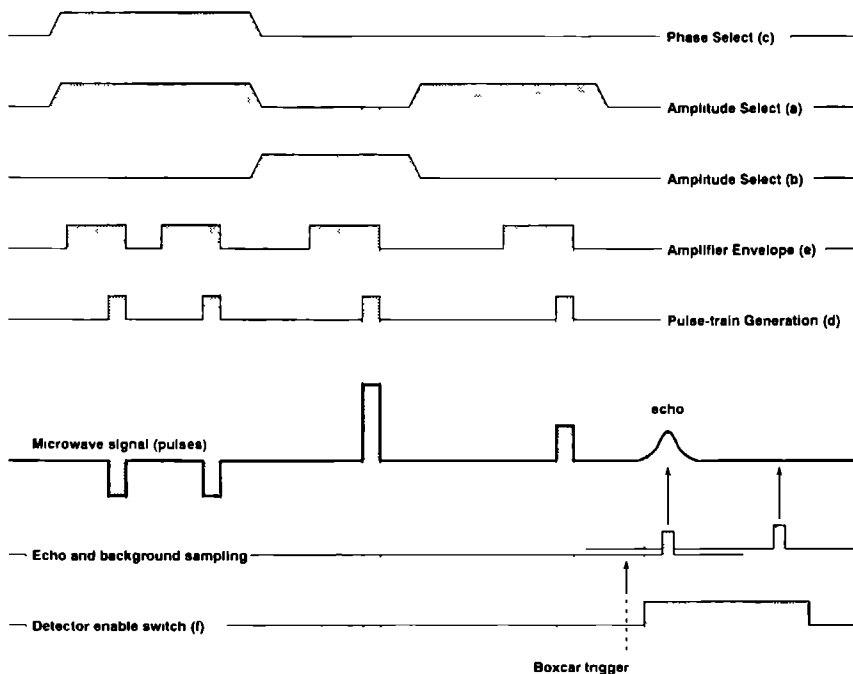


Figure 2.5. Timing sequence for a single phase cycle of a HYSCORE experiment performed using the X-band bridge (figure 2.1). The top five traces indicate output pulses for channels a through e, which generate the microwave pulse train (sixth trace). The bottom two traces illustrate the echo detection sequence. Oscilloscope trigger signals are not shown.

switched on or off during these intervals, generating the pulse sequence. When using pulses as short as 10 ns it becomes necessary to use properly terminated transmission lines from the outputs of the pulse generator to the switched devices. The outputs of the pulse generator are therefore driven by special 50 Ω line drivers and all cables terminated by 50 Ω resistors to ensure a proper pulse shape and to prevent reflections. Rise times of the order of 2 ns are typical for the pulse shapes at the switches.

The pulse generator is programmed by a dedicated personal computer, so that pulse sequences can be stored and retrieved from disk. A simple pulse programming language is used to describe complete pulse programs for experiments with up to three dimensions. Each pulse sequence is calculated by the computer and transmitted to the pulse generator and can contain up to about 1000 individual pulses of a total duration of up to about 80 seconds. For a HYSCORE experiment with four phase cycles (figure 3.4), approximately 64 intervals need to be defined, and the whole pulse sequence typically takes between 1 and 40 ms. To facilitate signal averaging by a boxcar averager, a single pulse sequence can be repeated up to 256 times without the need to reprogram the pulse generator, using an internal hardware repetition counter.

Timing sequences of pulse experiments

The arrows a through f in figures 2.1 and 2.2 indicate which devices in the microwave bridges are switched by the pulse generator. The remaining two pulse channels are used to trigger the boxcar averager and several display oscilloscopes. The timing sequence of the pulse generator for a typical four-pulse HYSOCORE experiment, performed using the X-band bridge, is shown in figure 2.5. The phase and amplitude of each microwave pulse is set by selectively enabling channels a, b or c. The TWT amplifier envelope pulse (e) is started some time before the actual pulse is generated, which is done by switching channel d. The amplifier envelope is switched off simultaneously with the end of the microwave pulse. Shortly before the echo signal occurs, the boxcar averager is triggered, and the echo detection circuit is enabled by channel f. The echo and background sampling have been discussed earlier. The timing sequence is slightly different when the C-band bridge is used, because that microwave bridge generates the microwave pulses by selectively enabling one of the pulse former channels (c or channels c and d). The function of pulses with various phases and amplitudes is discussed in chapter 3.

2.6 Data acquisition using an IBM PC/AT computer

The initial design of the pulsed EPR spectrometer built in 1982 already incorporated a computer system for data acquisition purposes. This computer, a DEC MINC-23 laboratory computer used a program named ESE which evolved into the *Interactive Data Acquisition and Processing System* described in [1]. This program was completely written in PDP-11 assembly language.

One of the changes in the spectrometer that occurred in the course of its modernization between 1988 and 1990 was the replacement of the aging MINC-23 computer with a modern IBM PC/AT compatible computer system. Although the MINC-23 system is a very versatile laboratory computer the new system has a number of significant advantages. Besides being much faster than the MINC-23 system it has significantly more memory and it has an internal hard disk unit enabling much faster access to data and programs. Also, programming this machine is much easier since there are many high-level programming languages available. Although the IBM PC/AT computer is much cheaper than the MINC-23 system the latter is eminently suitable for data acquisition purposes, which cannot be said of the IBM PC/AT.

The introduction of a new computer system also required that the data acquisition program be re-written since the old and new computers are completely incompatible in both software aspects (operating system and available programming languages) and hardware aspects. Although at the time a number of commercial data acquisition packages were available they were not suitable for the type of experiments performed by us. The major part of the new program, IDAPS/PC is written in the 'C' programming language, with some time-critical parts such as the graphics handling and some numerical procedures, e.g. the fast Fourier transform, written in 80286 assembly language.

The design of the data acquisition program

The necessity of writing a new program prompted us to introduce a number of improvements, but at the same time we wished to retain some useful features of the original program. The new program should have a user-friendly interface for both novice and experienced users. Multitasking facilities should be available to enable simultaneous data acquisition and data processing. Also, we wanted to exploit the additional features offered by the new computer, such as the memory expansion and the compatibility with other, widely used, software packages.

The user interface is perhaps the most visible part of the program. Since an important aspect of the program is data processing it is essential that the data is displayed on the screen. For the interpretation of the displayed spectrum the information on the spectrum should also be displayed. Most of the screen is devoted to displaying the spectrum and the associated information, such as the frequency axis and annotations.

To accommodate for both novice and experienced users, commands are entered through a menu structure in which each command in a menu is accessible either by a single keystroke, so that expert users can quickly navigate through the menu structure, or by selecting it with the arrow keys, which helps novice users. Some commands may lead to a sub-menu with related choices, whereas others immediately execute a specified function, such as starting an experiment or performing a fast Fourier transformation of the data.

It is very convenient if the data acquisition computer is available for processing recently measured spectra while new data is being recorded. This requires the availability of multitasking facilities. The dual functionality of the data acquisition program is most easily realized using a foreground/background strategy, which is implemented using *event driven data acquisition*. Only when a specified event occurs will the data acquisition routine be activated. At all other times the computer is free for data processing. Two possible ways of implementing this event driven data acquisition are discussed later in this section.

To facilitate processing and comparison of spectra, multiple pages are kept in memory for quick reference. One of the pages is the active page, which the user can select independent of any ongoing experiment. The spectrum on this active page will be displayed, together with all relevant parameters. A security mechanism is used to prevent accidentally destroying the spectrum on a page on which a measurement is in progress. For instance, it is impossible to perform a FFT on that page. All data relevant to a recorded spectrum as comments or descriptions given by the user, or the time-base of the spectrum, are stored together with recorded data. This data can be stored on and retrieved from disk in a number of formats, including the format used by the original program of the MINC-23 computer for data exchange purposes. Other formats that can be generated by the program are those used by the Bruker EPS-380 spectrometer and by other data processing programs. A native format resembling that of the Bruker spectrometer is normally used to store the data and all relevant information.

Several basic data processing functions, such as low-pass and high-pass filters, apodization, tapering, and a fast Fourier transform are provided in the program. When these functions need parameters, like cut-off frequencies, they can be supplied by the user. The program is written in such a way that new data processing functions that become available can easily be incorporated.

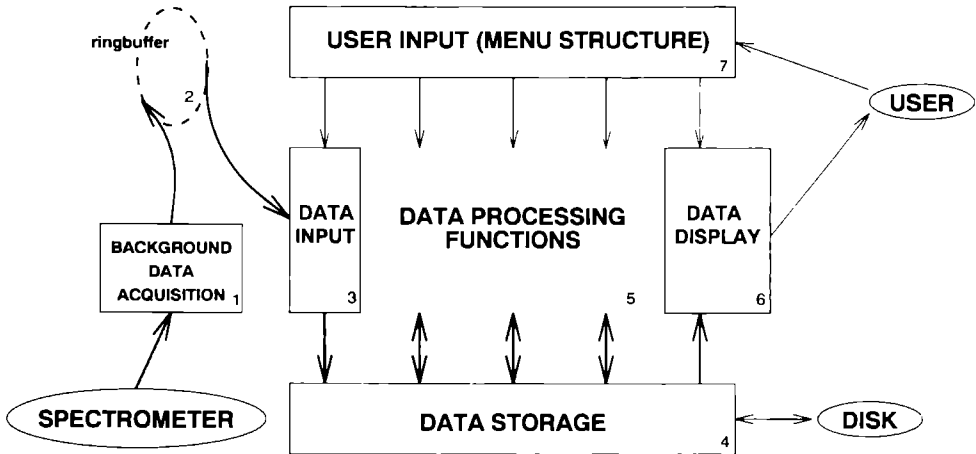


Figure 2.6: Logical structure of IDAPS/PC. There are four basic building blocks: the user interface, consisting of the menu structure and the data display module, the data storage module, the data processing modules and the spectrometer interface, consisting of the background data acquisition, the communication system and the data input module.

Details of the implementation

At the highest level, IDAPS/PC revolves around the *Idle loop*. From this loop all functions of IDAPS/PC are initiated. Below is a schematic listing of the idle loop in a Pascal-like pseudo-language.

```

DO
  GET user input
  IF the user has typed anything THEN
    Find and execute requested function
  ELSE
    Process all newly measured data
    Update the display
  UNTIL the user wants to stop

```

Any key-press of the user is immediately passed to the user interface. Most of the time, however, there is no user input available and the program then takes the opportunity to update the display with any recently measured data.

To understand the operation of the program it is best not to look at the flow of control, but at the flow of data through the program, visualized in figure 2.6. Analyzing this flow of data lets us identify four major building blocks: the user and spectrometer interfaces, the data storage module and the system of data processing modules.

The data are initially measured by the background data acquisition module¹ from which they are passed to a communication system, which is a ring-buffer². The data are taken from that ring buffer by the data input module³ and stored in a spectrum accumulation buffer³. These

three modules are the core of the spectrometer interface. The data storage module⁴ receives the recorded spectra from the accumulation buffer of the data input module and makes it available to the data processing functions⁵ and to the display module⁶ of the user interface.

At the other end of the program, the menu structure⁷ receives user input and, acting on that input, controls the spectrometer, the data processing functions and the display. The two inputs to the program, from the user and from the spectrometer, are completely independent. The user input is handled in the foreground by the menu structure, whereas the input from the spectrometer is handled by a background data acquisition module.

Possible data processing functions include low pass and high-pass filters, data tapering and apodization functions to smooth the frequency spectrum, Fourier transform functions to calculate frequency spectra and other functions aimed at removing the baseline decay and possible artifacts.

In the structure of the program only the user interface, built around the menu structure, and the data storage modules are fixed. All other components, including the spectrometer interface, are designed around these fixed modules and can be easily removed or changed. Different spectrometer interfaces can be designed for different requirements, or the spectrometer interface can be removed completely so that only the data processing capabilities remain.

The user interface

The central part of the user interface is the menu structure. An example of a menu structure is shown in figure 2.7. The menu structure is implemented as a linked list of command descriptor blocks. Such a command descriptor block holds four pieces of information about the menu option: the name of the option and the associated shortcut key (if any), the function that is to be executed when the option is selected and any data that the function may need.

When the user wants to execute a command, the linked list describing the menu is searched for that command. If it is found, the program calls the routine identified by the `code` parameter, using the `data` parameter as an argument. As an example, consider a parameter setup function. Such a function would ask the user to enter a list of parameters. The same function could be used in different commands for different parameter lists used in different modules. The command descriptor blocks of these menu items would then have the same `code` parameter but a different `data` parameter.

An other possibility is that the `data` parameter of a command points to a different linked list of menu items, or command descriptor blocks. With the appropriate function, this command could give access to a new, deeper-level menu as is illustrated in figure 2.7.

Data storage

To facilitate the comparison and retrieval of data and to enable the processing of previously recorded data while a new experiment is in progress the program keeps a number of spectra in memory in so-called data pages. Such a data page not only stores the measured data but also holds additional information describing the spectrum. There are four types of data stored on each page controlled by four independently operating sub-modules.

spectrum so that optimum display-settings for a specific page are not lost when switching pages

The selection of the active page as well as other page-management functions as copying and deleting pages are managed by a page-management module. One of the most important tasks of this module is the management of page security. To avoid accidentally writing to, or deleting a page, each page has associated with it a number of permission flags that control the access to it. Only one module at a time may write to a page, although several may read from it. When a data processing function is activated by the user it will ask for permission to write to this page. If the page is not in use by an other module, for instance the data input module, then write permission is granted and the page is locked to other modules. The page is released after the spectrum has been processed and all information has been updated. When a module needs to read some information from the data page it requests the relevant data storage sub-module for this information. While the information is needed the page cannot be deleted, although other modules may read from it or write to it. For example, when an experiment is in progress only the spectrometer interface module has permission to write to the page on which the spectrum is stored, so that it is impossible to perform a Fourier transformation on that page. It is, however, possible to copy the spectrum to an other page and process the copy.

Data acquisition in real-time

Earlier in this section we have seen how data is passed from the spectrometer to the computer. From the point of the data acquisition system an experiment is a black box with one or more outputs which must be sampled at certain times, which depend strongly on the experiment being performed. Usually, the computer cannot predict when these outputs must be sampled because it does not actively control the experiment. With respect to the program flow in the computer, the arrival of incoming data is an *asynchronous event*. The computer must adapt itself to the external conditions and in this sense it is a real-time system. In the following we describe how the computer handles such asynchronous events, and how the new data points are directed to the proper data page of the program.

There are two different techniques for handling external events which are suitable for our purposes.

Interrupt service. When an event occurs, the computer is interrupted in its current process, which can be anything, and immediately starts the data acquisition operation. The IBM PC/AT computer is not very well suited for this type of real-time data acquisition, especially if the computer must simultaneously be used for other tasks, since its operating system does not support multiple concurrent tasks. Although interrupt based data acquisition is possible, one cannot use the operating system during the data acquisition phase. The advantage of this method is that an experiment can continue independent of the foreground process.

Status polling. When an event occurs, a flag is set, which is examined at certain points in the program execution, typically in an idle loop. When an event is pending, the data

acquisition routine is called, and runs as a foreground process. Although this is relatively easy to implement, it has one major drawback. If for any reason the computer is not idle at any time during a long interval, for instance during a slow data processing procedure the experiment stops until the computer has time to handle the event.

It is possible to use either the interrupt service method or the status polling method. We have chosen to implement the data acquisition by using an interrupt service routine. This interrupt service routine can be seen as a background program, which talks to the main program through a communication system, but is not actually part of the main program. The problem we encountered in implementing this system is that it is not possible to use services provided by the MS-DOS operating system in the interrupt routine. Typically, DOS device driver software, such as that controlling the IEEE-488 interface bus, cannot be accessed which may reduce the functionality of an interrupt service routine.

When the spectrometer signals the presence of new data from, e.g., the analog-to-digital converter attached to the boxcar integrator, the computer is interrupted and activates the data acquisition module. This module then reads the data from the spectrometer and passes it to the communication system. Often only one point is measured, but when using a digitizing oscilloscope a complete spectrum would be transferred. After the data has been transferred to the communication system the data acquisition module will activate all sweep devices, i.e., it will load the pulse generator with the next set of times for a pulse sequence or, in an ENDOR experiment, it will step the RF frequency. When it has finished setting up the new experimental conditions the data acquisition module informs the spectrometer that it has finished the data acquisition cycle, and control is returned to the main program which will resume as if nothing had happened.

The communication system stores all information from the background data acquisition module in a ring buffer until the main program has time to handle the data. The ring buffer must be large enough to give the main program enough time to complete its present task, before the ring buffer fills up.

When IDAPS/PC is idle, waiting for user input after it has completed a command, it invokes the data input module, which asks the communication system for all new data that have been measured. The measured data are accumulated in an acquisition buffer. If the data page on which the experiment is being recorded is displayed on the screen the 32-bit data in the acquisition buffer will immediately be scaled and transferred to the data page where the new data is displayed. Often the user is processing data on a different page during the experiment in which case the data is not immediately displayed. Upon completion of the experiment the acquisition module is disabled and the spectrometer interface is prepared for a new experiment.

Implementation of the interrupt service routine

The data acquisition module described above is activated when an interrupt occurs. With the restriction that the data acquisition module cannot use operating system services during its execution it is not different from other modules. However, the implementation of the functions that allow this data acquisition module to be called at the appropriate time is difficult, although modern 'C'-language compilers can considerably simplify this task.

The first challenge is to connect the data-ready signal from an outside source, such as the spectrometer, to the interrupt structure of the computer itself. Although it is possible to purchase interface cards for the IBM PC/AT that provide this functionality it is also possible to use the already available serial communication (RS-232) ports of the computer for this purpose. In the IBM PC/AT each serial port, up to a total of four ports, is connected to one of eight interrupt lines (ports 1 and 3 use interrupt line 4 and the second and fourth ports use interrupt line 3). Because all installed serial ports are very similar (they are only distinguished by their I/O addresses) we can use the same interrupt service routine to service signals from all ports. Each serial port can issue four different types of interrupt signals indicating the status of the port. An interrupt is generated when a character has been transmitted by the port, when one is received, when one of the serial line control signals changes, or when there is a change in one of the modem status lines, such as the *carrier detect* and *ring indicator* lines, changes. The ring-indicator line is normally used by an attached modem to signal an incoming telephone call. Since there are no modems in the laboratory we decided to use the ring indicator signal to indicate the availability of data from the spectrometer.

The structure of the interrupt service routine that reacts to interrupts from the serial ports is listed below.

```

Disable further interrupts
FOR portnum = 1 TO 4 DO
  WHILE interrupt pending DO
    CASE interrupt type OF
      transmit      : transmit next character
      receive       : receive next character
      line status   : handle line status
      modem status  : handle modem status
    END
  END
END
Enable new interrupts

```

The `transmit character` and `receive character` routines are used serial data communication, and the `handle line status` routine checks for serial data transmission errors or line-break signals. The `handle modem status` routine is called if there is a change in any of the modem-status signals of the serial ports, such as the ring indicator signal. If the ring-indicator signal is activated by the spectrometer the `handle modem status` routine activates the background data acquisition module. The main advantage of this solution is that serial port communication remains possible. This port has been used for controlling the 'speedy II' pulse generator[1] from the data acquisition program.

Equipment for analog-to-digital conversion

One of the problems we encountered in the design of the data acquisition equipment was the quality and cost of commercial analog-to-digital conversion devices for IBM PC/AT computers. Usually when an IBM PC/AT computer is used for data acquisition purposes it is equipped with

a plug-in board for the analog-to-digital conversion. In our initial design we also used such a plug-in board. It soon appeared, however, that this device was qualitatively inadequate. Plug-in cards with the required capabilities from other manufacturers proved prohibitively expensive.

Investigation of the problem revealed that the power-supply of the personal computer was not suitable for use with the available ADC plug-in card. To circumvent these problems we built a data acquisition box with the functionality and flexibility we required. Most of the equipment which is controlled by the computer is either built into the data acquisition box, or is interfaced to the computer through this box. The box houses analog-to-digital converters necessary for the data acquisition, and may also contain interfaces to digital frequency counters and other devices. In order to enhance the accuracy of the analog-to-digital conversion a regulated high-stability power supply is included.

The backbone of the data acquisition box is a bus system consisting of eight address and eight data lines, completed by a number of bus control lines. The data acquisition box can house several devices, each responding to a unique set of addresses so that they can be individually operated by the computer. The READ and WRITE lines control whether a device should read data from the bus or place data on the bus when addressed. The four remaining control lines form a flexible, dedicated, fault-tolerant interrupt structure designed to lessen the burden on the attached data acquisition computer.

The data acquisition box is connected to the data acquisition computer by means of two cables. One of these cables carries all 22 bus lines and is connected to a general purpose digital input/output plug-in board containing an Intel 8255 PIC integrated circuit chip. The data acquisition box is designed in such a way that it can be connected to any computer that uses a 8255 PIC chip for input/output purposes. It is also possible to include a small microprocessor board in the data acquisition box to make it a completely stand-alone unit. The second cable connects the data acquisition box to a serial communication port of the computer to allow control of the ring-indicator signal. The serial communication port can still be used by means of a standard connector present on the data acquisition box.

Although the cost of the data acquisition box is not negligible its flexibility allows for the use of inexpensive, home-built interface devices to be used without expensive attachments to the computer itself. An inexpensive home-built 12-bit high-speed digital-to-analog converter card with excellent noise characteristics is used in all experiments performed on the spectrometer described in this chapter.

References

- [1] E. J. Reijerse. *Electron Spin Echo spectroscopy on transition metal complexes*. PhD thesis, University of Nijmegen, 1987.
- [2] P. Höfer, A. Grupp, H. Nebenfür, and M. Mehring. Hyperfine sublevel correlation (HYSCORE) spectroscopy: A 2D ESR Investigation of the squaric acid radical. *Journal of Chemical Physics* **132** (1986) 279.

- [3] C Bender and S Gedam An Interface Between a Source-Locking Frequency Counter and a YIG-Oscillator *EPR Newsletter* **4** (1992) 7
- [4] C Gemperle *Neue Elektronenspin-Echo-Experimente* PhD thesis, ETH Zurich, 1992
- [5] E J Reijerse and A A K Klaassen A Variable Temperature ESE-ENDOR resonator for Single Crystal Studies *Review of Scientific Instruments* **57** (1986) 2768
- [6] W Barendswaard, J A J M Disselhorst, and J Schmidt A Bimodal Cavity for Reducing the Dead Time in Electron Spin-Echo Spectroscopy *Journal of Magnetic Resonance* **58** (1984) 477
- [7] W Froncisz and J S Hyde The loop-gap resonator a new microwave lumped-circuit ESR sample structure *Journal of Magnetic Resonance* **47** (1982) 512
- [8] J S Hyde and W Froncisz Loop-Gap Resonators *Electron Spin Resonance* **10A** (1986) 175
- [9] S Plenniger, J Forrer, and A Schweiger Bridged loop-gap resonator A resonant structure for pulsed EPR transparent to high-frequency radiation *Review of Scientific Instruments* **59** (1987) 752
- [10] F Momo, A Sutgiu, and R Zonta On the design of a split-ring resonator for ESR spectroscopy between 1 and 4 GHz *Journal of Physics E Scientific Instruments* **16** (1982) 43
- [11] R D Britt and M P Klem A Versatile Loop-Gap Resonator Probe for Low-Temperature Electron Spin-Echo Studies *Journal of Magnetic Resonance* **74** (1987) 535
- [12] J P Hornak and J H Freed Electron Spin Echoes with a Loop-Gap Resonator *Journal of Magnetic Resonance* **62** (1985) 311
- [13] W Froncisz T Oles, and J S Hyde Q-band loop-gap resonator *Review of Scientific Instruments* **57** (1986) 1095
- [14] R L Wood, W Froncisz, and J S Hyde The Loop-Gap Resonator II Controlled Return Flux Three-Loop Two-Gap Microwave Resonators for ENDOR and ESR Spectroscopy *Journal of Magnetic Resonance* **58** (1984) 243
- [15] J S Hyde, W Froncisz, and T Oles Multipurpose Loop-Gap Resonator *Journal of Magnetic Resonance* **82** (1989) 223
- [16] J Forrer Puls-ESR-Spektrometer mit Loop Gap-Resonator *Bull ASE/UCS* **75** (1984) 21
- [17] T Oles, J S Hyde, and W Froncisz Gordon coupler for K-band EPR loop gap resonator *Review of Scientific Instruments* **60** (1989) 389

Chapter 3

The theory of ESEEM

In this chapter we shall explain the mechanism of ESE and ESEEM using the density matrix formalism in contrast to many other texts that introduce these phenomena using a vector model, it was felt that there is no need to repeat that description. The reader is referred to [1] for a vector model description.

We focus the discussion on only the basic elements of ESEEM so that we can direct our attention to the HYSCORE experiment. As a result, the well-known two-pulse primary echo and three-pulse stimulated echo FSEEM techniques are only touched upon briefly. A more comprehensive discussion of these experiments can be found in [2, 3].

In the first part of this chapter, sections 3.1 through 3.5, the density matrix formalism is presented. With that as a basis, we shall explain the mechanisms of electron spin echo and ESEEM spectroscopy. The second part, sections 3.6 through 3.8, will deal with the HYSCORE experiment. After an explanation of this experiment we shall derive expressions for the modulation effect and we shall indicate an efficient way of simulating HYSCORE.

3.1 The density matrix in EPR

The density matrix formalism has specifically been designed for the study of macroscopic systems, which are treated as an ensemble of microscopic systems for which the Hamiltonian and other quantum-mechanical properties are well-defined. As such, it is very suitable for the description of EPR, especially where it concerns the electron spin-echo phenomenon, as will be discussed later in this chapter. In this section we introduce the density matrix, as it is used in the description of EPR, in a concise manner, for more detailed discussions see [1, 4, 5]. The density matrix will be extensively used in this thesis for theoretical discussions of the electron spin-echo phenomenon.

The density matrix: an introduction

The density matrix of a pure state

In quantum mechanics the state of a system is conventionally characterized by a state vector $|\psi\rangle$. In a certain basis $|i\rangle$, the eigenfunctions of a complete set of commuting operators, we can

expand this state vector to

$$|\psi\rangle = \sum_i c_i |i\rangle \quad (3.1)$$

so that the state vector in that basis is completely defined by the coefficients c_i . As observers, we are not particularly interested in the shape of the state function $|\psi\rangle$, but we do want to be able to predict what we can measure. Quantum mechanics tells us that the expectation value $\langle \mathcal{A} \rangle$ of an observable \mathcal{A} can be calculated for a specific state $|\psi\rangle$ by

$$\langle \mathcal{A} \rangle = \langle \psi | \mathcal{A} | \psi \rangle = \sum_{mn} c_m^* c_n \langle m | \mathcal{A} | n \rangle \quad (3.2)$$

From this it appears that all information about the system must be contained in the products $c_m^* c_n$. We can view these products as elements of a matrix P , with $P_{mn} = c_m^* c_n$, which is called the *density matrix* of state $|\psi\rangle$. The matrix P is hermitian and is positive definite, i.e., P_{ii} is real and ≥ 0 and $\sum P_{ii} > 0$ and is, in fact, equal to 1. It is possible to associate an operator \mathcal{P} with the density matrix, the explicit form of this density operator is

$$\mathcal{P} = |\psi\rangle \langle \psi| \quad (3.3)$$

from which we immediately see that $\mathcal{P}^2 = \mathcal{P}$ and thus that \mathcal{P} must be a projection operator.

The expectation value of any operator \mathcal{A} can be determined from the density matrix by considering eq. 3.2 and noting that the factor $\langle m | \mathcal{A} | n \rangle$ is the A_{mn} element of the matrix representation of \mathcal{A} in the basis $|i\rangle$ of eq. 3.1 and thus

$$\langle \mathcal{A} \rangle = \sum_{mn} P_{nm} A_{mn} = \text{Tr}(\mathcal{P}\mathcal{A}) = \text{Tr}(\mathcal{A}\mathcal{P}) \quad (3.4)$$

Because the density matrix is an alternative representation of the state vector $|\psi\rangle$, it is important to find its time dependence. Realizing that

$$i\hbar \frac{\partial |\psi\rangle}{\partial t} = \mathcal{H}(t) |\psi\rangle \quad (3.5)$$

we find

$$i\hbar \frac{\partial \mathcal{P}}{\partial t} = i\hbar \frac{\partial |\psi\rangle \langle \psi|}{\partial t} = \mathcal{H}(t) |\psi\rangle \langle \psi| - |\psi\rangle \langle \psi| \mathcal{H}(t) = [\mathcal{H}, \mathcal{P}] \quad (3.6)$$

An explicit solution of eq. 3.5 for a time-independent operator $\mathcal{H}(t) = \mathcal{H}$ can be found by formally integrating that equation to find

$$|\psi_t\rangle = e^{-i/\hbar \mathcal{H}t} |\psi_0\rangle \text{ and thus} \quad (3.7)$$

$$\mathcal{P}(t) = e^{-i/\hbar \mathcal{H}t} \mathcal{P}_0 e^{+i/\hbar \mathcal{H}t} \quad (3.8)$$

It is interesting to note that in some respects the density matrix is a better representation of the state of a system than the state vector. The two *different* state vectors $|\psi'\rangle = |\psi\rangle e^{-i\Delta t}$ and $|\psi\rangle$ describe the same state, whereas there is no such ambiguity in the density matrix. A second advantage is that the expression for the expectation value is quadratic in the state vector, but it is linear in the density matrix.

A statistical mixture of states

A physically interesting macroscopic system is seldom correctly described by a single state vector. Rather, the many independent microscopic systems of which it is built must each be individually described by a state vector $|\psi^i\rangle$. The macroscopic system is correctly described only by statistical mixture of all microscopic systems. How does this affect the quantum mechanical treatment? Our first impulse would be to assign to the macroscopic system a state vector which is a statistical mixture of all state vectors of its microscopic constituents. Unfortunately, this will not work. A linear superposition of states $|\psi^i\rangle$ would suggest the occurrence of interference terms that do not exist in a statistical average. We can find a better way of describing the macroscopic system by looking at what we would expect to observe, namely an average of the expectation values of the microscopic systems

$$\langle \mathcal{A} \rangle = \sum_{mn} \overline{c_n^* c_m} \langle m | \mathcal{A} | n \rangle \tag{3.9}$$

which reduces to

$$\langle \mathcal{A} \rangle = \sum_{mn} \overline{c_n^* c_m} \langle m | \mathcal{A} | n \rangle \tag{3.10}$$

when we realize that $|m\rangle$, $|n\rangle$ and \mathcal{A} are the same for all systems. Recalling the definition of the density operator \mathcal{P} we see that a correct description of a statistical mixture of states is given by the average density operator $\rho = \overline{\mathcal{P}}$, whose matrix representation has elements

$$\rho_{mn} = \overline{c_n c_m^*} \tag{3.11}$$

By definition, the average expectation value is then

$$\langle \mathcal{A} \rangle = \sum_{mn} \rho_{nm} A_{mn} = \text{Tr}(\rho \mathcal{A}) = \text{Tr}(\mathcal{A} \rho) \tag{3.12}$$

An expression for the evolution of the density operator ρ follows directly from eq. 3.8 since that equation is linear in \mathcal{P} and ρ is a statistical (ensemble) average over \mathcal{P} , thus

$$\rho_t = e^{-i/\hbar \mathcal{H}t} \rho_0 e^{+i/\hbar \mathcal{H}t} \tag{3.13}$$

for a time-independent Hamiltonian. For the same reason, $\text{Tr}(\rho)$ still evaluates to 1. In contrast, since there is no longer a pure state $|\psi\rangle$ associated with ρ the relation $\mathcal{P}^2 = \mathcal{P}$ does not carry over to ρ which thus cannot be identified as a projection operator.

Because the density matrix was derived from the physical reality of expectation values, it is interesting to see whether the matrix elements of ρ have some physical meaning. From the definition of ρ , the diagonal elements $\overline{c_m^* c_m} = |c_m|^2$ are the average probabilities of finding, upon measurement, a microscopic system to be in state $|m\rangle$. In statistical terms, we would thus associate that element with the population of the state $|m\rangle$. The off-diagonal elements do not have such an obvious classical analogue, but since they express the statistically averaged interference terms, which can only be non-zero if a significant portion of the ensemble is in the same state, they are called coherences.

The density operator for the steady state

Macroscopic systems tend to be in thermal equilibrium with their surroundings, so it is not only insightful but also important to have an explicit form for a steady state density matrix. Let us express the density matrix in the basis of eigenstates of the (time independent) Hamiltonian. This has the advantage that the basis functions are independent of the time, and it is also the most commonly chosen basis in general and for density matrices in particular. In the steady state we know the populations of the individual states to be given by the Boltzmann factors

$$\overline{c_m^* c_m} = \frac{1}{\mathcal{Z}} e^{-E_m/kT} \quad \text{with} \quad (3.14)$$

$$\mathcal{Z} = \sum_m e^{-E_m/kT} \quad (3.15)$$

It is instructive to write for the coefficients $c_m = |c_m| e^{-i\alpha_m}$, from which

$$\overline{c_m^* c_n} = \overline{|c_m| |c_n|} e^{-i(\alpha_m - \alpha_n)} \quad (3.16)$$

Considering that the phases α_m are statistically independent of the $|c_m|$ and that all values of α_m are equally probable (the hypothesis of random phases [1]), we find that the off-diagonal elements all vanish. Of course, if they did not then from eq. 3.13 it follows that they would oscillate with frequency $(E_m - E_n)/\hbar$, which would violate the assumption of steady state. Thus

$$\langle m | \rho_0 | n \rangle = \delta_{mn} e^{-E_m/kT} / \mathcal{Z}, \quad (3.17)$$

which means that ρ_0 can be written as

$$\begin{aligned} \rho_0 &= \frac{1}{\mathcal{Z}} e^{-\mathcal{H}/kT} \quad \text{with} \\ \mathcal{Z} &= \text{Tr}(e^{-\mathcal{H}/kT}) \end{aligned} \quad (3.18)$$

independent of any basis

The density matrix for an electron spin

Consider a free, unperturbed electron in a static magnetic field B_0 . A complete description of this system would include both spatial and spin functions,

$$|electron\rangle = |space\rangle |spin\rangle, \quad (3.19)$$

but since we are effectively only interested in the spin part we will disregard the space function. The Hamiltonian for the electron then becomes

$$\mathcal{H} = g_e \beta \mathbf{B}_0 \cdot \mathbf{S}, \quad (3.20)$$

which we can write without loss of generality as

$$\mathcal{H} = g_e \beta B_0 S_z = \hbar \omega_0 S_z = \gamma \hbar B_0 S_z \quad (3.21)$$

3.1. THE DENSITY MATRIX IN EPR

when we take the z axis along the direction of the static magnetic field. For the electron, which has spin $S = 1/2$, the state of the system can be completely described by two spin functions $|\alpha\rangle$ and $|\beta\rangle$ corresponding to the two eigenvalues $m_S = +1/2$ and $m_S = -1/2$ of the S_z operator, respectively.

The steady state density matrix for this system can be written according to eq. 3.18 as

$$\begin{aligned}\rho_0 &= \frac{1}{2} e^{-\mathcal{H}/kT} = \frac{1}{2} e^{-\hbar\omega_0 S_z/kT} \\ &= \frac{1}{2} \left(\cosh\left(\frac{1}{2}\hbar\omega_0/kT\right) - 2S_z \sinh\left(\frac{1}{2}\hbar\omega_0/kT\right) \right) \\ &= A + \alpha S_z.\end{aligned}\tag{3.22}$$

Of course, for spectroscopic purposes we do not want the system to be in a steady state continuously: we are interested in observing transitions. When not in the steady state we can expect to see a non-equilibrium population distribution and also coherence terms, i.e., off-diagonal elements in the density matrix. In general then, we can write the density matrix as a sum of the identity matrix and the $S = 1/2$ spin matrices S_x , S_y and S_z

$$\rho = c_0 I + c_x S_x + c_y S_y + c_z S_z.\tag{3.23}$$

From a time-evolution view the contribution of the identity matrix is wholly uninteresting and we can write without loss of generality

$$\rho = c_x S_x + c_y S_y + c_z S_z\tag{3.24}$$

$$= c^+ S^+ + c^- S^- + c_z S_z,\tag{3.25}$$

where $S^+ = S_x + iS_y$ and $S^- = S_x - iS_y$. Of course we can also write the density *operator* as a combination of the spin operators for $S = 1/2$ in the same manner.

Since we have introduced the form of the non-equilibrium density matrix we should also discuss how we can bring the system out of equilibrium. In EPR spectroscopy this is done by the application of an oscillating or rotating magnetic field perpendicular to the B_0 field. The associated perturbation term in the Hamiltonian is

$$\mathcal{V}(t) = g_e \beta B_1 (S_y \cos(\omega t) + S_x \sin(\omega t))\tag{3.26}$$

so that while this additional field is applied the Hamiltonian for the system becomes

$$\mathcal{H}(t) = g_e \beta B_0 S_z + g_e \beta B_1 (S_y \cos(\omega t) + S_x \sin(\omega t)).\tag{3.27}$$

The rotating frame

Considering that for a time-independent Hamiltonian the expression for the time-evolution of the density matrix simplifies considerably, it is unfortunate that the perturbation Hamiltonian is time-dependent. By changing to a coordinate frame that rotates along with the perturbation field this time dependence can, however, be removed. Instead of working out the expressions from the point of view of the rotating coordinate frame, it is perhaps more instructive to follow a pragmatic reasoning. It can be shown without difficulty that eq. 3.27 can be written as

$$\mathcal{H} = g_e \beta B_0 S_z + g_e \beta B_1 e^{+i\omega S_z t} S_y e^{-i\omega S_z t}\tag{3.28}$$

which suggests that we can remove the time dependence by a transformation $R^{-1} \mathcal{H} R$ with $R = e^{+i\omega S_z t}$. The time-dependence of the density matrix under the influence of the Hamiltonian 3 27 must, according to eq 3 6, be derived from

$$\frac{d\rho}{dt} = \frac{i}{\hbar} [\rho, \mathcal{H}] = i\gamma\rho (B_0 S_z + B_1 R S_y R^{-1}) - i\gamma (B_0 S_z + B_1 R S_y R^{-1}) \rho \quad (3 29)$$

By defining

$$\rho_R = R^{-1} \rho R \quad \text{and thus } \rho = R \rho_R R^{-1} \quad (3 30)$$

we find, after multiplying both sides of eq 3 29 from the left by R^{-1} and from the right by R ,

$$\frac{d\rho_R}{dt} = \frac{i}{\hbar} [\rho_R, H_{\text{eff}}] \quad \text{and} \quad (3 31)$$

$$\mathcal{H}_{\text{eff}} = \hbar (\gamma B_0 + \omega) S_z + \gamma \hbar B_1 S_y \quad (3 32)$$

where \mathcal{H}_{eff} is the Hamiltonian we would expect to find from a classical argument. Since there is no longer a time dependence in eq 3 32 we can write the time evolution of ρ_R as

$$\rho_R(t) = e^{-i/\hbar \mathcal{H}_{\text{eff}} t} \rho_R(0) e^{+i/\hbar \mathcal{H}_{\text{eff}} t} \quad (3 33)$$

Note that for the steady state

$$\rho_{R0} = \rho_0, \quad \text{since, from eqs 3 30 and 3 22,} \quad (3 34)$$

$$\rho_{R0} = e^{-i\omega S_z t} (A + \alpha \sigma_z) e^{+i\omega S_z t} = A + \alpha \sigma_z$$

because S_z and σ_z commute

The situation is somewhat more complicated if there is an additional term \mathcal{H}_n in the Hamiltonian of eq 3 27,

$$\mathcal{H} = \gamma \hbar B_0 S_z + \gamma \hbar B_1 (S_y \cos(\omega t) + S_x \sin(\omega t)) + \mathcal{H}_n \quad (3 35)$$

In general, the effective Hamiltonian in the rotating frame then becomes

$$\mathcal{H}_{\text{eff}} = \hbar (\gamma B_0 + \omega) S_z + \gamma \hbar B_1 S_y + R^{-1} \mathcal{H}_n R \quad (3 36)$$

which again introduces a time dependence in the Hamiltonian. Only if \mathcal{H}_n commutes with S_z does the time-dependence disappear. For the typical case where \mathcal{H}_n represents the interaction of the electron with the surrounding nuclei, this is the case when the energy differences caused by the presence of \mathcal{H}_n are very small compared to $\gamma \hbar B_0$. This approximation, where \mathcal{H}_n commutes with S_z , is called the strong-field approximation, and we write

$$\mathcal{H}_{\text{eff}} = \hbar (\gamma B_0 + \omega) S_z + \gamma \hbar B_1 S_y + \mathcal{H}_n \quad (3 37)$$

It is important to know the appearance of observables in the rotating frame. For spectroscopic purposes the most interesting observables are those associated with a magnetization

$$\mathcal{M}_x = g_e \beta S_x, \quad \mathcal{M}_y = g_e \beta S_y, \quad \mathcal{M}_z = g_e \beta S_z \quad (3 38)$$

If we write the expectation value for the magnetization in the rotating frame x direction as

$$\langle \mathcal{M}_x \rangle = \text{Tr}(\rho_R M_x), \quad (3.39)$$

where M_x is the matrix representation of \mathcal{M}_x , we find that this expectation value is associated with a magnetization in the static frame

$$\begin{aligned} \langle \mathcal{M}_x \rangle &= \text{Tr}(R \rho_R R^{-1} R M_x R^{-1}) \\ &= \text{Tr}(\rho R M_x R^{-1}) \\ &= \cos(\omega t) \text{Tr}(\rho M_x) - \sin(\omega t) \text{Tr}(\rho M_y) \end{aligned} \quad (3.40)$$

which is identified as a rotating magnetization with a frequency equal to the frequency of the perturbation field; in EPR this would be a microwave signal.

From this point onward we will exclusively work in the rotating frame and we shall drop the R subscript from ρ_R .

Electron Spin Resonance

Let us now consider what happens to the density matrix under the influence of an oscillating magnetic field. In the rotating frame we have the Hamiltonian of eq. 3.32, which we can write somewhat simplified as

$$\mathcal{H} = \hbar \omega_0 S_z + \hbar \omega_1 S_y, \quad (3.41)$$

where $\omega_0 = \gamma B_0 + \omega$ and $\omega_1 = \gamma B_1$. The evolution of the density matrix from the steady state under the influence of this Hamiltonian is

$$\rho(t) = e^{-i(\omega_0 S_z + \omega_1 S_y)t} \sigma_z e^{+i(\omega_0 S_z + \omega_1 S_y)t}, \quad (3.42)$$

where we disregard the constant α . This cannot easily be evaluated because S_z and S_y do not commute. However, by a simple coordinate transformation such that the effective magnetic field $B_{\text{eff}} = (B_0 + \omega/\gamma)\hat{z} + B_1\hat{y}$ lies along the new z' axis the expression simplifies considerably. Defining the spin operators in the new axis frame as

$$S'_x = S_x, \quad S'_y = c \cdot S_y - s \cdot S_z, \quad S'_z = s \cdot S_y + c \cdot S_z \quad (3.43)$$

with

$$s = \omega_1/\omega_e \quad c = \omega_0/\omega_e, \quad \omega_e = \sqrt{\omega_0^2 + \omega_1^2},$$

we find, in terms of these new spin operators, for eq. 3.42

$$\rho_t = e^{-i\omega_e S'_z t} (c \cdot \sigma'_z - s \cdot \sigma'_y) e^{+i\omega_e S'_z t}, \quad (3.44)$$

which evaluates in the rotating frame to

$$\rho(t) = s \cdot \sin(\omega_e t) \sigma_x + s \cdot c (1 - \cos(\omega_e t)) \sigma_y + (s^2 \cos(\omega_e t) + c^2) \sigma_z. \quad (3.45)$$

This equation in itself is not very informative, but we can select two specific situations one where $s \gg c$ and one where $c \gg s$. Noting that c and s are between 0 and 1 we find for the case $s \gg c$

$$\rho(t) = \sigma_z \cos(\omega_1 t) + \sigma_x \sin(\omega_1 t) \tag{3 46}$$

and for the case $c \gg s$ we find that eq 3 45 reduces to

$$\rho(t) = \sigma_z = \rho_0 \tag{3 47}$$

The condition that $s \gg c$ holds if $\omega \approx -\gamma B_0$ and ω_1 is sufficiently large. This is the case when we are near resonance. Far from resonance, $\gamma B_0 + \omega \gg \omega_1$ and then eq 3 47 holds.

It appears then that an oscillating magnetic field only has an effect on the density matrix if the microwave frequency is close to resonance ($\hbar\omega \approx E_\alpha - E_\beta$). Since all interesting things happen near resonance we shall assume in the following that this is always the case. Note that we can then write for eq 3 42

$$\rho(t) = e^{-i\omega_1 S_y} \sigma_z e^{+i\omega_1 S_y} \tag{3 48}$$

or, more generally,

$$\rho(t) = e^{-i\omega_1 S_y} \rho(0) e^{+i\omega_1 S_y} \tag{3 49}$$

Relaxation

Since for the description of electron spin-echo spectroscopy relaxation is of secondary importance, we shall only touch briefly upon it.

The diagonal elements of the density matrix, which describe the populations of the different energy levels, relax to the equilibrium populations with a characteristic time T_1 . The processes responsible for this relaxation are resonant and near resonant (Raman) phonon-scattering processes. Obviously then, the relaxation rate $1/T_1$ must be strongly temperature dependent, increasing with increasing temperature. For most paramagnetic systems containing paramagnetic transition metal ions, the relaxation constant T_1 at low temperatures is of the order of milliseconds or less. This relaxation, usually called longitudinal relaxation, removes energy from the spin system as a whole.

The off-diagonal elements of the density matrix are subject to other relaxation processes, typically spin flip-flop processes of coupled spins. These relaxation processes do not influence the total energy of the spin system. It is assumed that this relaxation, usually called transversal or spin-spin relaxation, is described by a single exponential decay of the xy magnetization characterized by a time constant T_2^* . Since the xy magnetization can also decay as a result of inhomogeneities of the magnetic field, the total decay rate T_2 is given by

$$\frac{1}{T_2} = \frac{1}{T_2^*} + \frac{1}{T_2^*}, \tag{3 50}$$

where T_2^* accounts for the effect of the inhomogeneity. The complete relaxation of the density matrix of eq 3 25 is then given by

$$\rho = c^+ S^+ + c^- S^- + c_z S_z \xrightarrow{t} \left(\alpha + (c_z - \alpha) e^{-t/T_1} \right) S_z + e^{-t/T} \left(e^{-i\omega_1 t} c^+ S^+ + e^{+i\omega_1 t} c^- S^- \right) \tag{3 51}$$

In our discussions of the electron spin-echo phenomenon in the next sections we do not take relaxation into account, we assume that our experiments are performed on a time scale much smaller than both T_1 and T_2^* . Although this is not always the case, the only effect of including relaxation is to include a (finite) linewidth

For continuous wave electron spin resonance, the relaxation does play an important role. Realizing that the transversal relaxation processes are usually much faster than the longitudinal relaxation processes we assume in CW EPR that there is never any buildup of coherences, the off-diagonal elements of the density matrix are always zero. There are then two competing processes. On the one hand, the presence of microwaves causes the removal of the equilibrium magnetization,

$$M_z(t) = \cos(\omega_1 t) M_0, \quad (3.52)$$

while on the other hand, the longitudinal relaxation processes counteract this tendency of buildup of a non-equilibrium population distribution,

$$M_z(t) = M_0 + e^{-t/T_1} (M_z(0) - M_0) \quad (3.53)$$

where $M_z(0)$ is the initial non-equilibrium magnetization. These processes will compete with each other, and when $T_1 \approx 1/\omega_1$, there will be a continuous absorption by the system of microwave energy, and this absorption can be measured if ω_1 is sufficiently large.

When, however, ω_1 is much larger than $1/T_1$, there can no longer exist such an equilibrium state, and in fact, if ω_1 becomes of the order of, or even larger than, $1/T_2$ we can no longer disregard the buildup of coherences. In the next sections we will deal with the case $\omega_1 \gg 1/T_2$, and we shall, in fact, disregard relaxation completely as mentioned above.

3.2 The Electron Spin-Echo Phenomenon

In 1950, Erwin Hahn made a startling discovery. When he applied two RF pulses in rapid succession to a spin system, he not only observed the expected free induction decay signal (more about this later), but after some time a *second* microwave signal (the echo signal) appeared, long after the disappearance of the free induction signal (FID). Because the decay of the FID signal was thought to be irreversible the mechanism was somewhat of a mystery. Was there a Maxwell daemon at work here? Soon after the discovery, however, Hahn found that there wasn't when he was able to derive the existence of this echo signal from the Bloch equations. We shall take the simpler approach and use the density matrix to illuminate the mechanism behind the spin-echo phenomenon.

Microwave pulses and the free induction decay

Let us first look at what Hahn expected to see, a free induction signal. Starting from the steady state, the application of microwaves causes an evolution of the density matrix given by eq. 3.46, when we assume that $\omega_1 \gg \gamma B_0 + \omega$ we are near resonance. We can look at two special cases

$$\omega_1 t = \pi/2, \quad \rho(t) = \sigma_x \quad \text{and} \quad (3.54)$$

$$\omega_1 t = \tau \quad \rho(t) = -\sigma_z \quad (3.55)$$

Free precession:	$S_z \rightarrow S_z$	$S^+ \rightarrow e^{-i\omega_0 t} S^+$	$S^- \rightarrow e^{+i\omega_0 t} S^-$
Ideal 180° pulse: (along y -axis)	$S_z \rightarrow -S_z$	$S^+ \rightarrow -S^-$	$S^- \rightarrow -S^+$
Ideal 90° pulse: (along y -axis)	$S_z \rightarrow \begin{cases} -\frac{1}{2}S^+ \\ -\frac{1}{2}S^- \end{cases}$	$S^+ \rightarrow \begin{cases} +\frac{1}{2}S^+ \\ +S_z \\ -\frac{1}{2}S^- \end{cases}$	$S^- \rightarrow \begin{cases} -\frac{1}{2}S^+ \\ +S_z \\ +\frac{1}{2}S^- \end{cases}$
Non-ideal pulse:	$S_z \rightarrow \begin{cases} c^+ S^+ \\ c_0 S_z \\ c^- S^- \end{cases}$	$S^+ \rightarrow \begin{cases} c^+ S^+ \\ c_0 S_z \\ c^- S^- \end{cases}$	$S^- \rightarrow \begin{cases} c^+ S^+ \\ c_0 S_z \\ c^- S^- \end{cases}$

Table 3.1: Effects of free precession and of ideal microwave pulses on the various components of the density matrix. The microwave pulses are along the $+y$ axis of the rotating frame. At the bottom the effects of a non-ideal microwave pulse are listed. Note that only S^+ and S^- components give rise to an observable microwave signal.

If we switch off the microwaves at $\omega_1 t = \pi/2$ we have created from the steady state magnetization a density matrix with only coherence terms. Note that the expectation value for the magnetization vector $\langle \mathbf{M} \rangle$ has rotated over 90° . Such a limited burst of microwave radiation is called a 90° pulse. Similarly, when switching off the microwaves at $\omega_1 t = \pi$ we invert the steady state magnetization and we have made a 180° or π pulse.

The σ_x component of the density matrix that has been created after a 90° pulse gives rise to a rotating magnetization in the laboratory frame as has been discussed earlier (eq. 3.40). Of course, we expect this signal to decay according to eq. 3.51. Such an FID is normally observed in FT-NMR experiments and this is the signal that Hahn expected to see. Note that we usually do not observe this signal in pulse-EPR.

The system does not have to be in thermal equilibrium when the microwave pulses are applied. Because matrix multiplication is a linear operation we can look at what happens to the various components of the density matrix independently (eq. 3.24 and 3.25). It is most convenient to split the density matrix in S^- , S^+ and S_z components because of their simple time-evolution. Table 3.1 lists both the effect of free precession and the effects of ideal microwave pulses on these components. In this table we have assumed that the microwave field is along the $+y$ direction of the rotating frame. Although this can be done without loss of generality, it is sometimes convenient to have the B_1 field along some other direction in the xy plane; this corresponds to a phase shift of the microwaves. Expressions as those listed in table 3.1 are easily derived, but let us look at a special case which is used very often in ESE spectroscopy, the case where the B_1

field is along the $-y$ axis.

There is no difference between π pulses along the $+y$ and $-y$ axes, but the effects of $\pi/2$ pulses *are* different for the two cases: for a $\pi/2$ pulse along the $-y$ axis,

$$S_z \rightarrow \begin{cases} \frac{1}{2}S^+ \\ \frac{1}{2}S^- \end{cases} \quad S^+ \rightarrow \begin{cases} +\frac{1}{2}S^+ \\ -S_z \\ -\frac{1}{2}S^- \end{cases} \quad S^- \rightarrow \begin{cases} -\frac{1}{2}S^+ \\ -S_z \\ +\frac{1}{2}S^- \end{cases} \quad (3.56)$$

The analogous effects of a pulse along the $+y$ axis are listed in table 3.1. Note that the only difference is that the signs for coherence transfer from S_z to S^\pm and vice versa have changed. The ability to change the phase of a microwave pulse is an important tool in ESE spectroscopy, as will be discussed later.

Intermezzo: The Feynman-Vernon-Hellwarth model

In many books, review articles and PhD theses the electron spin-echo phenomenon is introduced in a classical vector model. In this work, however, it is presented using the density matrix formalism. It is then interesting to look at the correspondence between the two. For this purpose we make use of an elegant model devised by Feynman *et al.*[6]. Let us create from the Hamiltonian and the density matrix,

$$\mathcal{H} = \begin{pmatrix} \mathcal{H}_{\alpha\alpha} & \mathcal{H}_{\alpha\beta} \\ \mathcal{H}_{\beta\alpha} & \mathcal{H}_{\beta\beta} \end{pmatrix} \quad \text{and} \quad \rho = \begin{pmatrix} \rho_{\alpha\alpha} & \rho_{\alpha\beta} \\ \rho_{\beta\alpha} & \rho_{\beta\beta} \end{pmatrix}. \quad (3.57)$$

two vector quantities

$$\gamma\mathbf{B} = \frac{1}{\hbar} \begin{pmatrix} \mathcal{H}_{\alpha\beta} + \mathcal{H}_{\beta\alpha} \\ i(\mathcal{H}_{\alpha\beta} - \mathcal{H}_{\beta\alpha}) \\ \mathcal{H}_{\alpha\alpha} - \mathcal{H}_{\beta\beta} \end{pmatrix} \quad \text{and} \quad \boldsymbol{\mu} = g\beta \begin{pmatrix} \rho_{\alpha\beta} + \rho_{\beta\alpha} \\ i(\rho_{\alpha\beta} - \rho_{\beta\alpha}) \\ \rho_{\alpha\alpha} - \rho_{\beta\beta} \end{pmatrix}. \quad (3.58)$$

When $\mathcal{H} = g\beta\mathbf{B}_0 \cdot \mathbf{S}$ and $\rho = c_x S_x + c_y S_y + c_z S_z$ we find that

$$\gamma\mathbf{B} = \gamma \begin{pmatrix} B_{0,x} \\ B_{0,y} \\ B_{0,z} \end{pmatrix} \quad \text{and} \quad \boldsymbol{\mu} = g\beta \begin{pmatrix} c_x \\ c_y \\ c_z \end{pmatrix}. \quad (3.59)$$

From the time dependence of the density matrix,

$$\frac{d\rho}{dt} = \frac{i}{\hbar} [\rho, \mathcal{H}], \quad (3.60)$$

the time dependence of the vector $\boldsymbol{\mu}$ can be derived as

$$\frac{d\boldsymbol{\mu}}{dt} = \gamma\mathbf{B} \wedge \boldsymbol{\mu}, \quad (3.61)$$

which is the classical equation of motion for a magnetic moment in a magnetic field, the starting point of the classical vector model.

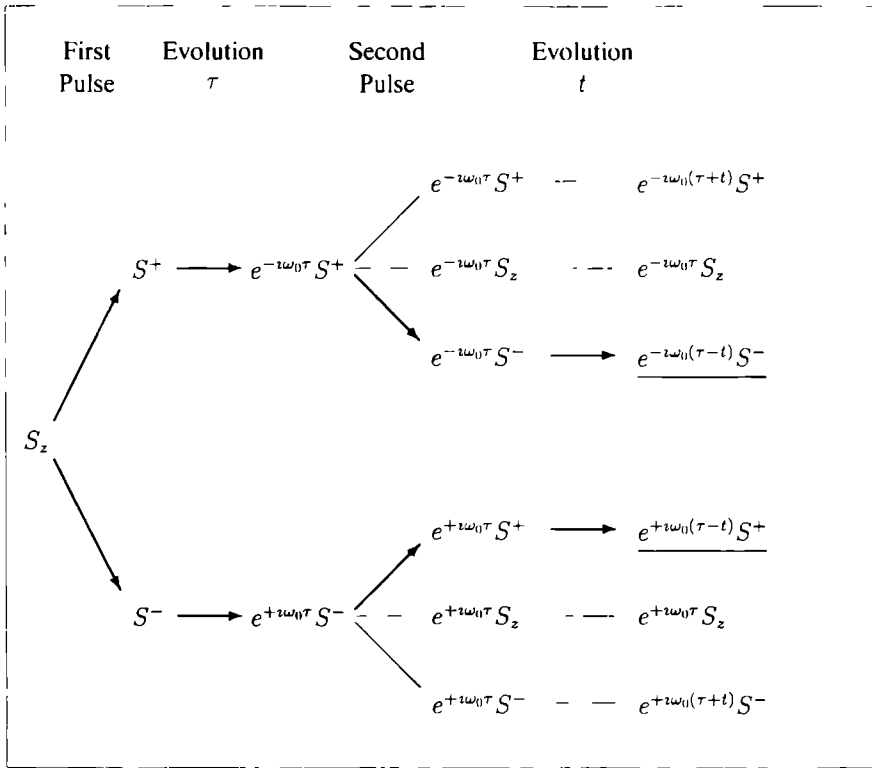


Table 3.2: Density matrix evolution tree of the Hahn echo experiment. Through this tree we can trace six coherence transfer pathways to give the six terms of the final density matrix. Only two coherence transfer pathways (indicated by arrows) lead to an echo, at $t = \tau$.

The Hahn echo experiment

For the description of Hahn's experiment we shall step through the density matrix starting from the steady state. The Hahn echo experiment consists of two $\pi/2$ pulses separated by an evolution interval τ . Using table 3.1 we can easily write down the tree of density matrix components, displayed in table 3.2. At each pulse each component of the density matrix is divided over a number of (other) components while the evolution intervals τ and t add a phase factor.

In table 3.2 we can follow several paths through the time evolution of the density matrix. During the final time interval t there are six terms in the density matrix. Of these terms two are of special interest: those terms containing a phase factor $e^{\pm i\omega_0(\tau-t)}$.

Consider that in a real physical system all individual spins will not feel exactly the same effective magnetic field \mathbf{B}_0 , due to a number of effects such as the inhomogeneity of the external magnetic field over the sample volume, differing local magnetic fields caused by slightly different local environments of the spins (for a review see [2]) and different orientations of the spins with

respect to the external magnetic field (in orientationally disordered systems) These effects result in a spread in ω_0 values apparent as an inhomogeneous line broadening, which is responsible for the echo For a free induction signal, represented by

$$FID = e^{-i\omega_0 t} S^+ + e^{+i\omega_0 t} S^-, \quad (3.62)$$

it causes a fast decay of the RF signal due to the dephasing of the magnetization Only around $t = 0$ can we observe any signal In the terms of the density matrix at a time t after the second pulse of the Hahn experiment we see a similar situation The terms

$$E(t) = e^{-i\omega_0(\tau-t)} S^- + e^{+i\omega_0(\tau-t)} S^+ \quad (3.63)$$

exhibit a relation similar to that found in the free induction decay, but now around $t = \tau$, the echo signal Although the *FID* signal has long disappeared due to destructive interference of the various spin packets, the information has *not* been lost At longer values of τ and t the echo signal will weaken as a result of transversal relaxation processes The characteristic time T_2^* associated with this relaxation is also called the phase memory time, based on the mechanism responsible for the echo

It is apparent from table 3.2 that only two terms contribute to the echo These terms can be identified by the path that is followed through the density matrix evolution tree These paths are called *coherence transfer pathways* and will be discussed in more detail later

The two echo terms can be measured individually using quadrature detection, but this is not often employed in ESE spectroscopy Usually only the $M_x = \frac{1}{2}(M^+ + M^-)$ component of the magnetization is detected, and both terms contribute to this Note that the path traced through the density matrix evolution tree leading to the M^+ magnetization is the mirror image of that leading to the M^- magnetization

The two-pulse primary echo experiment

The two-pulse experiment as it is normally used in ESE spectroscopy is not that of Hahn but is somewhat simpler, at least theoretically It consists of a $\pi/2$ pulse followed after a time τ by a π pulse The advantage of this pulse sequence is that the echo signal is stronger, which can easily be seen from the density matrix evolution tree the π pulse selectively changes the S^+ component that exists after the first evolution interval to a S^- state *exclusively* From table 3.1 it can be seen that the echo intensity must then be two times as strong as in the case of the Hahn experiment Note that the coherence transfer pathway leading to the echo in the conventional $(\pi/2 - \tau - \tau)$ experiment is the same as that in the Hahn experiment

The stimulated echo experiment

Another experiment can be created from the Hahn experiment by extending it with a third $\pi/2$ pulse (figure 3.1) To show how this forms an echo, part of the density matrix evolution tree for this experiment is displayed in table 3.3 Instead of looking at the coherence transfer pathway $S_z \rightarrow S^+ \rightarrow S^-$, leading to the Hahn echo, let us look at what happens when we select, during

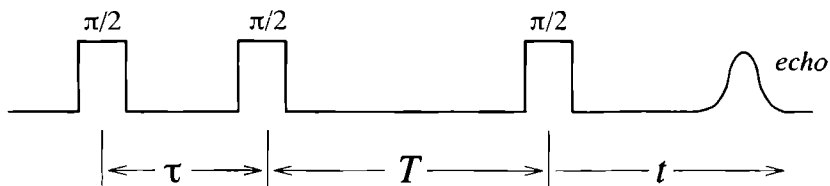


Figure 3 1 Pulse sequence of the three-pulse experiment. This is an extension of the Hahn echo experiment, which consists of two $\pi/2$ pulses, by a third $\pi/2$ pulse

T , the S_z contribution. The third microwave pulse generates from this component both S^+ and S^- components. Apparently, again an echo occurs, similar to that in Hahn's experiment, but now at a time $t = \tau$ after the *third* pulse. This echo is called the stimulated echo. Classically speaking, we have stored the magnetization along the z axis during the second evolution interval. Note that during this interval (T), only longitudinal relaxation processes affect the S_z component of the density matrix and the echo will be visible for very long values of T .

The description using the density matrix formalism is simpler than that using the vector model, but does not contain less information. Two-pulse and stimulated echo experiments are not the only ones available in ESE spectroscopy: by adding more pulses, possibly also with different phases or amplitudes, a great number of experiments can be devised. For an example see the discussion of the HYSORE experiment later in this chapter. For these more complicated experiments the density matrix formalism becomes a very powerful tool.

Multiple echoes in the three-pulse experiment

Because the three-pulse experiment is based on Hahn's experiment we expect to see at least two echoes occurring at different times, first the Hahn echo of the first two pulses and later the stimulated echo. But there are more echoes present. All echoes are identifiable by having a zero phase, and in this way we can find where echoes occur in a straightforward manner from the three-pulse density matrix evolution tree. In table 3.3 all components that may give rise to an echo have been underlined; there are 4. For example consider the path

$$\begin{aligned}
 S_z &\xrightarrow{\frac{\pi}{2}} S^+ \xrightarrow{\tau} e^{-i\omega_0\tau} S^+ \xrightarrow{\frac{\pi}{2}} e^{-i\omega_0\tau} S^+ \xrightarrow{T} \\
 &e^{-i\omega_0(\tau+T)} S^+ \xrightarrow{\frac{\pi}{2}} e^{-i\omega_0(\tau+T)} S^- \xrightarrow{t} e^{-i\omega_0(\tau+T-t)} S^-
 \end{aligned} \quad (3.64)$$

which gives rise to an echo at time $t = \tau + T$ after the third pulse. Note that the additional echoes discussed here are *not* artifacts but are an inherent part of the experiment. When we compare the coherence transfer pathway of the above echo ($S_z \rightarrow S^+ \rightarrow S^+ \rightarrow S^-$) to that of the two-pulse Hahn echo ($S_z \rightarrow S^+ \rightarrow S^-$) we see that they are very similar, and this echo is often termed the Hahn echo of pulses 1 and 3. A more detailed description of multiple echoes in ESE is given later in this chapter.

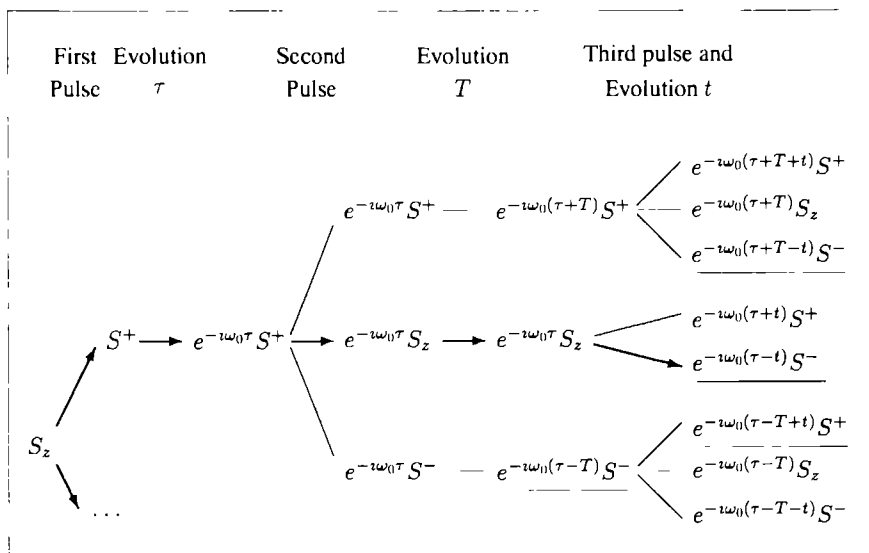


Table 3.3: Part of the density matrix evolution tree for the three-pulse experiment. In this tree we can see four positions where an echo may occur. These are underlined; the stimulated echo with a thick line.

Generalization of pulse effects

Up to now we have discussed only the effects of ideal pulses for which ω_1 is much larger than the inhomogeneous line width and the pulse shape is square. But this is not generally the case in ESE spectroscopy, especially where it concerns experiments on orientationally disordered systems in the solid state. Consider the two approximations that have been made:

1. When we are off-resonance such that $\omega_1 \approx \omega_0$ we can no longer use eq. 3.46, but we must revert to eq. 3.45. The consequence of this is that the description of the effects of ideal pulses given in table 3.1 is no longer applicable. In general we can expect to find that pulses generate S^+ , S^- and S_z components regardless of the initial density matrix, as expressed in the lower part of table 3.1.
2. In reality, microwave pulses are never sharply defined with infinitely short rise and fall times. The microwave field strength B_1 will have some complex time dependence and, to make things worse, the phase of the microwave pulses is not constant throughout the pulse duration. The formal solution, eq 3.33, of eq. 3.31 is then no longer strictly valid. The consequences of this are not readily apparent, but we can certainly expect to find the same effects as listed under point 1.

As an example consider the time evolution under a non-ideal $\pi/2$ pulse starting from the steady state density matrix S_z . Ideally we would expect to find only S^+ and S^- components in

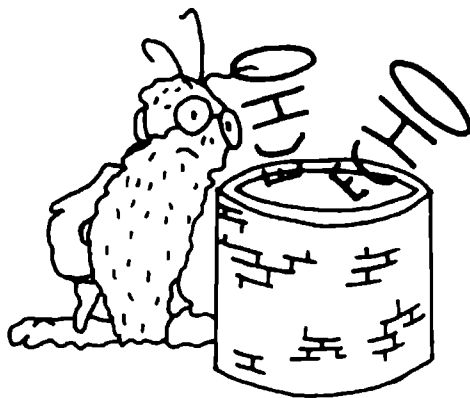
the resulting density matrix, but in reality there will also be an S_z component. In three-pulse experiments we would then see an additional echo, as can easily be derived from a density matrix evolution tree. In contrast to the four expected echoes discussed earlier, this fifth echo is an artifact, caused by imperfect pulse shapes.

3.3 Phase cycling in three- and four-pulse experiments

Introduction

In the previous section we have shown that we can expect to find five echo signals in a three-pulse experiment. It is obvious that for more complex experiments, such as the four-pulse HYSORE experiment [7] even more echoes can be expected to occur. In ESE spectroscopy, and in particular in ESEEM experiments such as those described in this thesis, we are interested only in *one* of these many echoes; in three-pulse ESEEM, for instance, we are interested only in the behavior of the stimulated echo.

For some values of τ and T some of the unwanted additional echoes that occur in this experiment may overlap with the desired echo, causing unacceptable artifacts in the modulation patterns that are the focus of this experiment (see section 3.4). Although the inter-pulse delays can be chosen so that no artifacts occur, this is usually unacceptable since in long delays much information is lost. An alternative solution is found in phase-cycling. The phase of selected microwave pulses is alternated to change the signs of the unwanted echoes. Using a linear accumulation of the echo signal the contribution of these unwanted echoes is eliminated, as is effectively illustrated for the stimulated echo experiment in [3].



... unwanted electron spin echoes

Positions of the echoes

In order to see how unwanted echoes may be removed we will first have to know how many we can expect and when they occur. In principle this can be determined from the density matrix evolution tree as shown earlier. Unfortunately, it can become very tedious to write down the density matrix evolution tree for longer pulse sequences. Gemperle *et al* [8] have demonstrated an elegant method for determining where echoes may occur by following the electron spin coherence during the entire experiment. As has been shown earlier, each echo signal, and in fact each term in the final density matrix of an experiment, can be identified by a coherence transfer pathway that is traced through the density matrix evolution tree. In the method of Gemperle these coherence transfer pathways are abstracted in terms of a coherence order $p = 0, \pm 1$. An S_z contribution to the density matrix is represented by a coherence order $p = 0$, and the S^\pm components are represented by $p = \pm 1$. We can write down the effects of microwave pulses on the various coherence order terms in the same way as we have done for their associated density matrix components (table 3.1), but since we are interested in the occurrence of echoes in a *real* experiment we have to assume that the pulses are not ideal. The microwave pulses can thus transfer any coherence order to $p = 0$, $p = +1$ and $p = -1$ terms, specifically $p = 0 \xrightarrow{\pm} p = 0, \pm 1$.

A coherence transfer pathway can be represented by the corresponding sequence of coherence order terms that occur during the interpulse delays, usually indicated by 0, +, - . For instance the coherence transfer pathway described by in eq. 3.64 is represented by (+ + -). The initial coherence order, which must always be $p = 0$, is normally not indicated. A convenient aspect of the description of the coherence transfer pathways by using coherence order terms is that these terms also define the time-dependence of the density matrix. Looking at the time evolution of the S_z, S^\pm components listed in table 3.1 we can see that with coherence order terms $p = \pm 1$ there is associated a phase factor $e^{\pm i\omega t}$. This can be used to determine whether a coherence transfer pathway leads to an echo (in which case the overall phase factor is unity) and, if so, where it occurs. An example for the sequence of coherence orders as they occur for the HYSORE echo in a four-pulse experiment is shown in figure 3.2.

There are many coherence transfer pathways possible but only a few lead to an observable echo. All pathways must start at coherence order $p_0 = 0$, the Boltzmann equilibrium polarization, and must end with $p_N = \pm 1$ in order to lead to an observable echo. The $N - 1$ intervening coherence states can have any coherence order. The total number of possible coherence transfer pathways for an N pulse experiment, N_p , from which the pathway leading to the desired echo must be selected, can be calculated as

$$N_p = 2 \cdot 3^{N-1} \quad (3.65)$$

Since any coherence transfer pathway has a mirror image which contributes equally to the observed magnetization (the echo amplitude) the actual number of possible echoes is $N_p/2$.

A number of coherence transfer pathways can never lead to an echo, namely those with only $p = 0$ and $p = +1$ terms (or, in their mirror image, those with only $p = 0$ and $p = -1$ terms). This number is equal to 2^{N-1} , the first and last coherence order terms are fixed at $p = 0$ and $p = +1$ respectively, and the $N - 1$ other terms can only take values $p = 0, +1$. Hence the total

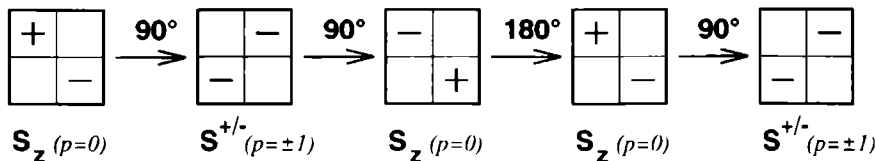


Figure 3.2 Transfer of electron spin coherence and polarization by microwave pulses for the coherence transfer pathway leading to the HYSORE echo, visualized in the density matrix. The number p represents the coherence state of the density matrix. An example of a coherence transfer pathway for the HYSORE echo of a 4-pulse experiment is shown at the bottom

number of coherence transfer pathways that may lead to an echo is

$$N_e = 3^{N-1} - 2^{N-1} \quad (3.66)$$

The position at which an echo occurs can be calculated from the condition that the overall phase factor must then be unity, which occurs if the total time spent in $p = +1$ equals the total time spent in $p = -1$. Indicating the interval between pulses i and $i + 1$ as t_i and the coherence order during that interval as p_i (and the final coherence order as p_N) we find that an echo occurs for a specific coherence transfer pathway at

$$t_{echo} = - \left(\sum_{i=1}^{N-1} t_i \times p_i \right) / p_N \quad (3.67)$$

relative to the last pulse. If $t_{echo} > 0$ the echo occurs *after* the last pulse, but if $t_{echo} < 0$ the echo occurs *before* the last pulse. In that case the last pulse had no effect on the electron spin coherence order.

As an example, we have tabulated in table 3.4 all possible echoes which can be formed for a four-pulse sequence as used in the HYSORE experiment. The coherence transfer pathways are indicated using the coherence orders $p = 0, \pm 1$ starting from Boltzmann equilibrium $p = 0$. The times at which the echoes occur have been calculated using eq. 3.67 and are also listed in that table, and we have also characterized each echo.

A few remarks are in order.

- It must be noted that not all allowed coherence transfer pathways do indeed lead to an echo for all possible intervals t_i . Consider the pathway $(+ - ++)$ for a four-pulse sequence. When $t_2 > t_1$ an echo will occur at a time t_1 in the second (t_2) interval, which will be refocussed by the third pulse to form echo number 3 of table 3.4. When, however, $t_2 < t_1$, no primary echo will occur that can be refocussed and echo number 3 cannot be observed.

3.3. PHASE CYCLING IN THREE- AND FOUR-PULSE EXPERIMENTS

Echo number	Coherence pathway	Echo position	Echo type	Phase cycle
1	+ - - -	$t_1 - t_2 - t_3$	Hahn (1,2)	+ - + - = 0
2	+ 0 - -	$t_1 - t_3$	Stim. (1,2,3)	+ + - - = 0
3	+ - + +	$t_2 - t_1 - t_3$	Hahn (1,2) Ref. 3	- + - + = 0
4	0 + - -	$t_2 - t_3$	Hahn (2,3)	+ - + - = 0
5	+ + - -	$t_2 + t_1 - t_3$	Hahn (1,3)	+ - + - = 0
6	+ 0 0 -	t_1	Stim. (1,2,4)	+ + + - = 4+
7	+ 0 0 -	t_1	HYSCORE (1,2,3,4)	- - - - = 4-
8	+ + - +	$t_3 - t_2 - t_1$	Hahn (1,3) Ref. 4	- + - + = 0
9	0 + - +	$t_3 - t_2$	Hahn (2,3) Ref. 4	- + - + = 0
10	+ - + -	$t_3 - t_2 + t_1$	Hahn (1,2) Ref. 3, Ref. 4	+ - + - = 0
11	+ - 0 +	$t_2 - t_1$	Hahn (1,2) Ref. (3,4)	- + + - = 0
12	0 + 0 -	t_2	Stim. (2,3,4)	+ - - + = 0
13	+ + 0 -	$t_2 + t_1$	Stim. (1,3,4)	+ - - + = 0
14	+ 0 - +	$t_3 - t_1$	Stim. (1,2,3) Ref. 4	- - + + = 0
15	0 0 + -	t_3	Hahn (3,4)	+ + - - = 0
16	+ 0 + -	$t_3 + t_1$	Accumulated (1,2,3,4)	- - + + = 0
17	+ - - +	$t_2 + t_3 - t_1$	Hahn (1,2) Ref. 4	- + - + = 0
18	0 + + -	$t_2 + t_3$	Hahn (2,4)	+ - + - = 0
19	+ + + -	$t_2 + t_3 + t_1$	Hahn (1,4)	+ - + - = 0
20	+ - 0 -	$t_1 - t_2$	Delayed (1,2,3,4)	+ - + - = 0

Table 3.4: Description of the 20 echoes occurring in a HYSCORE experiment. Echoes 6 and 7, the stimulated echo of pulses 1,2 and 4, and the HYSCORE echo always overlap. This stimulated echo cannot be removed by phase cycling. In some cases, an echo has been refocussed by later pulses, e.g. echo 1 has been refocussed by the third pulse to form echo 3. The echo position can be calculated from t_1 , t_2 and t_3 . The first 19 echoes are shown in figure 3.4. Echo 20 does not occur for the intervals chosen there. The HYSCORE echo can be isolated from the other echoes by using a phase cycling scheme that selects only that echo.

To determine whether a coherence transfer pathway will actually lead to an echo, consider the following. As mentioned earlier, an echo can only occur if the time spent in $p = +1$ states equals the time spent in $p = -1$ states. Let us define the *last effective pulse* for a coherence transfer pathway to be the last pulse that causes a change in coherence order; as an example, for the coherence transfer pathway (+ - + +), the third pulse would be the last effective pulse. Echoes must always occur *after* the last effective pulse of their coherence transfer pathway; those that occur before the last effective pulse are better described by another pathway. By comparing the time at which the echo occurs (see eq. 3.67) to the position of the last effective pulse we can determine if this is the case.

- Some coherence transfer pathways may lead to more than one echo; a coherence transfer pathway where a π -pulse transfers a S_z spin state to a $-S_z$ spin state as shown in figure 3.2 is indistinguishable from the coherence transfer pathway where this pulse does not occur. Such pathways must have two or more consecutive $p = 0$ states. In the four-pulse echo,

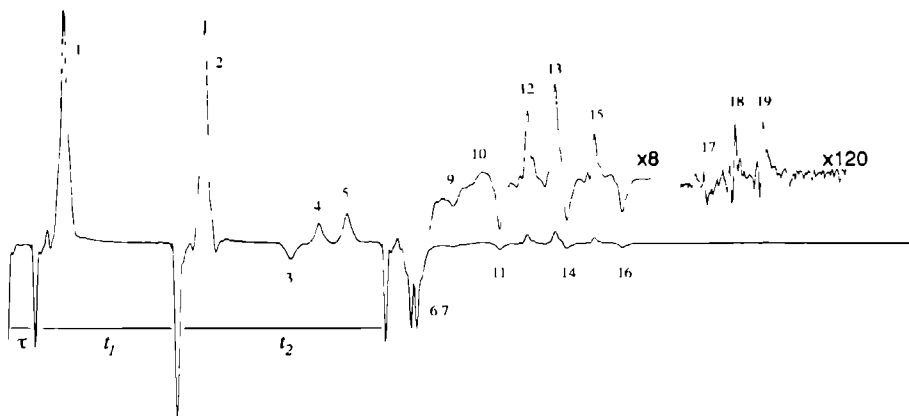


Figure 3.3: 4-pulse echoes of irradiated calcium formiate. Intervals between the pulses are indicated by τ , t_1 , t_2 with $\tau = 200$ ns, $t_1 = 1000$ ns and $t_2 = 1500$ ns. The whole spectrum spans $6.5 \mu\text{s}$ with a time resolution of 2 ns. This spectrum is the result of 5000 averages and was recorded on a Bruker EPS380 FT-EPR spectrometer

this occurs for the $(+ 0 0 -)$ coherence transfer pathway, which leads to the HYSORE echo, but also to the stimulated three-pulse echo of pulses 1, 2 and 4 (echoes 6 and 7 of table 3.4 and figure 3.4). This situation occurs only for non-ideal pulses.

Using this technique it can be easily shown that we expect to see five echoes in the stimulated three-pulse experiment: three two-pulse Hahn-echoes of the pairs (1,2), (1,3) and (2,3), the stimulated echo of pulses 1, 2 and 3, and we also may see the Hahn-echo of pulses 1 and 2 that is refocussed by pulse 3. This last echo is not usually described in the literature. The same technique can be used to show that there are in general 19 echoes possible in a 4-pulse experiment, or 20 when we count the two echoes for the coherence transfer pathway $(+ 0 0 -)$ separately (see table 3.4). Three of the echoes listed in this table may need some explanation. The accumulated echo, number 16 in the table, is related to the stimulated echo, but the third pulse is replaced by a Hahn echo sequence. The second special echo (number 11) is a two-pulse Hahn echo which is refocussed by a two-pulse sequence similar to the second and third pulses in a stimulated echo experiment. Echo number 20 is a Hahn echo of pulses 1 and 2, of which the formation has been delayed by the time between pulses 3 and 4.

In the description of the HYSORE experiment the intervals are usually indicated by τ , t_1 and t_2 , in that order (see figure 3.5). The positions and signs of all echoes occurring for intervals $\tau = 200$ ns, $t_1 = 1000$ ns and $t_2 = 1500$ ns is shown in figure 3.4. It must be borne in mind when considering these echoes that the refocussed echoes will usually be significantly weaker than their primary counterparts. Also, the Hahn echoes quickly decay for larger values of t_1 and t_2 , since they are dependent on T_2 relaxation processes. Figure 3.3 shows a recorded echo trace of a powdered sample of irradiated calcium formiate, generously provided by Professor Schweiger of the ETH Zürich, for the values of τ , t_1 and t_2 used earlier. In this echo trace, 18 of the 19 echoes that can be expected for these intervals are observed. Only echo number 8 is

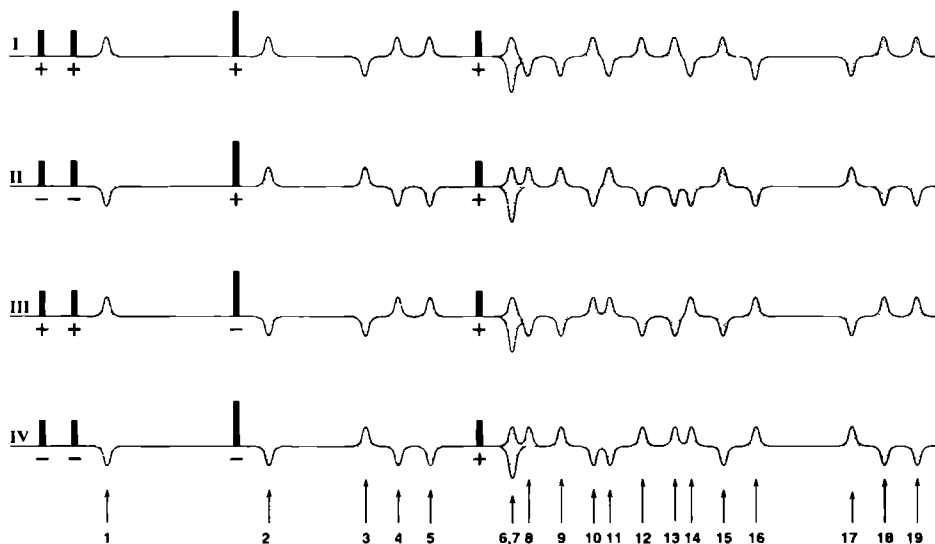


Figure 3.4: Effect of phase cycling. Phases of the pulses are indicated as (+) and (-), which indicate a 180° phase difference. 19 echoes are visible that are listed in table 3.4. On summation of the four cycles, only echoes 6 and 7 are not eliminated. Echo 20 of table 3.4 does not occur.

missing; it is presumably hidden under the echoes 6 and 7.

Phase cycling

The next step is to remove the unwanted echoes which we have found and identified. In ESE spectroscopy this removal is done by a technique known as phase cycling: By alternating the phase of selected pulses we can change the signs of the unwanted echoes and remove them by a linear accumulation of the echo signal. Most commonly, phase cycling is done using phase changes of 180° . The effects of microwave pulses with such a phase shift are listed in eq. 3.56. This phase shift affects $\pi/2$ pulses only to the extent that the coherence transfer from S_z , or $p = 0$ to S^\pm , or $p = \pm 1$, and vice versa, changes sign. By changing the phase of only one of the pulses that cause a $p = 0 \leftrightarrow p = \pm 1$ transition in a coherence transfer pathway the sign of the associated echo is changed (the same holds for any odd number of such pulses). By studying the possible coherence transfer pathways the optimum sequence of phase cycles can be found. Figure 3.4 shows the phase cycling scheme used in HYSORE spectroscopy, along with the signs of all 19 possible echoes for the chosen time intervals. This specific phase cycling scheme is chosen because it specifically selects the HYSORE echo. Other phase cycling schemes can be devised that select other echoes. Table 3.4 also lists the effects of this phase cycling scheme. Note that only the admixture of a stimulated echo component to the HYSORE signal cannot be removed, since the two echoes have the same coherence transfer pathway.

3.4 Derivation of an expression for the nuclear modulation effect in multi-pulse sequences

In this section we will show that when the electron is coupled to a nuclear spin system we will see that the echo intensity is modulated by the frequencies of the nuclear spin system. This effect can be used to investigate the properties of the nuclear spin system through the interaction parameters of the Hamiltonian.

The Hamiltonian for such a system, consisting of an electron spin S coupled to a nuclear spin system I_i , can be approximated by

$$\mathcal{H} = \mathcal{H}_0 + \mathcal{H}_n = \hbar\omega_0 S_z + \sum_i \langle S \rangle_z A_i \cdot I_i + \dots \quad (3.68)$$

where ω_0 is the off-resonance frequency of a spin packet in the rotating frame. This approximation, in which \mathcal{H}_0 and \mathcal{H}_n commute, is called the strong-field approximation. Because \mathcal{H}_n is not independent of \mathcal{H}_0 but is parametrized by $\langle S \rangle_z$, the eigenfunctions of this spin system can be expressed as a basis of products of the \mathcal{H}_0 eigenstates $|m\rangle$ and the associated \mathcal{H}_n eigenstates, $|i_m\rangle$, which are different for each $|m\rangle$,

$$|i\rangle = |m, i_m\rangle = |m\rangle |i_m\rangle. \quad (3.69)$$

The mechanism that is responsible for the modulation of the electron spin echo has its basis in the fact that the nuclear Hamiltonian and the nuclear spin levels are parametrized by the electron spin. When, as a result of the microwave pulses, there is a change in the effective electron spin, the nuclear Hamiltonian changes and the nuclear spins will suddenly find themselves no longer in an eigenstate of the (current) nuclear Hamiltonian. Due to the very strong coupling between the electron and the nucleus, the microwave pulses, which are resonant only with the electronic transitions, create both electron *and* nuclear spin coherences. The resulting evolution of these nuclear spin coherences causes an intensity modulation of the electron spin echo signal. The effect whereby the microwave pulses cause the coherences is called branching. In a way, this modulation effect is comparable to FT-NMR where RF pulses directly create coherences in the nuclear spin levels, which are, however, not coupled to an electron spin S .

To understand these electron spin echo modulation experiments we shall work out the expressions governing the changes in the density matrix describing the coupled spin system. When the system is in thermal equilibrium, this density matrix is

$$\begin{aligned} \rho_0 &= \frac{e^{-\mathcal{H}/kT}}{\mathcal{Z}} \approx \frac{1}{\mathcal{Z}} \left(e^{-\hbar\omega_0 S_z/kT} \right) \otimes \mathbb{I}_n \\ &= \frac{1}{\mathcal{Z}} \left\{ \mathbb{I} \cosh(\frac{1}{2}\hbar\omega_0/kT) - \sigma_z \sinh(\frac{1}{2}\hbar\omega_0/kT) \right\} \otimes \mathbb{I}_n \\ &= (A + \alpha \sigma_z) \otimes \mathbb{I}_n. \end{aligned} \quad (3.70)$$

where \otimes indicates the direct product. The approximation is valid if the energy difference between the electron spin eigenstates is much larger than that between the nuclear eigenstates, which is

the condition under which the strong-field approximation is valid. Because the electronic and nuclear Hamiltonians \mathcal{H}_0 and \mathcal{H}_n commute, we can expand the operator $\mathcal{U}(t) = e^{-i/\hbar \mathcal{H} t}$ to

$$\mathcal{U}(t) = \mathcal{U}_0(t) \otimes \mathcal{U}_n(t) = e^{-i/\hbar \mathcal{H}_0 t} \otimes e^{-i/\hbar \mathcal{H}_n t} \quad (3.71)$$

The matrix representation $U_0(t)$ of the electronic spin evolution operator in the basis of eigenstates of \mathcal{H}_0 is then

$$U_0(t) = \begin{pmatrix} e^{-i\omega_0 t/2} & 0 \\ 0 & e^{i\omega_0 t/2} \end{pmatrix} \text{ and thus} \quad (3.72)$$

$$U(t) = \begin{pmatrix} e^{-i\omega_0 t/2} & 0 \\ 0 & e^{i\omega_0 t/2} \end{pmatrix} \begin{pmatrix} T_n^+(t) & 0 \\ 0 & T_n^-(t) \end{pmatrix} \quad (3.73)$$

where $T_n^+(t)$ and $T_n^-(t)$ are the matrix representations of the evolution operator $\mathcal{U}_n(t)$ for the different eigenstates of \mathcal{H}_0 , indicated by $m_S = +1/2$ and $m_S = -1/2$.

It is interesting to discuss the representations of $T_n^+(t)$ and $T_n^-(t)$ in any basis $|i'\rangle, |j'\rangle$. The matrix elements of $T_n^\pm(t)$ are

$$\langle i' | T_n^\pm(t) | j' \rangle \quad (3.74)$$

which, for the basis of eigenstates of \mathcal{H}_n , takes on a very simple form,

$$[T_n^\pm(t)]_{ij} = \langle i_\pm | T_n^\pm(t) | j_\pm \rangle = \delta_{ij} e^{-i\omega_\pm t} \quad (3.75)$$

The matrix T_n^\pm in any basis $\Delta = |i'\rangle, |j'\rangle$ is then

$$T_n^\pm(t) = R_n^\pm D(t)^\pm (R_n^\pm)^{-1} \quad (3.76)$$

where $D_{ij}^\pm = \delta_{ij} e^{-i\omega_\pm t}$ are the elements of T_n^\pm expressed in the basis $|i_\pm\rangle, |j_\pm\rangle$ of eigenstates of \mathcal{H}_n . The transformation matrix R_n^\pm defines this basis in terms of the basis Δ ,

$$[R_n^\pm]_{i'j} = \langle i' | j_\pm \rangle \quad (3.77)$$

Combining eq. 3.73 with the expressions for $T_n^\pm(t)$ and writing $T_n^+(t) = A_t$ and $T_n^-(t) = B_t$, the matrix of the evolution operator $\mathcal{U}(t)$ (eq. 3.71) becomes

$$\mathcal{U}(t) = \begin{pmatrix} A_t e^{-i\omega_0 t/2} & \\ & B_t e^{+i\omega_0 t/2} \end{pmatrix} \quad (3.78)$$

The evolution operators for microwave pulses

The effect of strong microwave pulses at or near resonance on the density matrix in the rotating frame can be described by an interaction Hamiltonian

$$\mathcal{H}_1 = \hbar\omega_1 S_y \quad \text{or} \quad \mathcal{H}_1 = \hbar\omega_1 S_x \quad (3.79)$$

depending on the direction in the rotating frame of the interaction field (see eq. 3.32), under the condition that the pulses are very short and that the natural evolution of the nuclear spins

effectively stops during the pulses so that the Hamiltonian is complete by giving \mathcal{H}_1 . The evolution of the density matrix under these conditions is given by the operator

$$\begin{aligned} U(t) &= e^{-i/\hbar \mathcal{H}_1 t} = e^{-i\omega_1 \sigma_y t / \gamma} \otimes I_n \\ &= (I \cos(\omega_1 t / 2) - i\sigma_y \sin(\omega_1 t / 2)) \otimes I_n \\ &= U_1(t) \otimes I_n \end{aligned} \quad (3.80)$$

The matrix representation $U(t)$ of this operator in the basis $|m, \nu_m\rangle$ of the eigenstates of \mathcal{H}_0 and some basis of \mathcal{H}_n is then defined by

$$\begin{aligned} [U(t)]_{m, \nu_m, m', \nu_{m'}} &= \langle m, \nu_m | U(t) | m', \nu_{m'} \rangle \\ &= \langle m | U_1(t) | m' \rangle \langle \nu_m | \nu_{m'} \rangle \end{aligned} \quad (3.81)$$

The form of this matrix simplifies considerably if we choose the same basis for T_n^+ and T_n^- , for example the basis of eigenstates $|m_I\rangle$ of the spin operator I , so that $\langle \nu_m | \nu_{m'} \rangle = \delta_{\nu_m, \nu_{m'}}$, independent of m, m' and

$$U(t) = \begin{pmatrix} \cos(\omega_1 t / 2) & I_n & -\sin(\omega_1 t / 2) & I_n \\ \sin(\omega_1 t / 2) & I_n & \cos(\omega_1 t / 2) & I_n \end{pmatrix} \quad (3.82)$$

For ideal $\pi/2$ and π pulses the evolution matrices R_{90} and R_{180} evaluate to

$$R_{90} = \frac{1}{2}\sqrt{2} \begin{pmatrix} I_n & -I_n \\ I_n & I_n \end{pmatrix}, \quad R_{180} = \begin{pmatrix} 0 & -I_n \\ I_n & 0 \end{pmatrix} \quad (3.83)$$

The matrix M of transition probabilities between the nuclear sublevels of the $m_S = -1/2$ and $m_S = +1/2$ spin states, usually referred to as the sublevels of the different m_S manifolds, is defined by $M_{\nu_+ \nu_-} = \langle \nu_+ | j_- \rangle$ for eigenstates $|\nu_+\rangle$ and $|\nu_-\rangle$ of \mathcal{H}_n^\pm , but can also be written

$$M = (R_n^+)^{-1} R_n^-, \text{ since} \quad (3.84)$$

$$M_{\nu_+ \nu_-} = \langle \nu_+ | j_- \rangle = \sum_{m_I} \langle \nu_+ | m_I \rangle \langle m_I | j_- \rangle \quad (3.85)$$

when we choose to express T_n^\pm in terms of the functions $|m_I\rangle$

The derivation by Mims [2] of the modulation intensity was done in the eigenbasis of \mathcal{H}_n . This simplifies the evolution matrices A and B , but makes the form of the matrices describing the effect of the microwave pulses more complicated. Since the explicit form of these matrices is used many times in the derivations it is in this case more convenient to use the $|m_I\rangle$ basis

The two-pulse experiment

As an example, let us consider the evolution of the density matrix in a two-pulse primary echo experiment. The pulse sequence starts with a $(\pi/2)_y$ pulse, followed by an evolution interval τ and a $(\pi)_y$ pulse.

The initial density matrix of eq. 3.70 can for our purposes be written as

$$\rho_0 = \begin{pmatrix} I_n & \\ & -I_n \end{pmatrix} \quad (3.86)$$

3.4. AN EXPRESSION FOR THE NUCLEAR MODULATION EFFECT

The evolution of this matrix is described by the evolution operators for the $(\pi/2)_y$ and $(\pi)_y$ pulses and the free precession intervals (eqs. 3.83 and 3.78). We have to evaluate

$$\rho_t = R_t R_{180} R_\tau R_{90} \rho_0 R_{90}^{-1} R_\tau^{-1} R_{180}^{-1} R_t^{-1}. \quad (3.87)$$

The outcome of the successive steps is

$$\rho_0 \xrightarrow{(\pi/2)_y} \begin{pmatrix} I_n & \\ & I_n \end{pmatrix} \xrightarrow{\tau} \begin{pmatrix} A_\tau B_\tau^\dagger e^{-i\omega_0\tau} & \\ B_\tau A_\tau^\dagger e^{+i\omega_0\tau} & \end{pmatrix} \xrightarrow{(\pi)_y} \begin{pmatrix} B_\tau A_\tau^\dagger e^{+i\omega_0\tau} & \\ A_\tau B_\tau^\dagger e^{-i\omega_0\tau} & \end{pmatrix}. \quad (3.88)$$

The density matrix at a time t after the second microwave pulse is then given by

$$\rho_t = - \begin{pmatrix} A_t B_\tau A_\tau^\dagger B_t^\dagger e^{+i\omega_0(\tau-t)} & \\ B_t A_\tau B_\tau^\dagger A_t^\dagger e^{-i\omega_0(\tau-t)} & \end{pmatrix}, \quad (3.89)$$

which can be used to calculate the electron spin magnetization in the x (or y) direction after the last pulse. This magnetization is given by

$$\begin{aligned} S(\tau, t) &= g\beta \text{Tr}(\rho_t S_x) \\ &= -\frac{1}{2}g\beta \text{Tr} \left(A_t B_\tau A_\tau^\dagger B_t^\dagger e^{+i\omega_0(\tau-t)} + B_t A_\tau B_\tau^\dagger A_t^\dagger e^{-i\omega_0(\tau-t)} \right). \end{aligned} \quad (3.90)$$

As explained in section 3.2, there will usually be some inhomogeneous line broadening in a physical system, which is represented here by a spread in off-resonance frequencies ω_0 . The consequence of this is that a magnetization will be observed only for $t \approx \tau$. The echo intensity is normally identified by the value of $S(\tau, t)$ at $t = \tau$, and thus we find

$$\begin{aligned} E(\tau) = S(\tau, \tau) &= -\frac{1}{2}g\beta \text{Tr} \left(A_t B_\tau A_\tau^{-1} B_t^{-1} + B_t A_\tau B_\tau^{-1} A_t^{-1} \right) \\ &= -g\beta \text{Re} \left(\text{Tr}(A_t B_\tau A_\tau^{-1} B_t^{-1}) \right). \end{aligned} \quad (3.91)$$

By making use of eqs. 3.78 and 3.84 we can write this as

$$E(\tau) = -g\beta \text{Re} \left[\text{Tr}(U P_\tau U^\dagger V Q_\tau V^\dagger U P_\tau^\dagger U^\dagger V Q_\tau^\dagger V^\dagger) \right] \quad (3.92)$$

$$= -g\beta \text{Re} \left[\text{Tr}(U^\dagger U P_\tau U^\dagger V Q_\tau V^\dagger U P_\tau^\dagger U^\dagger V Q_\tau^\dagger V^\dagger U) \right] \quad (3.93)$$

$$= -g\beta \text{Re} \left[\text{Tr}(P_\tau M Q_\tau M^\dagger P_\tau^\dagger M Q_\tau^\dagger M^\dagger) \right] \quad (3.94)$$

where for simplicity we have written $R_n^+ = U$, $R_n^- = V$, $D_\tau^+ = P_\tau$ and $D_\tau^- = Q_\tau$. The step from eq. 3.92 to eq. 3.93 can be explained by noting that the trace of a matrix does not change on a unitary transformation.

Eq. 3.94 can be evaluated when we note that P_τ and Q_τ are diagonal matrices, and thus

$$\begin{aligned} E(\tau) &= -g\beta \text{Re} \left(\sum_{ij,kl} M_{ik} M_{kj}^\dagger M_{jl} M_{li}^\dagger e^{-i\omega_i^0\tau} e^{-i\omega_k^1\tau} e^{+i\omega_j^2\tau} e^{+i\omega_l^3\tau} \right) \\ &= -g\beta \text{Re} \left(\sum_{ij,kl} M_{ik} M_{kj}^\dagger M_{jl} M_{li}^\dagger e^{-i\omega_{ij}^0\tau} e^{-i\omega_{kl}^1\tau} \right). \end{aligned} \quad (3.95)$$

An analogous expression for the modulation intensity in the three-pulse stimulated echo experiment is derived according to Mims' method in section 3.7.

		Pulses
$\{a\}_0$	$\xrightarrow{\pm(\pi/2)_y}$	$\frac{1}{2}\{a+b\}_0 \pm \frac{1}{2}\{a-b\}_1$
$\{a\}_0$	$\xrightarrow{\pm(\pi/2)_x}$	$\frac{1}{2}\{a+b\}_0 \pm \frac{1}{2}i\{a-b\}_1$
$\{a\}_0$	$\xrightarrow{\pm(\pi)_x \text{ or } y}$	$\{b\}_0$
$\{c\}_1$	$\xrightarrow{\pm(\pi/2)_y}$	$\mp \frac{1}{2}\{c+c^*\}_0 + \frac{1}{2}\{c-c^*\}_1$
$\{c\}_1$	$\xrightarrow{\pm(\pi/2)_x}$	$\mp \frac{1}{2}i\{c-c^*\}_0 + \frac{1}{2}\{c+c^*\}_1$
$\{c\}_1$	$\xrightarrow{\pm(\pi)_y}$	$-\{c^*\}_1$
$\{c\}_1$	$\xrightarrow{\pm(\pi)_x}$	$\{c^*\}_1$
Free precession		
$\{a\}_0$	\xrightarrow{t}	$\{A_t a A_t^\dagger\}_0$
$\{c\}_1$	\xrightarrow{t}	$\{A_t c B_t^\dagger \Phi_t\}_1$, where $\Phi_t = e^{-i\omega_0 t}$
Trace of the magnetization		
$\{a\}_0$	$\xrightarrow{\mathcal{M}^\pm}$	0
$\{c\}_1$	$\xrightarrow{\mathcal{M}^+}$	$g\beta \text{Tr}(c^*)$
$\{c\}_1$	$\xrightarrow{\mathcal{M}^-}$	$g\beta \text{Tr}(c)$

Table 3.5: Operations on the density matrix in the shorthand notation. The top seven operations indicate the effects of microwave pulses on the density matrix. The next two terms indicate the effect of free precession. At the bottom some notes, useful in calculating the magnetization, are listed.

3.5 A shorthand notation

The method described above leads to an expression for the echo intensity with less work than the method described by Mims [2]. Its main advantage is the simple form of the pulse evolution matrices R_{90} and R_{180} . Still, this method can be improved upon since we have not taken into account the symmetry that is present in the density matrix.

We wish to present here an alternative, shorthand, notation for the density matrix and the evolution operators that occur in ideal pulsed EPR experiments. We shall characterize the density matrices by the two terms

$$\{a\}_0 \equiv \begin{pmatrix} a & 0 \\ 0 & b \end{pmatrix} \text{ and } \{c\}_1 \equiv \begin{pmatrix} 0 & c \\ c^* & 0 \end{pmatrix}. \quad (3.96)$$

The diagonal elements of the density matrix are identified by the subscript 0, and the off-diagonal elements by a subscript 1. It is interesting to note that the elements $\{a\}_0$ correspond to a coherence order $p = 0$ and the elements $\{c\}_1$ to a coherence order $p = \pm 1$ (see for a discussion of coherence order section 3.3 and [9]) In the general case, a , b and c will be matrices, in which case $c^* = c^\dagger$. Note that the diagonal terms a and b are given only by a . This implies that b can somehow be derived from a , and we will show later how this can be done. The matrices a and b must be hermitian, but c does not have to be.

The next step is to describe the effect of the various evolution operators on these two terms. This can most easily be done by expanding these terms to the full density matrices and applying the evolution operators to this density matrix,

$$\rho_t = \mathcal{U}(t) \rho_0 \mathcal{U}^{-1}(t) \tag{3.97}$$

and then writing the new density matrix ρ_t in terms of $\{a\}_0$ and $\{c\}_1$. Because the evolution is a linear operation, we only need to calculate what happens to $\{a\}_0$ and $\{c\}_1$ individually

$$\begin{aligned} \rho_t &= \mathcal{U}(t) \rho_0 \mathcal{U}^{-1}(t) = \mathcal{U}(t) (\alpha \{a\}_0 + \gamma \{c\}_1) \mathcal{U}^{-1}(t) \\ &= \alpha \mathcal{U}(t) \{a\}_0 \mathcal{U}^{-1}(t) + \gamma \mathcal{U}(t) \{c\}_1 \mathcal{U}^{-1}(t) \end{aligned} \tag{3.98}$$

Table 3.5 lists the effects of all operators used in pulsed EPR on the terms $\{a\}_0$ and $\{c\}_1$. This table also lists expressions for the magnetization $\rho_e S^+$ and $\rho_e S^-$ for both the $\{a\}_0$ and $\{c\}_1$ terms.

The density matrix evolution during a multipulse experiment can be followed by repeatedly applying the operations listed in table 3.5 to the density matrix. If we are interested in deriving an expression for the echo intensity, the calculation can be simplified by considering the coherence transfer pathway of the echo, as described in section 3.3. For every evolution interval, we need only retain the $\{a\}_0$ terms if the coherence order p during that interval equals 0 and conversely, we need only retain the $\{c\}_1$ terms for $p = \pm 1$. This can be verified by following the phase factor Φ_t during the experiment.

As noted above, it must be possible to derive b from a by some transformation T so that we may reconstruct the density matrix, but knowledge of b is also essential for performing the operations of table 3.5. Fortunately, there is a very simple recipe for deriving b from a , which is given below. The formal derivation of this operation is tedious and not very instructive and will not be reproduced here.

The transformation T consists of the following three steps:

1. Multiply a by -1
2. Change all matrices A_t to B_t , and B_t to A_t , and
3. Take the complex conjugate of any phase factor Φ_t .

Operation (1) stems from the fact that $b = -a$ for ρ_0 . Operation (2) is a result of the fact that during a free precession the terms b will acquire factors B_t, B_t^\dagger , whereas the terms a will acquire factors A_t and A_t^\dagger . Operation (3) is less obvious, but it can be seen that this must be so when we consider that the terms in b that have acquired a phase factor Φ_t must also have factors A_t, B_t^\dagger , which suggests that a has terms with factors B_t, A_t^\dagger which have associated with them a phase factor Φ_t^* . Note that this operation is only valid for hermitian a and b . In particular, if we split $\{a\}_0$ into $(\{a_1\}_0 + \{a_2\}_0)$ then

$$T \{a\}_0 = T \{a_1\}_0 + T \{a_2\}_0 = \{b\}_0 \tag{3.99}$$

but it is not necessarily true that

$$\{b_1\}_0 = T \{a_1\}_0 \text{ or } \{b_2\}_0 = T \{a_2\}_0 \quad (3.100)$$

because a_1 and a_2 need not be hermitian. The recipe for taking the hermitian conjugate of c to find c^* is given here for completeness:

1. Take the complex conjugate of any phase factor Φ and other constants in c .
2. For every term in c , reverse the order of the matrices A and B , and take their hermitian conjugate.

The two-pulse experiment revisited

The derivation of the echo intensity of the two-pulse echo using the shorthand method outlined above becomes very simple. From the equilibrium density matrix $\rho_0 = \{1\}_0$ we find

$$\rho_0 = \{1\}_0 \xrightarrow{(\pi/2)_y} \{1\}_1 \xrightarrow{\tau} \{A_\tau B_\tau^\dagger \Phi_\tau\}_1 \xrightarrow{(\pi)_y} -\{B_\tau A_\tau^\dagger \Phi_\tau^*\}_1 \xrightarrow{t} -\{A_t B_\tau A_\tau^\dagger B_t^\dagger \Phi_{t-\tau}\}_1,$$

and from table 3.5 we can immediately read that the magnetization must be

$$\rho_t \xrightarrow{M_z} -g\beta\text{Re} \left(\text{Tr}(A_t B_\tau A_\tau^\dagger B_t^\dagger \Phi_{t-\tau}) \right) \quad (3.101)$$

which is identical to eq. 3.91 for $t = \tau$.

3.6 The HYSORE experiment

Introduction

Multidimensional correlation techniques have become a cornerstone of NMR spectroscopy with different types of experiments routinely being used in a wide range of investigations. In contrast, the development of multidimensional pulsed EPR techniques is of much later date, and the use of these techniques has mostly been limited to demonstrating the feasibility the proposed experiments. Since the original proposal for a multidimensional pulsed EPR technique was published in 1979 (Merks and De Beer, [10]) a number of multidimensional FT-EPR and electron spin-echo techniques have been developed by Freed and co-workers [11], Schweiger and co-workers [12] and by others.

The HYSORE (Hyperfine Sublevel Correlation Spectroscopy) experiment was conceived in 1986 by Höfer *et al.* [7] as an alternative to the two-dimensional version of the stimulated echo proposed by Merks and De Beer. It is a two-dimensional correlation technique that correlates frequencies from different m_S states of the same electron. The advantages of HYSORE over the two-dimensional stimulated echo experiment are a high frequency resolution in both dimensions and a simpler correlation pattern. The HYSORE experiment is closely related to the one-dimensional stimulated echo experiment. The pulse sequence of the HYSORE experiment, shown in figure 3.5, is derived from the pulse sequence for the stimulated echo experiment by the insertion of a 180° inversion pulse between the second and third pulses of the stimulated echo sequence.

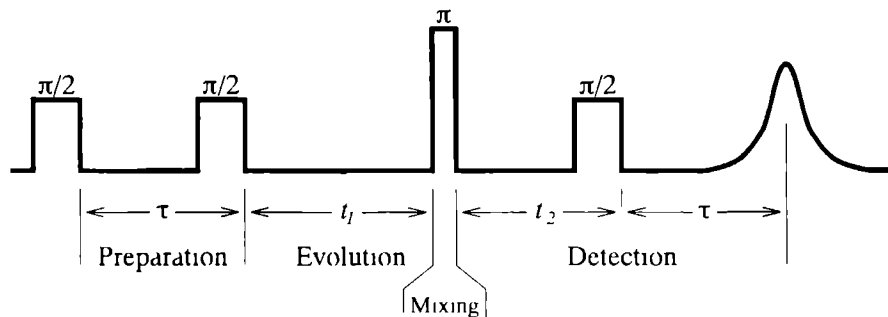


Figure 3.5 Basic pulse sequence of the four pulse experiment

The four-pulse experiment as a correlation technique

In NMR, a correlation experiment is usually described in terms of four intervals: preparation, evolution, mixing and detection [13]. Probably the most basic correlation experiment is the homonuclear COSY experiment in NMR proposed by Jeener in 1971 [14] in which the couplings between two spin systems S and I are investigated. In this experiment the system is first prepared by means of a 90° RF pulse into a state where there are nuclear coherences. These nuclear coherences are then allowed to evolve during a time t_1 . A second 90° pulse causes the transfer of magnetization between the two coupled spin systems S and I . The experiment is then concluded by recording the resulting FID during t_2 [1, 15].

To understand the HYSOCORE technique it is instructive to follow the evolution of a spin packet through the four intervals indicated in figure 3.5. We will illustrate the experiment by following the density matrix of an $S = 1/2$, $I = 1/2$ system during these four intervals.

The purpose of the preparation interval is to prepare the system so that there exist coherences between the nuclear spin levels of a single electron spin m_S state. This is achieved by means of two $\pi/2$ microwave pulses spaced by an interval τ . The first microwave pulse transfers the spin population to electron spin coherence (figure 3.6a). At the same time, due to branching of the nuclear spin states, the microwave pulses cause the occurrence of nuclear coherences, represented in the density matrix by the off-diagonal elements in the 2×2 submatrices (lightly shaded).

The electron and nuclear spin coherences are allowed to evolve during the time τ , after which a second $\pi/2$ pulse transfers the electron spin coherence back into a polarized state. For times $\tau > 0$, this second pulse causes the appearance of coherence terms in the diagonal submatrices, as shown in figure 3.6b. For $\tau = 0$ the two pulses merge into a π -pulse, and no nuclear coherences occur.

During the evolution interval t_1 the nuclear coherences in the submatrices of the density matrix for each m_S state undergo a phase shift proportional to t_1 which is retained during the mixing interval consisting of a single π -pulse. This mixing pulse transfers population from the $m_S = +1/2$ state to the $m_S = -1/2$ state and vice versa (figure 3.6c). In general, spin packets in one of the coherence states of the $m_S = +1/2$ electron spin manifold will be transferred to any of the nuclear states of the *other* electron spin manifold. These spin packets will continue to

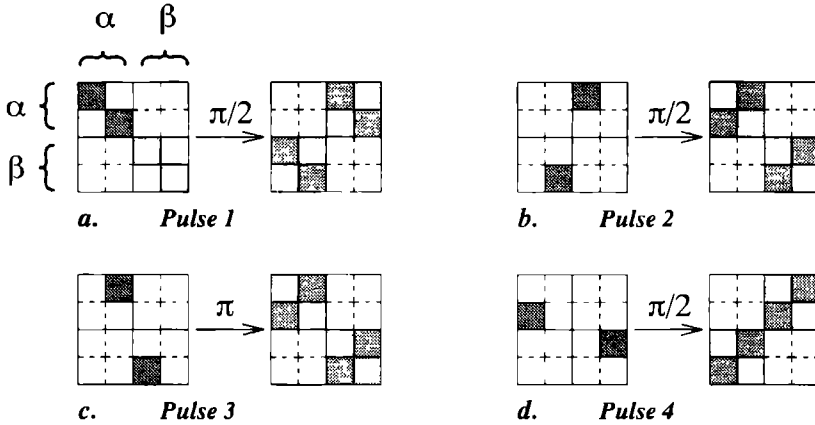


Figure 3.6: Effect of microwave pulses on the density matrix describing the changes occurring during a HYSORE experiment performed on a $S = 1/2$, $I = 1/2$ system. The four figures illustrate what happens to a only few density matrix elements as representative for the other elements.

evolve during the detection interval t_2 . Compared to the three-pulse stimulated echo experiment, a spin packet in an $m_S = +1/2$ state will thus have associated with it an additional phase factor proportional to some nuclear frequency of the $m_S = -1/2$ state.

The evolution of the nuclear coherences during the detection interval t_2 stops when a $\pi/2$ probing pulse is applied to the spin system. This probing pulse serves to transform the electron spin polarization to a detectable magnetization (figure 3.6d), in the form of an electron spin-echo after a time τ . As in the stimulated three-pulse echo sequence, the phase factor accumulated by the spin packets during the intervals t_1 and t_2 will affect the total magnetization at the time of the echo and is observable as a modulation of the echo intensity when changing either t_1 or t_2 ,

$$S(\tau, t_1, t_2) = R_2(2\tau) \cdot R_1(t_1 + t_2) \cdot \sum_{ik, mn} \left[\chi_{ik, mn}^a e^{-i\omega_{ik}^\alpha t_2} e^{-i\omega_{mn}^\beta t_1} + \chi_{ik, mn}^b e^{-i\omega_{ik}^\alpha t_1} e^{-i\omega_{mn}^\beta t_2} \right], \quad (3.102)$$

where R_1 and R_2 represent relaxation due to longitudinal (T_1) and transverse (T_2^*) relaxation processes. A complete expression will be presented in section 3.7.

It is obvious that we expect to see in a two-dimensional frequency-domain HYSORE spectrum cross peaks at the crossings of nuclear frequencies from the $m_S = +1/2$ manifold and nuclear frequencies of the $m_S = -1/2$ manifold, i.e., the spectrum shows correlations between frequencies from the different m_S manifold. Note that during both t_1 and t_2 only longitudinal (T_1) relaxation processes are active because there is no electron spin coherence. This enables a high resolution in both dimensions as has been noted earlier.

Applications and variations of the HYSORE experiment

Two variations of the four-pulse HYSORE experiment have been proposed:

- The four-pulse experiment can be seen as a one-dimensional experiment, where $t = t_1 = t_2$. When varying t we expect to see sum and difference frequencies of the nuclear frequencies in the same manner as in the two-pulse primary echo experiment [8, 16], but now the signal will be subject only to longitudinal relaxation processes leading to a much higher frequency resolution.
- It is also possible to extend the HYSCORE experiment to three dimensions by varying τ as well as t_1 and t_2 . This experiment was proposed by Hofer [17]. In this case, the modulation of the echo intensity by τ (see section 3.7) is used to select particular features in a powder HYSCORE spectrum.

The HYSCORE technique has been successfully employed in the investigation of both single crystals (this thesis, chapter 5 and [7, 9]) and of powders (this thesis, chapters 4, 6 and 7). In the remainder of this chapter we will present an expression for the modulation intensity in the HYSCORE experiment. In section 3.8 we will present an efficient method for simulating HYSCORE spectra using the formula derived in section 3.7

3.7 An expression for the echo modulation intensity in the HYSCORE experiment

In order to derive an expression for the echo modulation intensity in the HYSCORE experiment, we will follow the method used by Mims [2]. In this derivation, we describe the state of the spin system using the density operator ρ . In the absence of microwave radiation, the evolution of the density matrix ρ during a time t can be described by

$$\rho' = R_t \rho \cdot R_t^{-1}, \text{ where} \tag{3.103}$$

$$R_t = \begin{pmatrix} P_t & 0 \\ 0 & Q_t \end{pmatrix}. \tag{3.104}$$

P_t and Q_t are diagonal sub-matrices with elements

$$(P_t)_{ii} = e^{-i\omega_i^{\alpha}t} e^{-\lambda_{\pm}t}, \quad (Q_t)_{mm} = e^{-i\omega_m^{\beta}t} \cdot e^{-\lambda_{\pm}t} \tag{3.105}$$

The frequencies ω_i^{α} and ω_j^{β} are the eigenfrequencies of the unperturbed Hamiltonian, and the inhomogeneous linewidth of the resonance line is represented by λ_{\pm} , which can be different for each spin packet. The evolution of the density matrix as a result of the $\pi/2$ and π microwave pulses can be described by rotation matrices R_{90} and R_{180} , respectively, which are defined by Mims as

$$R_{90} = \frac{1}{2}\sqrt{2} \begin{pmatrix} I_n & -M \\ M^{\dagger} & I_n \end{pmatrix}, \quad R_{180} = \begin{pmatrix} 0 & -M \\ M^{\dagger} & 0 \end{pmatrix}, \tag{3.106}$$

under the condition that the microwave pulses induce transitions between two different m_S states only (see note on page 311 of [2]). M is the matrix that describes the branching that occurs as a result of the microwave pulses (see eq. 3.84). The rotation operator R that describes the

evolution of the density matrix as the result of a three-pulse sequence up to the formation of the echo is given by

$$R = R_\tau R_{90} R_t R_{90} R_\tau R_{90} \quad (3.107)$$

so that the density matrix at the time of the echo can be calculated as

$$\rho_e = R_\tau R_{90} R_t R_{90} R_\tau R_{90} \rho_0 R_{90}^{-1} R_\tau^{-1} R_{90}^{-1} R_t^{-1} R_{90}^{-1} R_\tau^{-1}. \quad (3.108)$$

Similar evolution operators can be defined for any pulse sequence. The echo intensity can be easily determined from the density matrix by taking the expectation value of the magnetization. For simplicity we shall first consider only the M^+ component of the magnetization, defined by

$$E = \text{Tr}(\rho_e M^+), \text{ where } M^+ = g\beta \begin{pmatrix} 0 & M \\ 0 & 0 \end{pmatrix} \quad (3.109)$$

since

$$M_{m, i_m; m', j_{m'}}^+ = g\beta \langle m, i_m | S^+ | m', j_{m'} \rangle = g\beta \langle m | S^+ | m' \rangle \langle i_m | j_{m'} \rangle. \quad (3.110)$$

The modulation intensity for a three-pulse experiment

It is instructive to follow Mims's derivation of the expression for the modulation intensity in the three-pulse echo, because the four-pulse echo is so closely related. From the Boltzmann equilibrium state

$$\rho_0 = \begin{pmatrix} I_n & 0 \\ 0 & -I_n \end{pmatrix},$$



... to derive an expression for the echo modulation intensity

we find that the density matrix after the first two pulses is

$$\begin{aligned}
 \rho_{II} &= R_{y_0} R_\tau R_{y_0} \rho_0 R_{y_0}^{-1} R_\tau^{-1} R_{y_0}^{-1} \\
 &= -\frac{1}{2} \begin{pmatrix} P_\tau M Q_\tau^\dagger M^\dagger + M Q_\tau M^\dagger P_\tau^\dagger & -P_\tau M Q_\tau^\dagger + M Q_\tau M^\dagger P_\tau^\dagger M \\ M^\dagger P_\tau M Q_\tau^\dagger M^\dagger - Q_\tau M^\dagger P_\tau^\dagger & -M^\dagger P_\tau M Q_\tau^\dagger - Q_\tau M^\dagger P_\tau^\dagger M \end{pmatrix} \quad (3.111) \\
 &= -\frac{1}{2} \begin{pmatrix} a & b \\ c & d \end{pmatrix}
 \end{aligned}$$

The off diagonal submatrices b and c of this matrix do not need to be included in the remainder of the derivation. These elements will continue to precess during the interval t that follows the second pulse due to the inhomogeneous broadening and cannot be refocused by the third pulse. To illustrate this, we add the evolution operator of the interval t ,

$$\rho = R_t \rho_{II} R_t^{-1} = -\frac{1}{2} \begin{pmatrix} P_t a P_t^\dagger & P_t b Q_t^\dagger \\ Q_t c P_t^\dagger & Q_t d Q_t^\dagger \end{pmatrix} \quad (3.112)$$

and note that the off diagonal terms must contain factors $e^{-i(\lambda_+ - \lambda_-)t}$. This phase factor cannot be compensated for during the third interval, τ , and thus these components cannot contribute to the stimulated echo. From the reduced density matrix we can derive the density matrix at the time of the echo as

$$\begin{aligned}
 \rho_{\text{echo}} &= -\frac{1}{2} R_\tau R_{y_0} \begin{pmatrix} e & 0 \\ 0 & f \end{pmatrix} R_{y_0}^{-1} R_\tau^{-1} \\
 &= -\frac{1}{4} \begin{pmatrix} P_\tau e P_\tau^\dagger + P_\tau M f M^\dagger P_\tau^\dagger & -P_\tau e M Q_\tau^\dagger + P_\tau M f Q_\tau^\dagger \\ -Q_\tau M^\dagger e P_\tau^\dagger + Q_\tau f M^\dagger P_\tau^\dagger & Q_\tau M^\dagger e M Q_\tau^\dagger + Q_\tau f Q_\tau^\dagger \end{pmatrix} \quad (3.113)
 \end{aligned}$$

where

$$\begin{aligned}
 e &= P_t P_\tau M Q_\tau^\dagger M^\dagger P_t^\dagger + P_t M Q_\tau M^\dagger P_t^\dagger \\
 f &= -Q_t M^\dagger P_\tau M Q_\tau^\dagger Q_t^\dagger - Q_t Q_\tau M^\dagger P_\tau^\dagger M Q_t^\dagger \quad (3.114)
 \end{aligned}$$

from which we calculate the echo intensity

$$E(\tau - t) = -\frac{1}{4} g^3 \text{Tr} \left(Q_\tau M^\dagger e P_\tau^\dagger M - Q_\tau f M^\dagger P_\tau^\dagger M \right) \quad (3.115)$$

which expands to

$$\begin{aligned}
 E(\tau - t) &= -\frac{1}{4} g^3 \text{Tr} \left(Q_\tau M^\dagger P_t P_\tau M Q_\tau^\dagger M^\dagger P_t^\dagger P_t^\dagger M + \right. \\
 &\quad \left. Q_\tau Q_t M^\dagger P_\tau M Q_\tau^\dagger Q_t^\dagger M^\dagger P_t^\dagger M + \right. \\
 &\quad \left. Q_\tau M^\dagger P_t M Q_\tau M^\dagger P_t^\dagger P_t^\dagger M + \right. \\
 &\quad \left. Q_\tau Q_t Q_\tau M^\dagger P_\tau^\dagger M Q_t^\dagger M^\dagger P_t^\dagger M \right) \quad (3.116)
 \end{aligned}$$

The last two terms in this expression do not contribute to the echo, since the phase shifts $(\lambda_+ - \tau)$ and $(\lambda_- - \tau)$ are not compensated in these terms as the phase shift introduced by a factor P_τ would have to be compensated for by a factor P_t^\dagger and the same holds for Q_τ and Q_t^\dagger . Equation

3.116 can easily be evaluated under these conditions when we realize that the P and Q matrices are diagonal:

$$\begin{aligned}
 E(\tau, t) &= -\frac{1}{4}g\beta \sum_{ij,kl} \left(e^{-i\omega_k^\beta \tau} M_{ki}^\dagger e^{-i\omega_i^\alpha t} e^{-i\omega_i^\alpha \tau} M_{il} e^{+i\omega_l^\beta \tau} M_{lj}^\dagger e^{+i\omega_j^\alpha t} e^{+i\omega_j^\alpha \tau} M_{jk} + \right. \\
 &\quad \left. e^{-i\omega_k^\beta \tau} e^{-i\omega_k^\beta t} M_{ki}^\dagger e^{-i\omega_i^\alpha \tau} M_{il} e^{+i\omega_l^\beta \tau} e^{+i\omega_l^\beta t} M_{lj}^\dagger e^{+i\omega_j^\alpha \tau} M_{jk} \right) \\
 &= -\frac{1}{4}g\beta \sum_{ij,kl} M_{ki}^\dagger M_{il} M_{lj}^\dagger M_{jk} e^{-i(\omega_{ij}^\alpha + \omega_{kl}^\beta)\tau} \left(e^{-i\omega_{ij}^\alpha t} + e^{-i\omega_{kl}^\beta t} \right). \quad (3.117)
 \end{aligned}$$

The real and imaginary components of the complex magnetization in this equation represent the in-phase and 90° out-of-phase components of the magnetization that are measured when quadrature detection is used. In electron spin-echo experiments normally only the in-phase component is measured, which corresponds to the real component of equation 3.117. This component is more commonly presented in a format where no complex exponents, but only cosines, occur [18].

Derivation of the stimulated echo modulation formula using the shorthand notation

We can also derive the expression for the modulation intensity using the shorthand method outlined in section 3.5. The power of this method becomes clear if we make use of the coherence transfer pathway (+0-) leading to the stimulated echo by disregarding the $\{c\}_1$ contribution that is created by the second pulse and also the $\{a\}_0$ contribution formed by the third pulse. Then

$$\begin{aligned}
 \{1\}_0 &\xrightarrow{(\pi/2)_y} \{1\}_1 \\
 &\xrightarrow{\tau} \{A_\tau B_\tau^\dagger \Phi_\tau\}_1 \\
 &\xrightarrow{(\pi/2)_y} -\frac{1}{2} \{A_\tau B_\tau^\dagger \Phi_\tau + B_\tau A_\tau^\dagger \Phi_\tau^*\}_0 \\
 &\xrightarrow{t} -\frac{1}{2} \{A_t A_\tau B_\tau^\dagger A_t^\dagger \Phi_\tau + A_t B_\tau A_\tau^\dagger A_t^\dagger \Phi_\tau^*\}_0 \\
 &\xrightarrow{(\pi/2)_y} -\frac{1}{4} \{A_t A_\tau B_\tau^\dagger A_t^\dagger \Phi_\tau + A_t B_\tau A_\tau^\dagger A_t^\dagger \Phi_\tau^* + \\
 &\quad B_t B_\tau A_\tau^\dagger B_t^\dagger \Phi_\tau^* + B_t A_\tau B_\tau^\dagger B_t^\dagger \Phi_\tau\}_1 \\
 &\xrightarrow{\tau} -\frac{1}{4} \{A_\tau A_t A_\tau B_\tau^\dagger A_t^\dagger B_\tau^\dagger \Phi_{2\tau} + A_\tau A_t B_\tau A_\tau^\dagger A_t^\dagger B_\tau^\dagger + \\
 &\quad A_\tau B_t B_\tau A_\tau^\dagger B_t^\dagger B_\tau^\dagger + A_\tau B_t A_\tau B_\tau^\dagger B_t^\dagger B_\tau^\dagger \Phi_{2\tau}\}_1. \quad (3.118)
 \end{aligned}$$

In this result we can disregard the two terms with phase factor $\Phi_{2\tau}$ since they do not contribute to the echo. The M^+ magnetization of the echo is then given in table 3.5 as

$$M^+ = -\frac{1}{4}g\beta \text{Tr} \left(B_\tau A_t A_\tau B_\tau^\dagger A_t^\dagger A_\tau^\dagger + B_\tau B_t A_\tau B_\tau^\dagger B_t^\dagger A_\tau^\dagger \right) \quad (3.119)$$

which evaluates to

$$\begin{aligned}
 M^+ &= -\frac{1}{4}g\beta \text{Tr} \left(Q_\tau M^\dagger P_t P_\tau M Q_\tau^\dagger M^\dagger P_t^\dagger P_\tau^\dagger M \right. \\
 &\quad \left. + Q_\tau Q_t M^\dagger P_\tau M Q_\tau^\dagger Q_t^\dagger M^\dagger P_\tau^\dagger M \right) \quad (3.120)
 \end{aligned}$$

in the same manner as in the derivation of eq. 3.94. This equation is similar to eq. 3.116 when, in that equation, only the terms that lead to the echo are retained.

Extension of the formula to the four-pulse sequence

The evolution of the density matrix in the four-pulse experiment is identical to that in the three-pulse experiment up to the start of the inversion pulse in the 4-pulse experiment (but note that t is replaced by t_1). The inversion pulse thus operates on the density matrix of eq. 3.112, producing

$$\rho_{\text{inv}} = -\frac{1}{2} R_{180} \begin{pmatrix} e & 0 \\ 0 & f \end{pmatrix} R_{180}^{-1} = -\frac{1}{2} \begin{pmatrix} MfM^\dagger & 0 \\ 0 & M^\dagger eM \end{pmatrix}. \quad (3.121)$$

The matrices e and f are defined in eq. 3.114. The evolution during t_2 adds the evolution matrices P and Q :

$$\rho = -\frac{1}{2} \begin{pmatrix} P_t MfM^\dagger P_t^\dagger & 0 \\ 0 & Q_{t_2} M^\dagger eMQ_{t_2}^\dagger \end{pmatrix} = -\frac{1}{2} \begin{pmatrix} e' & 0 \\ 0 & f' \end{pmatrix} \quad (3.122)$$

which is identical in form to eq. 3.112, but with e' and f' replacing e and f . Analogous to eq. 3.116 the expression for the echo modulation becomes

$$E(\tau, t) = \frac{1}{4} g^3 \text{Tr} (Q_\tau M^\dagger P_t, MQ_{t_1} M^\dagger P_\tau MQ_\tau^\dagger Q_{t_1}^\dagger M^\dagger P_t^\dagger, P_t^\dagger M + Q_\tau Q_{t_2} M^\dagger P_{t_1} P_\tau MQ_\tau^\dagger M^\dagger P_{t_1}^\dagger MQ_{t_2}^\dagger M^\dagger P_\tau^\dagger M) \quad (3.123)$$

where we have removed those terms that do not contribute to the echo in the same manner as we have done in the derivation of eq. 3.117. The evaluation of eq. 3.123 yields

$$E(\tau, t_1, t_2) = \frac{1}{4} g^3 \times \sum_{ijklmn} M_{li}^\dagger M_{im} M_{mj}^\dagger M_{jn} M_{nk}^\dagger M_{kl} \times \left(e^{-i(\omega_{in}^j + \omega_{jk}^i)\tau} e^{-i\omega_{ik}^\alpha t_1} e^{-i\omega_{mn}^j t_1} + e^{-i(\omega_{im}^j + \omega_{ik}^i)\tau} e^{-i\omega_{ij}^\alpha t_1} e^{-i\omega_{in}^j t_2} \right). \quad (3.124)$$

If we are only interested in two-dimensional experiments, it is possible to combine the amplitude factor with the factor describing the τ modulation. The resulting expression becomes more readable if we permute the indices of the second term according to $(l, j, k) \rightarrow (i, k, j)$ and $(l, m, n) \rightarrow (m, l, n)$, which changes the amplitude factor to its complex conjugate. The modulation intensity is then written as

$$E(\tau, t_1, t_2) = \frac{1}{4} g^3 \sum_{ik,mn} \left(A_{ik,mn} \cdot e^{-i\omega_{ik}^\alpha t_2} \cdot e^{-i\omega_{mn}^j t_1} + B_{ik,mn} \cdot e^{-i\omega_{ik}^\alpha t_1} \cdot e^{-i\omega_{mn}^j t_2} \right). \quad (3.125)$$

where $A_{ik,mn}$ and $B_{ik,mn}$ are defined as

$$\begin{aligned} A_{ik,mn} &= \sum_{j,l} \left(M_{kl} M_{li}^\dagger M_{mj}^\dagger M_{jn} M_{im} M_{nk}^\dagger \right) e^{-i(\omega_{jk}^i + \omega_{in}^j)\tau} \text{ and} \\ B_{ik,mn} &= \sum_{j,l} \left(M_{kl} M_{li}^\dagger M_{mj}^\dagger M_{jn} M_{im} M_{nk}^\dagger \right)^* e^{+i(\omega_{jk}^i + \omega_{in}^j)\tau}. \end{aligned} \quad (3.126)$$

The values for $A_{ik,mn}$ and $B_{ik,mn}$ give the intensities in the frequency domain spectrum of the cross peaks at $(\omega_{mn}^j, \omega_{ik}^\alpha)$ and $(\omega_{ik}^\alpha, \omega_{mn}^j)$. Note that the spectrum is *not* symmetric, i.e., $A_{ik,mn}$ is not equal to $B_{ik,mn}$, or to its complex conjugate.

The x -component of the magnetization

In electron spin-echo spectroscopy quadrature detection is not usually employed and only the x -component of the magnetization is detected. It can easily be shown that the substitution of

$$M_x = \frac{1}{2} (M^+ + M^-) = \frac{1}{2} \begin{pmatrix} 0 & M \\ M^\dagger & 0 \end{pmatrix} \quad (3.127)$$

in place of M^+ in eq. 3.109 corresponds to taking only the real part of eq. 3.125, i.e, we must add the complex conjugate, and the expression for the modulation intensity can then be written as

$$E(\tau, t_1, t_2) = \frac{1}{4} g \beta \sum_{ik, mn} \left(\begin{aligned} & \mathcal{A}_{ik, mn} \cdot e^{-i\omega_{ik}^\alpha t_2} \cdot e^{-i\omega_{mn}^\beta t_1} + \\ & \mathcal{B}_{ik, mn} \cdot e^{-i\omega_{ik}^\alpha t_1} \cdot e^{-i\omega_{mn}^\beta t_2} \end{aligned} \right), \quad (3.128)$$

with

$$\begin{aligned} \mathcal{A}_{ik, mn} &= \mathcal{A}_{ik, mn} + \mathcal{A}_{ki, nm}^* \text{ and} \\ \mathcal{B}_{ik, mn} &= \mathcal{B}_{ik, mn} + \mathcal{B}_{ki, nm}^* \end{aligned} \quad (3.129)$$

The amplitude factors \mathcal{A} and \mathcal{B} revert to their complex conjugate under reversal of the indices $i \leftrightarrow k$ and $m \leftrightarrow n$, which is the necessary condition for a real time domain. The amplitude factors \mathcal{A} and \mathcal{B} themselves are not real. Note that the amplitude factors of the two terms in both \mathcal{A} and \mathcal{B} are the same, so that we can write

$$\begin{aligned} \mathcal{A}_{ik, mn} &= \sum_{j, l} \left(M_{kl} M_{li}^\dagger M_{mj}^\dagger M_{jn} M_{im} M_{nk}^\dagger \right) \left(e^{-i(\omega_{jk}^\alpha + \omega_{in}^\beta)\tau} + e^{+i(\omega_{ji}^\alpha + \omega_{lm}^\beta)\tau} \right) \text{ and} \\ \mathcal{B}_{ik, mn} &= \sum_{j, l} \left(M_{kl} M_{li}^\dagger M_{mj}^\dagger M_{jn} M_{im} M_{nk}^\dagger \right)^* \left(e^{-i(\omega_{jk}^\alpha + \omega_{in}^\beta)\tau} + e^{+i(\omega_{ji}^\alpha + \omega_{lm}^\beta)\tau} \right) \end{aligned} \quad (3.130)$$

Derivation of the HYSORE modulation formula using the shorthand notation

We can also derive the expression for the modulation intensity using the shorthand method outlined in section 3.5. The derivation follows the same line as in eq. 3.118. We make use of the coherence transfer pathway (+ 0 0 -) leading to the HYSORE echo, and thus we disregard the $\{c\}_1$ contribution that is created by the second pulse and also the $\{a\}_0$ contribution formed by the fourth pulse,

$$\begin{aligned} \{1\}_0 &\xrightarrow{(\pi/2)_y} \{1\}_1 \\ &\xrightarrow{\tau} \{A_\tau B_\tau^\dagger \Phi_\tau\}_1 \\ &\xrightarrow{(\pi/2)_y} -\frac{1}{2} \{A_\tau B_\tau^\dagger \Phi_\tau + B_\tau A_\tau^\dagger \Phi_\tau^*\}_0 \\ &\xrightarrow{t_1} -\frac{1}{2} \{A_{t_1} A_\tau B_\tau^\dagger A_{t_1}^\dagger \Phi_\tau + A_{t_1} B_\tau A_\tau^\dagger A_{t_1}^\dagger \Phi_\tau^*\}_0 \end{aligned}$$

$$\begin{aligned}
 \xrightarrow{(\pi)_\nu} & +\frac{1}{2} \left\{ B_{t_1} B_{\tau} A_{\tau}^{\dagger} B_{t_1}^{\dagger} \Phi_{\tau}^* + B_{t_1} A_{\tau} B_{\tau}^{\dagger} B_{t_1}^{\dagger} \Phi_{\tau} \right\}_0 \\
 \xrightarrow{t_2} & +\frac{1}{2} \left\{ A_{t_2} B_{t_1} B_{\tau} A_{\tau}^{\dagger} B_{t_1}^{\dagger} A_{t_2}^{\dagger} \Phi_{\tau}^* + A_{t_2} B_{t_1} A_{\tau} B_{\tau}^{\dagger} B_{t_1}^{\dagger} A_{t_2}^{\dagger} \Phi_{\tau} \right\}_0 \\
 \xrightarrow{(\pi/2)_\nu} & +\frac{1}{4} \left\{ A_{t_2} B_{t_1} B_{\tau} A_{\tau}^{\dagger} B_{t_1}^{\dagger} A_{t_2}^{\dagger} \Phi_{\tau}^* + A_{t_2} B_{t_1} A_{\tau} B_{\tau}^{\dagger} B_{t_1}^{\dagger} A_{t_2}^{\dagger} \Phi_{\tau} + \right. \\
 & \quad \left. B_{t_2} A_{t_1} A_{\tau} B_{\tau}^{\dagger} A_{t_1}^{\dagger} B_{t_2}^{\dagger} \Phi_{\tau} + B_{t_2} A_{t_1} B_{\tau} A_{\tau}^{\dagger} A_{t_1}^{\dagger} B_{t_2}^{\dagger} \Phi_{\tau} \right\}_1 \\
 \xrightarrow{\tau} & +\frac{1}{4} \left\{ A_{\tau} A_{t_2} B_{t_1} B_{\tau} A_{\tau}^{\dagger} B_{t_1}^{\dagger} A_{t_2}^{\dagger} B_{\tau}^{\dagger} + A_{\tau} A_{t_2} B_{t_1} A_{\tau} B_{\tau}^{\dagger} B_{t_1}^{\dagger} A_{t_2}^{\dagger} B_{\tau}^{\dagger} \Phi_{2\tau} + \right. \\
 & \quad \left. A_{\tau} B_{t_2} A_{t_1} A_{\tau} B_{\tau}^{\dagger} A_{t_1}^{\dagger} B_{t_2}^{\dagger} B_{\tau}^{\dagger} \Phi_{2\tau} + A_{\tau} B_{t_2} A_{t_1} B_{\tau} A_{\tau}^{\dagger} A_{t_1}^{\dagger} B_{t_2}^{\dagger} B_{\tau}^{\dagger} \right\}_1. \quad (3.131)
 \end{aligned}$$

As in the derivation of the three-pulse modulation formula, we disregard the two terms with phase factor $\Phi_{2\tau}$ since they do not contribute to the echo. The M^+ magnetization of the echo is

$$M^+ = \frac{1}{4} g \beta \text{Tr} \left(B_{\tau} A_{t_2} B_{t_1} A_{\tau} B_{\tau}^{\dagger} B_{t_1}^{\dagger} A_{t_2}^{\dagger} A_{\tau}^{\dagger} + B_{\tau} B_{t_2} A_{t_1} A_{\tau} B_{\tau}^{\dagger} A_{t_1}^{\dagger} B_{t_2}^{\dagger} A_{\tau}^{\dagger} \right) \quad (3.132)$$

which transforms to eq. 3.123,

$$\begin{aligned}
 M^+ = \frac{1}{4} g \beta \text{Tr} \left(Q_{\tau} M^{\dagger} P_{t_2} M Q_{t_1} M^{\dagger} P_{\tau} M Q_{\tau}^{\dagger} Q_{t_2}^{\dagger} M^{\dagger} P_{t_1}^{\dagger} P_{\tau}^{\dagger} M \right. \\
 \left. + Q_{\tau} Q_{t_2} M^{\dagger} P_{t_1} P_{\tau} M Q_{\tau}^{\dagger} M^{\dagger} P_{t_1}^{\dagger} M Q_{t_2}^{\dagger} M^{\dagger} P_{\tau}^{\dagger} M \right). \quad (3.133)
 \end{aligned}$$

The effect of τ on the modulation intensity

We can arrive at an alternative representation of the modulation intensity if we multiply \mathcal{A} and \mathcal{B} by the factor $(e^{-i(\omega_{ik}^{\alpha} + \omega_{mn}^{\beta})\tau/2}) \cdot (e^{+i(\omega_{ik}^{\alpha} + \omega_{mn}^{\beta})\tau/2}) = 1$. We can rewrite equation 3.128 to become

$$\begin{aligned}
 E(\tau, t_1, t_2) &= \frac{1}{4} g \beta \sum_{ik, mn} \left(\mathcal{A}'_{ik, mn} \cdot e^{-i(\omega_{ik}^{\alpha} t_2 + \omega_{mn}^{\beta} t_1 + (\omega_{ik}^{\alpha} + \omega_{mn}^{\beta})\tau/2)} + \right. \\
 & \quad \left. \mathcal{B}'_{ik, mn} \cdot e^{-i(\omega_{ik}^{\alpha} t_1 + \omega_{mn}^{\beta} t_2 + (\omega_{ik}^{\alpha} + \omega_{mn}^{\beta})\tau/2)} \right) \\
 &= \frac{1}{4} g \beta \sum_{ik, mn} \left[\left(\sum_{jl} \text{Re}(\chi) \cos \psi \right) (\cos \varphi^+ + \cos \varphi^-) + \right. \\
 & \quad \left. \left(\sum_{jl} \text{Im}(\chi) \cos \psi \right) (\sin \varphi^+ - \sin \varphi^-) \right], \quad (3.134)
 \end{aligned}$$

where

$$\begin{aligned}
 \chi &= (M_{kl} M_{li}^{\dagger}) (M_{mj}^{\dagger} M_{jn}) (M_{im} M_{nk}^{\dagger}), \\
 \psi &= (\omega_{ji}^{\alpha} + \omega_{jk}^{\alpha} + \omega_{lm}^{\beta} + \omega_{ln}^{\beta}) \tau / 2, \\
 \varphi^+ &= \omega_{ik}^{\alpha} t_2 + \omega_{mn}^{\beta} t_1 + (\omega_{ik}^{\alpha} + \omega_{mn}^{\beta}) \tau / 2, \\
 \varphi^- &= \omega_{ik}^{\alpha} t_1 + \omega_{mn}^{\beta} t_2 + (\omega_{ik}^{\alpha} + \omega_{mn}^{\beta}) \tau / 2.
 \end{aligned}$$

This representation of the echo modulation intensity shows the contributions to the real time-domain spectrum more clearly than eq. 3.128. The asymmetry of the HYSOCORE spectrum is easily recognized.

In two-dimensional correlation spectroscopy we are mostly interested in the cross-terms, i.e. those terms for which $i \neq k$ and $m \neq n$. For the specific case of an $S = 1/2$, $I = 1/2$ system the cross terms are given by Gemperle [9]¹:

$$\begin{aligned}
 S(\tau, t_1, t_2) \propto & C_c \times \left(c^2 \cos(\omega^\alpha t_1 + \omega^\beta t_2 + (\omega^\alpha + \omega^\beta)\tau/2) \right. \\
 & + c^2 \cos(\omega^\alpha t_2 + \omega^\beta t_1 + (\omega^\alpha + \omega^\beta)\tau/2) \\
 & - s^2 \cos(\omega^\alpha t_1 - \omega^\beta t_2 + (\omega^\alpha - \omega^\beta)\tau/2) \\
 & \left. - s^2 \cos(\omega^\alpha t_2 - \omega^\beta t_1 + (\omega^\alpha - \omega^\beta)\tau/2) \right), \text{ where} \quad (3.135) \\
 C_c = & -2 \sin(\omega^\alpha \tau/2) \sin(\omega^\beta \tau/2)
 \end{aligned}$$

There are clearly two different contributions of τ to the modulation intensity, the amplitude factor C_c and the phase factor $(\omega^\alpha \pm \omega^\beta)\tau/2$. The effects of phase modulation and amplitude modulation in two-dimensional FT-NMR spectroscopy have been extensively discussed in [13]; similar considerations are valid for the HYSCORE experiment. To avoid the lineshape distortion due to phase modulation, frequency domain HYSCORE spectra are usually presented in the amplitude mode which eliminates the phase factor, and the effect of the modulation in τ is limited only to the amplitude factor C_c [19, 20]. Although this term is relatively simple, the resulting suppression effects are much more complicated than those that occur in the one-dimensional three-pulse experiment.

For a system with $I \geq 1$, the suppression effects are complicated by the presence of multiple terms in the amplitudes of the cross-peaks and we can no longer easily separate the amplitude and phase modulation terms, as can be inferred from eq. 3.134.

3.8 Simulating HYSCORE spectra

With the expression for the modulation intensity available, it becomes possible to simulate HYSCORE spectra. The most convenient form of the modulation formula for computer simulations is that given in eq. 3.125. Without any further considerations, we would expect that we would need of the order of N^6 multiplications to calculate the HYSCORE spectrum; there are N^4 peaks in the spectrum and each of these peaks is described by N^2 terms. N is the total number of energy levels of the nuclear spins that are coupled to the electron spin.

Inspection of the amplitude terms **A** and **B** shows that it is possible to write them in a form that is more convenient for simulation purposes,

$$A_{ik,mn} = A \cdot B \cdot C, \quad B_{ik,mn} = A' \cdot B' \cdot C', \quad \text{where} \quad (3.136)$$

$$\left. \begin{aligned}
 A &= \left(\chi_{ik,mn} e^{+i\omega_k^\alpha \tau} e^{+i\omega_n^\beta \tau} \right) & A' &= \left(\chi_{ik,mn}^* e^{-i\omega_k^\alpha \tau} e^{-i\omega_n^\beta \tau} \right) \\
 B &= \left(\sum_j \chi_{ki,ll} e^{-i\omega_j^\alpha \tau} \right) & B' &= \left(\sum_j \chi_{ki,ll}^* e^{+i\omega_j^\alpha \tau} \right) \\
 C &= \left(\sum_l \chi_{jj,nm} e^{-i\omega_l^\beta \tau} \right) & C' &= \left(\sum_l \chi_{jj,nm}^* e^{+i\omega_l^\beta \tau} \right)
 \end{aligned} \right\} \quad (3.137)$$

and

$$\chi_{ik,mn} = \left(M_{im} M_{nk}^\dagger \right). \quad (3.138)$$

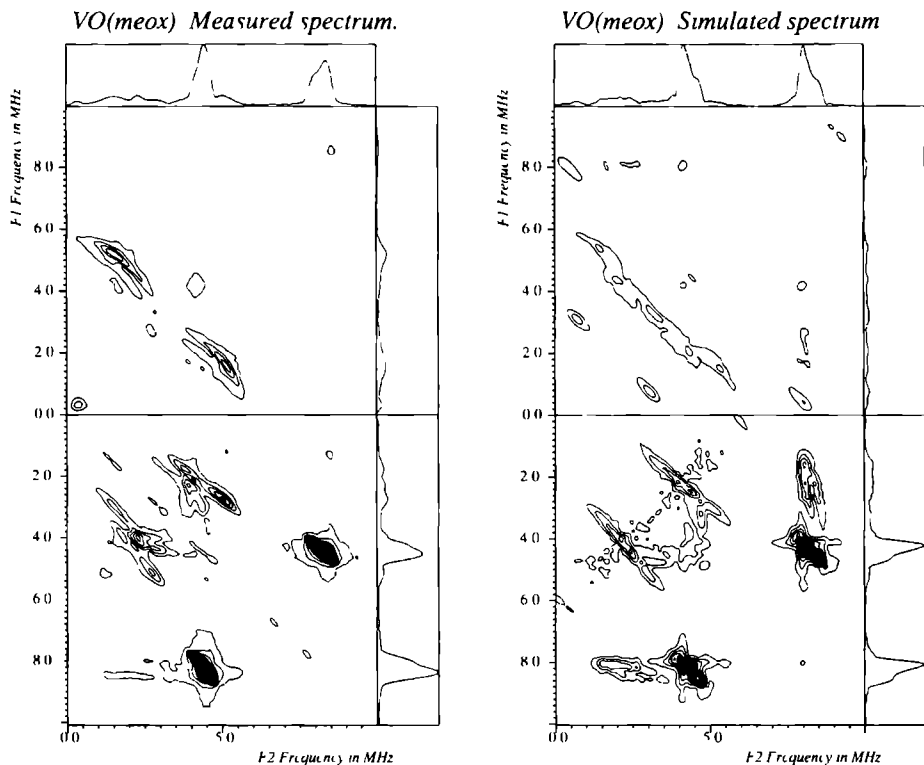


Figure 3.7 Measured (left) and simulated (right) HYSORE spectra of oxobis(2-methylquinolin-8-olato) vanadium(IV) with the field set at the central (powder) peak in the ESE spectrum. The left spectrum was recorded using microwave pulse lengths of 60 ns for the $\pi/2$ pulses and 30 ns for the π pulse, τ was set at 200 ns, but the effective τ was longer as a result of the finite pulse length. The simulation was performed with $\tau = 200$ ns. The Hamiltonian parameters used in the simulation are those listed in table 7.1 (page 135).

The HYSORE frequency spectrum can then be calculated in four steps:

1. Precalculate the modulation factors $e^{-i\omega_j^0 \tau}$ and $e^{-i\omega_l^0 \tau}$ for each j and l , and calculate $\chi_{ik,mn}$ for every (ik, mn) .
2. Calculate the factors B and B' for every (i, k) , and C and C' for every (m, n) .
3. Calculate the factors A and A' for every (ik, mn) .
4. For each peak, c.q. for each (ik, mn) , calculate the modulation intensity from A , B and C or from A' , B' and C' .

¹In the original work, some signs were reversed, these have been corrected here

Steps 1 and 3 take $\mathcal{O}(N^4)$ multiplications and step 2 takes $\mathcal{O}(N^3)$ multiplications. Step 4, in which the actual spectrum is generated, consists of $2 \times N^4$ steps of three multiplications each. The simulation process has now been reduced to an $\mathcal{O}(N^4)$ process, at the cost of having to store $\mathcal{O}(N^4)$ intermediate factors.

When simulating a powder HYSORE spectrum, the calculated modulation intensities for each orientation are accumulated in a 256×256 grid which represents a two-dimensional frequency stick spectrum. To account for the line width this stick spectrum is subsequently transformed to the time-domain using a two dimensional Fourier transform and multiplied by a decay function. Inspection of the time-domain spectrum thus generated shows that there are contributions to the spectrum for $t_1 < 0$ and $t_2 < 0$. Since the HYSORE technique is limited to the positive time domain the data for $t_1, t_2 < 0$ have to be discarded. The reduced time-domain spectrum can then be transformed back to the frequency domain.

Figure 3.7 shows measured and simulated spectra of oxobis(2-methylquinolin-8-olato) vanadium(IV). In the simulation, the nitrogen hyperfine and quadrupole tensors from [21] (chapter 7 in this thesis) were used. The simulation was performed with an adapted version of the MAGRES simulation program [22] in which the procedure described here has been implemented. The main features of the measured spectrum are very well reproduced in the simulation. The line shape and intensity do not match perfectly which is attributed to the fact that a different τ value was used for the simulation than was used in the experiment. Also, the tensors used in the simulation are probably only approximately correct. These preliminary results show that simulations of HYSORE spectra promise to be a valuable spectroscopic tool for refining tensor values determined from powder-ESEEM experiments.

References

- [1] C. P. Slichter *Principles of Magnetic Resonance*. Springer Verlag, Berlin, third edition, 1990.
- [2] W. Mims. Electron Spin Echoes. In S. Geschwind, editor, *Electron Paramagnetic Resonance*, p. 263. Plenum Press, New York, 1972.
- [3] E. J. Reijerse. *Electron Spin Echo spectroscopy on transition metal complexes*. PhD thesis, University of Nijmegen, 1987.
- [4] K. Blum. *Density Matrix Theory and Applications*. Plenum Press, New York, 1981.
- [5] C. Cohen-Tannoudji, B. Diu, and F. Laloe. *Quantum Mechanics*, volume 1. Wiley Interscience, New York, 1977. Translated from the French.
- [6] R. P. Feynman, F. L. Vernon, and R. W. Hellwarth. Geometrical Representation of the Schrodinger Equation for Solving Maser Problems. *Journal of Applied Physics* **28** (1957) 49.

- [7] P Hofer, A Grupp H Nebentur, and M Mehring Hyperfine sublevel correlation (HYSCORE) spectroscopy A 2D FSR Investigation of the squaric acid radical *Journal of Chemical Physics* **132** (1986) 279
- [8] C Gemperle, G Aebli, A Schweiger, and R Ernst Phase Cycling in pulse EPR *Journal of Magnetic Resonance* **88** (1990) 241
- [9] C Gemperle *Neue Elektronenspin Echo-Experimente* PhD thesis, ETH Zurich, 1992
- [10] R P J Merks and R de Beer Two dimensional Fourier transform of electron spin echo envelope modulation An alternative for ENDOR *Journal of Physical Chemistry* **83** (1979) 3319
- [11] J H Freed The Bruker lecture Modern techniques in electron paramagnetic resonance spectroscopy *Journal of the Chemical Society Faraday Transactions* **86** (1990) 3173
- [12] A Schweiger Excitation and detection schemes in pulsed EPR *Pure and Applied Chemistry* **64** (1992) 809
- [13] A P M Kentgens *Two Dimensional Solid State NMR* PhD thesis, University of Nijmegen, 1987
- [14] J Jeener, 1971 Ampere International Summer School, Basko Polje - Yugoslavia
- [15] R K Harris *Nuclear Magnetic Resonance Spectroscopy A Physicochemical View* Longman Scientific & Technical, Harlow, England, 1986
- [16] A M Tyryshkin, S A Dikanov, and D Goldfarb Sum combination harmonics in four-pulse ESEEM spectra Application for the study of the ligand geometry in aqua oxovanadium complexes in powder and glass matrices Accepted for publication in the *Journal of Magnetic Resonance*
- [17] P Hofer, 1993 Workshop on High frequency EPR and electron spin echo spectroscopy Amsterdam - The Netherlands
- [18] W B Mims Amplitudes of Superhyperfine Frequencies Displayed in the Electron Spin Echo Envelope *Physical Review* **6** (1972) 3543
- [19] J J Shane, P Hofer, E J Reijerse and E de Boer Hyperfine Sublevel Correlation Spectroscopy (HYSCORE) of Disordered Solids *Journal of Magnetic Resonance* **99** (1992) 596
- [20] P Hofer Experimental Aspects of 2D ESEEM Techniques In N Yordanov, editor, *Electron Magnetic Resonance of Disordered systems II*, p 1 World Scientific, Singapore, 1991
- [21] E J Reijerse, J J Shane, E de Boer, P Hofer, and D Collison One and two dimensional ESEEM of nitrogen coordinated Oxo Vanadium(IV) complexes In N Yordanov, editor, *Electron Magnetic Resonance of Disordered systems II*, p 253 World Scientific, Singapore, 1991

- [22] C. P. Keijzers, E. J. Reijerse, P. Stam, M. F. Dumont, and M. C. M. Gribnau. MAGRES: A General Program for Electron Spin Resonance, ENDOR and ESEEM. *Journal of the Chemical Society, Faraday Transactions I* **83** (1987) 3493.

Chapter 4

Hyperfine Sublevel Correlation Spectroscopy (HYSCORE) of Disordered Solids¹

J.J. Shane, P. Höfer², E.J. Reijerse, and E. de Boer,

In the study of small hyperfine interactions unresolved in the EPR spectrum, in diluted paramagnetic systems, electron spin-echo envelope modulation has proven to be a very useful technique [1]. For example, in a three-pulse (stimulated-echo) experiment [2, 3], the nuclear spin frequencies of the nuclei that are coupled to the unpaired electron will appear as a modulation on the electron spin echo (ESE) intensity, which is recorded as a function of the time T between the second and third microwave pulses. The first two microwave pulses, which are separated by time τ , will create nuclear spin coherences in the two electron spin m_S manifolds, while the last microwave pulse will transform these coherences into a detectable electron spin-echo signal. The stimulated-echo ESEEM experiment has also been demonstrated as a two-dimensional technique, i.e., recording the electron spin-echo amplitude as a function of both times τ and T to show the correlation of the nuclear spin coherences of the two electron spin m_S manifolds to each other [4]. A serious drawback of this experiment is the limited time range available in the τ direction due to the usually very short T_2 relaxation time of the electron spin system.

In the last decade many new ESEEM experiments have been introduced [5]. In particular, the two-dimensional four-pulse stimulated-echo experiment introduced by P. Höfer *et al.* as HYSCORE (hyperfine sublevel correlation spectroscopy) [6] provides a useful alternative to the classical two-dimensional 3-pulse technique. The HYSCORE experiment is derived from the three-pulse experiment by the insertion during the second time interval (see figure 4.1) of a π pulse which exchanges the populations of the m_S manifolds. In terms of two-dimensional correlation spectroscopy this pulse serves as a mixing pulse which creates correlations between nuclear spin transitions associated with the two electron spin m_S manifolds. The mixing pulse terminates the evolution interval t_1 and is followed by the detection interval t_2 . As in the three-pulse experiment, the nuclear coherences evolving during this time interval are sampled by the last microwave pulse creating an electron spin echo. Compared to the classical two-dimensional three-pulse experiment a spectacular resolution enhancement can be obtained with the HYSCORE technique, which results mainly from the fact that during both t_1 and t_2 the electron spin system is subject only to longitudinal relaxation processes. Two other major

¹This article has been published in the November 1992 issue of the Journal of Magnetic Resonance

²Bruker Analytische Messtechnik, Am Silberstreifen, 7512 Rheinstetten 4, Germany

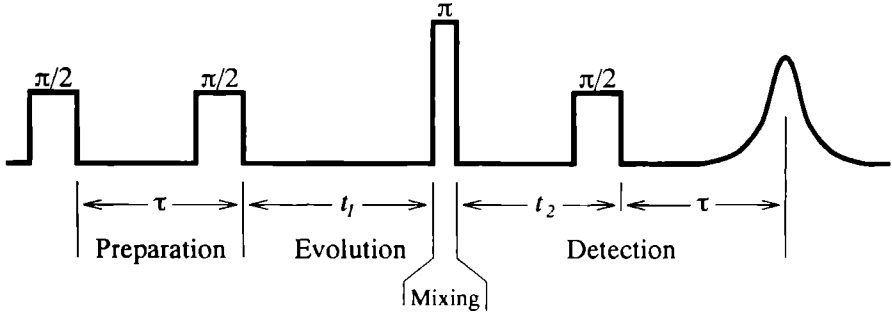


Figure 4.1: Basic pulse sequence of the four-pulse experiment

advantages of HYSORE we want to address in this paper are the separation of lines due to a discrimination between positive and negative phase modulations [7] and the appearance of an echo-modulation echo [8] which allows the detection of anisotropically broadened ESEEM lines free from dead-time distortions.

The general expression for the four-pulse echo signal is

$$E(\tau, t_1, t_2) = R_2(\tau)R_1(t_1 + t_2)S(\tau, t_1, t_2), \quad (4.1)$$

where R_1 and R_2 are the electron spin-echo decays caused by longitudinal and transverse relaxation processes, respectively. The nuclear modulation signal S is described by

$$S(\tau, t_1, t_2) = \frac{1}{4} \frac{1}{2I + 1} \sum_{ikln} \left\{ \chi_{ikln}^a(\tau) e^{-i\omega_{ik}^\alpha t_2} e^{-i\omega_{ln}^\beta t_1} + \chi_{ikln}^b(\tau) e^{-i\omega_{ik}^\alpha t_1} e^{-i\omega_{ln}^\beta t_2} \right\}, \quad (4.2)$$

where

$$\chi_{ikln}^a = \sum_{jm} \left(M_{il} M_{lj}^\dagger M_{jn} M_{nk}^\dagger M_{km} M_{mi}^\dagger \right) \left(e^{-i(\omega_{ij}^\alpha + \omega_{lm}^\beta)\tau} + e^{i(\omega_{kj}^\alpha + \omega_{nm}^\beta)\tau} \right), \quad (4.3)$$

$$\chi_{ikln}^b = \sum_{jm} \left(M_{il} M_{lj}^\dagger M_{jn} M_{nk}^\dagger M_{km} M_{mi}^\dagger \right)^* \left(e^{-i(\omega_{ij}^\alpha + \omega_{lm}^\beta)\tau} + e^{i(\omega_{kj}^\alpha + \omega_{nm}^\beta)\tau} \right). \quad (4.4)$$

The M_{il} are the EPR transition moments between nuclear spin level i of the α electron spin manifold and nuclear spin level l of the β electron spin manifold.

It is important to note that the complex amplitude factors χ_{ikln}^a and χ_{ikln}^b will be replaced by their complex conjugate only under permutation of both i to k and l to n (which is the necessary condition for obtaining a real time domain). The correlation peaks at frequencies $(\nu_{ik}^\alpha + \nu_{ln}^\beta)$ will therefore differ in amplitude from those at frequencies $(\nu_{ik}^\alpha, -\nu_{ln}^\beta)$. This is in contrast to the classical three-pulse two-dimensional experiment described by:

$$S(\tau, T) = \sum_{ijlm} \chi_{ijlm} e^{-i(\omega_{ij}^\alpha + \omega_{lm}^\beta)\tau} (e^{-i\omega_{ij}^\alpha T} + e^{-i\omega_{lm}^\beta T}) + c.c. \quad (4.5)$$

$$= \sum_{ijlm} \chi_{ijlm} \left(e^{-i\omega_{ij}^\alpha(\tau+T)} e^{-i\omega_{lm}^\beta \tau} + e^{-i\omega_{lm}^\alpha(\tau+T)} e^{-i\omega_{ij}^\beta \tau} \right) + c.c., \quad (4.6)$$

where the amplitude factor is

$$\chi_{ijlm} = M_{il}M_{ij}^\dagger M_{jm}M_{mi}^\dagger. \quad (4.7)$$

For this case, the complex amplitude factor will change to its complex conjugate under permutation of either i to j or l to m but remains invariant under both permutations simultaneously. After complex FT with respect to $(\tau + T)$ and τ the $(++)$ and $(+-)$ quadrants will therefore contain the same information (as can be inferred from eq. 4.6).

It should be noted that the complex Fourier transform with respect to τ and T of the three-pulse data, i.e., according to eq. 4.6, will yield a different 2D spectrum. The spectral information will now be spread over two quadrants (for $\omega_{ij} < \omega_{lm}$) and each pair of correlated lines will be represented by six peaks in the 2D frequency domain: $(\omega_{ij}^\alpha, \omega_{ij}^\alpha)$, $(\omega_{ij}^\alpha \pm \omega_{lm}^\beta, \omega_{ij}^\alpha)$, $(\omega_{lm}^\beta, \omega_{lm}^\beta)$, and $(\omega_{lm}^\beta \pm \omega_{ij}^\alpha, \omega_{lm}^\beta)$. The appearance in the ω_τ domain of combination frequencies $(\omega_{ij}^\alpha \pm \omega_{lm}^\beta)$ can be described as the result of a combined phase modulation and amplitude modulation [7] of the signal in the T domain by the correlated modulation frequencies in the τ domain. This fact can easily be inferred from the three-pulse modulation expressions in the cosine form [2, 3],

$$S(\tau, T) \propto \sum_{i \geq j, l \geq m} \text{Re}(\chi_{ijlm}) \left\{ \cos(\omega_{lm}^\beta \tau) \cos(\omega_{ij}^\alpha \tau + \omega_{ij}^\alpha T) \right. \\ \left. + \cos(\omega_{ij}^\alpha \tau) \cos(\omega_{lm}^\beta \tau + \omega_{lm}^\beta T) \right\}, \quad (4.8)$$

where $\text{Re}(\chi_{ijlm})$ represents the real part of χ_{ijlm} . In the conventional presentation of the 2D FT spectrum the amplitude mode is calculated after the first FT, i.e., with respect to T . This will discard the phase modulation contribution $\cos(\omega_{ij}^\alpha T)$ in the term $\cos(\omega_{lm}^\beta \tau) \cos(\omega_{ij}^\alpha \tau + \omega_{ij}^\alpha T)$, leaving only the amplitude modulation factor $\cos \omega_{lm}^\beta \tau$. Therefore, the combination frequencies $(\omega_{lm}^\beta \pm \omega_{ij}^\alpha)$ in the ω_τ domain will disappear.

The alternative presentation of the 2D data (a complex FT with respect to both τ and T) is especially useful for disordered systems, because usually one of the combination features is less susceptible to anisotropic broadening and thus provides important information about the magnetic interaction parameters [9]. As will be shown later in this paper, the HYSORE experiment performed on disordered systems will also benefit from this mechanism and may yield even more detailed information about the interaction parameters.

It is instructive to investigate the modulation formula in more detail using the expressions for the case $S = 1/2$, $I = 1/2$, which were recently derived by Gemperle *et al.*[10]. The signal contribution due exclusively to the correlation features is given by³:

$$S(t_1, t_2) = \frac{k}{4} C \left[\begin{aligned} & c^2 \cos(\omega_\alpha t_1 + \omega_\beta t_2 + \delta_+) - s^2 \cos(\omega_\alpha t_1 - \omega_\beta t_2 + \delta_-) \\ & + c^2 \cos(\omega_\alpha t_2 + \omega_\beta t_1 + \delta_+) - s^2 \cos(\omega_\alpha t_2 - \omega_\beta t_1 + \delta_-) \end{aligned} \right]. \quad (4.9)$$

The dependence on the initial waiting time τ is contained in the amplitude factor $C = -2 \sin(\omega_\alpha \tau / 2) \sin(\omega_\beta \tau / 2)$ and in the phase factors $\delta_+ = (\omega_\alpha + \omega_\beta) \tau / 2$ and $\delta_- = (\omega_\alpha - \omega_\beta) \tau / 2$.

Note that the contributions with positive phase modulation ($\omega_\beta t_2 + \omega_\alpha t_1$ and $\omega_\alpha t_2 + \omega_\beta t_1$) have amplitude c^2 , whereas the contributions with negative phase modulation ($\omega_\beta t_2 - \omega_\alpha t_1$ and

³In the original work, some signs were reversed, these have been corrected here.

$\omega_\alpha t_2 - \omega_\beta t_1$) have amplitude s^2 . These amplitude factors are determined by the angle θ between the two effective magnetic fields at the nucleus for each $m_S = \pm 1/2$:

$$s^2 = \sin^2(\theta/2) = \left| \frac{\omega_I^2 - (\omega_\alpha + \omega_\beta)^2/4}{\omega_\alpha \omega_\beta} \right|, \quad (4.10)$$

$$c^2 = \cos^2(\theta/2) = \left| \frac{\omega_I^2 - (\omega_\alpha - \omega_\beta)^2/4}{\omega_\alpha \omega_\beta} \right|, \quad (4.11)$$

$$k = 4c^2 s^2. \quad (4.12)$$

In the limiting case of small hyperfine interaction with respect to the Zeeman interaction, θ will be small and the c^2 term, i.e., the positive phase modulation, will be dominant, while for large hyperfine interaction θ will be close to π and the negative phase modulation will prevail. A complex FT with respect to t_1 will discriminate between the signs of the phase modulation and therefore the correlation peaks of large and small HFI appear in different quadrants of the 2D spectrum. In the presence of both large and small HFI this gives a resolution enhancement of a factor 2 compared to the three-pulse method, where only the mutual amplitude modulation is taken into account.

It is interesting to note that in these limiting cases of pure phase modulation a 1D slice of a HYSORE spectrum will show no suppression of $\omega_\beta t_2$ by $\omega_\alpha t_1$. Blind spots with respect to t_1 will only occur in case of amplitude modulation as in the three-pulse experiment with respect to τ . The HYSORE experiment may still suffer from blind spots with respect to τ as is expressed in the amplitude factor C of eq. 4.9. These can, however, to a large extent be predicted by studying a limited series of three-pulse ESEEM experiments [7].

We will now demonstrate the important implications this limiting case of pure phase modulation has on the HYSORE spectra of disordered solids. Figure 4.2 shows the 2D time domain (figure 4.2a) and frequency domain (figure 4.2b) of a HYSORE experiment on oxotetra(1-methyl imidazole) vanadium(IV) chloride ($\text{VO}(\text{mim})_4 \text{Cl}^+$) [11, 12, 13].

The spectrum has been measured on a Bruker ESP 380 FT-EPR spectrometer using pulse-lengths of 64 ns for the $\pi/2$ pulses and 32 ns for the inverting π -pulse. The time interval τ was set at 120 ns and times t_1 and t_2 were stepped with 24 ns increments. A four-step phase cycle was used to compensate for the effect of unwanted electron spin echoes [10]. The 2D time domain data have been corrected for the unmodulated relaxation decay in t_1 and t_2 by a third-order polynomial background correction in both dimensions, which also eliminates all signals modulated in t_1 but not in t_2 and vice versa and thus removes all frequency-domain axial peaks. Before Fourier-transformation the corrected data were apodized using a phased sine-bell function and expanded to the next power of two.

The field was positioned on the central line in the EPR spectrum (not shown) where all orientations of the molecule with respect to the magnetic field contribute. The hyperfine and quadrupole interactions with four chemically equivalent nitrogen nuclei directly coordinated to the VO unit are responsible for the modulation signals [13]. Because of the large isotropic part of the hyperfine interaction ($A_1 = -6.9$, $A_2 = -6.0$, $A_3 = -7.3$ MHz) and relatively small quadrupole interaction ($P_1 = -0.7$, $P_2 = -0.1$, $P_3 = 0.8$ MHz) the ESEEM spectra are dominated by strong double quantum ($\Delta m_I = 2$) transitions around 5 MHz and 9 MHz [14]. In

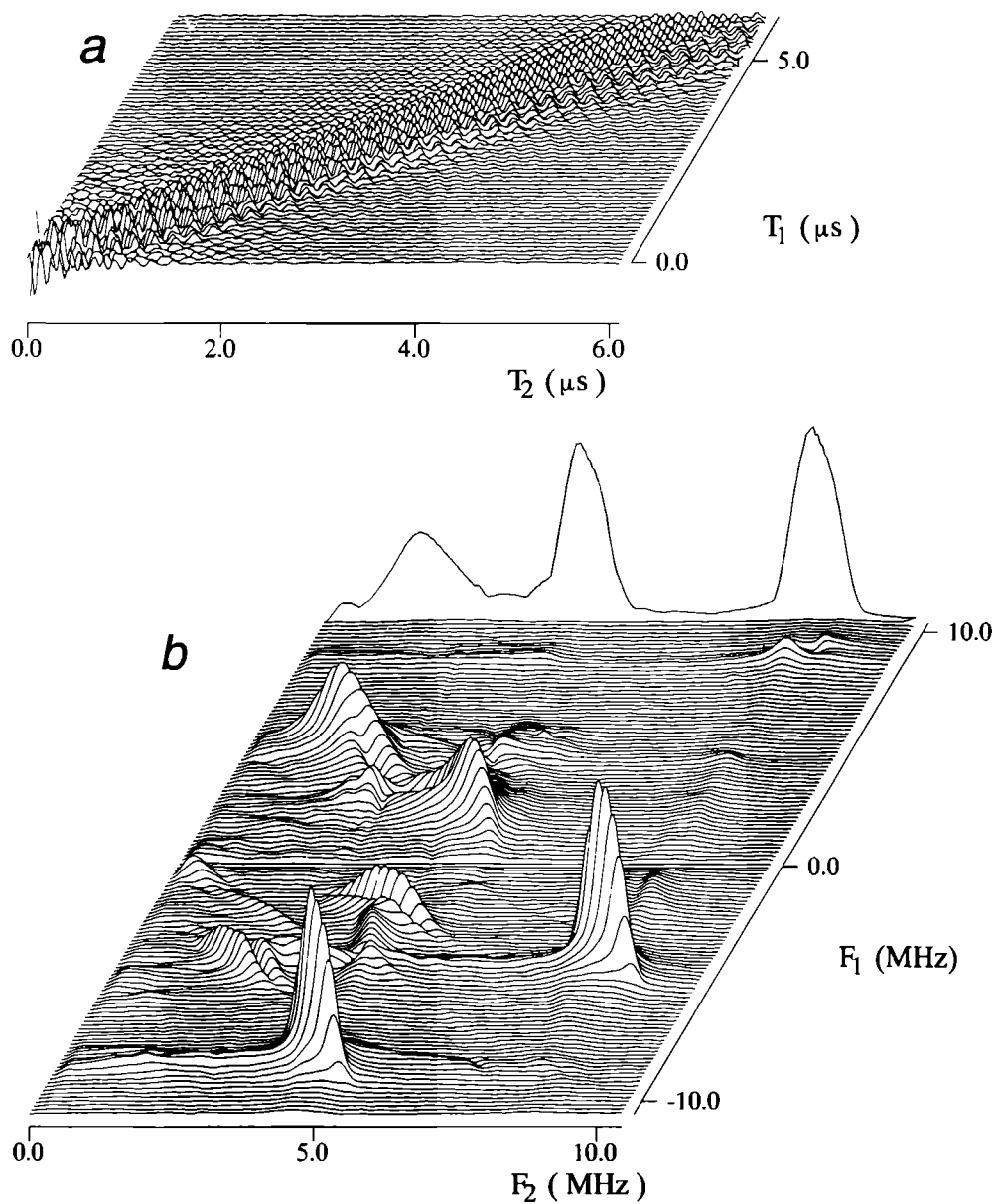


Figure 4.2: 2D HYSORE experiment on $\text{VO}(\text{mim})_4\text{Cl}^+$, measured at the powder position. (a) The time domain, corrected for the unmodulated decay in t_1 and t_2 . (b) The frequency domain, obtained by a complex Fourier transformation in both directions.

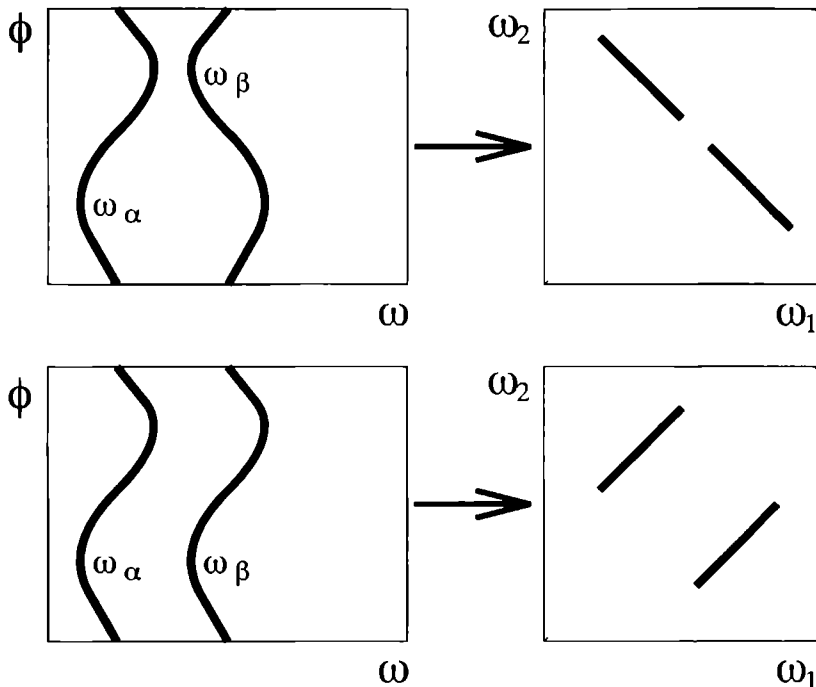


Figure 4.3 Two nuclear spin frequency positions ω_α and ω_β of some spin system plotted as a function of the angle ϕ in an arbitrary plane of the crystal (left). When the two transitions have opposite orientation dependence, a correlation ridge perpendicular to the diagonal is observed, whereas when the two transitions have a similar orientation dependence a correlation ridge along the diagonal appears.

the one-dimensional 3-pulse ESEEM spectrum, these double-quantum peaks are not strongly broadened, because the quadrupole interaction will cause only a very small second order broadening of these transitions so that the powder lineshape will be governed by the relatively small hyperfine anisotropy.

In particular the correlation features between the double-quantum frequencies can be understood quite well using the expressions for $S = 1/2$, $I = 1/2$, although we must keep in mind that in principle these are not applicable to this case. Since we are clearly in the limiting case of dominating isotropic hyperfine interaction the negative phase modulation is dominant and the $(\nu_{13}^\alpha, \nu_{13}^\beta)$ correlation features appear in the $(+ -)$ quadrant. Furthermore, it is striking that the 2-D correlation features are very narrow and parallel to the diagonal. This is because the relatively small anisotropic hyperfine interaction, which is responsible for the lineshape of the double quantum transitions, affects the ν_{13}^α frequency in the same way as the ν_{13}^β frequency. There is a one to one relationship between the different frequency positions of the two double quantum lineshapes at any given orientation of the magnetic field (see figure 4.3).

Interestingly, the Fourier counterpart of this effect is clearly visible in the time domain (figure 4.2a). At $t_1 = t_2$, an echo-modulation echo appears, which is caused by constructive

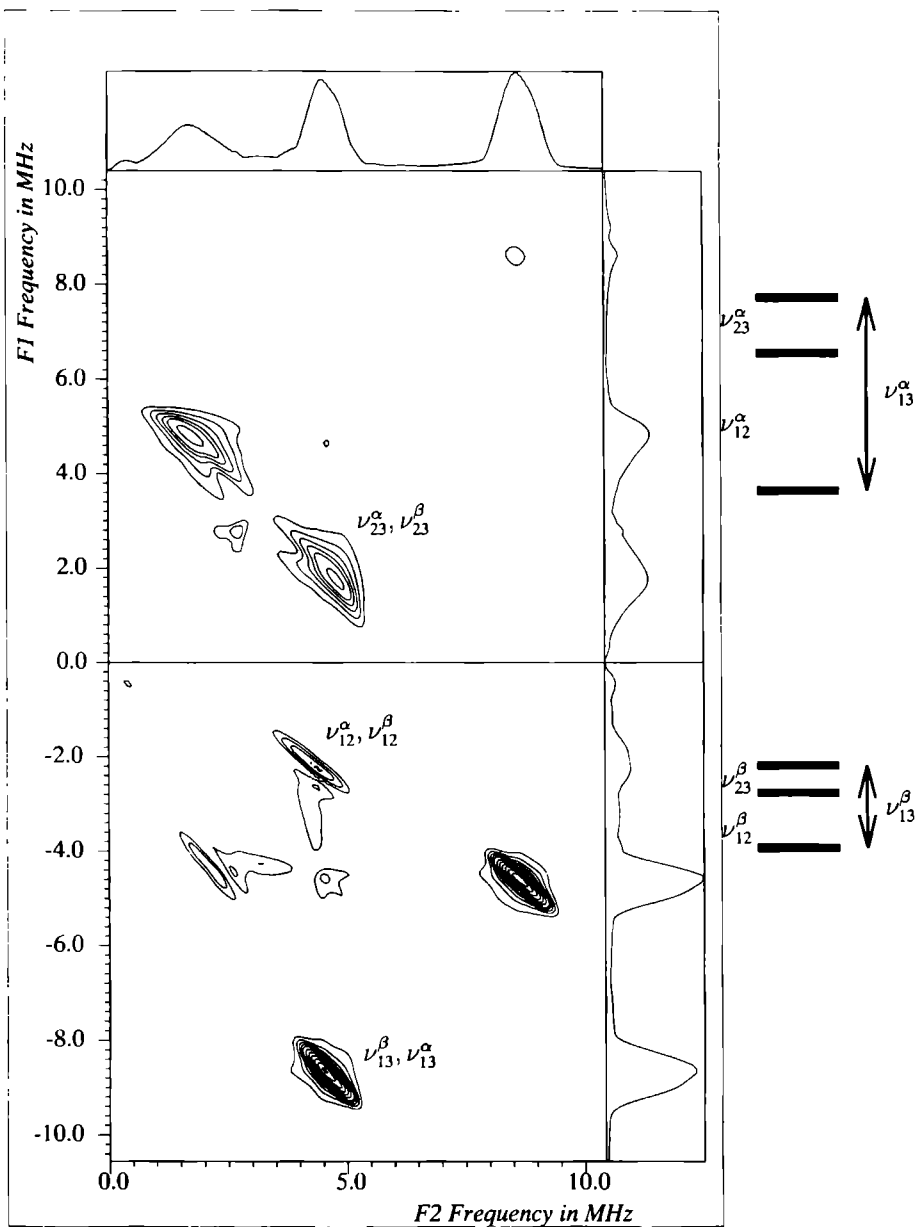


Figure 4.4: Contour plot of the 2D frequency domain shown in figure 4.2b. A preliminary assignment of the correlation features is given in terms of the nuclear spin transitions of the $S = 1/2, I = 1$ system (see inset on right).

interference from the echo modulation patterns of all contributing orientations. A similar effect is also described by Fauth *et al* [8] for 3-pulse ESEEM patterns measured using a long waiting time τ . This 3-pulse echo-modulation echo requires a large separation of the first two pulses, consequently the sensitivity is strongly dependent on the transverse relaxation time. In the HYSORE experiment the echo-modulation echo, created during t_1 and detected in t_2 , is only damped by the longitudinal relaxation time which is usually much longer than the transverse relaxation time. Therefore, this time-domain feature, which essentially contains information about the strong parallel and perpendicular correlation ridges, is much better retained in the HYSORE experiment.

Returning to figure 4 2b, we observe many features around 5 MHz, apart from the very strong correlation between the double quantum peaks. These features originate from the single-quantum transitions ν_{12}^α , ν_{12}^β , ν_{23}^α and ν_{23}^β . The main source of anisotropy for these transitions is the quadrupole interaction (which is much smaller than the isotropic HFI). To first order, frequencies ν_{12}^α and ν_{12}^β , as well as frequencies ν_{23}^α and ν_{23}^β , are affected in the same way, which leads to ridges parallel to the diagonal in the $(+-)$ quadrant, as in the case of the double quantum features. Obviously, the anisotropies of frequencies ν_{12}^α and ν_{23}^β will now counteract each other, which leads to ridges perpendicular to the diagonal in the $(++)$ quadrant. A preliminary assignment of all 2D correlation features is given in the contour plot (figure 4 4).

In conclusion, 2D HYSORE is a very powerful technique for studying disordered solids, that offers many advantages over the classical three-pulse 2D technique. Of particular importance for the spectroscopy of disordered systems is the recovery of broad ESEEM lines by the detection of the echo-modulated echo, which leads to the appearance of narrow ridges in the two-dimensional frequency domain.

In addition to the high spectral resolution in both dimensions we also have the advantage of a further disentanglement of the correlation features over the two quadrants in the 2D frequency domain. Notice, in particular, the spectacular enhancement in spectral information obtained with regard to the single quantum transitions which, in the 1D projection, are all buried under a featureless bump below 5 MHz.

References

- [1] S. A. Dikanov and A. V. Astashkin. ESEEM of Disordered Systems. Theory and Applications. In A. J. Hoff, editor, *Advanced EPR, Applications in Biology and Biochemistry*. Elsevier, Amsterdam, 1989.
- [2] W. B. Mims. Envelope Modulation in Spin-Echo Experiments. *Physical Review* **5** (1972) 2409.
- [3] W. B. Mims. Amplitudes of Superhyperfine Frequencies Displayed in the Electron Spin Echo Envelope. *Physical Review* **6** (1972) 3543.
- [4] R. P. J. Merks and R. de Beer. Two-dimensional Fourier transform of electron spin echo envelope modulation. An alternative for ENDOR. *Journal of Physical Chemistry* **83** (1979) 3319.

- [5] A. Schweiger. Pulse electron spin resonance spectroscopy: principles, procedures and applications. *Angew. Chem. Int. Ed. Engl.* **30** (1991) 265.
- [6] P. Höfer, A. Grupp, H. Nebenfür, and M. Mehring. Hyperfine sublevel correlation (HYSCORE) spectroscopy: A 2D ESR Investigation of the squaric acid radical. *Journal of Chemical Physics* **132** (1986) 279.
- [7] P. Höfer. Experimental Aspects of 2D-ESEEM Techniques. In N. Yordanov, editor, *Electron Magnetic Resonance of Disordered systems II*, p. 1. World Scientific, Singapore, 1991.
- [8] J. M. Fauth, A. Schweiger, and R. R. Ernst. Recovery of Broad Hyperfine Lines in Electron Spin-Echo Envelope Modulation Spectroscopy on Disordered Systems. *Journal of Magnetic Resonance* **81** (1989) 262.
- [9] E. J. Reijerse and S. A. Dikanov. Electron spin echo envelope modulation spectroscopy on orientationally disordered systems: Line shape singularities in $S = 1/2$, $I = 1/2$ spin systems. *Journal of Chemical Physics* **95** (1991) 836.
- [10] C. Gemperle, G. Aebli, A. Schweiger, and R. Ernst. Phase Cycling in pulse EPR. *Journal of Magnetic Resonance* **88** (1990) 241.
- [11] E. de Boer *et al.* ^{14}N coordination to VO^{2+} in reduced vanadium bromoperoxidase, an electron spin echo study. *FEBS Letters* **235** (1988) 93.
- [12] E. J. Reijerse, J. J. Shane, E. de Boer, and D. Collison. ESEEM of nitrogen coordinated Oxo-Vanadium(IV) complexes. In N. D. Yordanov, editor, *Electron Magnetic Resonance of Disordered systems I*, pp. 189–204. World Scientific, Singapore, 1989.
- [13] E. J. Reijerse, J. J. Shane, E. de Boer, P. Höfer, and D. Collison. One and two dimensional ESEEM of nitrogen coordinated Oxo-Vanadium(IV) complexes. In N. Yordanov, editor, *Electron Magnetic Resonance of Disordered systems II*, p. 253. World Scientific, Singapore, 1991.
- [14] A. V. Astashkin and S. A. Dikanov. Coordination of Vanadyl Acetylacetonate with nitrogen-containing donor bases. *Journal of Structural Chemistry* **26** (1985) 363.

Chapter 5

An ESEEM investigation of single crystals and powders of copper-doped *l*-histidine hydrochloride monohydrate¹.

J.J. Shane, P.A.A.W. van der Heijden, E.J. Reijerse and E. de Boer

Department of Molecular spectroscopy, University of Nijmegen, Toernooiveld, 6525 ED Nijmegen, The Netherlands

ABSTRACT

In this paper we present an investigation of the remote nitrogen of imidazole in copper-doped *l*-histidine hydrochloride monohydrate, which is a model system for a wide range of biologically important copper-imidazole complexes. Since these systems are mostly not available in a crystalline form it is interesting to investigate to what extent information that can be obtained from these disordered systems using ESEEM techniques is reliable. From single crystal ESEEM and HYSCORE experiments we have determined the hyperfine and quadrupole coupling tensors of the remote nitrogen in this model system. Additionally, we determined information on these tensors from powdered material, independent of the single crystal results, using orientation selective multifrequency and two-dimensional experiments. The availability of the coupling tensors from the single crystal investigation allowed an assessment of the applicability of the employed powder techniques to this important class of systems. The two-dimensional stimulated echo experiment was found to be a very useful spectroscopic tool for the study of these systems when combined with simulations.

5.1 Introduction

Histidine and imidazole moieties often occur in nature as ligands to copper ions, for instance in the blue copper proteins plastocyanin and stellacyanin and in enzymes as laccase and dopamine- β -hydroxylase [1, 2], and have been the subject of EPR and similar investigations for a number of years. ESEEM techniques are increasingly used to investigate the coordination of imidazole ligands to the metal ion [3, 4]. Often in these investigations, use is made of model systems [5]. Usually, the systems under investigation can only be obtained in an orientationally disordered state, i.e., in a frozen solution or in a polycrystalline host. A number of authors have proposed

¹Submitted for publication in *Applied Magnetic Resonance*

ways to obtain detailed information on the coupling tensors of the nuclei that are visible in the ESEEM spectrum, usually ^1H or $^{14,15}\text{N}$ [6, 7, 8]

It is our aim to investigate to what extent useful and reliable information can be extracted from disordered systems using these techniques. To this end, we have performed extensive ESEEM studies on single crystals and powders of copper-doped *l*-histidine hydrochloride monohydrate (figure 5.1) which, because of the low symmetry of the copper site, is a good model system for copper-containing proteins in which the copper is ligated to histidine groups. The accuracy, applicability and limitations of the techniques described above can only be assessed when we have at our disposal accurate information about the coupling tensors of the various nuclei, which can only be obtained from single crystals.

The copper-doped *l*-histidine hydrochloride monohydrate single crystal and deuterated variants thereof have been the subject of a number of investigations [9, 10], which have characterized this system to a great extent, and for this reason it was selected as a model system to test the applicability of the above techniques on disordered systems. From X-ray diffraction work by Donahue and co-workers [11, 12] the crystal structure of the host is accurately known, and it appears that the space and point groups of the crystal are not changed upon doping [10] although it is likely that a small structural change of the histidine molecule occurs near the dope location. The host crystal belongs to the space group $P2_12_12_1$, which has three mutually perpendicular screw axes, thus there are four equivalent molecules in the unit cell. The unit cell dimensions are $a = 15.36 \text{ \AA}$, $b = 8.92 \text{ \AA}$ and $c = 6.88 \text{ \AA}$.

The doped crystal was first investigated by Hirasawa and Kon [10] using Q-band CW EPR and optical polarized absorption spectroscopy. The EPR spectrum is unusual for a copper imidazole complex in that the largest copper hyperfine interaction coincides with the smallest g -value. It is characterized by a very large inhomogeneous linewidth caused by hyperfine interactions from the surrounding nitrogen nuclei and from the two chlorine nuclei. Despite this linewidth these authors were able to determine approximate values for the electron g and copper hyperfine tensors. From these tensors, and from spatial considerations, they determined the most probable dope site, later confirmed by McDowell *et al* [9]. This dope site is an interstitial site with low local symmetry. The metal ion is coordinated directly to two histidine molecules and to two chlorine nuclei, and also to two oxygen nuclei, which are not visible in the EPR spectrum. The dope site is shown in figure 5.1.

McDowell *et al* [9] used X-band EPR and ENDOR to refine the g and copper hyperfine tensors and also determined the hyperfine and quadrupole coupling tensors of the directly coordinating nitrogen ($^{14}\text{N}_1$ and $^{14}\text{N}_3$) nuclei and of the magnetically equivalent chlorine nuclei in the isostructural copper-doped *l*-histidine deuteriochloride monodeuterate variant. More recently, Colaneri and Peisach [13] determined the hyperfine and quadrupole coupling tensors for the remote ($^{14}\text{N}_2$) nitrogen using ESEEM experiments performed at X-band frequencies.

In this paper we focus again on the determination of the coupling tensors of the remote nitrogen of imidazole. We will demonstrate to what extent it is possible to extract from disordered material the same information on these tensors that can be obtained from single crystals. As for most copper-imidazole complexes a special condition known as exact cancellation [14] is fulfilled for the coupling tensors of the remote nitrogen for magnetic field strength corresponding to resonance frequencies near 7 GHz (in the C band). Powder ESEEM spectra recorded under

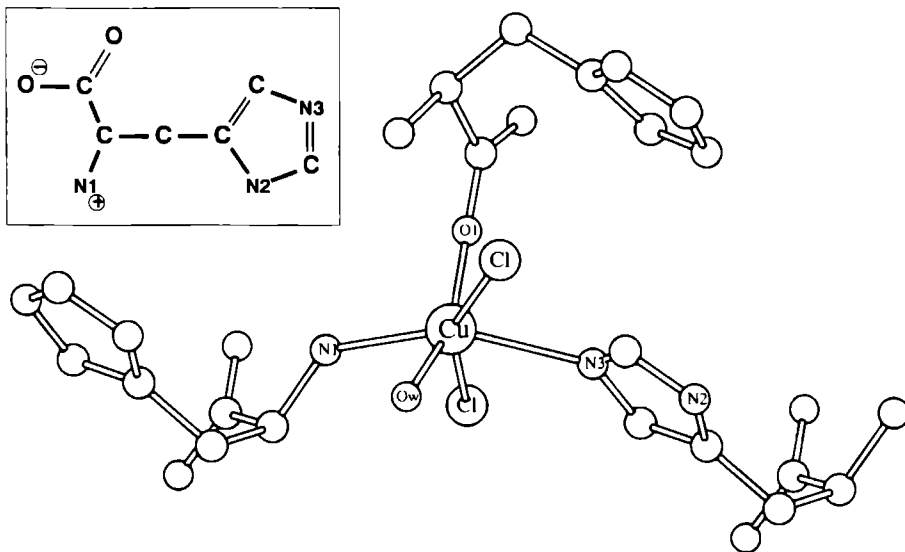


Figure 5.1. Structure of the dope site of copper-doped *l*-histidine. There is a strongly distorted octahedral surrounding of the copper nucleus, which is ligated to two close nitrogen nuclei from different histidine molecules, to two chlorine atoms and to two oxygen atoms, one from a water molecule (O_w) and one from a carboxylate group. The nucleus of interest in this work is the remote ($^{14}N_2$) nitrogen nucleus. Atomic positions were taken from [11, 12]. The position of the copper nucleus is determined from [9]. The inset shows the histidine molecule itself. Hydrogen atoms are not shown in either figure.

this condition are particularly informative. In order to facilitate the comparison of powder and single crystal data the single crystal experiments reported in this paper have been carried out at C-band frequencies.

5.2 Experimental

Sample preparation

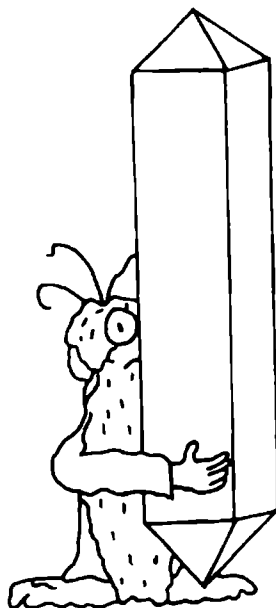
Copper-doped *l*-histidine was prepared by adding 0.5 mol % copper(II) chloride (Merck) to an aqueous solution of 98% pure *l*-histidine hydrochloride monohydrate (Aldrich). Well-defined single crystals with sizes ranging from $1 \times 1 \times 1$ to $10 \times 10 \times 5$ mm³ were obtained from this solution by slow evaporation of the water over a period of a few days. Crystals with a size of approximately $2 \times 2 \times 2$ mm³ were selected for the ESEEM experiments. Some of the remaining material was crushed to be used in powder-ESEEM measurements. The actual copper content of the crystals was determined to be 0.35 mol %, using atomic absorption spectroscopy.

Equipment

The spectra of single crystals were measured using the home-built C-band ESE spectrometer described in chapter 2. Powder spectra were recorded using either this instrument or a Bruker ESP380 FT-EPR spectrometer. In the single crystal experiments the spectrometer operated at 8.251 GHz. Powder spectra were measured using microwave frequencies of 6.563, 7.245 and 7.808 GHz on the home-built spectrometer and 9.806 GHz on the Bruker instrument. In all cases the temperature of the crystal was kept constant at about 15 ± 2 K using Oxford Instruments CF200 or CF935 liquid-helium flow cryostats. The microwave frequency was measured using a Hewlett-Packard type 5246 frequency counter with a type 5255A frequency converter insert and the magnetic field strength was determined using a Bruker ER 035M NMR gaussmeter. A Philips PU9200X atomic absorption spectrometer was used in the determination of the copper content of the samples.

Data acquisition and processing

A three-pulse stimulated echo sequence with two phase cycles was used to measure the ESEEM spectra. The pulse length for the 90° pulses was usually set to around 20 ns. The interval between the first and second pulses (τ) was 200 ns for most one-dimensional spectra. The interval between the second and third pulses (T) was increased in steps of 40 ns from a starting



Well-defined single crystals. . .

value of 80 ns. The echo intensity was recorded as a function of T and sampled at 2048 points in experiments on single crystals and at 512 points for powders. After acquisition, the raw time-domain ESEEM data were corrected for an exponentially decaying baseline, after which they were apodized using a cosine roll-off function. The resulting data were Fourier transformed to the frequency-domain and are presented as amplitude spectra. No attempts were made to reconstruct points missing from the time-domain ESEEM data as a result of spectrometer dead time.

A single crystal HYSORE spectrum consists of a matrix of 512 by 512 points spaced 40 ns in both t_1 and t_2 , leading to a frequency resolution of approximately 50 kHz. The pulse length of the 90° pulses was 60 ns. In order to suppress the contribution of the three-pulse echo to the measured signal the length of the inversion pulse was reduced to 30 ns and the microwave power was increased accordingly [15]. As in the three-pulse experiments, τ was set at 200 ns. The time domain data were corrected for an unmodulated relaxation decay in both t_1 and t_2 using a third-order polynomial background correction, which removes all frequency-domain axial peaks. Before Fourier transformation the data were apodized using a squared sine-bell window, and zeroes were added to the data to bring the total size of the time domain to 1024 by 1024 points.

Crystal mounting and orientation

In order to orient the crystal with respect to the externally applied magnetic field we used a resonator in which the crystal could be rotated around the laboratory y -axis. The magnet itself was mounted on a rotating base with the axis of rotation along the laboratory z -axis, which allowed us to place the crystal in any desired orientation with respect to the magnetic field direction. At all orientations the microwave field was perpendicular to the externally applied magnetic field.

The crystal was oriented by inspection of ESEEM spectra. The crystallographic symmetry axes were located by rotating the crystal until the contributions from all four sites overlapped. Along these symmetry axes only six lines attributed to the remote nitrogen are visible. We estimate the accuracy with which we were able to locate these axes at better than 0.5° for the b and c axes, and better than 1° for the a axis.

5.3 Theory

The Hamiltonian for the spin system under investigation can be written as

$$\mathcal{H} = \beta \mathbf{B}_0 \cdot \mathbf{g} \cdot \mathbf{S} + \sum_i (\mathbf{S} \cdot \mathbf{A}_i \cdot \mathbf{I}_i + \mathbf{I}_i \cdot \mathbf{Q}_i \cdot \mathbf{I}_i - g_i \beta \mathbf{B} \cdot \mathbf{I}_i) \quad (5.1)$$

where the sum is taken over $^{14}\text{N}_1$, $^{14}\text{N}_2$, $^{14}\text{N}_3$ and two equivalent chlorine nuclei. When we are only interested in the ESEEM spectrum of the remote nitrogen we can write this in the strong-field approximation as

$$\mathcal{H}_{\pm} = g_{\text{eff}} \beta \mathbf{B}_0 \cdot \mathbf{S} - g_n \beta_n \mathbf{B}_0 \cdot \mathbf{I} + A \langle \mathbf{S} \rangle_{\pm} \cdot \mathbf{I} + \mathbf{I} \cdot \mathbf{P} \cdot \mathbf{I} \quad (5.2)$$

under the assumption that the hyperfine interaction is isotropic. In this equation, the expectation value of the effective spin operator $\langle \mathbf{S} \rangle_{\pm} = \pm \hat{\mathbf{B}}_0/2$ where $\hat{\mathbf{B}}_0$ is the direction of the externally applied magnetic field. The effective magnetic field at the nucleus is then

$$\mathbf{B}_{eff} = (2\nu_n \mp A)/(2g_n\beta_n) \hat{\mathbf{B}}_0 \quad (5.3)$$

From this equation it is evident that the effective magnetic field vanishes in one m_S state for $A = 2\nu_n$, the condition of exact cancellation. When this condition is fulfilled, the nuclear Hamiltonian for that m_S state reduces to

$$\mathcal{H}_{n(\pm)} = \mathbf{I} \cdot \mathbf{P} \cdot \mathbf{I} \quad (5.4)$$

Note that this Hamiltonian is completely independent of the direction of the magnetic field, and accordingly the ESEEM frequencies will give the principal values for the quadrupole tensor directly. The presence of non-secular terms in the hyperfine tensor does not necessarily invalidate these arguments, provided the anisotropy is relatively small.

The quadrupole tensor \mathbf{Q} is customarily described by the quadrupole coupling constant $K = e^2qQ/4h$ (for $I = 1$) and the asymmetry parameter η . The NQR frequencies measured under the condition of exact cancellation are then expressed as

$$\nu_- = 2K\eta, \quad \nu_0 = K(3 - \eta), \quad \nu_+ = K(3 + \eta) \quad (5.5)$$

Whereas, at exact cancellation, the effective magnetic field of eq. 5.3 vanishes in one electron spin manifold, it is enhanced in the other manifold. For a strong effective magnetic field, the nuclear spin eigenstates are quantized along this effective magnetic field, and the m_I are thus good quantum numbers. The only transition in this manifold that is relatively isotropic, and can therefore be expected to be observed in orientationally disordered systems, is the $\Delta m_I = 2$ transition, referred to as the double-quantum transition. In the case where the hyperfine tensor is isotropic this transition is expected to be observed at

$$2\nu_m = 2 \left[\nu_{eff}^2 + K^2(3 + \eta^2) \right]^{1/2}, \text{ where} \quad (5.6)$$

$$\nu_{eff} = g_n\beta_n B_{eff}$$

When $A \gg P$, the anisotropy of the hyperfine tensor gives a first-order correction to this frequency.

The approximate Hamiltonian of eq. 5.2 is used in the analysis of the powder ESEEM spectra. The complete Hamiltonian (eq. 5.1), but where the summation includes only the remote nitrogen, was used in all simulations. An energy level diagram for this system is shown in figure 5.5.

5.4 ESEEM of single crystals

Experimental results

In principle, a rotational EPR or ESEEM study of a single crystal can be performed by measuring spectra in three arbitrary, mutually perpendicular planes. For the crystals we used, however, it is

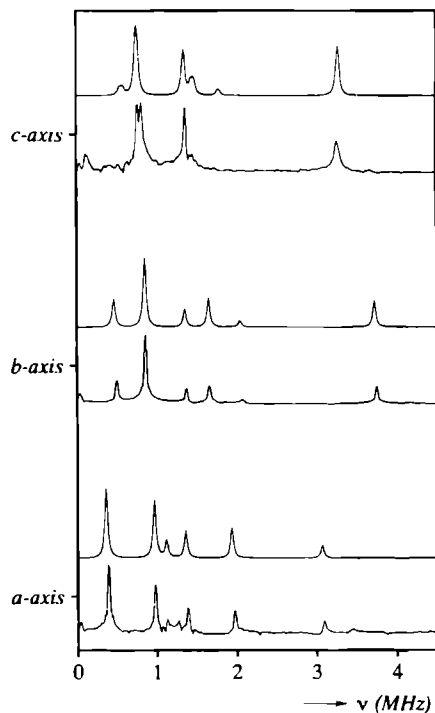


Figure 5.2: ESEEM spectra measured and simulated with the magnetic field direction along the a , b and c -axes. The bottom spectrum of each pair is the measured spectrum, the top spectrum is the result of a simulation.

advantageous to use the planes perpendicular to the symmetry axes, i.e., the ab , ac and bc planes, because the number of observed lines in the ESEEM spectra is then reduced by a factor of two. This leads both to a higher intensity of the observed lines and a simplification of the spectra.

A complication for this specific system is that the copper hyperfine and electron g tensors are nearly coincident with the crystallographic symmetry axes which, in combination with the large inhomogeneous linewidth, causes the four different sites to be indistinguishable in the EPR spectra for most orientations. Therefore, all four sites are present in the ESEEM spectra, although because the sites are pairwise equivalent in the symmetry planes only two sites are observed. Spectra were taken at 10° intervals over 180° in the ab and ac planes, and over 90° in the bc plane. Figure 5.2 shows the ESEEM spectra measured with the magnetic field direction along the a , b and c -axes.

All peaks observed below 4 MHz are attributed to the remote nitrogen (N_2) of the imidazole ring. For most orientations a number of peaks are visible in the region above 4 MHz. These are attributed to ^1H , $^{35,37}\text{Cl}$ or to the directly coordinating nitrogen nuclei (N_1 , N_3). Also, in most spectra additional peaks with low intensity were observed at frequencies below 4 MHz

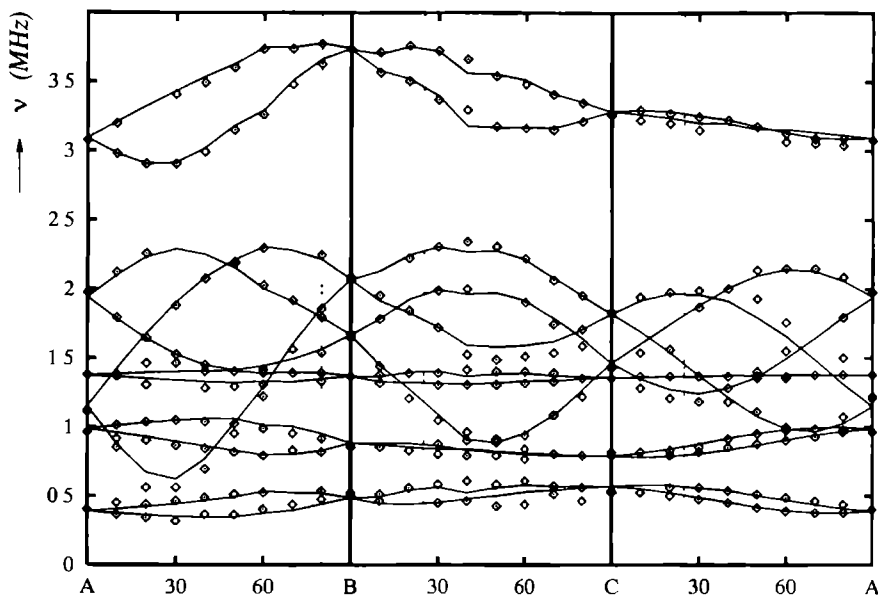


Figure 5.3 Observed nuclear frequencies of the remote nitrogen, plotted versus the angle in either the ab , ac or bc plane. Only the first quadrant of each plane is shown. The other quadrants can be obtained by mirroring the plot. Drawn lines link frequencies obtained from a simulation using the tensors arrived at later in this article. The dashed vertical lines indicate the orientations at which HYSORE experiments were performed.

that are attributed to small crystal fragments or to contributions from unidentified copper species incorporated at other locations in the crystal, which species occur with only low probability. In some spectra a small line splitting was observed, which we attribute to a deviation of the direction of the external magnetic field from the plane. In these cases the average of the two frequencies was used in the analysis. From the magnitude of these splits we estimate an accuracy of the magnetic field orientation with respect to the crystal symmetry planes of better than 1° .

The frequencies of the peaks we could assign to the remote nitrogen are shown in figure 5.3 for one quadrant in each plane; the other quadrants give identical information. In all planes two sets of six lines corresponding to the different sites are observed. As expected, the spectra taken at positions lying symmetrically with respect to the a , b and c axes were identical.

To facilitate the analysis of the ESEEM spectra, we recorded HYSORE spectra [16, 17] at a single orientation in each plane. The orientations were carefully selected so that the spectra showed little overlap between contributions from different sites, yet gave acceptable intensities for all lines, so that many correlations could be observed. Figure 5.4 shows a representative HYSORE spectrum, taken in the ab -plane 10° from the b -axis. We can observe many correlation peaks in this figure. Connecting these peaks by horizontal and vertical lines which link peaks with a common frequency reveals that these correlation peaks can be divided into two sets, one

set belonging to site 1 and one set belonging to site 2. In each plane we were able to make an unambiguous assignment of manifolds to sites. The assignments of the individual lines could be extrapolated to the complete plane because they could be followed for all orientations in the ESEEM spectra. Due to the very small anisotropy of the low-frequency single quantum transitions, the HYSORE spectra had to be acquired with a very high frequency resolution in order to separate the contributions of the sites.

Analysis and simulations

From the single crystal spectra discussed in the previous section we have determined the hyperfine and quadrupole tensor parameters using the simulation program MAGRES [18], and the method outlined in this section. The MAGRES program is a general purpose magnetic resonance simulation program that, in combination with the minimization package MINUITS [19], can find tensor values for a number of tensors by minimizing the mean square error in the simulated transition frequencies with respect to the measured transition frequencies.

Identification of sites

At each orientation, except along the symmetry axes, up to 12 lines (6 from each site) are observed that are attributed to the remote nitrogen. We can combine these lines into four sets of three lines each by making use of the sum-relation, which states that the energy of a double-quantum ($\Delta m_I = 2$) transition must be equal to the sum of the energies of the corresponding single-quantum ($\Delta m_I = 1$) transitions. Each set corresponds to a manifold of energy levels from one particular site and m_S state, m_S being the electron spin quantum number. Each of the two sites observed in the measured planes has two sets of transitions associated with it, where each of these sets corresponds to a particular m_S state. From the spectra, we cannot determine which set of lines originated from which site or from which electron spin manifold, and thus in each plane there are four possibilities for assigning the observed transitions to a site. Because we need to identify the lines belonging to a site in all three planes, we are confronted with $4^3 = 64$ possibilities for assigning the sets of lines in the three planes to a site.

Using the HYSORE technique we can determine which sets of lines in a plane belong to the same site. For a system with multiple sites the ESEEM or HYSORE echo intensity is simply the sum of the contributions from the individual sites. The HYSORE spectra will therefore show correlations of transitions from an α -manifold with transitions from the β -manifold of only the same site, which enables us to separate the transitions of one site, arbitrarily labeled site 1, from those of the other site (site 2). Note that no such separation is possible in the classical one-dimensional ESEEM spectrum.

Figure 5.4 shows the identified correlations for both sites in the ab -plane. In some cases the correlations in the $(+)$ quadrant could be used as an additional aid in determining the assignment. Because we could observe most of the expected correlation peaks we have a high degree of confidence in the assignment. As a result of the information in the HYSORE spectra, in each plane two of the four possibilities for assigning observed transitions to a site have been eliminated, and only $2^3 = 8$ ways remain to assign the sets of lines in all three planes to a site.

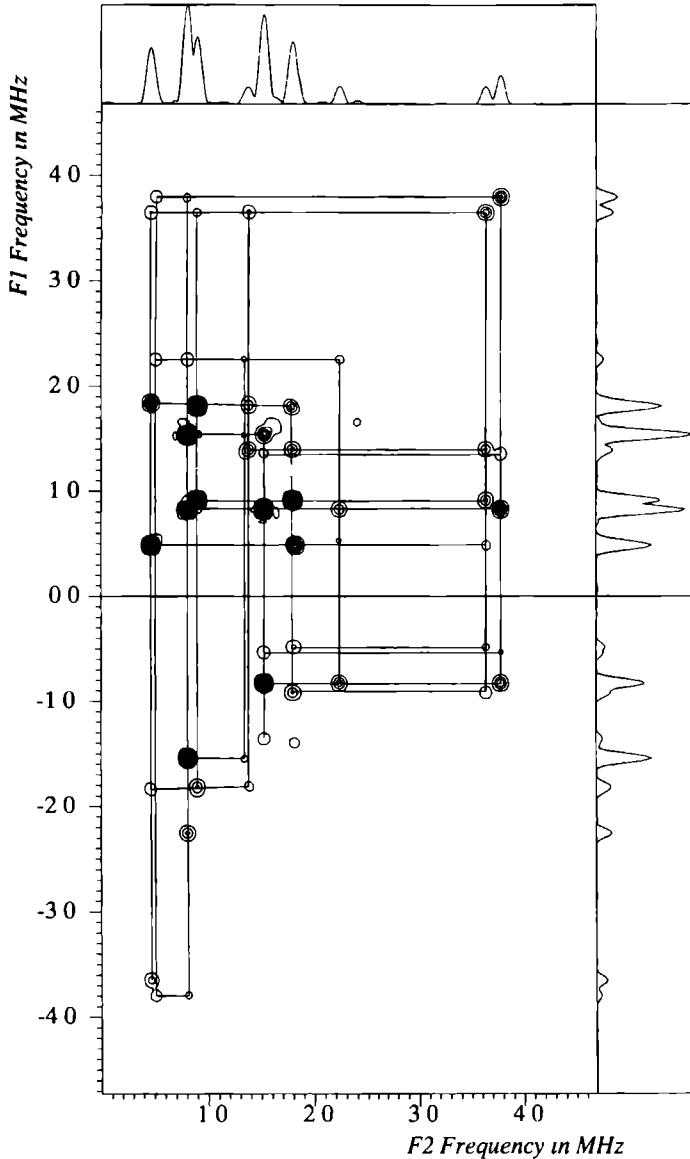


Figure 5.4 Frequency domain HYSCORE spectrum taken at 10° from the b axis in the ab -plane. Inspection of the cross correlation features shows separate contributions from two sites. Similar spectra were taken in the ac and bc planes, but are not shown. The lines in this figure link contributions from the same site. For one site, two lines overlap so that only five lines are visible (see also figure 5.3). Two low-intensity peaks could not be assigned to any site.

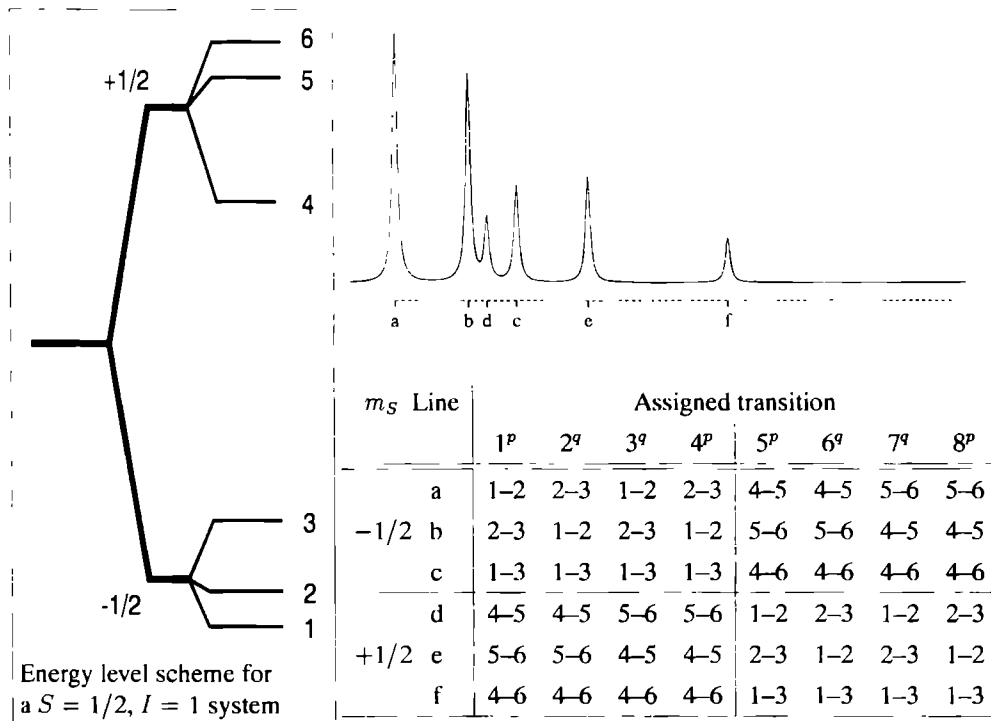


Figure 5.5: The eight possible ways to assign transitions to observed lines. In a spectrum such as the one shown above, six lines, labeled *a* through *f*, are observed. There are eight ways to assign these lines to transitions between the levels shown in the energy level scheme on the left. These eight ways are listed in the table. Possible assignments that have the same label (*p* or *q*) differ only in the sign of the hyperfine and/or quadrupole interactions (see text).

A further reduction can be achieved by utilizing the symmetry relations that exist between the four sites in the unit cell. The space-group of the crystal is $P2_12_12_1$, so that the four sites are related by three two-fold screw axes. We only need to find the hyperfine and quadrupole tensors for one site, since those of the other sites are related to it by the symmetry elements of the point-group of the crystal. Utilizing the symmetry relation one can show that the eight possibilities for assignment of sets of lines to the sites can be divided into two groups of four. Within each group all possible assignments are symmetry related, so that only one assignment within each group has to be taken into consideration, from which the others can be trivially deduced. This reduces the number of possible assignments to two.

Assignment of transitions

Before we can use the MAGRES program to find tensor values that optimally describe the spectra we must assign transitions to the observed frequencies. However, because it is not possible to determine the signs of the hyperfine and quadrupole interactions from ESEEM experiments, an

Tensor Component	Principal Value (MHz)	direction cosines		
		<i>a</i>	<i>b</i>	<i>c</i>
A_{xx}	1.274	-0.3127	-0.2666	-0.9117
A_{yy}	1.061	-0.8790	0.4449	0.1714
A_{zz}	1.741	0.3600	0.8550	-0.3735
A_{iso}	1.355			
P_{xx}	-0.123	0.1770	0.6203	-0.7641
P_{yy}	-0.586	-0.8902	0.4320	0.1445
P_{zz}	0.711	0.4200	0.6546	0.6287

Table 5.1: Principal values and direction cosines of the hyperfine and quadrupole tensors for the remote imidazole nitrogen (N_2) are listed for one particular site, labeled site 2. Tensors for the other sites can be deduced by rotations of 180° about the a , b and c axes. The estimated error is approximately 0.02 MHz in A and 0.002 MHz in P . The rotation angles are accurate to about 2° .

ambiguity in the assignment, in addition to that indicated above, arises. A change in the sign of the hyperfine interaction interchanges the m_S labels characterizing each set of three lines. The sign of the quadrupole interaction determines the position of the middle levels (level 2 and 5) in each manifold. Reversing this sign changes the position of both of these levels without changing the observed frequencies in each manifold.

Figure 5.5 lists the eight possible ways in which we can assign transitions between the energy levels to the observed lines. To see how the signs of the hyperfine and quadrupole interactions affect these assignments, we arbitrarily select possibility 1^p . From this assignment, possibilities 4^p , 5^p and 8^p can be generated by changing only the sign of the hyperfine interaction (5^p), changing only the sign of the quadrupole interaction (4^p), or by changing the signs of both interactions simultaneously (8^p). Similarly, we can start from assignment 2^q , which differs from assignment 1^p only in the assignments of transition 1–2 to line b instead of line a , and of transition 2–3 to line a , instead of line b . Again, from this assignment (2^q) the assignments labeled 3^q , 6^q and 7^q can be generated. It is therefore sufficient to calculate tensors for only one possibility within in each group p and q . The others can easily be generated.

Resulting tensors

Each of the two possibilities determined for the assignment of a set of lines to a site has been combined with a possible assignment of transitions to these lines (see above), and a minimizing fit was performed using these combinations in order to find the hyperfine and quadrupole tensors.

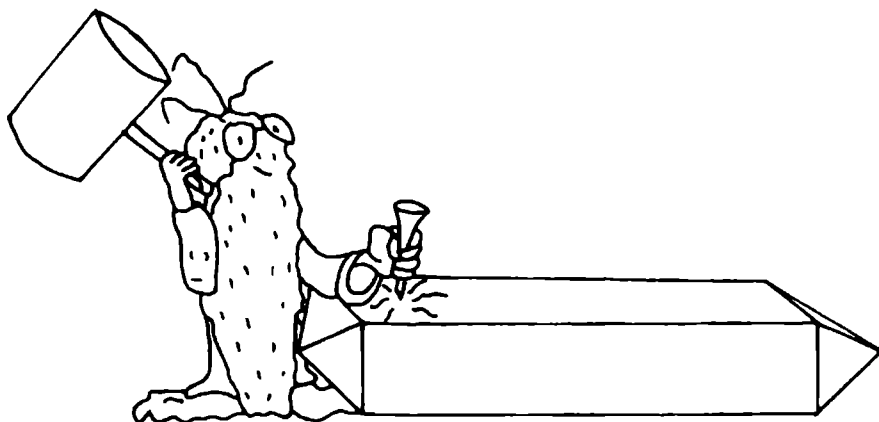
One of these combinations was selected as the right one, based on the quality of the resulting tensors as determined by the average error in the simulated frequencies. The best fit showed an average error of approximately 36 kHz, which is significantly less than the average observed linewidth of 57 kHz. The second-best fit showed an average error of about 87 kHz. The tensors of the best fit are listed in table 5.1.

Using these tensors, we simulated ESEEM spectra with the magnetic field along the a , b and c axes (figure 5.2). Figure 5.3 shows lines connecting simulated frequencies of the same transition for a number of orientations in the ab , ac and bc planes. These simulations show that we have obtained a good fit. As noted before, it is not possible to determine from the ESEEM spectra the signs of the hyperfine and quadrupole interactions; they must be determined from other considerations. The tensor values determined by us are in good agreement with those determined by Colaneri and Peisach [13]. The different signs of some of the direction cosines in the tensors listed by these authors compared to those listed in table 5.1 can be explained by the fact that their tensors may refer to a different site.

5.5 ESEEM of Powders

The determination of the hyperfine and quadrupole tensors of the remote nitrogen as presented in the previous sections gives us a reference system for investigating the usefulness of techniques aimed at determining those interactions from orientationally disordered systems. As stated in the introduction, the aim of this work is to assess the accuracy and reliability of information obtained from those systems.

The techniques that will be discussed here focus on the phenomenon of exact cancellation, discussed extensively by Flanagan and Singel in [6, 14]. We combined multifrequency experiments, as suggested by these authors, with orientation selection techniques [8, 20, 21] and two-dimensional experiments [22] to form a complete picture of the ESEEM modulation patterns. By utilizing the special properties these modulation patterns exhibit when the condition of exact cancellation is fulfilled, it was possible to deduce information on both the quadrupole and hyperfine interactions. In this analysis extensive computer simulations were used to derive



... the remaining material was crushed

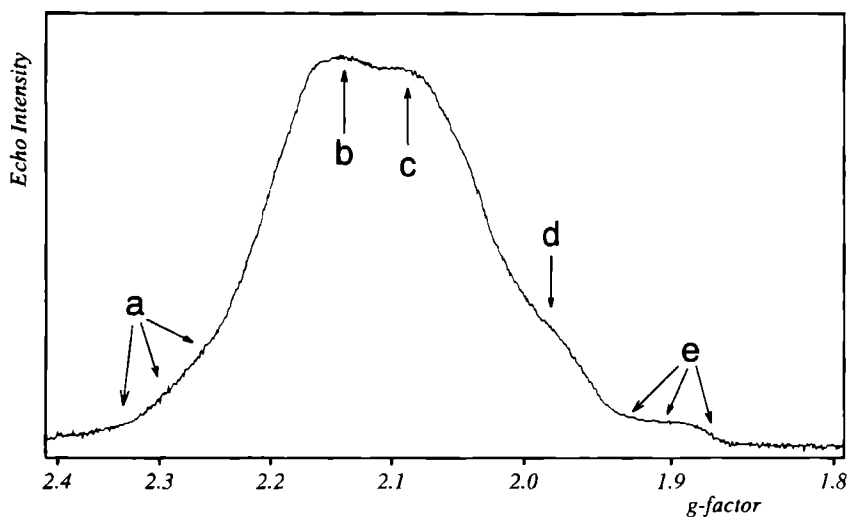


Figure 5.6: Echo-induced EPR (ESE) spectrum of powdered copper-doped *l*-histidine hydrochloride monohydrate. This spectrum was recorded at a microwave frequency of 9.791 GHz, using a 2-pulse echo sequence with τ set at 200 ns. Arrows indicate the positions where ESEEM spectra were recorded. ESE spectra recorded at lower microwave frequencies are somewhat broader than the spectrum presented here

information that could not be directly be determined from the ESEEM spectra.

Experimental results

ESEEM spectra of the powdered material were recorded for a number of microwave frequencies and at different positions in the EPR spectrum. Figure 5.6 shows the powder ESE spectrum. The g -values at which experiments were performed are indicated in this figure by a, at the low-field edge, through e, at the high-field edge.

At the central peak of the ESE spectrum ($g \approx 2.15$, peak b in figure 5.6), we recorded ESEEM spectra for microwave frequencies of 9.806, 7.804, 7.245 and 6.563 GHz, which are shown in figure 5.7. The microwave pulse length used in these experiments was 16–25 ns at 9.806, 7.245 and 6.563 GHz and 60 ns at 7.804 GHz. The time τ between the first and second pulses was fixed at 200 ns in each experiment.

Field-dependent orientation selective experiments were performed at the low-field and high-field edges of the ESE spectrum, near positions a and e, respectively, using a microwave frequency of 7.804 GHz. At position e, 17 ESEEM spectra with a waiting time τ of 200 ns were recorded between 303.2 mT ($g = 1.841$) and 285.9 mT ($g = 1.954$); these are shown in figure 5.8b. Figure 5.8a shows 14 ESEEM spectra that were recorded in the region between 236.0 mT ($g = 2.366$) and 249.0 mT ($g = 2.242$), near field position a. In these experiments τ was set at 270 ns.

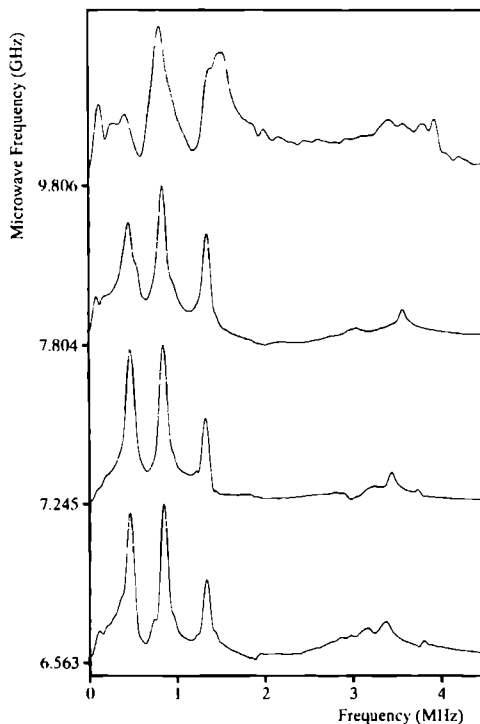


Figure 5.7: Multifrequency ESEEM spectra taken at the central peak, $g = 2.15 \pm 2$, peak b in figure 5.6.

We also carried out orientation selective two-dimensional stimulated-echo ESEEM experiments using a microwave frequency of 7.245 GHz, to determine the τ -dependence of the ESEEM spectra. These spectra, shown in figures 5.9a and 5.10a, were recorded at field positions a (221.3 mT, $g = 2.339$) and e (277.9 mT, $g = 1.862$). Similar experiments were also performed at positions b (234.3 mT, $g = 2.210$), c (245.1 mT, $g = 2.112$) and d (263.5 mT, $g = 1.965$) (not shown). Due to the limited time-range in the T -direction, the frequency resolution in these spectra is limited to about 250 kHz. The natural linewidth at this microwave frequency is about 100 kHz, as could be determined from one-dimensional experiments where the frequency resolution is higher (spectra are not shown).

In all spectra we can discern two regions of interest. In the region below 2 MHz, we observe three lines at approximately 0.47, 0.85 and 1.33 MHz, which we attribute to a single m_S state. The multifrequency ESEEM spectra of figure 5.7 show a pronounced narrowing of these three lines on going to lower microwave frequencies, consistent with the onset of exact cancellation. Between approximately 2.5 MHz and 4 MHz we observe a single feature. This feature is relatively narrow only in the orientation selective spectra taken at the high-field edge (e) of the ESE spectrum. In all other spectra it is strongly broadened and shows some additional

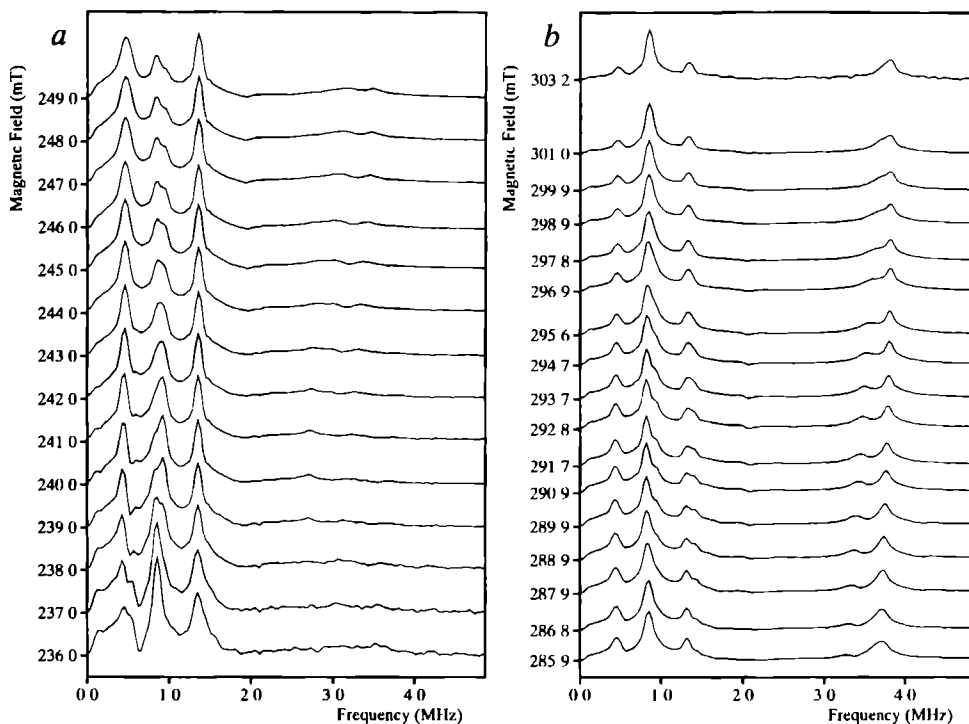


Figure 5.8. Figures *a* (left) and *b* (right) show a series of orientation selective spectra taken at various field values, using a microwave frequency of 7.8 GHz. Figure *a* shows spectra taken at the low-field edge, which is selective for orientations near the *a*-axis. Figure *b* shows spectra at the high-field edge, selective for the *b* axis. The spectra are normalized with respect to the ν_+ line.

structure.

Because we are close to exact cancellation in all spectra, the frequencies of the lines below 2 MHz are close to the pure NQR frequencies. The lines are labeled, with increasing frequency, as ν_- , ν_0 and ν_+ , and we shall collectively refer to these lines as the ‘NQR lines’. The high-frequency feature is identified as arising from double-quantum transitions belonging to the other m_S manifold and is usually referred to as the $2\nu_m$ line (see also eqs. 5.6 and 5.5 and refs. [8, 14]).

The orientation selective spectra taken at the high-field edge all are very similar. The most interesting change that can be observed is that on going to lower magnetic field values the double-quantum feature broadens as additional orientations start to contribute to the spectrum. The relative intensities of the NQR lines do not change dramatically, but some small broadening effects can be observed (figure 5.8*b*). The situation is radically different at the other edge of the spectrum (figure 5.8*a*). Here the intensity of the ν_0 line decreases strongly as we increase the magnetic field. This decrease is accompanied by a small increase in linewidth. The relative

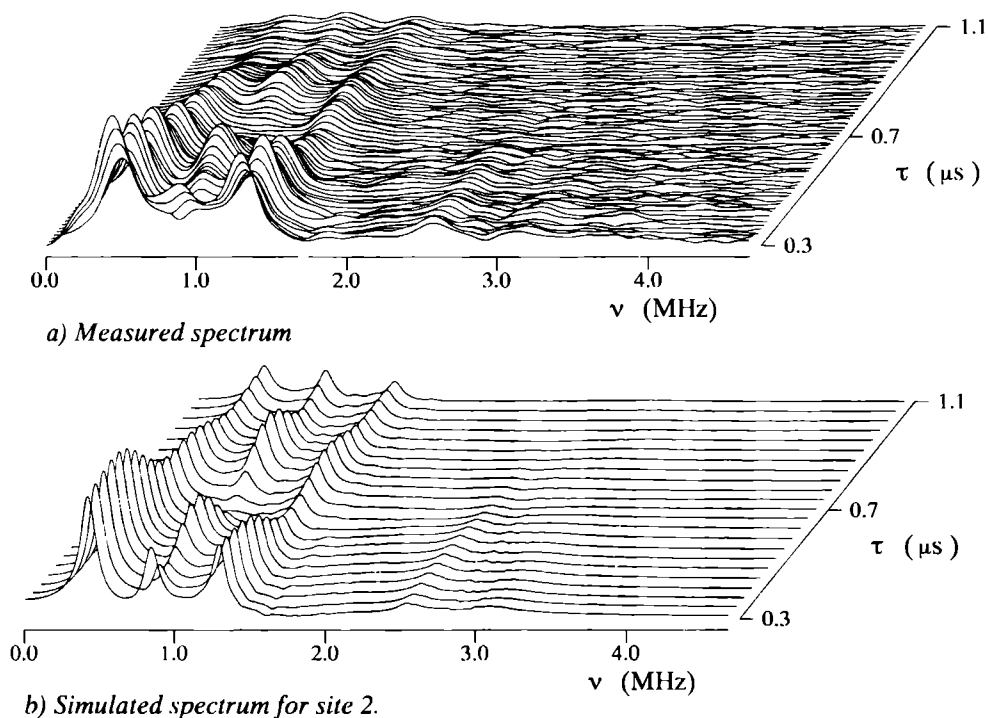


Figure 5.9: Measured (a) and simulated (b) ESEEM spectra as a function of τ , recorded at a magnetic field strength of 221.3 mT (field position a) and a microwave frequency of 7.245 GHz. The simulation was performed using the g and copper hyperfine tensors determined by McDowell *et al.*, and the $^{14}\text{N}_2$ hyperfine and quadrupole tensor listed in table 1.

intensities and widths of the ν_- and ν_+ lines do not change significantly. The double-quantum feature, visible only weakly at the lower field values slightly increases in intensity and shifts significantly to higher frequencies as the magnetic field increases.

On inspecting the two-dimensional ESEEM spectra shown in figures 5.9 and 5.10, we see that the intensities of all lines are strongly modulated. In particular, the ν_+ line in the spectra recorded at positions b through e shows a pure single-frequency modulation with a frequency of about 3.8 MHz, which is the frequency of the $2\nu_m$ line. This line itself also shows, in the spectrum of field position e, a modulation pattern apparently with only one frequency, about 1.3 MHz. Furthermore, the intensity of this line is strongly orientation dependent, almost disappearing at orientations near the a axis (figure 5.9, field position a). The modulation patterns of the ν_- and ν_0 lines are much less well-defined than the modulation patterns of the ν_+ and $2\nu_m$ lines. The modulation patterns of the ν_+ and $2\nu_m$ lines in the spectrum recorded at field position a are much less striking than those observed in the spectra at field positions b through e. In some spectra, we can observe a modulation of some lines with a frequency of approximately 12 MHz,

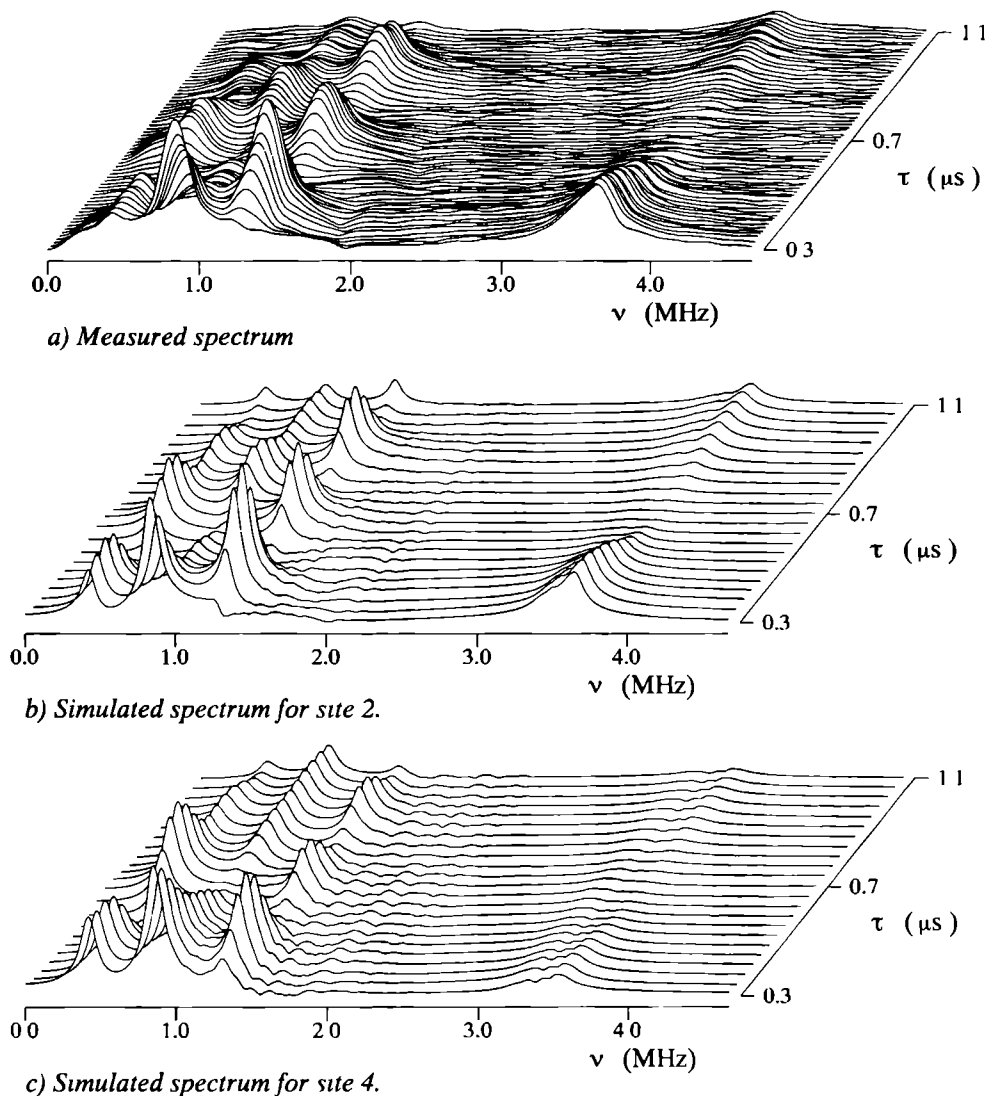


Figure 5.10 Figure a shows the measured 2-dimensional ESEEM spectra for a magnetic field of 279.7 mT (field position e) at a microwave frequency of 7.245 GHz. Figures b and c show simulations that were calculated using the same copper-hyperfine and electron g -tensors, but with $^{14}\text{N}_2$ hyperfine and quadrupole tensors determined for different sites. Note the difference in τ -behavior of the ν_0 line, and the difference in intensity of the $2\nu_m$ line.

the origin of which is unknown. Since the modulation patterns of the NQR lines are not similar, we see significant changes in their relative intensities for different τ -values. Note especially the behavior at field position **e** (figure 5.10) of the ν_0 line, which is dominant for small τ -values, but quickly diminishes in intensity as τ increases from 300 ns to 500 ns, clearly illustrating this τ -dependence of the relative intensities of the NQR lines.

Since we expect the orientation selective spectra in figure 5.8, taken at field positions **a** and **e** to resemble the single crystal spectra taken along the *a* and *b* symmetry axis it is interesting to compare these spectra. The single crystal spectrum taken along the *b* axis, shown in figure 5.2, is very similar in both the observed frequencies and the intensity distribution to the spectra of figure 5.8*b*, which were taken at the high field edge of the ESE spectrum. We do not expect to see in the powder ESEEM spectra the single quantum transitions of the high-frequency manifold due to their anisotropy. For the single crystal spectrum taken at the *a* axis, however, the agreement with its orientation selective partner, shown in figure 5.8*a*, taken at the low-field edge of the ESE spectrum (**a**) is less good. This is not very surprising, since the low-field edge is much less selective for the *a* axis than the high-field edge is for the *b* axis. Another factor that hampers the comparison is the fact that the spectra were recorded at different τ -values. Finally, we must note that the single crystal spectrum for the *a*-axis was not recorded at the low-field copper line in the EPR spectrum, but rather at the high-field line.

Simulations of the powder ESEEM spectra

Since the tensors relevant for the description of the spectra are known from the single crystal results, we first attempted to simulate the powder ESEEM spectra using the single crystal data. Subsequently, we examined what kind of information could be extracted directly and indirectly from the powder spectra. This information was then compared to the single crystal data, giving information on its reliability. Before we discuss the results of our simulations, we wish to make three general remarks.

1. Simulations of the powder spectra were performed either using the simulation program MAGRES discussed earlier or a recently developed simulation program, MR2, which has been specifically designed to analyze ESEEM powder spectra. All simulations included the copper hyperfine (\mathbf{A}_{Cu}) and electron *g* tensors, for the reasons outlined below. In addition to these tensors, some simulations performed using the new program included the two directly coordinating nitrogen nuclei, $^{14}\text{N}_1$ and $^{14}\text{N}_3$, and two equivalent chloride nuclei. The tensors for these additional interactions, as well as *g* and \mathbf{A}_{Cu} have been taken from [9]
2. The simulations of the powder ESEEM spectra are complicated by the presence of anisotropic copper hyperfine and electron *g* tensors. For many systems, the central peak in ESE spectrum can be assumed to have a flat distribution of orientations. Although this is often a valid assumption in axially symmetric systems, it is not a good approximation for (ortho)rhombic systems. For copper-doped *l*-histidine, predominantly orientations near the *c*-axis contribute to the central part of the ESE spectrum, but other orientations are also present. Another complication for this system is that, due to the large EPR linewidth, even

at the high and low edge of the spectrum that are selective for the b and a axes, respectively, many orientations contribute to the ESEEM signal. In order to incorporate these effects all simulations included the anisotropy of the \mathbf{A}_{Cu} and \mathbf{g}

- 3 The presence of multiple sites in the crystal complicates matters, because these different sites cannot be resolved in the EPR spectra. As a consequence, the ESEEM spectra contain peaks originating from more than one site (*cf.* figure 5.3). For the analysis of the powder ESEEM spectra it is essential to know which peaks belong to which site, or, to be more precise, which \mathbf{g} , \mathbf{A}_{Cu} and nitrogen tensors belong to the same site (or molecule). This cannot be determined from the experiments. To solve this problem, we have combined a particular set of \mathbf{A}_{Cu} and \mathbf{g} tensors. Because in our crystal there are four sites in the unit cell, we need to perform simulations for four combinations of \mathbf{g} , \mathbf{A}_{Cu} and $^{14}\text{N}_2$ tensors. These simulations have been labeled by the number of the site that was used for the $^{14}\text{N}_2$ tensors.

Figures 5.9 and 5.10 show the results of the simulations for the two-dimensional orientation selective measurements at 7.245 GHz, using the tensors obtained from the single crystals listed in table 5.1. For field position **a**, figure 5.9 there is only little difference between the simulations for the above-mentioned four combinations. Therefore only the simulations for site 2, the tensors of which are reported in table 5.1, are shown.

For field position **e** (the high-field edge) there is a significant difference between the simulations for the four combinations, especially for the ν_0 and the high-frequency double-quantum ($2\nu_m$) line, as can be seen in figure 5.10 for sites 2 and 4. Similar differences are observed between site 2 and sites 1 and 3. Comparing these simulations to the measured spectra shows that for site 2 only does the simulation match the measurement well, from which we conclude that the tensors from table 5.1 are given for the site we have labeled site 2. This is confirmed by simulations for field positions **c** and **d**. We were not able to derive this information from the single crystal data, because it was not possible to isolate a single site in the single crystal ESE spectra. The agreement of the simulations for site 2 with measured spectra is striking. In all cases there is a very good match for both the intensity of the lines and the modulation pattern. The only feature that is not reproduced in the simulations is the high-frequency modulation that is visible on some of the lines in figures 5.9, which also occurred for field position **b**.

Determination of parameters from the powder ESEEM spectra

Introduction

As has been noted in the introduction, all experiments were performed at or near exact cancellation. For an isotropic hyperfine interaction the modulation intensities of the three low-frequency NQR lines discussed earlier are then completely determined by the orientation of the quadrupole interaction. However, as Flanagan *et al* [14] already noted, if the hyperfine interaction is not axial then these modulation intensities can be strongly dependent on the orientation of the hyperfine anisotropy. However, as long as we are close to exact cancellation, the modulation patterns are dependent mainly on the orientation of the quadrupole tensor [14]. This fact can help us

determine the orientation of the quadrupole tensor from simulations, since it reduces the number of unknown parameters needed to describe the modulation patterns.

The second feature in the ESEEM spectra, the line corresponding to the double-quantum transition in the other manifold can be used to determine information on the hyperfine interaction. By comparing the measured frequencies of this line in orientation selective spectra to the expected frequency for an isotropic hyperfine tensor it is possible to obtain information on the magnitude of this anisotropy and, possibly, also on the its anisotropy.

In our description of the system we limit ourselves to an axial hyperfine tensor, described by the isotropic hyperfine interaction A_{iso} , the parallel part of the anisotropy of the hyperfine tensor, A_{\parallel} , and the polar angles θ and ϕ describing the orientation of the major axis of the hyperfine tensor. The limitation to an axial hyperfine interaction expresses our expectation that we shall not be able to determine significant values for the rhombicity, which is described by an asymmetry parameter for the axial hyperfine anisotropy and the associated Euler angle, since the spectra are very insensitive to these parameters. Of course, when strong rhombicity of the hyperfine tensors occurs, the accuracy of our analysis will suffer. The quadrupole tensor is customarily described by the parameters K and η introduced earlier and its orientation is defined by Euler angles α , β and γ .

Some of the parameters used in the description can be extracted, directly or indirectly, from the measured spectra without the need to resort to computer simulations. These parameters include the principal values of the quadrupole and hyperfine interactions and possibly also the orientation of the hyperfine interaction. Other parameters, notably the orientation of the quadrupole interaction, cannot be determined directly, but can be estimated by comparison of the measured spectra with simulations in which these parameters are varied. The other parameters, determined directly from the spectra, are fixed in these simulations.

Determination of parameters directly from the spectra

The positions of the NQR peaks in the spectra taken at exact cancellation, as shown in figure 5.7, are used to determine the quadrupole coupling constant $K = 0.363 \pm 0.005$ MHz and the asymmetry parameter $\eta = 0.67 \pm 0.01$. This corresponds to principal values of the quadrupole tensor of -0.12 MHz, -0.60 MHz and 0.72 MHz, with an uncertainty of about 0.02 MHz. These same spectra can be used to estimate the size of the isotropic part of the hyperfine tensor, since that value determines the field value at which exact cancellation occurs. From our observation that exact cancellation occurs at frequencies in the range of 6.5 to 7.2 GHz for the central peak at $g = 2.15$ we estimate the isotropic part of the hyperfine interaction to be 1.4 MHz, with an uncertainty of about 0.1 MHz.

From the orientation selective spectra it is possible to determine the anisotropy in the hyperfine interaction by comparison of the observed position of the $2\nu_m$ line with the expected position for a purely isotropic hyperfine interaction. The orientation selective spectra in figure 5.8b show a relatively narrow $2\nu_m$ line, which is shifted to higher frequencies by about 0.35 MHz relative to its expected position. It is more difficult to assess the shift in the orientation selective spectra at the low-field edge, partly because the $2\nu_m$ line in these spectra has a very low intensity, but also because it is strongly broadened. The shift is estimated between 0 and -0.3 MHz.

These data suggest that the anisotropy of the hyperfine interaction is about 0.35 MHz, and that the major axis is more or less aligned with the direction of the largest copper hyperfine interaction. The hyperfine tensor is shown not to be axial from the width of the $2\nu_m$ feature in the spectra taken at field positions other than \mathbf{e} (cf. figure 5.9). It appears that there is a rhombic component which can be described by an asymmetry parameter of somewhat less than 1. Unfortunately, no further information can be obtained about this rhombicity. Typically, we could not get information on the orientations of the two minor axes of the hyperfine tensor.

Determination of parameters through simulations

The undetermined parameters that remain are principally the orientation of the quadrupole tensor and, at least partially, the orientation of the hyperfine tensor. Following Flanagan *et al.* [7] and Goldfarb *et al.* [8], we have used computer simulations of the orientation selective spectra to determine these orientations. As Goldfarb *et al.* already noted, the (relative) intensities in the ESEEM spectra are very dependent on spectrometer dead-time and other artifacts, and therefore one should consider not individual spectra but rather compare series of spectra, such as a series in which τ was varied. We have taken this one step further by considering complete two-dimensional spectra (figures 5.9 and 5.10), in which τ as well as T were varied.

In the analysis of these spectra, we began by considering the two-dimensional spectrum taken at the high-field edge of the ESE spectrum at 278.0 mT (figure 5.10). The orientation selection is most pronounced at this orientation, and thus we expect to find the highest degree of correspondence between simulations and experimental data at this position.

One of the most striking features in the two-dimensional spectra is the almost pure 3.8 MHz modulation of the ν_+ peak. We expect to see such a pure modulation pattern only if no branching occurs during the microwave pulses in at least one pair of levels. This can occur only if the quadrupole interaction, which determines the quantization in the low-frequency manifold, has at least one axis that is to some extent aligned with the effective magnetic field direction, which determines the quantization in the high-frequency manifold [14]. This condition is fulfilled at the high-field edge of the ESE spectrum. Simulations using the above conditions for a number of orientations of the quadrupole interaction, shown in figure 5.11, confirmed this and showed that the quadrupole axis corresponding to the principal quadrupole tensor value of -0.12 MHz is approximately aligned with the b symmetry axis. Since the orientation of the quadrupole tensor with respect to the crystallographic axis system is most conveniently described using the Euler angles α , β and γ , we will label the -0.12 MHz principal quadrupole axis the quadrupole Z axis, although this is customarily assigned to the major quadrupole axis. The reference xyz frame is chosen such that for angles $\alpha = 0$, $\beta = 0$, $\gamma = 0$ the quadrupole Z axis is aligned with the crystallographic b axis, which means that $x = c$, $y = a$ and $z = b$. The angle β then describes the deviation of the Z axis from the z axis, and the angle α describes in which direction this deviation occurs. The angle γ determines the orientation of the other two (X and Y) axes in the plane perpendicular to the Z axis. The orientation of the hyperfine interaction, described by the angles θ and ϕ was chosen such that for $\theta = 0$ and $\phi = 0$ its major axis was aligned with the reference z axis, the crystallographic b axis. These angles completely determine the orientation of the major axis of the hyperfine interaction because we take the hyperfine interaction as axial.

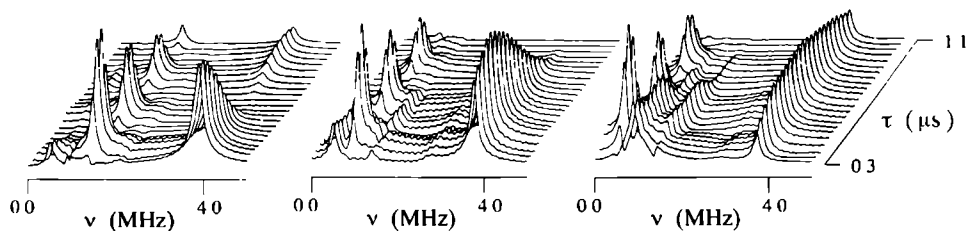


Figure 5.11: Simulations for different orientations of the quadrupole tensor with respect to the crystallographic symmetry axes. The simulations were performed for field position e where the magnetic field is aligned with the crystallographic b axis. In each simulation a different quadrupole principal axis has been taken parallel with the magnetic field. Note that a pure modulation pattern is in each case visible on a different NQR line: from left to right at the ν_+ , the ν_0 and the ν_- line

Our primary goal in these simulations is to find the orientation of the quadrupole interaction, defined by the angles α , β and γ . To this end, we have investigated the influence of these individual parameters on the simulated spectra.

From our initial guess, $\alpha = \beta = \gamma = 0^\circ$ we first started changing β . From simulations it appeared that the modulation pattern of the ν_+ line could be reproduced for angles β not larger than 60° , independent of the angles α and γ . The cumulative intensities of the ν_- and ν_0 lines were also independent of α , but changed significantly with β as can be seen in figure 5.12 where simulations for $\beta = 20^\circ$, 40° and 60° are shown. For angles $\beta \leq 30^\circ$ the ν_- and ν_0 lines were significantly weaker than in the experimental spectra, suggesting a value for β of about $45 \pm 10^\circ$.

On changing the angle α while keeping γ fixed at 0° the modulation patterns of the ν_- and ν_0 lines changed strongly. For α near 0° , the ν_- line is stronger than the ν_0 line, whereas for α near 90° , the ν_0 line is stronger which corresponds more closely to the measured spectrum. The intensity distribution and modulation patterns suggested values for α of about 90° or 270° . For values for γ different from 0 the same considerations held, but the optimal values for α that were thus found varied slightly with γ , but never deviated more than about 20° from the optimal values for that were found for $\gamma = 0^\circ$. The modulation pattern of the fourth feature in the spectrum, the $2\nu_m$ feature, corroborates the possible values for α . As this angle approaches 90° (or 270°), the intensity of the $2\nu_m$ line drops somewhat, so that it matches the measured intensity better. Stronger evidence for these values for α is that the simulated modulation pattern of this feature closely follows the observed pattern for these angles, but is completely different for α near 0° or 180° .

An exhaustive search of angles γ was performed for a number of angles α . Spectra were simulated for $0^\circ \leq \gamma < 360^\circ$ in steps of 30° . β was fixed at the earlier determined optimal value of 45° . A good correspondence of the NQR lines to the experimental spectra could be obtained for almost any value of γ , although it appeared that values near 180° were less likely to be correct. On changing γ , the modulation pattern and modulation depth of the ν_+ peak did not change very much, but its intensity dropped somewhat for values of γ between 150° and

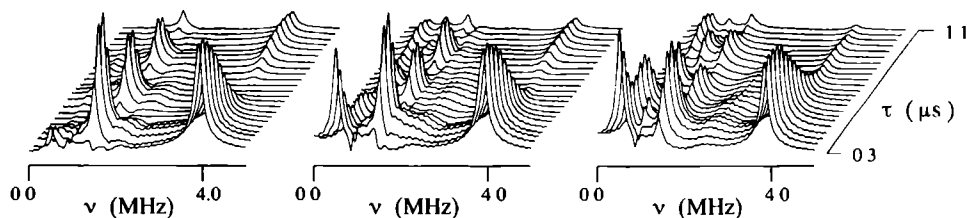


Figure 5.12: Simulations for different values of β : 20° at the left, 40° in the middle and 60° at the right. In all cases α and γ were fixed at 0° . The leftmost spectrum is very similar to the spectrum for $\beta = 0^\circ$ shown in figure 5.11. As β increases the intensities of the ν_0 and ν_- lines also increase. In the interpretation, these spectra are compared to figure 5.10a

270° . In this same range, the intensity of the $2\nu_m$ line also dropped, and the intensities of the ν_- and ν_0 lines increased. These effects could not be counteracted by changing α . Changing β did have an effect on the intensity of the ν_+ line, suggesting that for these values of γ a value for β of about 35 to 40° would be more appropriate. For values of γ larger than 270° or smaller than 150° , the intensity distribution was very similar to that in the experiments. The effect of changing γ in this range is limited to a change in modulation pattern and depth for the ν_- and ν_0 lines. The features that changed with γ could not be significantly influenced by changing α , and vice versa. The striking behavior, described earlier, of the ν_0 line, which is strong for small τ -values, but decreases rapidly with increasing τ , was observed in the simulations only for α between 60° and 90° , or between 240° and 270° . An optimum for γ was found between -45° and 45° . Outside this region, the modulation pattern on the ν_- line was too intense. However, for somewhat larger γ , the intensity of the $2\nu_m$ line more closely matched the experiment

Simulations of the spectra taken at other field values confirmed the previous assignments to α , β and γ . We were especially interested in the simulations of the spectrum shown in figure 5.9a which were taken at 221.3 mT, since for this spectrum the orientation of the magnetic field with respect to the quadrupole axis is completely different from its orientation in the spectrum discussed above. Unfortunately, differences in linewidth and degree of orientation selectivity make this spectrum much more difficult to simulate properly, as can be seen from the simulation performed using the hyperfine and quadrupole tensor values determined from the single crystals (figure 5.9b). Disregarding this, however, it could be shown that the modulation patterns for the NQR lines at angles γ near 0° most closely follow the behavior observed in the measured spectra. For $\gamma = -30^\circ$, the modulation pattern is very similar to that in the experimental spectra and the intensity distribution is also very well reproduced.

In all simulations performed in the course of the powder analysis the $2\nu_m$ line appeared stronger than in the measurements. We ascribe this to our use of a purely axial hyperfine tensor: changing the orientation of the hyperfine interaction by as much as 45° from its assumed orientation had no significant effect on the simulated spectra. The spread in hyperfine values especially in the ac plane is in reality much larger than in the simulations. As we had expected, adding some non-axiality to the hyperfine tensor caused the $2\nu_m$ line to drop significantly in intensity in the simulations for field position a. Other than that the hyperfine interaction was not

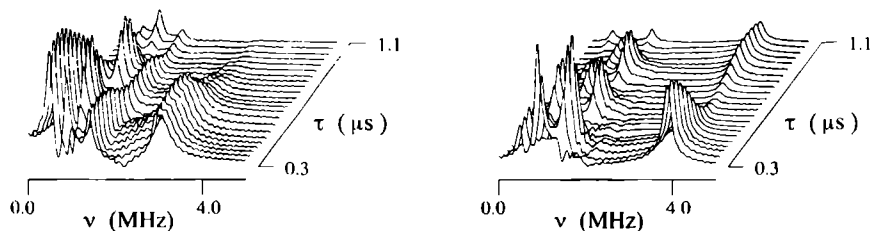


Figure 5.13: Simulations for $\alpha = 75^\circ$, $\beta = 45^\circ$ and $\gamma = 0^\circ$. On the left is the simulation for field position **a**, on the right that for **e**. These spectra best reproduce the measured spectra of figures 5.9a and 5.10a.

axial no further information could be obtained from these simulations.

Summarizing, we have determined optimal values $\alpha = 75^\circ$, $\beta = 45^\circ$ and $\gamma \approx 0^\circ$. Simulations for this orientation at field positions **a** and **e** are shown in figure 5.13. The principal values and orientations for the hyperfine and quadrupole tensors determined from the powder ESEEM spectra are listed in table 2. The values for the direction cosines in this table are given for comparison with table 1. Due to the relatively large uncertainty in the Euler angles, there is a significant error margin in these values. The direction cosines given for the hyperfine interaction are partially undetermined. Those that are given reflect our impression that the major axis of the hyperfine tensor is approximately aligned with the crystallographic *b* axis.

5.6 Conclusions

We have been able to determine tensor values for the remote nitrogen ($^{14}\text{N}_2$) in copper-doped *l*-histidine hydrochloride monohydrate from both the single crystal spectra and from the powder spectra. Comparing these results, it can be concluded that the principal values of the tensors can be determined accurately from the powder measurements, with the restriction that the hyperfine interaction is axial. When considering the orientations we have determined for the hyperfine and quadrupole interactions, we should bear in mind that there still is a significant error margin in the parameters listed in table 5.2. That being said, we must still conclude that there is a very good agreement between the tensors determined from the powder and single crystal data.

Although the tensor elements match closely, we must note that this is not the case for the Euler angles. It is important to consider these angles, since it is from them that the tensor elements are determined. The Euler angles for the single crystal data are $\alpha = 34^\circ$, $\beta = 49^\circ$ and $\gamma = 146^\circ$. It appears that we have been able to fix β to within the expected accuracy. The value for α is somewhat surprising, as it is in the range we had excluded early in the analysis, but the deviation of 40° from the actual value is not extremely large. The actual γ is considerably higher than the value we believed optimal from the powder simulations. However, the determination of γ is the most difficult, since it relies on the interpretation of the spectrum that is expected to be reproduced least well. The most severe problem with which we are faced is the large deviation from axiality that is exhibited by the hyperfine interaction. This is reflected in the poor quality of

Tensor Component	Principal Value (MHz)	direction cosines		
		<i>a</i>	<i>b</i>	<i>c</i>
A_{xx}	1.2 ± 0.15	–	0	–
A_{yy}	1.2 ± 0.15	–	0	–
A_{zz}	1.75 ± 0.1	0	1	0
A_{iso}	1.4 ± 0.1			
P_{xx}	-0.12 ± 0.02	0.0	0.70	-0.70
P_{yy}	-0.60 ± 0.02	-0.97	0.18	0.18
P_{zz}	0.72 ± 0.02	0.26	0.68	0.68

Table 5.2. Tensors for the hyperfine and quadrupole interactions of the remote imidazole nitrogen determined from the powders spectra. The tensor values for the quadrupole interaction correspond to Euler angles of $\alpha = 75^\circ$, $\beta = 45^\circ$ and $\gamma = 0^\circ$.

the simulations for the low-field spectra and in the difficulty we had in determining the optimal values for α and γ .

Concluding, we can say that the techniques we applied can give accurate information on the coupling tensors, especially on the quadrupole interaction. The anisotropy of the hyperfine interaction appears to be more important than previously suggested [14, 20], but it can easily be included in the simulations. Much more difficult to assess is the influence of a rhombic hyperfine tensor, such as that for the remote nitrogen studied in this work. Unfortunately, it appears that this parameter has significant influence on the modulation patterns of the NQR lines and can severely hamper the determination of the quadrupole orientation.

The quality of the resulting tensor information can probably be improved somewhat if the rhombic component of the hyperfine interaction is included in the search process. This, however, increases the number of unknown interacting parameters by two, severely complicating the simulation process. The use of two-dimensional 3-pulse stimulated ESEEM powder spectra clearly has its advantages over the more traditional ways of using a limited number of τ -values [8] or using the 2-pulse ESEEM technique, in which no suppression effect occur [7]. In the two-dimensional spectra, not only the relative intensities of the observed features, but also the modulation patterns give useful information. Especially for systems for which the condition of exact cancellation is (nearly) fulfilled, such as many biologically important copper-imidazole complexes, the additional information contained in these modulation patterns lines is very valuable.

References

- [1] J. Peisach, P. Aisen, and W. E. Blumberg, editors. *The Biochemistry of copper*, New York, 1966. Academic Press.
- [2] E. I. Solomon, K. W. Penfield, and D. E. Wilcox. Active Sites in Copper Proteins, An Electronic Structure Overview. In *Structure and Bonding* 53, pp. 1–58. Springer Verlag, Berlin, 1983.
- [3] W. B. Mims and J. Peisach. Assignment of a ligand in Stellacyanin by a Pulsed Electron Paramagnetic Resonance method. *Biochemistry* 15 (1976) 3863.
- [4] F. Jiang, J. McCracken, and J. Peisach. Nuclear Quadrupole Interactions in Copper(II)-Diethylenetriamine-substituted Imidazole Complexes and in Copper(II) Proteins. *Journal of the American Chemical Society* 112 (1990) 9035.
- [5] Y. D. Tsvetkov and S. A. Dikanov. Electron Spin Echo: Applications to Biological Systems. In H. Sigel, editor, *Metal Ions in Biological Systems, ENDOR, EPR and Electron Spin Echo for Probing Coordination Spheres*, p. 207. Marcel Dekker, Inc, New York and Basel, 1987.
- [6] H. L. Flanagan and D. J. Singel. The impact of excitation frequency on the nuclear modulation of electron spin echoes: ^{14}N hyperfine and quadrupole interactions of DPPH in disordered solids. *Chemical Physics Letters* 137 (1987) 391.
- [7] H. L. Flanagan, G. J. Gerfen, A. Lai, and D. J. Singel. Orientation-selective electron spin echo envelope modulation (ESEEM): The determination of ^{14}N quadrupole tensor principal axis orientations in orientationally disordered solids. *Journal of Chemical Physics* 88 (1988) 2162.
- [8] D. Goldfarb, J. M. Fauth, O. Farver, and I. Pecht. Orientation Selective ESEEM Studies on the Blue Oxidases Laccase and Ascorbate Oxidase. *Applied Magnetic Resonance* 3 (1992) 333.
- [9] C. A. McDowell, A. Naito, D. L. Sastry, Y. U. Cui, K. Sha, and S. X. Yu. Ligand ENDOR study of Cu(II)-doped *l*-histidine deuteriochloride monodeuterate Single Crystals at 4.2K. *Journal of Molecular Structure* 195 (1989) 361.
- [10] R. Hirasawa and H. Kon. Electron Paramagnetic Resonance and Polarized Absorption Spectra of Cu(II)-Doped Single Crystal of *l*-histidine hydrochloride monohydrate. *Journal of Chemical Physics* 56 (1972) 4467.
- [11] J. Donahue, L. R. Lavine, and J. S. Rollett. The Crystal Structure of Histidine Hydrochloride Monohydrate. *Acta Crystallographica* 9 (1956) 655.
- [12] J. Donahue and A. Caron. Refinement of the Crystal Structure of Histidine Hydrochloride Monohydrate. *Acta Crystallographica* 17 (1964) 1178.

- [13] M. J. Colaneri and J. Peisach. An Electron Spin-Echo Envelope Modulation Study of Cu(II)-Doped Single Crystals of *l*-histidine hydrochloride monohydrate. *Journal of the American Chemical Society* **114** (1992) 5335.
- [14] H. L. Flanagan and D. J. Singel. Analysis of ^{14}N ESEEM patterns of randomly oriented solids. *Journal of Chemical Physics* **87** (1988) 5606.
- [15] C. Gemperle, G. Aebli, A. Schweiger, and R. Ernst. Phase Cycling in pulse EPR. *Journal of Magnetic Resonance* **88** (1990) 241.
- [16] P. Höfer, A. Grupp, H. Nebenfür, and M. Mehring. Hyperfine sublevel correlation (HYSCORE) spectroscopy: A 2D ESR Investigation of the squaric acid radical. *Journal of Chemical Physics* **132** (1986) 279.
- [17] J. J. Shane, P. Höfer, E. J. Reijerse, and E. de Boer. Hyperfine Sublevel Correlation Spectroscopy (HYSCORE) of Disordered Solids. *Journal of Magnetic Resonance* **99** (1992) 596.
- [18] C. P. Keijzers, E. J. Reijerse, P. Stam, M. F. Dumont, and M. C. M. Gribnau. MAGRES: A General Program for Electron Spin Resonance, ENDOR and ESEEM. *Journal of the Chemical Society, Faraday Transactions I* **83** (1987) 3493.
- [19] F. James and M. Roos. MINUITS. CERN-Geneva. Program no. D-506.
- [20] E. J. Reijerse, J. J. Shane, E. de Boer, and D. Collison. ESEEM of nitrogen coordinated Oxo-Vanadium(IV) complexes. In N. D. Yordanov, editor, *Electron Magnetic Resonance of Disordered systems I*, pp. 189–204. World Scientific, Singapore, 1989.
- [21] E. J. Reijerse, J. J. Shane, E. de Boer, P. Höfer, and D. Collison. One and two dimensional ESEEM of nitrogen coordinated Oxo-Vanadium(IV) complexes. In N. Yordanov, editor, *Electron Magnetic Resonance of Disordered systems II*, p. 253. World Scientific, Singapore, 1991.
- [22] R. P. J. Merks and R. de Beer. Two-dimensional Fourier transform of electron spin echo envelope modulation. An alternative for ENDOR. *Journal of Physical Chemistry* **83** (1979) 3319.

Chapter 6

ESEEM of Nitrogen-coordinated Oxo-Vanadium(IV) Complexes¹

E. J. Reijerse*, J. J. Shane*, E. de Boer* and D. Collison†

(*) Department of Molecular spectroscopy, University of Nijmegen, Toernooiveld, 6525 ED Nijmegen, The Netherlands

(†) Chemistry Department, University of Manchester, Manchester M13 9PL, England

ABSTRACT

ESEEM spectra of oxobis(2-methylquinolin-8-olato) vanadium(IV) ($\text{VO}(\text{meox})_2$), an oxovanadium complex with hydrotris(3,5-dimethyl-1-pyrazolyl) borate and dithiocarbamate ($\text{LVO}(\text{dtc})$), oxobis(acetylacetonate) 1-methyl imidazole vanadium(IV) ($\text{VO}(\text{acac})_2\text{mim}$) and oxotetra(1-methyl imidazole) chloride vanadium(IV) ($\text{VO}(\text{mim})_4\text{Cl}^+$), which act as model compounds for the enzyme bromoperoxidase (BPO), are analyzed in order to reveal the nitrogen coupling parameters (hyperfine and quadrupole). The ESEEM spectra of $\text{VO}(\text{meox})_2$, $\text{VO}(\text{mim})_4\text{Cl}^+$ and $\text{VO}(\text{acac})_2\text{mim}$ exhibit strong modulations around 4.5 and 8.5 MHz. According to field dependent studies these are assigned to so-called *double-quantum* transitions in the ^{14}N -spin manifolds of the directly coordinating nitrogens. From the frequency positions of these modulations the isotropic hyperfine interaction and the quadrupole interaction parameters of the ^{14}N -nuclei in the various types of ligands are estimated. The A_{iso} values are in the range 6.0–7.0 MHz while the quadrupole parameter K is estimated to be in the range 0.4–0.7 MHz. Using orientation selective ESEEM spectra of $\text{VO}(\text{meox})_2$ and $\text{VO}(\text{mim})_4\text{Cl}^+$ the orientation of the quadrupole tensor with respect to the molecular frame in these complexes is estimated and related to the crystal structures. The ESEEM spectra of $\text{LVO}(\text{dtc})$ deviate strongly from those of the other model complexes. The low value for the nitrogen hyperfine interaction (1.7 MHz) is discussed in terms of an electronic ground state of the complex which deviates from those of the other compounds.

6.1 Introduction

Vanadium is essential for the brominating activity of bromoperoxidases purified from several algae [1, 2]. It is suggested that the vanadium(V) of the native enzyme serves to bind hydrogen

¹This is a slightly revised version of an article that appeared in the proceedings of the conference on Electron Magnetic Resonance of Disordered Systems that was held June 1989 in Pravitz, Bulgaria. These proceedings were published by World Scientific publishers.

peroxide and bromide during the catalytic activity. In order to study the coordination of the vanadium ion in the protein, EPR and ESEEM studies on the reduced protein (vanadium(IV)) and on several model compounds have been performed [3, 4]. The ESEEM spectra indicated a coordination of the $V = O$ center to nitrogen-containing ligands and it turned out that especially a frozen solution of oxobis(2-methylquinolin-8-olato) vanadium(IV) gave ESEEM spectra similar to those of the reduced protein. In order to explain this correspondence a deeper understanding of the frozen solution ESEEM spectra of nitrogen-coordinated oxovanadium(IV) complexes is necessary. In general, ESEEM spectra of disordered systems, i.e., powders and frozen solutions, are difficult to analyze. Careful simulations are needed for a full interpretation of the spectra in terms of the hyperfine and quadrupole coupling parameters [5, 6]. In this communication we report the ESEEM spectra of oxobis(2-methylquinolin-8-olato) vanadium(IV), hereafter called 'VO (meox)₂', an oxovanadium complex with hydrotris(3,5-dimethyl-1-pyrazolyl) borate and dithiocarbamate, hereafter called 'L VO (dte)', oxobis(acetylacetonate) 1-methyl imidazole vanadium(IV), indicated as 'VO (acac)₂mim' and oxotetra(1-methyl imidazole) chloride vanadium(IV), hereafter called 'VO (mim)₄Cl⁺'. The structure of these compounds is given in figure 6.1. Using spectral simulations the spectra are interpreted in terms of the nitrogen coupling parameters.

6.2 Experimental

The compounds were prepared as described previously [4, 8]. The ESEEM spectra were recorded on a home-built ESE spectrometer [9]. In all experiments the three-pulse stimulated echo was used: $t_{90} - \tau - t_{90} - T - t_{90} - \text{echo}$. The pulse length was 20 ns, τ -values ranged from 150 ns to 600 ns. The time T was stepped up from 200 ns in steps of 20 ns. To suppress the interference due to the crossing of unwanted echoes, the following phase cycling scheme was used. $t_{90} - \tau - t_{90} - T - t_{90} - \text{echo}$, $t_{90}(\pi) - \tau - t_{90}(\pi) - T - t_{90} - \text{echo}$ [10].

6.3 ESEEM experiments

The EPR spectrum of BPO is characteristic of many oxovanadium(IV) complexes (d^1 configuration, $S = 1/2$, $I = 7/2$). It is well known that the frozen solution X-band EPR spectrum of many VO^{2+} complexes is not very sensitive to the type and coordination mode of the ligands. This is due to the essentially non-bonding character of the vanadium d_{xy} orbital in which the unpaired electron in axially symmetric complexes resides [11]. It is therefore not surprising that the EPR spectra of BPO and many model compounds are virtually indistinguishable. The g -tensor and vanadium hyperfine tensor of many compounds coincide and appear axial at X-band frequency with \mathbf{g} and \mathbf{A} tensor parameters close to those of BPO [3] ($g_{\parallel} = 1.95$, $g_{\perp} = 1.98$, $A_{\parallel} = 160 \times 10^{-4} \text{cm}^{-1}$, $A_{\perp} = 50 \times 10^{-4} \text{cm}^{-1}$). As is indicated in figure 6.2, the singularities in the EPR powder or glass spectrum of the oxovanadium(IV) compounds correspond to accumulations of intensity caused by selected sets of orientations of the magnetic field with respect to the molecular axis system. The features in the wings of the spectrum indicated as **c** and **d** correspond to orientations *parallel* to the molecular z -axis in axially symmetric systems, i.e.,

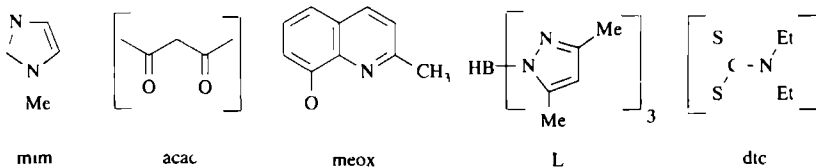
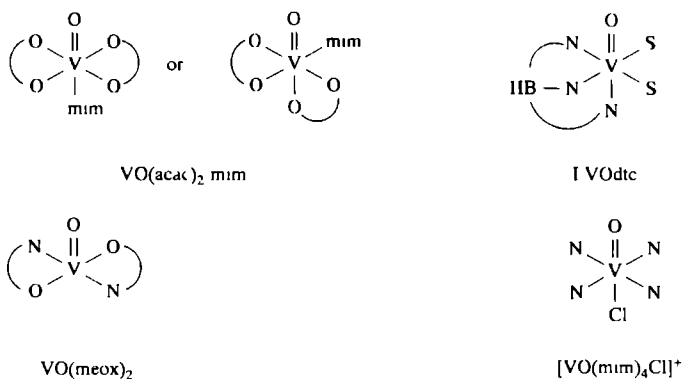
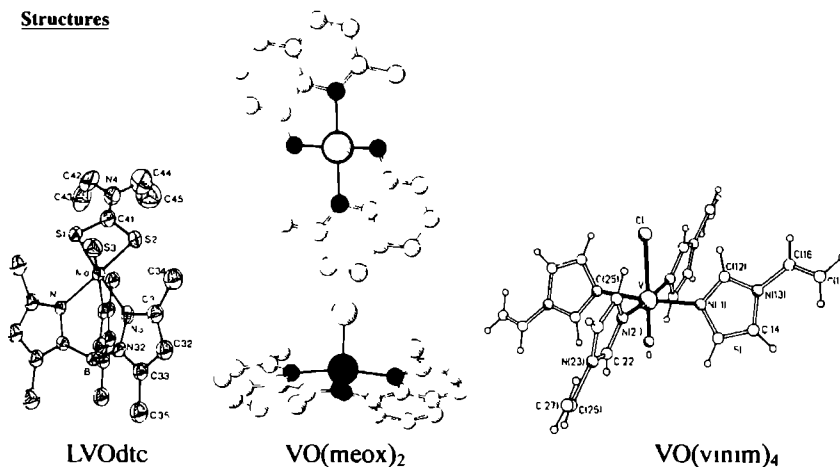
Ligands**Complexes****Structures**

Figure 6.1 Composition and structure of the complexes used in this study. The crystal structure indicated as LVO(dt c) is actually that from the isostructural host LMoS(dt c) (structure taken from [7]). The structure indicated as VO(vnim)₄Cl⁺, where the coordinating ligand 1-vinyl-imidazole replaces 1-methyl-imidazole, is used as a model for VO(mim)₄Cl⁺.

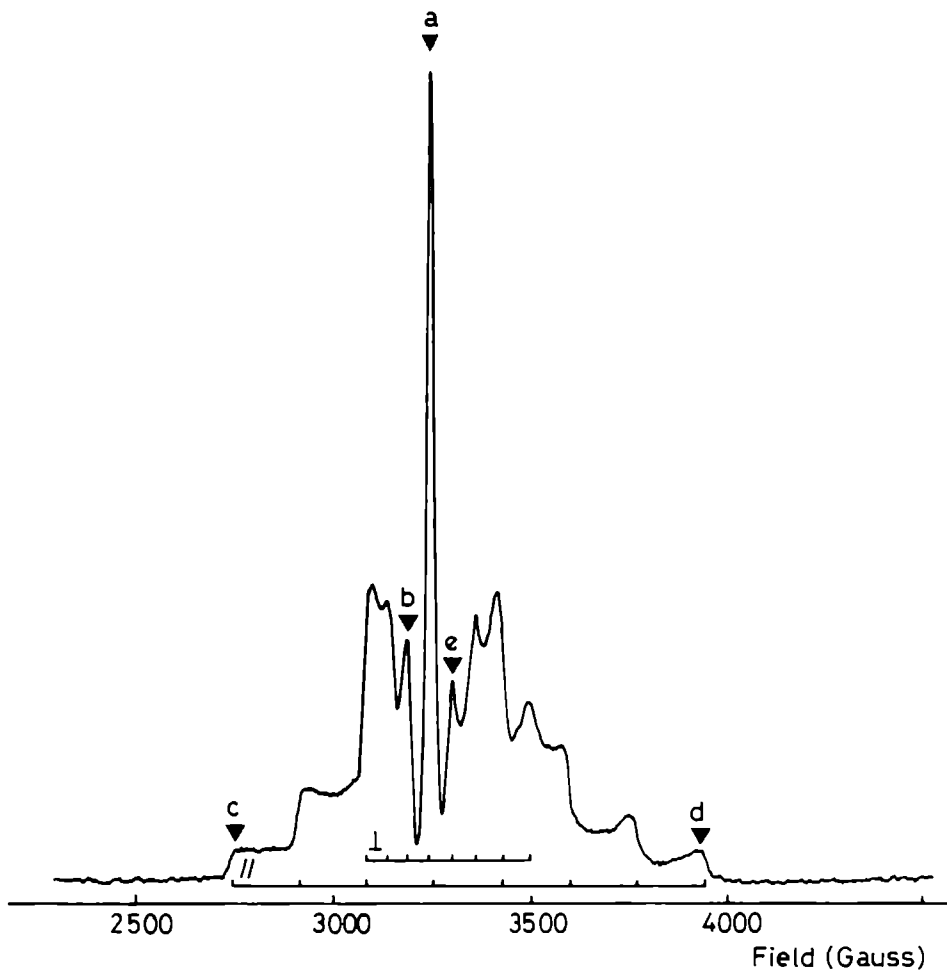


Figure 6 2. The echo-induced EPR spectrum of LVO(dtc). All compounds give an identical spectrum. The interpretation of the singularities (peaks) in the spectrum in terms of angular contributions is illustrated as discussed in the text. ESEEM spectra were recorded at the field positions indicated by a, b, c and d.

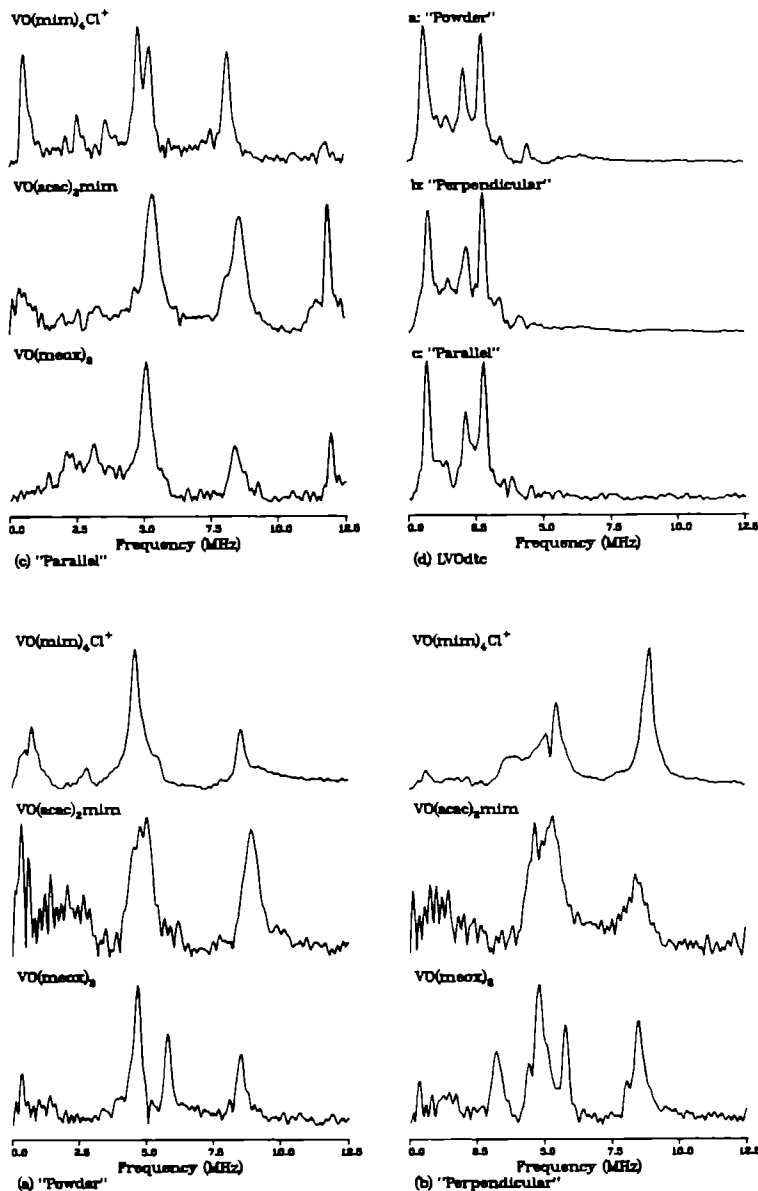


Figure 6.3: (a, b and c) Experimental FT-ESEEM spectra of $\text{VO}(\text{meox})_2$, $\text{VO}(\text{acac})_2\text{mim}$ and $\text{VO}(\text{mim})_4\text{Cl}^+$ measured at field positions a, b, and c indicated in figure 6.2. Experimental conditions: $\text{VO}(\text{meox})_2$: (a) $\tau = 580$ ns, (b) $\tau = 480$ ns, (c) $\tau = 310$ ns; $\text{VO}(\text{acac})_2\text{mim}$: (a) $\tau = 270$ ns, (b) $\tau = 290$ ns, (c) $\tau = 250$ ns; $\text{VO}(\text{mim})_4\text{Cl}^+$: (a) $\tau = 270$ ns, (b) $\tau = 260$ ns, (c) $\tau = 510$ ns. (d) Experimental FT-ESEEM spectra of $\text{LVO}(\text{dte})$. $\tau = 570$ ns.

the z -axis of the g and Vanadium hyperfine tensor ($V = O$ bonding axis) whereas the features indicated as b and c are caused by orientations *perpendicular* to the molecular z -axis. At the position indicated as a all orientations contribute. For the complex $VO(\text{meox})_2$, it is a crystallographic requirement (two-fold axis) that both g and the metal hyperfine tensor align with the $V = O$. For $VO(\text{mim})_4 Cl^+$ such an alignment is also very likely.

In figure 6.3 the ESEEM spectra for the model compounds measured at the field positions indicated in figure 6.2 are presented. For most compounds, the ESEEM spectra measured at position a , the powder position, exhibit strong peaks at approximately 4.5 and 8.5 MHz. These and all other features in the range 0–9 MHz are assigned to nitrogen modulations.

6.4 Interpretation of sharp features in powder ESEEM

There are only a few instances in which we expect to observe sharp spectral features in nitrogen powder ESEEM spectra. In one case, known as *exact cancellation*, there is a dominant isotropic hyperfine interaction which cancels the nuclear Zeeman interaction in one of the m_S manifolds ($A_{iso} = 2\nu_I$). In that manifold, the nuclear spin levels are only affected by the quadrupole interaction. Therefore, in the ESEEM spectra we expect a set of quadrupole frequencies $2K\eta$, $K(3 - \eta)$, and $K(3 + \eta)$. K and η are the well known quadrupole parameters, defined as $K \equiv e^2qQ/4 = P_z/2$ and $\eta \equiv (P_x - P_y)/P_z$ where P_x , P_y , and P_z are the principal values of the quadrupole tensor. Apart from the quadrupole frequencies, we also expect to observe a high-frequency double-quantum peak from the other m_S manifold at

$$\nu_{dq}^{\pm} = 2[(\nu_I \pm A_{iso}/2)^2 + K^2(3 + \eta^2)]^{1/2} \quad (6.1)$$

which, for small a quadrupole interaction, amounts to four times the nuclear Zeeman frequency ν_I . The double-quantum feature is observed only when the quadrupole interaction is not dominant over the hyperfine interaction.

Another instance in which sharp spectral ESEEM features are observed is when the isotropic hyperfine interaction is dominant over both the nuclear Zeeman and the quadrupole interaction. In that case the double-quantum transitions of *both* manifolds are observed. The frequency positions can be used to estimate the isotropic hyperfine interaction and the parameter $K^2(3 + \eta^2)$ using the relations

$$A_{iso} = \frac{\nu_+^2 - \nu_-^2}{8\nu_I} \quad (6.2)$$

and

$$K^2(3 + \eta^2) = \left(\frac{\nu_{\pm}}{2}\right)^2 - (\nu_I \pm \frac{1}{2}A_{iso})^2 \quad (6.3)$$

where ν_{\pm} is defined in eq. 6.1. Of course no information can be obtained about the orientation of the quadrupole tensor in the molecular axis system. To this end investigation of orientation-selective ESEEM spectra is necessary.

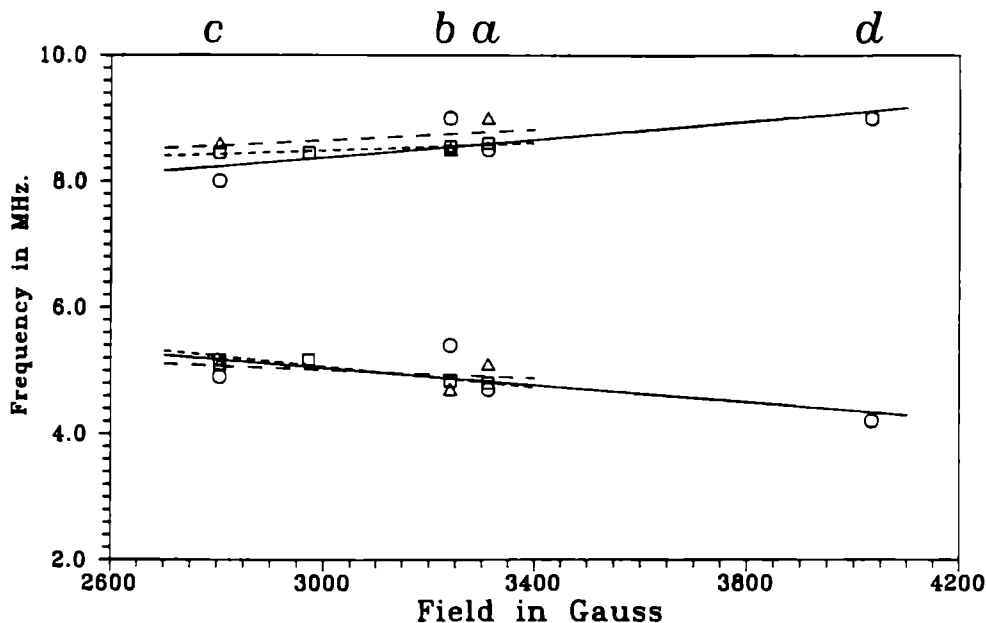


Figure 6.4 Frequencies of double quantum transitions obtained from the orientation-selective ESEEM spectra shown in figure 6.3 for $\text{VO}(\text{meox})_2$ (\square), $\text{VO}(\text{acac})_2\text{mim}$ (\triangle), and $\text{VO}(\text{mim})_4\text{Cl}^+$ (\circ)

6.5 Interpretation of powder ESEEM spectra

The strong modulations around 4.5 and 8.5 MHz present in most spectra can be assigned to the double-quantum transitions described above. Similar features were reported by Astashkin and Dikanov in an ESEEM study of $\text{VO}(\text{acac})_2(\text{L})$ compounds, with L various nitrogen-donor bases [12]. The frequency values measured at the different field positions in the EPR spectrum are plotted in figure 6.4 as a function of the magnetic field. Since the frequencies obtained from orientation-selective ESEEM spectra are linearly dependent on the external magnetic field, it is concluded that the isotropic hyperfine interaction dominates all other interactions (eq. 6.1). The values derived for the double-quantum transitions for the model compounds using 6.2 and 6.3 are listed in table 6.1. The A_{iso} values are all in the range 6.0–7.0 MHz and the $K^2(3 + \eta^2)$ parameters are all lower than 1.5 MHz^2 . According to ENDOR studies on similar complexes, the nitrogen interactions observed in the ESEEM spectra are caused by directly coordinating nitrogen donor-atoms [13, 14]. Cu^{2+} complexes with similar ligands show much higher nitrogen interactions from the directly coordinating nitrogen atoms [15]. The low hyperfine interactions found in the VO^{2+} complexes are attributed to the non-bonding character of the half-occupied ground state orbital, assigned as d_{xy} in axial complexes, where the unpaired electron density is pointing between the ligands[11]

The ESEEM spectra of the $\text{LVO}(\text{dtc})$ complex clearly deviate from those of the other complexes. The spectrum is dominated by three strong low-frequency modulations at 0.6, 2.2

field-position		a	b	c	d
or. selection		powder	perpendicular	parallel	parallel
VO(meox) ₂	A_{iso}	6.25	6.24	6.35	
	$K^2(3 + \eta^2)$	1.32	1.31	1.33	
VO(acac) ₂ mim	A_{iso}	6.75	6.24	6.62	
	$K^2(3 + \eta^2)$	0.94	1.10	1.45	
VO(mim) ₄ Cl ⁺	A_{iso}	6.32	6.77	6.35	6.40
	$K^2(3 + \eta^2)$	0.81	1.05	0.75	0.65

Table 6.1: A_{iso} and $K^2(3 + \eta^2)$ parameters (in MHz and MHz² respectively) obtained from double-quantum peaks.

and 2.8 MHz with a sum relation. Also a weak feature at 4.5 MHz is observed, which is assigned to a double-quantum transition. According to the analysis using the theory of exact cancellation, the following parameters can be derived: $K = 0.83$ MHz, $\eta = 0.36$ and $A_{iso} = 1.7$ MHz. With these parameters the double quantum transition is calculated to lie at 4.6 MHz. Since for exact cancellation the isotropic hyperfine interaction should be 2 MHz, the parameters must be regarded with some caution. Previous simulations have indicated, however, that the quadrupole parameters are usually reliable to within 10% if the deviation from exact cancellation ($\nu_I - A_{iso}/2$) does not exceed 25% [5]. The low value for the isotropic hyperfine interaction compared to that of the other model compounds is rather puzzling since according to the crystal structure [16, 7] the coordination mode and type of the ligands does not deviate strongly from the other complexes. Single crystal Q-band EPR studies of the LVO(dtc) complex doped in an LMoO(dtc) host indicate that both \mathbf{g} and the vanadium hyperfine tensor do *not* coincide with the molecular axis-system! The z -axis of the interaction tensors are not aligned along the V = O bonding axis. In fact, there is strong evidence for a *pseudo threefold axis* symmetry at the vanadium center with the threefold axis pointing between the arms of the tri-dentate ligand (L) [16]. Note that the powder or glass EPR spectrum does not give any indication of the strongly deviating electronic ground state of this complex whereas the ESEEM spectrum clearly shows a strong deviation from the standard spectrum. Since the nitrogen ligand bonds are no longer necessarily situated in the plane of the unpaired electron density, it is clear that the hyperfine interaction will be strongly reduced. We may conclude that a deviation of the unpaired electron density from the plane defined by the nitrogen-donor and vanadium atoms will have a strong influence on the nitrogen hyperfine interaction.

This means that for a d_{xy} ground-state, axially coordinated ligands are not expected to give modulations in the ESEEM spectrum. Therefore, the ESEEM spectra observed from the VO(acac)₂mim complex *may* be explained by assuming that one of the axially coordinated oxygens of VO(acac)₂mim is replaced by the methyl imidazole ligand (see figure 6.1). The same suggestion emerged from ESEEM studies of similar complexes with pyridine-like ligands [12]. In addition, there is slight non-axiality of \mathbf{g} and of the vanadium hyperfine tensor for these complexes, which is observed at Q-band frequencies [16].

6.6 Spectral simulations

We will now concentrate on the compounds $\text{VO}(\text{mim})_4\text{Cl}^+$ and $\text{VO}(\text{meox})_2$, remembering that the assignment of the $\text{V} = \text{O}$ direction as the molecular z -direction has been shown to be very probably appropriate for these two complexes. The data obtained from the double quantum modulations measured on the powder EPR peak do not give much information to distinguish between the two model complexes. The other features, and especially those observed in the orientation selective ESEEM spectra, however, clearly enable a distinction to be made, and they are characteristic of each model complex.

In order to get a deeper insight into dependence of the intensity behavior of the modulations at the various field positions on the magnitude and orientation of the quadrupole tensor and the isotropic hyperfine interaction, a series of computer simulations was carried out. The spectra were simulated using the 3-pulse modulation relations derived by Mims [17, 18] and complete diagonalisation of the spin Hamiltonian matrix [19]. Figure 6.5a shows the effect of varying the K parameter for a powder-ESEEM spectrum (position a). The isotropic hyperfine interaction was fixed at 6.3 MHz and the quadrupole asymmetry parameter η was set to zero. The double-quantum peaks emerge only for K -values larger than 0.3 MHz. The experimentally determined $K^2(3 + \eta^2)$ parameters (table 6.1) are in accordance with this. Figure 6.5b illustrates that the powder ESEEM spectra are insensitive to anisotropic contributions to the nitrogen hyperfine tensor of up to 1.2 MHz. Figure 6.5c shows the same for the asymmetry parameter: varying η from 0 to 1 while keeping $K^2(3 + \eta^2)$ constant at 1.92 MHz^2 has little effect on the spectra. The simulations in figure 6.6a are a series of orientation-selective ESEEM spectra taken at the parallel position c where the angle of the quadrupole principal axis with respect to the molecular frame (the $\text{V} = \text{O}$ axis) is varied. The other parameters are set as follows: $K = 0.71$ MHz, $\eta = 0$ or 0.6 as indicated and $A_{\text{iso}} = 6.3$ MHz. The highest resolution is, of course, obtained when the quadrupole tensor is completely aligned with the molecular axis system ($\alpha = 0^\circ$ or 90°). Since the major resonances broaden quickly when α deviates more than 20 degrees from either 0 or 90, we may conclude that pseudo single crystal spectra can only be observed for $0^\circ < \alpha < 20^\circ$ or $70^\circ < \alpha < 90^\circ$.

Because the quadrupole interaction is relatively small ($K \ll (\nu_I \pm A_{\text{iso}}/2)$), a first order approximation is valid and the pseudo single crystal spectra can be conveniently interpreted in terms of a quadrupole splitting. The nuclear spin transition frequencies in both electron-spin m_S manifolds are given by:

$$\begin{aligned}
 \text{B along x: } \nu_{1,2} &= \nu_{\text{eff}} \pm \frac{3}{2}K(\eta - 1) & \nu_{\text{dq}} &= 2\nu_{\text{eff}} \\
 \text{B along y: } \nu_{1,2} &= \nu_{\text{eff}} \pm \frac{3}{2}K(\eta + 1) & \nu_{\text{dq}} &= 2\nu_{\text{eff}} \\
 \text{B along z: } \nu_{1,2} &= \nu_{\text{eff}} \pm 3K & \nu_{\text{dq}} &= 2\nu_{\text{eff}}.
 \end{aligned} \tag{6.4}$$

This means that the quadrupole splitting for the magnetic field oriented along the x , y or z -axes is given by $3K(1 - \eta)$, $3K(1 + \eta)$ and $6K$, respectively. The peak positions obtained from the simulated spectra at $\alpha = 0^\circ$ and $\alpha = 90^\circ$ are consistent with this analysis.

The simulations in figure 6.6b are of a series of orientation-selective spectra taken at the perpendicular position b with the same set of parameters as in figure 6.6a. Obviously, the highest resolution is obtained when the quadrupole tensor is completely aligned with the molecular axis

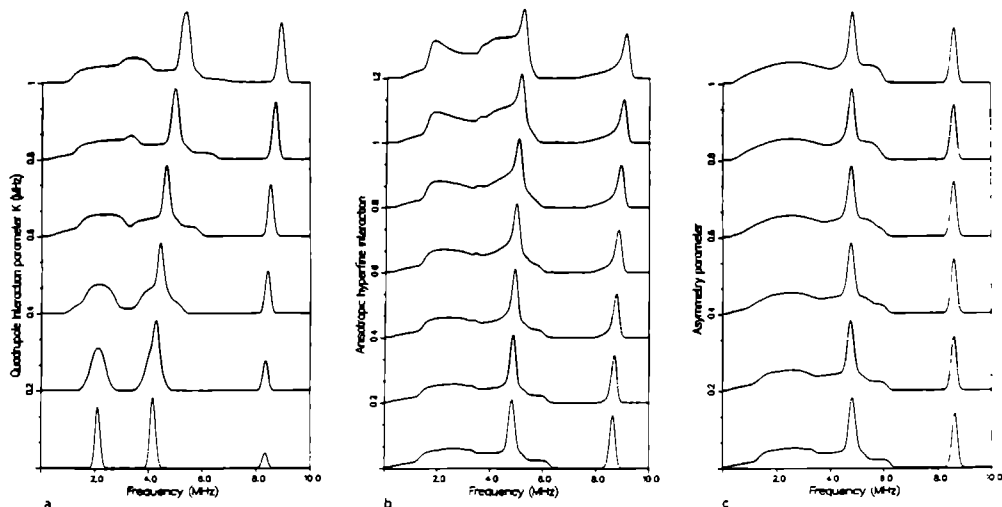


Figure 6.5: ESEEM simulations of spectra measured on the powder peak (position a): (a) as a function of the K parameter while A_{1so} is kept constant at 6.3 MHz and $\eta = 0$; (b) as a function of the anisotropic part of the hyperfine interaction, $K = 0.71$ MHz ($P_z = 1.42$ MHz), $A_{1so} = 6.3$ MHz, and $\eta = 0$; (c) as a function of the asymmetry parameter η , $K^2(3 + \eta^2) = 1.51$ MHz², $A_{1so} = 6.3$ MHz.

system ($\alpha = 0^\circ$). Towards $\alpha = 90^\circ$ the modulations broaden quickly leaving only the double-quantum peaks. It is striking that the feature on the high frequency side of the ν_{dq}^- peak at about 6 MHz is also present in many of the experimental spectra. This feature must be interpreted as the edge singularity of one of the principal transitions in the ν^+ manifold. In principle it can be used to estimate the maximum effective quadrupole splitting (in a first order approximation) in the xy -plane of the molecular axis system (see equation 6.4).

It must be born in mind, however, that the features in the experimental spectra will be distorted by the suppression effect, which is always present in 3-pulse ESEEM spectra, and by the instrumental dead-time. These effects are not (yet) included in the simulations. Therefore, one should take a substantial margin of error into account.

6.7 Interpretation of orientation-selective ESEEM spectra

The parallel spectra of the $\text{VO}(\text{mim})_4\text{Cl}^+$ complex show sharp peaks which can be interpreted as a pseudo single-crystal spectrum. With the magnetic field oriented along the $\text{V} = \text{O}$ bonding axis all four imidazole ligands are approximately equivalent and they will yield the same modulation spectrum. Careful analysis of the ESEEM spectra taken at the **c** and **d** positions with different τ values yielded all 6 transition frequencies present in each pseudo single-crystal spectrum. They can be divided into 4 quadrupole triplets: (2.8, 5.3, 8.1 MHz) and (1.2, 3.7, 4.9 MHz) for the **c** position and (0.9, 3.3, 4.2 MHz) and (3.3, 5.7, 9.0 MHz) for the **d** position. All four sets are consistent with a quadrupolar splitting of 2.5 ± 0.1 MHz. According to the averaged $K^2(3 + \eta^2)$

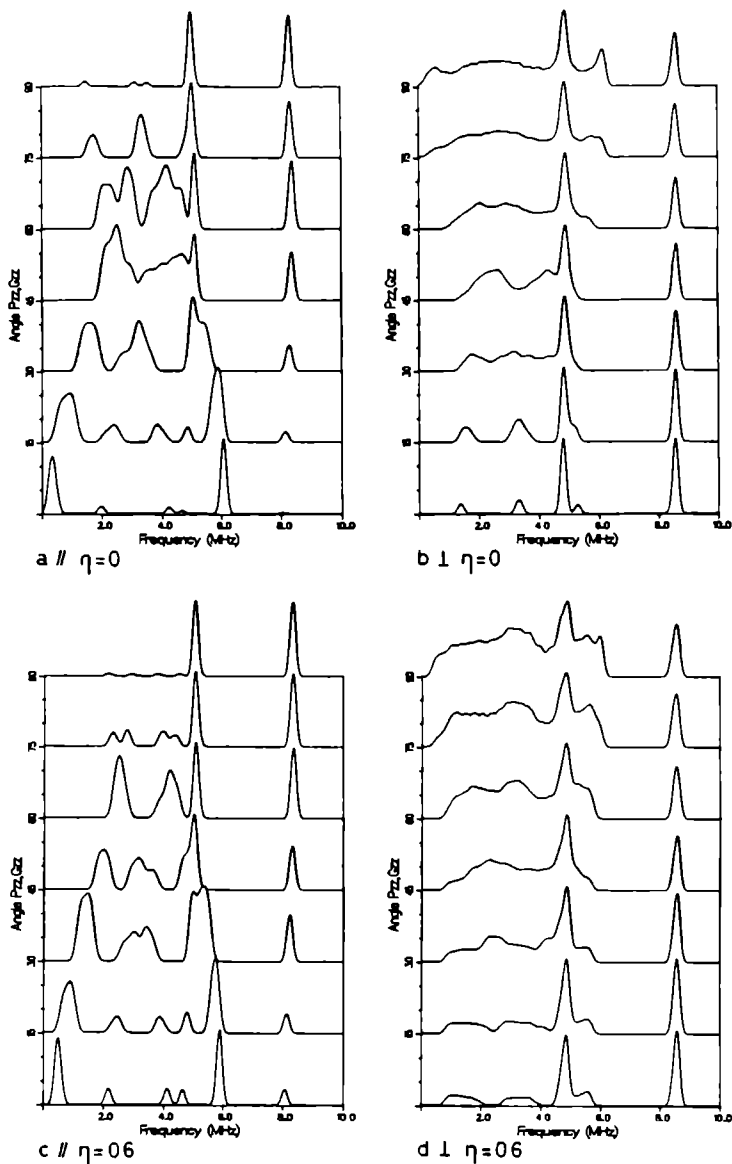


Figure 6.6 ESEEM simulations of orientation selective spectra as a function of the angle between main principal axis of the quadrupole tensor and the main principal axis of the g -tensor (in the zz -plane of the quadrupole principal axis system). The interaction parameters are $K = 0.71$ MHz, $\eta = 0$ or 0.6 , and $A_{1,5,0} = 6.3$ MHz. (a) and (c) are simulations for position c (parallel) with $\eta = 0$ and $\eta = 0.6$ respectively. (b) and (d) show simulations for position b (perpendicular) with the same parameters.

parameter of 0.7 MHz^2 (table 6.1), the maximum effective quadrupolar splitting will amount to 2.9 MHz . This suggests an alignment of the nitrogen quadrupole tensor with the molecular axis-system, i.e., the largest principal value is oriented along the $\text{V} = \text{O}$ axis.

The determination of the maximum quadrupolar splitting in the xy -plane from the ESEEM spectra measured at position **b** is not very accurate since the edge singularity seems to coincide with the ν_{dq}^- peak. We estimate an upper bound of 1.8 MHz . This confirms the impression that the quadrupole tensor is oriented along the z -axis of the molecular frame.

Using a similar procedure on the spectra of the $\text{VO}(\text{meox})_2$ compound, we find that the maximum quadrupolar splitting of $3.2 \pm 0.1 \text{ MHz}$ is observed in the xy plane. Along the z axis a value of 2.0 MHz is found. According to the estimate of the $K^2(3 + \eta^2)$ parameter of 1.3 MHz^2 , the maximum effective quadrupolar splitting for $\eta = 0$ is 3.9 MHz . These values are consistent with the assumption that the nitrogen quadrupole tensor in $\text{VO}(\text{meox})_2$ is oriented in the xy -plane of the molecular frame.

According to the crystal structures of $\text{VO}(\text{meox})_2$ [20] and $\text{VO}(\text{vinox})_4\text{Cl}^+$ [8] (figure 6.1) the planes of the two types of ligands are indeed rotated over 90° with respect to one another. This would suggest that the largest principal value of the quadrupole interaction is oriented in the plane of the ligands and perpendicular to the $\text{V} - \text{N}$ coordination axis.

6.8 Conclusions

We have demonstrated the power of ESEEM spectroscopy in the characterization of nitrogen coordinated oxo-vanadium complexes

- Any deviation from equatorial coordination and any deviation of the electronic ground state from the standard [11] will have a strong influence on the nitrogen hyperfine interaction tensor, as was concluded from the ESEEM spectra of $\text{LVO}(\text{dte})$ and $\text{VO}(\text{acac})_3\text{mim}$.
- Spectral simulations demonstrated that it is possible to obtain information about the magnitude and orientation of the nitrogen quadrupole tensor using the double-quantum features and orientation selective ESEEM spectra, provided that the relationship between the ESR tensor axes and the molecular structure is known.
- Analysis of orientation selective ESEEM spectra of the $\text{VO}(\text{meox})_2$ and $\text{VO}(\text{mim})_4\text{Cl}^+$ complexes in terms of first order quadrupole splittings suggests that the largest principal value of the quadrupole tensor for $\text{VO}(\text{meox})_2$ is found in the xy -plane, i.e., perpendicular to the $\text{V} = \text{O}$ bonding axis, while for the $\text{VO}(\text{mim})_4\text{Cl}^+$ compound it is found parallel to the $\text{V} = \text{O}$ bonding axis.

References

- [1] E. de Boer, Y. van Kooyk, M. G. M. Tromp, H. Plat, and R. Wever. Bromoperoxidases from *Ascophyllum Nodosum* – a novel class of enzymes containing Vanadium as a prosthetic group? *Biophysica Biochimica Acta* **869** (1986) 48.

6.8. CONCLUSIONS

- [2] E. de Boer, M. G. M. Tromp, H. Plat, B. E. Krenn, and R. Wever. Vanadium(V) as an essential element for haloperoxidase activity in marine brown algae: Purification and characterization of a Vanadium(V)-containing bromoperoxidase from *Laminaria Saccharina*. *Biophysica Biochimica Acta* **872** (1986) 104.
- [3] E. de Boer, K. Boon, and R. Wever. Electron Paramagnetic Resonance Studies on Conformational States and Metal Ion Exchange Properties of Vanadium Bromoperoxidase. *Biochemistry* **27** (1988) 1629.
- [4] E. de Boer *et al.* ^{14}N coordination to VO^{2+} in reduced vanadium bromoperoxidase, an electron spin echo study. *FEBS Letters* **235** (1988) 93.
- [5] E. J. Reijerse and C. P. Keijzers. Model calculations of frequency domain ESEEM spectra of disordered systems. *Journal of Magnetic Resonance* **71** (1987) 83.
- [6] E. J. Reijerse and C. P. Keijzers. ESEEM spectra of ordered and disordered systems. In C. P. Keijzers, E. J. Reijerse, and J. Schmidt, editors, *Pulsed EPR, a new field of applications*, p. 114. North Holland, Amsterdam, 1989.
- [7] C. G. Young, S. A. Roberts, R. B. Ortega, and J. H. Enemark. Mononuclear Oxo- and Sulfidomolybdenum(IV) Complexes: Synthesis and Crystal Structures of $\{\text{HB}(\text{Me}_2\text{C}_3\text{N}_2\text{H})_3\}\text{MoE}(\text{S}_2\text{CNEt}_2)$ ($\text{E}=\text{O},\text{S}$) and Related Complexes. *Journal of the American Chemical Society* **109** (1987) 2938.
- [8] L. J. Calviou *et al.* Imidazole and related heterocyclic ligand complexes of oxovanadium(IV) - potential models for the reduced vanadium site of seaweed bromoperoxidases. *Polyhedron* **8** (1989) 1835.
- [9] C. P. Keijzers, E. J. Reijerse, and J. Schmidt, editors. *Pulsed EPR, a new field of applications*, page 65, p. 65. North Holland, Amsterdam, 1989.
- [10] E. J. Reijerse. *Electron Spin Echo spectroscopy on transition metal complexes*. PhD thesis, University of Nijmegen, 1987.
- [11] N. D. Chasteen. Vanadyl(IV) EPR spin probes. Inorganic and Biochemical aspects. In L. Berliner and J. Reuben, editors, *Biological magnetic resonance*, volume 3, p. 53. Plenum Press, New York, 1981.
- [12] A. V. Astashkin and S. A. Dikanov. Coordination of Vanadyl Acetylacetonate with nitrogen-containing donor bases. *Journal of Structural Chemistry* **26** (1985) 363.
- [13] C. F. Mulks and H. van Willigen. ENDOR study of Oxovanadium(IV) Tetraphenylporphyrine Randomly Oriented in Rigid Solution. *Journal of Physical Chemistry* **85** (1981) 1220.
- [14] C. F. Mulks, V. Kirste, and H. van Willigen. ENDOR Study of VO^{2+} Imidazole Complexes in Frozen Aqueous Solution. *Journal of the American Chemical Society* **104** (1982) 5906.

- [15] W. B. Mims and J. Peisach. The Nuclear Modulation effect in Electron Spin Echoes for Complexes of Cu^{2+} and Imidazole with ^{14}N and ^{15}N . *Journal of Chemical Physics* **69** (1978) 4921.
- [16] W. E. Cleland Jr. and D. Collison. Private communication.
- [17] W. B. Mims. Envelope Modulation in Spin-Echo Experiments. *Physical Review* **5** (1972) 2409.
- [18] W. B. Mims. Amplitudes of Superhyperfine Frequencies Displayed in the Electron Spin Echo Envelope. *Physical Review* **6** (1972) 3543.
- [19] C. P. Keijzers, E. J. Reijerse, P. Stam, M. F. Dumont, and M. C. M. Gribnau. MAGRES: A General Program for Electron Spin Resonance, ENDOR and ESEEM. *Journal of the Chemical Society, Faraday Transactions I* **83** (1987) 3493.
- [20] M. Shiro and Q. Fernando. Structures of two five-coordinated metal chelates of 2-methyl-8-quinolinol. *Analytical Chemistry* **43** (1971) 1222.

Chapter 7

One- and two-dimensional ESEEM of Nitrogen-coordinated Oxo-Vanadium(IV) Complexes¹

E.J. Reijerse, J. Shane, E. de Boer, P. Hofer*, and D. Collison†

Department of Molecular spectroscopy, University of Nijmegen, Toernooiveld, 6525 ED Nijmegen, The Netherlands

(*) Bruker EPR laboratory, Bruker Analytische Messtechnik, Am Silberstreifen, 7512 Rheinstetten 4, Germany

(†) Chemistry Department, University of Manchester, Manchester M13 9PL, England

ABSTRACT

The oxo-Vanadium complexes oxobis(2-methylquinolin-8-olato) vanadium(IV) ($\text{VO}(\text{meox})_2$) and oxotetra(1-methyl imidazole) chloride vanadium(IV) ($\text{VO}(\text{mim})_4\text{Cl}^+$), which act as model compounds for the enzyme bromoperoxydase, were studied with orientation selective three-pulse ESEEM and two-dimensional four-pulse ESEEM techniques. Using orientation selective FSEEM we were able to estimate the magnitudes and orientations of the quadrupole and hyperfine interaction tensors of the nitrogen nuclei which are coordinated to the VO-unit. The two-dimensional four-pulse ESEEM (HYSCORE) experiments on these complexes are, to the best of our knowledge, the first experiments of this type applied to orientationally disordered solids. The 2D-spectra reveal that, despite the anisotropic broadening of the hyperfine lines in 1D-ESEEM, considerable spectral resolution is retained in the 2D frequency domain. As in single crystal measurements, the correlation between the hyperfine transitions from different m_S manifolds can be used to confirm the assignment of spectral features. In our study the 2D-ESEEM spectra confirm our assignment of the anisotropically broadened features and support the estimation of the interaction tensors. While for $\text{VO}(\text{meox})_2$ the largest hyperfine value is found along the $\text{V} = \text{O}$ bonding axis, for $\text{VO}(\text{mim})_4\text{Cl}^+$ the largest hyperfine value is found perpendicular to the $\text{V} = \text{O}$ axis. A similar relationship is found for the quadrupole tensors of both systems. Since the crystal structures of the studied complexes indicate that the ligand planes in $\text{VO}(\text{meox})_2$ and $\text{VO}(\text{mim})_4\text{Cl}^+$ are respectively perpendicular and parallel to the $\text{V} = \text{O}$ bonding axis we may conclude that the tensor parameters have a strong structural implication.

¹This is a slightly revised version of an article that appeared in the proceedings of the conference on Electron Magnetic Resonance of Disordered Systems that was held June 1991 in Gjulechitsa, Bulgaria. These proceedings were published by World Scientific publishers.

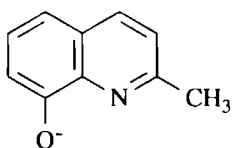
7.1 Introduction

Vanadium plays an active role in several biological processes. It is essential for the brominating activity of bromoperoxidases (BPO) purified from several marine algae [1, 2]. It is suggested that the vanadium(V) of the native enzyme serves to bind hydrogen peroxide and bromide during the catalytic activity. EPR techniques may be used to probe the environment of the oxo-Vanadium unit present in the reduced form of these enzymes. Since EPR is relatively insensitive to the coordination structure of the VO^{2+} -unit, ESEEM is used to study the hyperfine and quadrupole interactions from nitrogen containing ligands. Previous studies of BPO and model complexes suggested an equatorial coordination of one or more nitrogen containing ligands to the VO^{2+} -unit [3, 4]. In particular, the ESEEM spectra of oxobis(2-methylquinolin-8-olato) vanadium(IV) show a strong correlation with those of BPO. In order to explain this correspondence a deeper understanding of the frozen solution ESEEM spectra of nitrogen coordinated oxovanadium(IV) complexes is necessary.

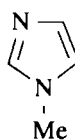
In general ESEEM spectra of disordered systems (powders and frozen solutions) are difficult to analyze. On the one hand, anisotropic interactions (hyperfine and quadrupole) lead to deep modulations effects, while on the other hand the spectral features are broadened and deformed by the anisotropic behavior of the modulation intensity. Therefore, the spectral features no longer assume their familiar powder lineshape reflecting the angular probability distribution but are instead a complicated function of both angular distribution and anisotropic modulation intensity. The situation can be further complicated by serious overlap of broad lines. Usually, careful simulations are needed for a full interpretation of the spectra in terms of the hyperfine and quadrupole coupling parameters [5, 6].

With nitrogen coordinated oxovanadium(IV) complexes we are in the fortunate situation that the anisotropy of the hyperfine interaction is relatively small. This leads to sharp dominant double-quantum transitions caused by the quadrupole interaction. This effect enabled us, in previous studies, to estimate the isotropic hyperfine interaction and the quadrupole parameter. In addition, orientation selective ESEEM experiments enabled us to obtain a rough indication of the orientation of the quadrupole tensor relative to the molecular frame [7]. Although the anisotropic broadening of the double-quantum transitions was quite apparent, we were not able to extract accurate information about the components of the anisotropic hyperfine tensor.

In this communication we concentrate our attention to the complexes oxobis(2-methylquinolin-8-olato) vanadium(IV), referred to as $\text{VO}(\text{meox})_2$, and oxotetra(1-methylimidazole) chloride vanadium(IV), labeled $\text{VO}(\text{mim})_4\text{Cl}^-$. We present a careful analysis of the double-quantum transitions at several field positions in the EPR spectrum. These frequency tracking experiments enable us to obtain an accurate estimate of the anisotropic hyperfine tensor components in the molecular axis system. The study of the single-quantum transitions in the orientation selective ESEEM spectra lead to a reliable estimate of the quadrupole parameters. Furthermore, we demonstrate the power of 2D-ESEEM spectroscopy in disentangling the overlapping single-quantum features broadened by the quadrupole interaction.



meox



mim

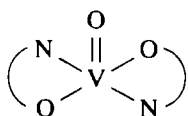
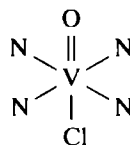
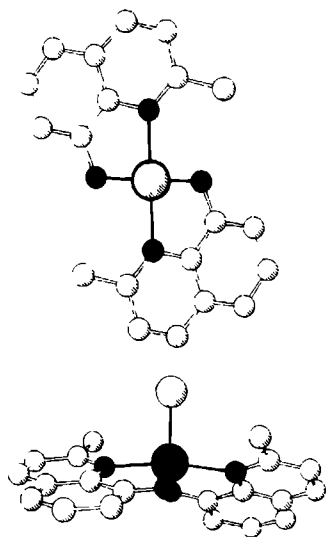
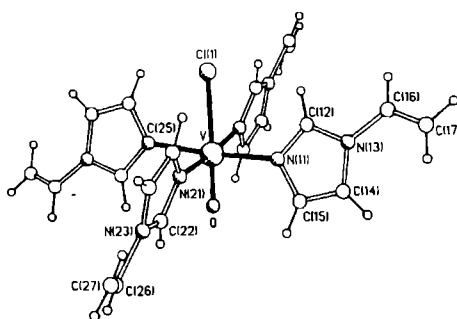
 $\text{VO}(\text{meox})_2$  $[\text{VO}(\text{mim})_4\text{Cl}]^+$  $\text{VO}(\text{meox})_2$  $\text{VO}(\text{vinim})_4\text{Cl}$

Figure 7 1: Composition and structure of the complexes used in this study. The structure indicated as $\text{VO}(\text{vinim})_4\text{Cl}^+$, where the coordinating ligand 1-vinyl-imidazole replaces 1-methyl-imidazole, is used as a model for $\text{VO}(\text{mim})_4\text{Cl}^+$.

7.2 Experimental

The compounds were prepared as described previously [4, 8]. The ESEEM spectra were recorded on a home-built ESE spectrometer [9]. In all three pulse ESEEM experiments the pulse length was fixed at 20 ns; τ -values ranged from 150 ns to 600 ns. The waiting time t between the second and third microwave pulses was stepped upward from 200 ns in steps of 20 ns. To suppress interference due to the crossing of unwanted echoes, the following phase cycling scheme was used:

$$t_{90} - \tau - t_{90} - T - t_{90} - \text{echo}, \quad t_{90}(\pi) - \tau - t_{90}(\pi) - T - t_{90} - \text{echo} \quad [10].$$

The 2D-ESEEM experiments were performed on a Bruker ESP380 FT-EPR spectrometer located at the Bruker EPR laboratory. In the 4-pulse (HYSCORE) experiments a combination of relatively soft $\pi/2$ -pulses (64 ns) and a hard π pulse was used to suppress the admixture of the 3-pulse stimulated echo from pulses 1, 2 and 4 into the 4-pulse stimulated echo. A 4-phase cycling scheme was used as proposed by Gemperle *et al.*[11].

7.3 EPR and orientation selective ESEEM of nitrogen coordinated oxovanadium(IV)-complexes

In figure 7.1 the composition and structure of the complexes that were studied is shown. The general features of EPR spectra of oxovanadium(IV) complexes ($S=1/2$, $I=7/2$) have been described extensively in the literature [12]. The g -tensor and the vanadium hyperfine tensor of many compounds coincide and appear axial at X-band frequencies with \mathbf{g} and \mathbf{A} tensor parameters close to ($g_{\parallel} = 1.95$, $g_{\perp} = 1.98$, $A_{\parallel} = 160 \times 10^{-4} \text{cm}^{-1}$ and $A_{\perp} = 50 \times 10^{-4} \text{cm}^{-1}$). As is indicated on the echo induced EPR spectra displayed in figures 7.3a and 7.4a, the singularities in the EPR powder or glass spectrum of the oxovanadium(IV) compounds correspond to accumulations of intensity caused by selected sets of orientations of the magnetic field with respect to the molecular axis system. For the complex $\text{VO}(\text{meox})_2$ it is a crystallographic requirement (two-fold axis) that the (virtually axial) g and metal hyperfine tensors are aligned with the $\text{V} = \text{O}$ direction; for $\text{VO}(\text{mim})_4\text{Cl}^+$ such an alignment is also very likely. In figure 7.2 a schematic representation of the ESEEM spectra of nitrogen coordinated VO-complexes based on the knowledge from previous studies [7] is presented. Due to the mainly isotropic hyperfine interaction, the ESEEM spectra are governed by strong double-quantum features (indicated by $\nu_{\alpha}^{(3)}$ and $\nu_{\beta}^{(3)}$). The quadrupole interaction, which is the main source of anisotropy in these spin systems, affects the double-quantum transitions only to second order. Therefore, these features remain relatively sharp. The single-quantum transitions, however, are affected to first order by the quadrupole interaction and will therefore be strongly broadened in powder ESEEM spectra. Only the edge singularity of the $\nu_{\alpha}^{(1)}$ feature may appear on the high frequency side of the $\nu_{\beta}^{(3)}$ double quantum line. In figures 7.3a and 7.4a the frequency positions of the most pronounced features in the three-pulse ESEEM spectra are plotted against the field position in the echo induced EPR spectrum displayed on top of the figures. Some selected experimental FT-ESEEM spectra are shown in figures 7.3b and 7.4b. In all spectra the double-quantum transitions are clearly visible. By comparing ESEEM spectra recorded at one field position but with different values for τ with

7.3. EPR AND ORIENTATION SELECTIVE ESEEM

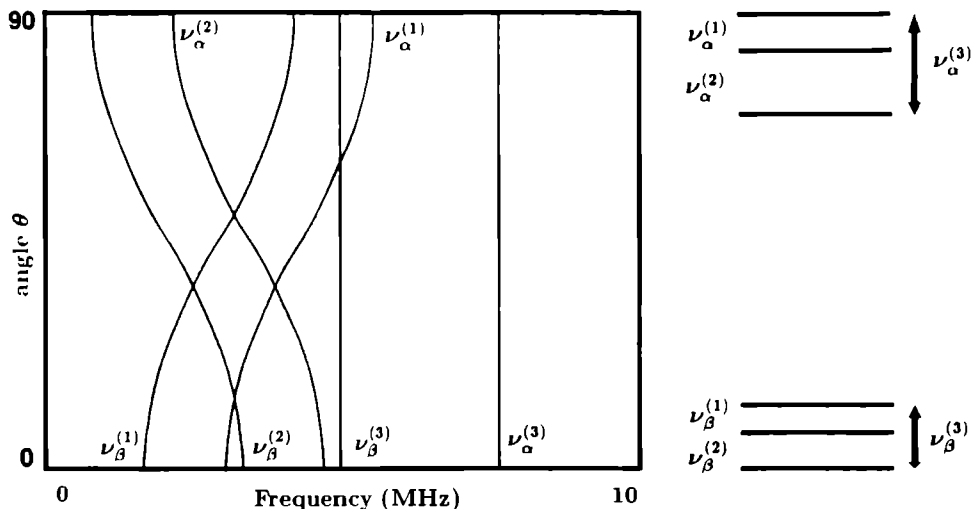


Figure 7.2 Schematic representation of the angle-dependent ESEEM spectra of nitrogen coordinated oxovanadium(IV) complexes assuming an isotropic hyperfine interaction and an axial quadrupole tensor. The angle θ represents the orientation of the magnetic field in the axis system of the quadrupole tensor.

one another, the anisotropic broadening of the double-quantum lines can be probed (see figure 7.3b, the first two spectra). Astashkin *et al.* [13] demonstrated that, assuming a strictly isotropic hyperfine interaction and no orientation selection, the double quantum features can be used to estimate the isotropic hyperfine coupling and the quadrupole interaction. In these studies the following expression for the position of the double-quantum lines was used:

$$\nu_{dq}^{\pm} = 2[(\nu_{eff}^{\pm})^2 + K^2(3 + \eta^2)]^{\frac{1}{2}} \quad (7.1)$$

where

$$\nu_{eff}^{\pm} = (\nu_I \pm A_{iso}/2)^2 \quad (7.2)$$

leading to

$$A_{iso} = \frac{\nu_+^2 - \nu_-^2}{8\nu_I} \quad (7.3)$$

and

$$K^2(3 + \eta^2) = \left(\frac{\nu_{\pm}}{2}\right)^2 - \left(\nu_I \pm \frac{1}{2}A_{iso}\right)^2. \quad (7.4)$$

Obviously, one should be cautious in applying these procedures to our orientation selective ESEEM spectra with clearly apparent anisotropy of the hyperfine interaction. However, spectral simulations indicated that in case K is of the same order of magnitude as the anisotropic part of the hyperfine interaction and both are much smaller than the isotropic part of the hyperfine interaction, (as is the case for our spectra) these relations provide very good starting values for the effective hyperfine interaction and the $K^2(3 + \eta^2)$ parameter. Furthermore, since $K \ll \nu_{eff}$ the positions of the double-quantum transitions are almost linearly dependent on the magnetic field. For this

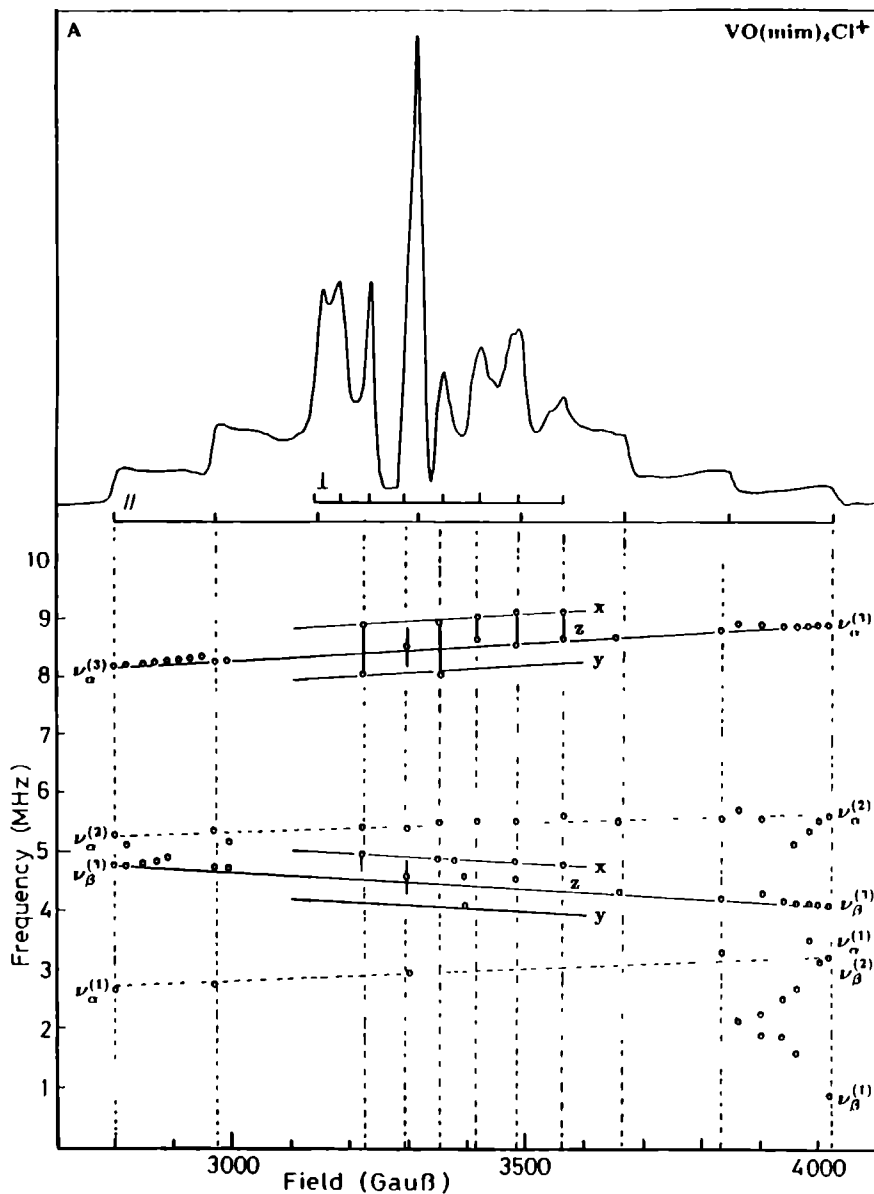
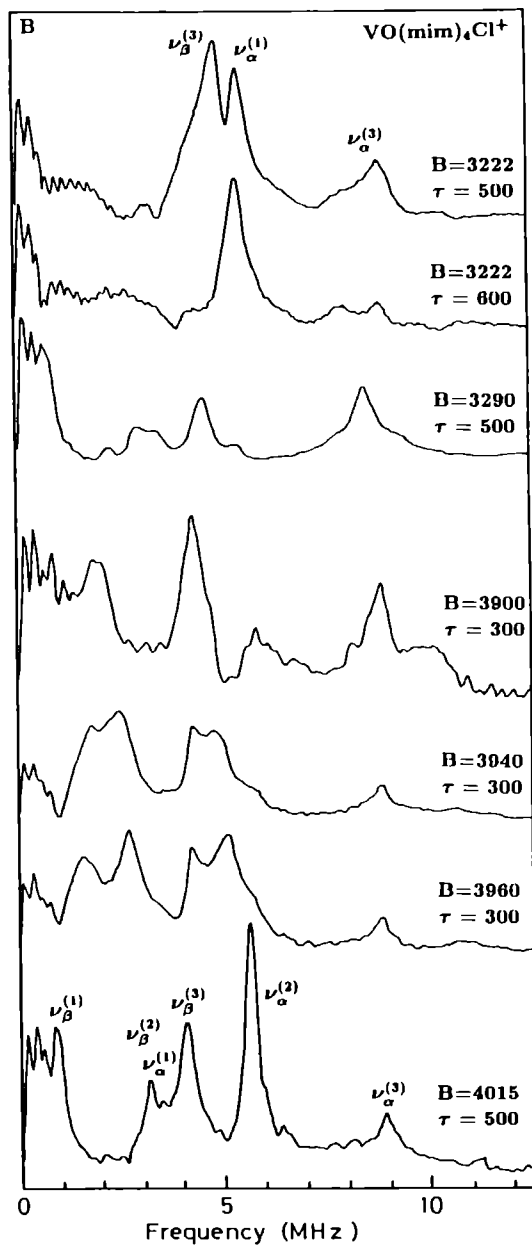


Figure 73 a) Frequency positions of spectral features observed in orientation selective ESEEM spectra of $\text{VO}(\text{mim})_4\text{Cl}^+$ as a function of the field position in the echo-induced EPR spectrum (displayed on top). Spectral features measured at identical orientation selection positions (\parallel or \perp) are connected by straight lines, the vertical lines indicate the linewidths of the double quantum features. The frequency labels refer only to the parallel positions. b) Selected ESEEM spectra from $\text{VO}(\text{mim})_4\text{Cl}^+$



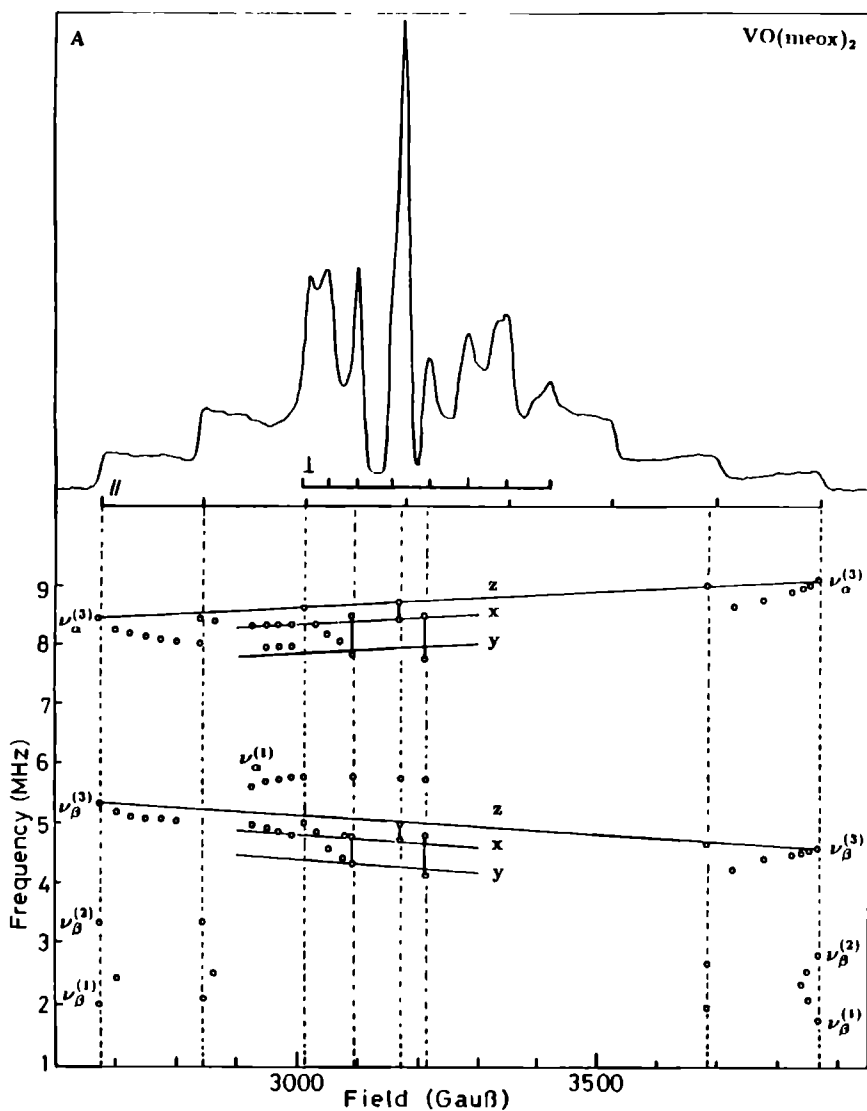
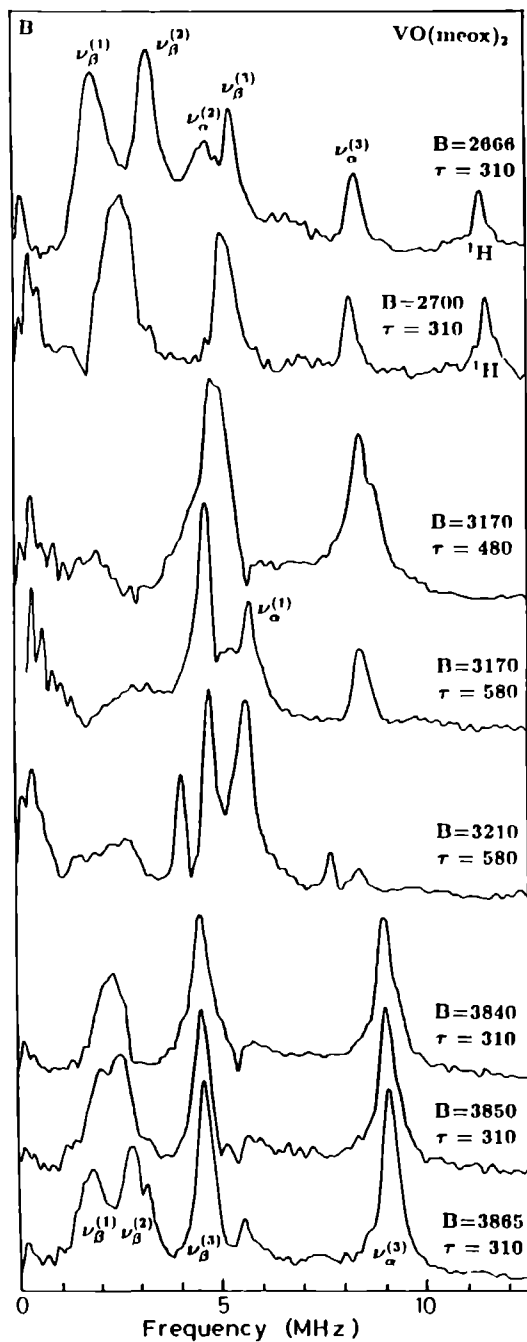


Figure 7.4: *a*) Frequency positions of spectral features observed in orientation selective ESEEM spectra of $\text{VO}(\text{meox})_2$ as a function of the field position in the echo-induced EPR spectrum (displayed on top). The same comments as in figure 7.3a apply. *b*) Selected ESEEM spectra from $\text{VO}(\text{meox})_2$.



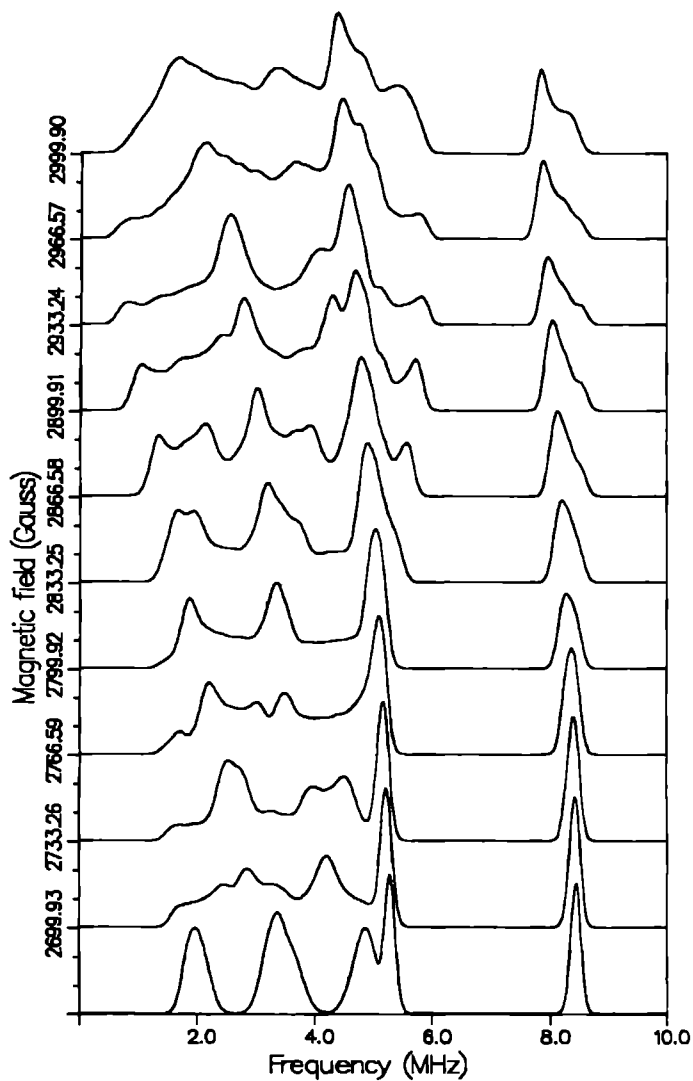


Figure 7.5: Simulation of suppressionless orientation-selective ESEEM spectra of $\text{VO}(\text{mcox})_2$ using the interaction parameters in table 7.1.

7.3. EPR AND ORIENTATION SELECTIVE ESEEM

1 st order	VO(mim) ₄ Cl ⁺		VO(meox) ₂		simulation	VO(meox) ₂
A_{xx}	-0.51	-6.94	-0.07	-6.1	A_x	-0.23
A_{yy}	+0.43	-6.00	+0.44	-5.6	A_y	+0.56
A_{zz}	+0.08	-6.35	-0.37	-6.4	A_z	-0.33
A_{iso}	-6.43		-6.03		A_{iso}	-6.27
					α	20°
Interp.	(a)	(b)	(a)	(b)	β	0°
P_{xx}	-0.7	0.1	-1.1	0.6	P_x	0.46
P_{yy}	-0.1	-0.9	0.5	-1.2	P_y	-1.20
P_{zz}	0.8	0.8	0.6	0.6	P_z	0.74
K	0.4	0.45	0.55	0.6	α	20°
η	0.75	-0.77	0.10	0.0	β	30°

Table 7.1: Hyperfine and quadrupole tensor components (MHz) derived from first order analysis and used in simulations. The meaning of α , β , (a) and (b) is described in the text.

reason we believe it justified to plot the frequency positions of all spectral features as a function of the magnetic field and correlate the features corresponding to the same orientation selection in a linear way. The two extreme frequency positions of the double quantum lines measured at the perpendicular selection fields were plotted separately. As can be judged from figures 7.3a and 7.4a, the $\nu_\alpha^{(3)}$ and $\nu_\beta^{(3)}$ features measured at the parallel position (also in overlapping regions) can be correlated quite satisfactorily with a straight line. Also the extreme positions of the double quantum features measured at the perpendicular positions could be correlated nicely with a linear dependence on the magnetic field. The effective hyperfine values, calculated according to eq. 7.3 (A_{zz} for the \parallel position, A_{xx} and A_{yy} for the \perp positions) are listed in table 7.1. The coordinate system used in table 7.1 is chosen such that the z -axis corresponds to the $V = O$ bond and the the y -axis coincides with the $V - N$ bond to the ligand. Furthermore, we define the angle α as a rotation of the \mathbf{A} or \mathbf{P} tensor of nitrogen around the x -axis; subsequently, we define an additional rotation over angle β around the new y -axis. The smallest hyperfine value in the xy -plane is assigned as the A_{yy} component.

For the estimation of the quadrupole parameters we will use a first order treatment of the pseudo single crystal information obtained from the ESEEM spectra measured at the parallel and perpendicular positions. In general we cannot expect that the quadrupole principle axes will coincide with the molecular frame of the $V = O$ unit. The first order quadrupole splitting is therefore given by:

$$\nu_{\alpha,\beta}^{(1,2)} = \nu_{eff}^{\alpha,\beta} \pm \frac{3}{2} (l_x^2 Q_x + l_y^2 Q_y + l_z^2 Q_z) \quad (7.5)$$

where l represents the selected orientation (e.g. the $V = O$ direction) in the quadrupole principal axis system. Measuring the quadrupole splitting at the parallel and perpendicular position would enable us to estimate the diagonal elements of the quadrupole tensor in the molecular axis frame. In fact, because \mathbf{P} is a traceless tensor, it is sufficient to determine the effective quadrupole splittings in only two of the three directions of the molecular frame. We will have to make use of this property because the ESEEM spectra measured at the perpendicular positions permit the

determination of only one quadrupole splitting. In these spectra the $\nu_{\alpha}^{(1)}$ edge singularity is the only single-quantum feature which survives the anisotropic broadening and dead-time artifacts. Together with the double quantum feature $\nu_{\alpha}^{(3)} = 2\nu_{eff}$, this feature can be used to estimate the maximum effective quadrupole splitting in the molecular xy -plane. Of course, an additional complication arises because of the anisotropic broadening of the $\nu_{\alpha}^{(3)}$ double quantum feature due to the anisotropic hyperfine interaction. It is not clear with which position in the $\nu_{\alpha}^{(3)}$ line the $\nu_{\alpha}^{(1)}$ edge singularity should be associated. As a starting point we assume that the **A** and **P** tensors have common principle axes in the xy -plane, and therefore the $\nu_{\alpha}^{(1)}$ positions will be associated either with the high or low frequency edge of the $\nu_{\alpha}^{(3)}$ double-quantum line. In table 7.1 we list the calculated effective quadrupole splittings based on both choices. Choice (a) associated $\nu_{\alpha}^{(1)}$ with the high-frequency edge of $\nu_{\alpha}^{(3)}$ (x -axis) whereas choice (b) associated it with the low-frequency edge (y -axis).

Since we are also interested in the orientations of the **P** tensor relative to the molecular frame, we studied the behavior of the $\nu_{\beta}^{(1)}$ and $\nu_{\beta}^{(2)}$ lines in the ESEEM spectra measured near the parallel orientation selective field positions. Unfortunately, the orientation-selective method often successfully used in ENDOR [14] cannot be used in ESEEM spectroscopy since the so-called turning points of the hyperfine lineshapes usually do not give rise to singularities. Due to the τ -suppression effect, the anisotropic modulation intensity and dead-time effects, the ESEEM lineshapes are strongly deformed. Therefore, the orientation-selective method can be used only in a very limited field range close to the pseudo single-crystal positions. We expect the splitting between the $\nu_{\beta}^{(1)}$ and $\nu_{\beta}^{(2)}$ lines and the overall resolution of the ESEEM spectrum to be reduced when the field is scanned away from the parallel position. This collapse of the quadrupole splitting is a measure of the alignment and the anisotropy of the **P** tensor near the parallel orientation.

As can be judged from figures 7.3 and 7.4, the effective quadrupole splitting in the spectra of $\text{VO}(\text{meox})_2$ is much more sensitive to deviations from the parallel position than that of $\text{VO}(\text{mim})_4\text{Cl}^+$. This indicates that the quadrupole tensor of $\text{VO}(\text{meox})_2$ will probably be rotated away significantly from the molecular frame. In order to estimate this deviation we performed a series of spectral simulations of orientation selective ESEEM spectra allowing the **P** and **A** tensor to be rotated away from the molecular axis system. In figure 7.5 a series of simulations is presented which reproduces some of the most pronounced experimental features of the $\text{VO}(\text{meox})_2$ spectra. In particular the rapid collapse of the quadrupole splitting between $\nu_{\beta}^{(1)}$ and $\nu_{\beta}^{(2)}$ is reproduced quite well. It must be noted that for simplicity the τ -suppression and dead-time effects were not included in the simulations. Therefore the absolute intensities of the spectral features may deviate from the experimental ones. Moreover, due to the large number of unknown parameters, the parameter set used will probably not be unique. However, it gives some estimate of the substantial deviation (20-30 degrees) of the **A** and **P** principle directions of the coordinating nitrogens from the molecular frame in $\text{VO}(\text{meox})_2$.

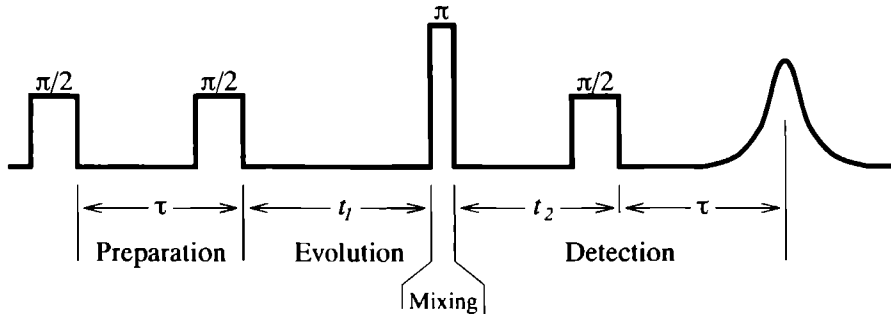


Figure 7.6: Basic pulse sequence of the 4-pulse echo experiment.

7.4 2D-ESEEM experiments

Figure 7.7 shows four-pulse 2D-ESEEM (HYSCORE) spectra measured at the parallel, perpendicular and powder positions of the EPR spectrum of $\text{VO}(\text{mim})_4\text{Cl}^+$. The basic pulse sequence of the HYSCORE experiment is shown in figure 7.6. The echo signal can be regarded as a four-pulse stimulated echo [15]. For every spectrum the echo is recorded in a two-dimensional time domain as a function of both waiting times t_1 and t_2 . Since during both of these waiting times the relevant electron spin coherence is stored along the magnetic z -axis, the main cause of echo decay will be the spin-lattice relaxation time. Therefore, as compared to the three-pulse 2D-ESEEM experiment, where during waiting time τ spin-spin relaxation is active, the spectral resolution in the second dimension (t_1 for the HYSCORE experiment) is substantially improved. However, in order to avoid interference of unwanted echoes with the stimulated four-pulse echo, extensive phase-cycling is necessary [11]. Also, the 2D-FT pattern will be dependent on the fixed waiting time τ , which may induce so-called *blind spots* in the modulation pattern. The general expression for the echo envelope of the four-pulse stimulated echo is

$$E(\tau, t_1, t_2) = R_2(\tau)R_1(t_1 + t_2)\text{Mod}(\tau, t_1, t_2), \quad (7.6)$$

where $R_{1,2}$ are the relaxation decays caused by T_1 and T_2 relaxation. $\text{Mod}(\tau, t_1, t_2)$ is the modulated part of the echo:

$$\begin{aligned} \text{Mod}(\tau, t_1, t_2) = & \sum_{ijklmn} M_{il}M_{lj}^\dagger M_{jm}M_{mk}^\dagger M_{kn}M_{nz}^\dagger e^{-\omega_{ij}\tau} e^{-\omega_{ik}t_2} e^{-\omega_{in}\tau} e^{-\omega_{lm}t_1} \\ & + \sum_{ijklmn} M_{il}M_{lj}^\dagger M_{jm}M_{mk}^\dagger M_{kn}M_{nz}^\dagger e^{-\omega_{ik}\tau} e^{-\omega_{jk}t_1} e^{-\omega_{ln}t_2} e^{-\omega_{mn}\tau} \\ & + c.c., \end{aligned} \quad (7.7)$$

where M represents the matrix of EPR transition probabilities between the nuclear spin levels in the α manifold (ijk) and the β manifold (lmn). The experimental details and the derivation of eq. 7.7 will be published elsewhere². It is important to note, however, that the 2D-HYSCORE spectra can be interpreted without knowledge of the mechanisms behind the experiment. Exactly

²This thesis, chapters 2 and 3

as in three-pulse 2D-ESEEM, the nuclear spin transitions in the two m_S manifolds are related to each other by crosspeaks in the 2D-frequency domain. In case of powder spectra, the correlation peaks may become ridge-like. Indeed, the experimental HYSORE spectra of $\text{VO}(\text{mim})_4\text{Cl}^+$ show a rich pattern of ridges, thus enabling a disentanglement of the strongly overlapping single-quantum transitions from one another and from the double quantum transitions. When the real 2D-time domain is transformed using a complex Fourier transformation, the correlation features are distributed over two frequency quadrants (figure 7.7). The exact nature of this effect is still under investigation but the net result is a further disentanglement of the correlation features.

The HYSORE spectra of $\text{VO}(\text{mim})_4\text{Cl}^+$ can be interpreted readily in terms of the single-quantum and double-quantum transitions. In particular the parallel HYSORE spectrum shows a beautiful correlation between the α and β nuclear spin transitions. Furthermore, the nature of the $\nu_\alpha^{(1)}$ edge singularity is confirmed by the correlation ridge in figure 7.7. The labeling of the 2D features in figure 7.7 is consistent with that of figures 7.2, 7.3 and 7.4. The reader can verify that indeed correlation features occur only between nuclear spin transitions from different manifolds.

7.5 Discussion

Taking into account the large isotropic part of the hyperfine interaction the mechanism of the hyperfine interaction is clearly dominated by spin polarization since the basic d_{xy} ground state has no direct spin density on the ligands. The fact, however, that the smallest hyperfine value for both complexes is found in the xy -plane suggests that a substantial dipolar contribution could still be present. The dominating negative isotropic hyperfine contribution is counteracted by the positive dipolar part along the bonding axis (which is the y -axis in our coordinate system). However, because of the large error margin, a reliable estimation of the dipolar contribution is impossible. Another remark that can be made is the fact that for $\text{VO}(\text{meox})_2$ the largest hyperfine component is found along the z -axis, while for $\text{VO}(\text{mim})_4\text{Cl}^+$ it is found in the xy -plane. This may be indicative of the way in which, according to the crystal structure, the nitrogen p -functions of the two ligands may be mixed into the ground state. In the case of $\text{VO}(\text{mim})_4\text{Cl}^+$, the π -type nitrogen functions are in the most favorable position to overlap with the d_{xy} vanadium orbitals, whereas in the case of $\text{VO}(\text{meox})_2$ the sp^2 -type nitrogen functions will have this priority.

Also, the significant rotation of the A and P tensors of the nitrogens of $\text{VO}(\text{meox})_2$ can be related to the crystal structure. The O – V – N bond angle is about 100° , whereas in the case of $\text{VO}(\text{mim})_4\text{Cl}^+$ virtually no deviation from 90° was found.

7.6 Concluding remarks

Although the derived tensor values are still approximate in nature, we may conclude that one-dimensional orientation selective ESEEM is a useful tool to obtain information about the magnitude and relative orientation of the hyperfine and quadrupole tensors of the directly coordinating nitrogens in $\text{VO}(\text{meox})_2$ and $\text{VO}(\text{mim})_4\text{Cl}^+$. The tensor parameters reflect the coordination mode as determined by the crystal structures. Especially the coordination angle of $\text{VO}(\text{meox})_2$

2D HYSORE, VO(mim)4-Cl, parallel position

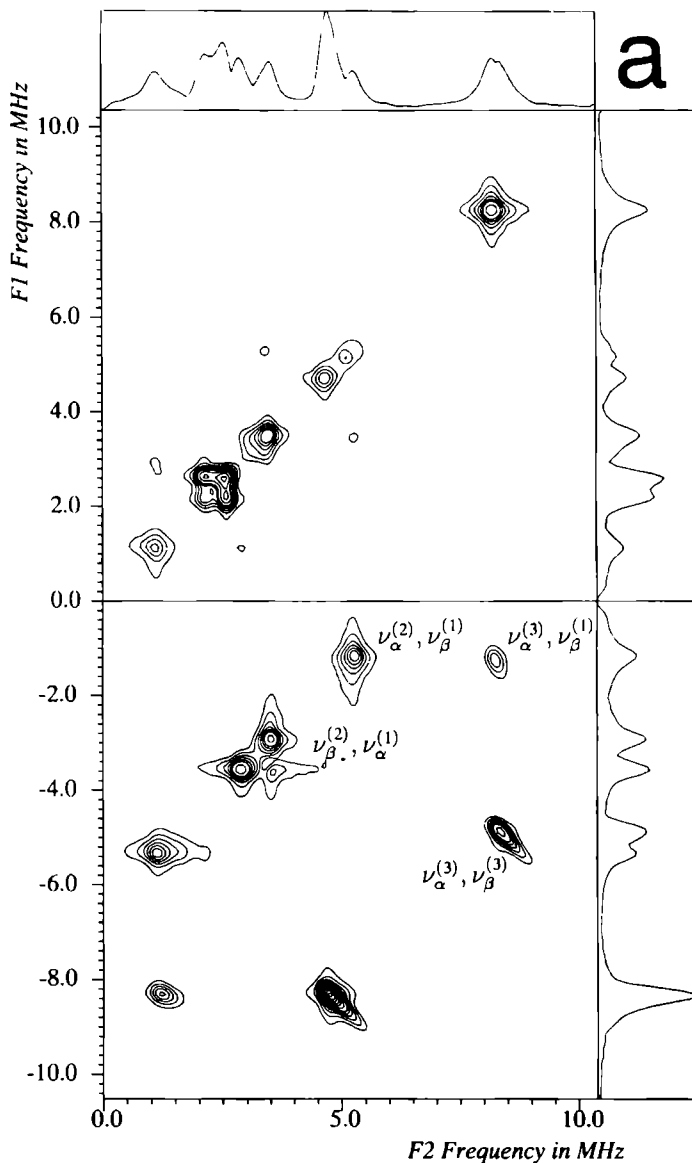
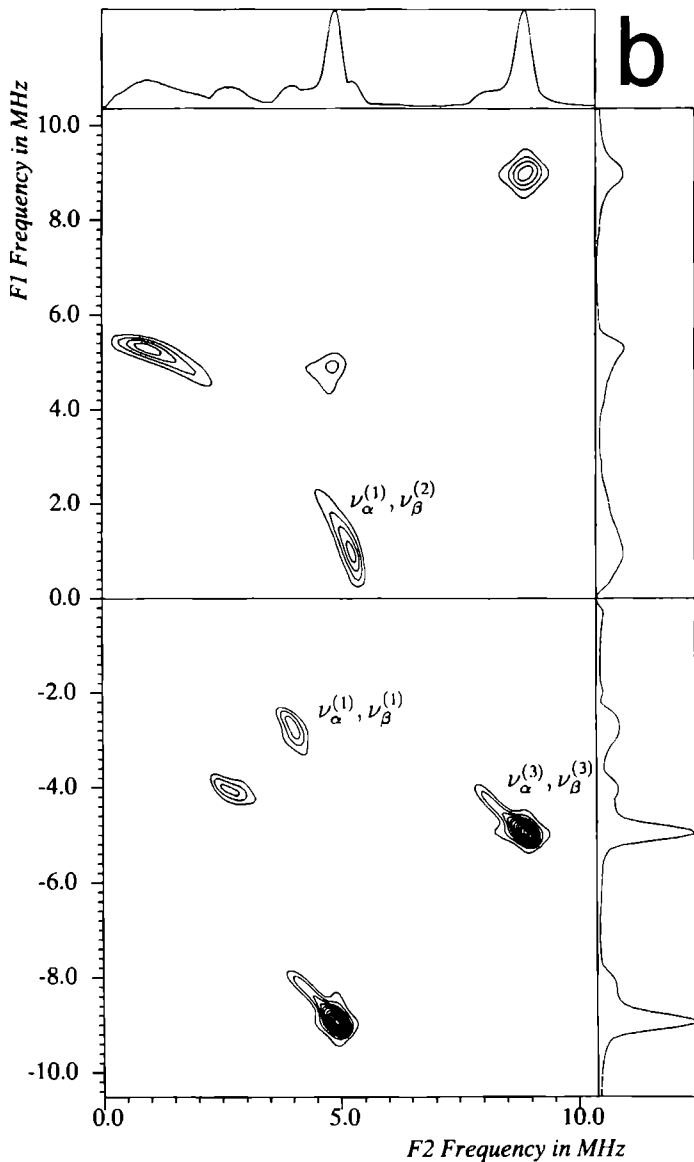
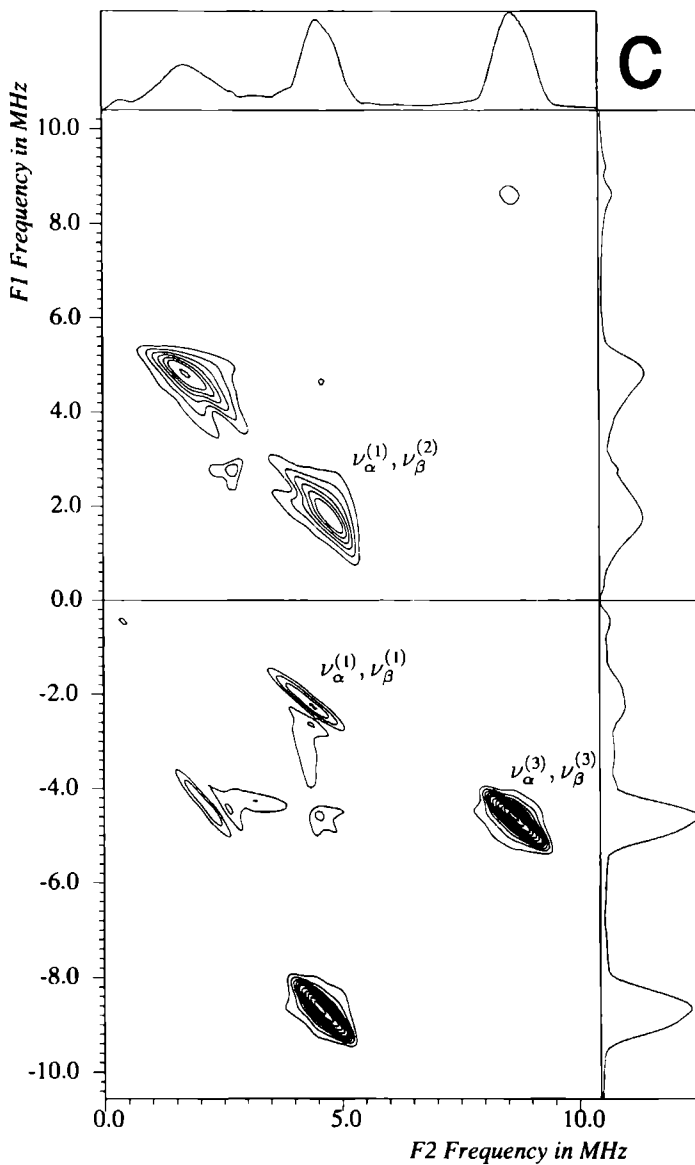


Figure 77: (This and following pages) Four-pulse 2D-ESEEM experiments of VO(mim)₄Cl⁺ measured at the parallel (a), perpendicular (b) and powder (c) positions. The first label of the correlation peaks refers to the horizontal frequency axis while the second is related to the vertical axis. In all spectra the fixed waiting time τ was 120 ns, the $\pi/2$ pulses had a duration of 32 ns whereas the π pulse was 16 ns in length.

2D HYSORE, VO(mim)4-Cl, perpendicular position



2D HYSORE, VO(mim)4-Cl, powder position



clearly deviates from 90° as well as the orientation of the ligands with respect to the plane normal to the $V = O$ axis.

Two-dimensional ESEEM spectroscopy of disordered solids certainly holds a promise for the future. In our experimental spectra, not only the sharp features were retained (double-quantum transitions), but also the strongly broadened single-quantum transitions were recovered from the dead-time. Extension of 2D-ESEEM techniques to orientation selective studies will enable a much more accurate estimation of the **A** and **P** tensor parameters. Also the way is open to study systems with multiple, nonequivalent interacting nuclei since the contributions from the individual nuclei can be readily separated in the 2D-frequency domain.

References

- [1] E. de Boer, Y. van Kooyk, M. G. M. Tromp, H. Plat, and R. Wever. Bromoperoxidases from *Ascophyllum Nodosum*: a novel class of enzymes containing Vanadium as a prosthetic group? *Biophysica Biochimica Acta* **869** (1986) 48.
- [2] E. de Boer, M. G. M. Tromp, H. Plat, B. E. Krenn, and R. Wever. Vanadium(V) as an essential element for haloperoxidase activity in marine brown algae: Purification and characterization of a Vanadium(V)-containing bromoperoxidase from *Laminaria Saccharina*. *Biophysica Biochimica Acta* **872** (1986) 104.
- [3] E. de Boer, K. Boon, and R. Wever. Electron Paramagnetic Resonance Studies on Conformational States and Metal Ion Exchange Properties of Vanadium Bromoperoxidase. *Biochemistry* **27** (1988) 1629.
- [4] E. de Boer *et al.* ^{14}N coordination to VO^{2+} in reduced vanadium bromoperoxidase, an electron spin echo study. *FEBS Letters* **235** (1988) 93.
- [5] E. J. Reijerse and C. P. Keijzers. Model calculations of frequency domain ESEEM spectra of disordered systems. *Journal of Magnetic Resonance* **71** (1987) 83.
- [6] E. J. Reijerse and C. P. Keijzers. ESEEM spectra of ordered and disordered systems. In C. P. Keijzers, E. J. Reijerse, and J. Schmidt, editors, *Pulsed EPR, a new field of applications*, p. 114. North Holland, Amsterdam, 1989.
- [7] E. J. Reijerse, J. J. Shane, E. de Boer, and D. Collison. ESEEM of nitrogen coordinated Oxo-Vanadium(IV) complexes. In N. D. Jordanov, editor, *Electron Magnetic Resonance of Disordered systems I*, pp. 189–204. World Scientific, Singapore, 1989.
- [8] L. J. Calviou *et al.* Imidazole and related heterocyclic ligand complexes of oxovanadium(IV) - potential models for the reduced vanadium site of seaweed bromoperoxidases. *Polyhedron* **8** (1989) 1835.
- [9] C. P. Keijzers, E. J. Reijerse, and J. Schmidt, editors. *Pulsed EPR, a new field of applications*, page 65, p. 65. North Holland, Amsterdam, 1989.

- [10] E J Reijerse *Electron Spin Echo spectroscopy on transition metal complexes* PhD thesis, University of Nijmegen, 1987
- [11] C Gemperle, G Aebli, A Schweiger, and R Ernst Phase Cycling in pulse EPR *Journal of Magnetic Resonance* **88** (1990) 241
- [12] N D Chasteen Vanadyl(IV) EPR spin probes. Inorganic and Biochemical aspects. In L Berliner and J Reuben, editors, *Biological magnetic resonance*, volume 3, p 53 Plenum Press, New York, 1981
- [13] A V Astashkin and S A Dikanov Coordination of Vanadyl Acetylacetonate with nitrogen containing donor bases *Journal of Structural Chemistry* **26** (1985) 363
- [14] N D Yordanov Recent EPR and ENDOR studies on the structure and solute-solute solvent interactions of transition metal complexes. In N D Yordanov, editor, *Electron Magnetic Resonance of Disordered systems I*, p 149 World Scientific, Singapore, 1989
- [15] P Hofer, A Grupp, H Nebenfur, and M Mehring Hyperfine sublevel correlation (HYSCORE) spectroscopy. A 2D ESR Investigation of the squaric acid radical *Journal of Chemical Physics* **132** (1986) 279

Electron Spin Echo Envelope Modulation Spectroscopie van Wanordelijke Vaste Stoffen

Een Samenvatting

In de laatste 15 jaar heeft het gebied van gepulste EPR een sterke groei doorgemaakt. Ontwikkelingen in snelle electronica en microgolffapparatuur hebben de problemen overwonnen die de ontwikkeling van gepulste EPR sinds de eerste experimenten in 1958 in de weg hebben gestaan. In de laatste jaren is een groot aantal nieuwe technieken voorgesteld en sinds 1988 is er een commerciële FT-EPR spectrometer op de markt.

Electron Paramagnetische Resonantie spectroscopie werd bijna 50 jaar geleden uitgevonden door E. Zavoiskii. Kort daarna werd de techniek door Bloch, Purcell en Pound uitgebreid naar de toepassing op kernspins. Omdat het kernspinresonantie experiment technisch minder gecompliceerd is dan EPR concentreerden de ontwikkelingen zich in de eerste jaren voornamelijk op NMR. Al in 1946 presenteerde Bloch de eerste gepulste NMR experimenten. Deze ontwikkeling kon echter niet direct worden toegepast in electron paramagnetische resonantie daar in EPR de directe detectie van het FID signaal in het gepulste NMR experiment meestal niet mogelijk is.

De ontdekking van spin echo's door Erwin Hahn in 1950 opende een weg uit dit dilemma. De eerste electron spin-echo experimenten werden uitgevoerd in 1958 door Gordon en Bowers, met de bedoeling electronspinrelaxatietijden te meten. Een jaar eerder had Blume al met behulp van een gepulste EPR techniek met een RF frequentie van 17.4 MHz, overeenkomend met een magneetveld van 6.2 Gauss, electronspinrelaxatietijden in een natrium-ammonia oplossing gemeten. Het experiment van Gordon en Bowers is echter significanter daar zij een frequentie in het microgolfgedebiet gebruikten.

De volgende stap in de ontwikkeling van gepulste EPR gebeurde in 1961, toen Mims en zijn medewerkers modulaties die afkomstig waren van een ^{183}W kern observeerden op de echo intensiteit gemeten aan een CaWO_4 monster. Deze experimenten werden nader verklaard in een artikel van Rowan, Hahn en Mims, getiteld „Electron-Spin-Echo Envelope Modulation”, dat gepubliceerd werd in 1965. Zeven jaar later verschenen er een aantal artikelen van de hand van W.B. Mims, een van de pioniers van ESEEM, waarin hij in detail het mechanisme van het ESEEM experiment verklaarde en tevens een aantal formules presenteerde die het kernmodulatie effect beschreven. Deze formules vormden de basis van veel later onderzoek.

Na de ontwikkeling van tweedimensionale NMR experimenten door Jeener kwamen Merks en de Beer in 1979 met een tweedimensionale variant van het ESEEM experiment. In de tachtiger jaren onstonden vele nieuwe experimenten vooral ook door het beschikbaar komen van de daarvoor benodigde electronica en microgolf componenten. Een belangrijke ontwikkeling met betrekking tot dit proefschrift is de ontwikkeling door Hofer van de tweedimensionale

HYSORE techniek en het opkomen van multifrequentie technieken voorgesteld door Singel en medewerkers Samen met orientatie-selectieve technieken, bekend van ENDOR spectroscopie, vormen deze technieken de basis van dit proefschrift

Het ESEEM experiment

In Continuous Wave EPR zijn zwakke electron-kern interacties vaak verborgen onder de inhomogene lijnbreedte Deze kleine interacties kunnen echter vaak worden opgelost door gebruik te maken van ENDOR of ESEEM spectroscopie Met deze technieken wordt het mogelijk de interactieparameters van zwak gebonden kernen en kernen die zich ver van het electron bevinden te meten Dit maakt deze technieken uitermate geschikt voor het onderzoeken van de elektronische en ruimtelijke structuur van paramagnetische metallo-organische verbindingen Het mechanisme van het ESEEM experiment wordt behandeld in hoofdstuk 3, en tevens in het boek „Electron Spin Echo Envelope Modulation (ESEEM) Spectroscopy” geschreven door Sergei Dikanov en Yuri Tsvetkov (CRC Press, Boca Raton) Dit boek geeft verder een uitstekend overzicht van de toepassingen van ESEEM

Een belangrijke toepassing ligt op het gebied van het metallo enzym onderzoek, waar het gebruikt wordt voor het ophelderen van de locale structuur van het actieve centrum De parameters die de electron-kern interacties beschrijven geven accurate informatie over de elektronische en ruimtelijke structuur rond het metaalion Deze parameters kunnen het meest nauwkeurig bepaald worden uit eenkristallen Een probleem is echter dat metallo-enzymen, en vele andere biologisch interessante systemen, niet beschikbaar zijn in eenkristal vorm en dus slechts in poedervorm of in een bevroren oplossing bestudeerd kunnen worden

Dit proefschrift gaat voornamelijk over de problemen die optreden bij de toepassing van ESEEM spectroscopie aan stikstof-14 (kernspin $I = 1$) kernen in wanordelijke systemen, speciaal die stikstofkernen die aanwezig zijn in de liganden van het metaalion in metallo-enzymen In het kader van het project zijn model systemen voor twee klassen van enzymen met totaal verschillende spectroscopische eigenschappen als onderwerp gekozen

- Hoofdstuk 5 bespreekt de metingen aan éenkristallen en poeders van *l*-histidine waarin een kleine hoeveelheid koperionen is aangebracht Dit systeem is een model voor type II koper-bevattende enzymen, zoals laccase en β -dopamine hydroxylase
- Hoofdstukken 6 en 7 beschouwen een aantal modelsystemen voor oxo-vanadium bevattende enzymen zoals bromoperoxidasen

Deze modelsystemen zijn onderzocht met behulp van multidimensionale en orientatie-selectieve ESEEM technieken bij verschillende microgolffrequenties in een poging niet alleen de structuur van deze modelsystemen te bepalen, maar tevens te onderzoeken hoe goed deze technieken bruikbaar zijn voor dit type systeem

Inhoud

Dit proefschrift bestaat uit zeven hoofdstukken. Hoofdstuk 1 is een korte introductie, waarvan deze samenvatting de Nederlandse vertaling is. Hoofdstuk 2 beschrijft de spectrometer die gebruikt is in dit proefschrift. Het eerste deel gaat over de apparatuur, zoals de microgolflussen en de resonatoren, en het tweede deel beschrijft de computer en bijbehorende programmatuur die ontwikkeld is voor het project.

Hoofdstuk 3 introduceert de theorie van electronspinecho spectroscopie aan de hand van het dichtheidsmatrix formalisme, in contrast met vele andere teksten over dat onderwerp. Dit formalisme wordt verder gebruikt om het kernmodulatie effect te verklaren. Tevens wordt het HYSORE experiment geïntroduceerd en er wordt een algemene uitdrukking afgeleid die het kernmodulatie effect in het tweedimensionale HYSORE experiment beschrijft. Hoofdstuk 4 gaat dan dieper in op dat experiment. De toepassingen van HYSORE in het onderzoek van wanordelijke systemen is een belangrijk onderwerp van dit hoofdstuk, dat gepubliceerd is in het *Journal of Magnetic Resonance*.

Hoofdstukken 5 tot en met 7 beschrijven de experimenten gedaan aan een aantal modelsystemen. In hoofdstuk 5 worden de resultaten van metingen aan eenkristallen en poeders van met koper gedoteerd *l*-histidine vergeleken. Zo is het mogelijk om een indruk te krijgen van de nauwkeurigheid van de informatie verkregen uit wanordelijke materialen door middel van multifrequentie experimenten gecombineerd met orientatie-selectieve tweedimensionale (3-puls) ESEEM technieken. De interactieparameters van het niet directgebonden stikstofatoom uit de imidazole ring van het histidine molecuul kunnen dan gebruikt worden voor de bepaling van de locale structuur rond het metaalion. Dit systeem staat model voor blauwe (type II) koper enzymen, welke al geruime tijd met behulp van ESEEM bestudeerd worden door een aantal onderzoeksgroepen. Dit hoofdstuk is ter publicatie voorgelegd aan de redactie van *Applied Magnetic Resonance*.

Hoofdstukken 6 en 7 handelen over modelsystemen voor een tweede klasse van metallo-enzymen. De spectroscopische eigenschappen van oxo-vanadium verbindingen verschillen sterk van die van type II koper enzymen. De stikstofkernen die onderzocht worden zijn nu direct gebonden aan het metaalion, maar de electron-kern koppeling is vrij zwak. De multifrequentie experimenten die zo belangrijk waren in de studie van de kopercomplexen zijn minder goed toepasbaar op deze systemen. Daarentegen blijkt dat de HYSORE techniek voor deze systemen zeer waardevolle informatie kan leveren. De twee artikelen waarop deze hoofdstukken zijn gebaseerd zijn gepubliceerd in de „proceedings” van de in 1989 en 1991 in Pravitz en in Gjulechitsa (Bulgarije) gehouden conferenties over „Electron Magnetic Resonance of Disordered Solids”.

Curriculum Vitae

Ik ben geboren op 2 Juli 1966 te Leiden. Na dertien kinderjaren in Oegstgeest doorgebracht te hebben verhuisde ik naar Nijmegen waar ik in 1984 eindexamen ongedeeld VWO behaalde. In datzelfde jaar begon ik aan de studie Natuurkunde aan de Katholieke Universiteit Nijmegen. Deze studie zette ik vanaf September 1985 voort aan de Rijksuniversiteit Leiden.

Mijn eerste laboratorium ervaring deed ik op tussen mei 1987 en Augustus 1988 bij de vakgroep Biofysica, waar ik onder leiding van Professor A.J. Hoff en Dr. E.J. Lous werkte aan optisch gedetecteerde magnetische resonantie en magneetveldeffecten in fotosynthetische reactiecentra. Gedurende deze periode was ik tevens lid van het vakgroepsbestuur van deze vakgroep. Deze periode werd afgesloten met het behalen van mijn doctoraal-bul in 1988.

Direct na mijn afstuderen verhuisde ik terug naar Nijmegen om onder leiding van Professor E. de Boer en Dr. E.J. Reijerse onderzoek te doen naar electron spin-echo envelop modulatie technieken voor het bestuderen van wanordelijke systemen als poeders en bevroren oplossingen van eenvoudige systemen die model staan voor meer gecompliceerde bio-moleculen zoals metallo-enzymen. De bevindingen van dit onderzoek zijn gepresenteerd in een viertal artikelen en tijdens een aantal conferenties, zowel in Nederland als daarbuiten. Dit proefschrift is de afronding van dit onderzoek.

Sinds 26 Oktober 1993 ben ik als postdoctoraal medewerker verbonden aan het Weizmann Instituut in Rehovot, Israel.

STELLINGEN

behorend bij het proefschrift

'Electron Spin Echo Envelope Modulation Spectroscopy of Disordered Solids'

- i De vijf-puls variant van het HYSORE experiment heeft als voordeel boven het meer gebruikelijke vier-puls experiment dat er geen storende bijdrage van de drie-puls gestimuleerde echo in het spectrum aanwezig is
Dit proefschrift, hoofdstuk 3

- ii Het vermoeden van Hirasawa en Kon dat in het met koper gedoteerde histidine kristal rond het koper-ion een verstoring van de structuur van de imidazole ring optreedt wordt niet bevestigd door ESEEM metingen
R Hirasawa en H Kon, J Chem Phys 56 (1972), 4467
M Colaneri en J Peisach, J Am Chem Soc 114 (1992), 5335
Dit proefschrift, hoofdstuk 5

- iii Het gebruik van computerprogrammas voor symbolische algebra geeft op zich geen garantie dat de gepubliceerde formules ook correct zijn
C Gemperle en A Schweiger, J Magn Reson 88 (1990), 241
Dit proefschrift, hoofdstuk 3

- iv De IBM Personal Computer in combinatie met het MS-DOS operating system is niet bijzonder geschikt voor real-time data acquisitie
Dit proefschrift, hoofdstuk 2

- v. Dat bij EPR spectroscopie gebruik wordt gemaakt van onderdelen die ook bij het leger in gebruik zijn wordt pijnlijk duidelijk tijdens internationale gewapende conflicten.

- vi. De beschikbaarheid van tekstverwerkings programmatuur is niet noodzakelijk een zegen voor de promovendus.

- vii. De staatscourant als medium voor het bekendmaken van regeringsbesluiten lijkt te worden vervangen door het laten uitlekken van geheime nota's.

- viii. Op het gebied van de gezondheidszorg lijken veel politieke partijen van Nederland hun verkiezingsprogramma's te hebben gebaseerd op het systeem beschreven door Samuel Butler in 'Erewhon'.

Jaap Shane
25 Oktober 1993

